A STUDY OF TURBULENCE IN TRANSIENT CHANNEL FLOWS

A Dissertation Submitted for the Degree of Doctor of Philosophy

By

Sam Gorji

Department of Mechanical Engineering

The University of Sheffield

April 2015

Abstract

A water flow loop facility is designed, built and commissioned to investigate the effects of flow unsteadiness on the mean and turbulent characteristics of smooth and rough wall channel flows. Measurements of flow and turbulence are made by means of non-intrusive measurement techniques such as Particle Image Velocimetry (PIV) and Laser Doppler Velocimetry (LDV). The main objective of these investigations is to advance our understanding on the behaviour of turbulence under transient conditions.

The unsteady flows considered, consist of an excursion of flow rate from an initial turbulent state to another over smooth or rough surfaces. A systematic study of turbulence under various initial and final conditions reveals novel insights into the turbulence dynamics of unsteady flows. It is shown that the unsteady flows behave strikingly similar to the so-called boundary layer bypass transition due to free-stream-turbulence. Consistent with the direct numerical simulations (DNS) of He and Seddighi (J. Fluid Mech., 715: 60-102), the process begins with the elongation of streaks much similar to the Klebanoff modes in the buffeted laminar boundary layer in a bypass transition. During the second stage, the formation and propagation of the isolated turbulent spots eventually lead to a complete breakdown of the organised streaky structures resulting in a new turbulent flow corresponding to the final Reynolds number. The present investigation covers a range of initial and final Reynolds numbers over smooth and rough surfaces to elucidate the underlying mechanisms involved in transient flows.

The mean velocity profiles obtained from various unsteady cases are shown to correlate with each other during the pre-transition regime, coinciding with the Stokes solution for unsteady laminar boundary layer flows. The fluctuating velocity profiles are also correlated with each other during this period. The response of the perturbing wall-normal fluctuating velocity is

shown to mark the onset of transition, providing a good measure for the duration of the pre-transition phase.

It is shown that an equivalent critical Reynolds number can be defined to express the duration of the pre-transition regime in unsteady flows. The critical Reynolds number is shown to have a power-law relationship with the initial free-stream turbulence intensity levels.

The unsteady rough flows investigated herein encompass a hydrodynamically smooth initial flow that is increased to either a transitionally or fully rough final state. The measurements of the fluctuating streamwise velocities in the wall region reveal a similar transition-like behaviour to the smooth-wall flows. It is shown that the particular roughness pattern investigated herein causes a significant decrease in the duration of the pre-transition regime, promoting an early transition. For relatively high intensity levels, an inner-scaled non-dimensional time correlates the period of the pre-transition regime.

In addition to the experimental investigations, numerical simulations are performed to assess the applicability and robustness of various turbulence models under unsteady conditions. For this purpose, performance of a number of low-Reynolds number turbulence models is evaluated against DNS data. All models are applied to an unsteady flow comprising a ramp-type excursion of flow rate inside a channel. The flow rate is increased linearly with time from an initial Reynolds number of $Re_0 = 9{,}308$ (based on hydraulic diameter and bulk velocity) to a final Reynolds number of $Re_1 = 29{,}650$. The acceleration rate is varied to cover low, intermediate and high accelerations. It is shown that among the models investigated, the $k - \varepsilon$ models of Launder and Sharma (Lett. Heat Mass Transfer, 1(2), 131-137) and Chang et al. (J. Fluids Eng., Trans. ASME, 117(3): 417-423) and $\gamma - Re_\theta$ of Langtry and Menter (AIAA Journal, 47(12): 2894-2906) capture well the key flow features of these unsteady turbulent flows. These three models yield predictions of wall shear stress that agree well with the corresponding DNS data, though for the case of high acceleration, the model of Chang et al. exhibits instabilities.

Acknowledgements

My sincere gratitude goes to my supervisors, Professors Shuisheng He, Dubravka Pokrajac and Tom O'Donoghue for providing such a unique opportunity for me to carry out this work. Primarily, I would like to thank Professor He for the guidance, support and encouragement he has given me throughout this study without which, completion of this project was barely possible.

I would also like to thank Professor Alan Vardy and Dr Mehdi Seddighi for their guidance and encouragement.

Thanks to the technical staff of the Mechanical Engineering Workshop, in particular, Karl, John and Wayne for their work on the water flow loop facility.

I would like to deeply thank my wife, Niloufar, for her patience, support and endless love. I would also like to thank my parents Mehran and Roshanak for the inspiration, vision and support they have given me throughout my life.

I would like to gratefully acknowledge the funding provided by the UK Engineering and Physical Sciences Research Council (EPSRC) and the Department of Mechanical Engineering of the University of Sheffield which enabled me to undertake this project.

Contents

List of figures

List of tables

Nomenclature

B	Constant
C_f	Friction factor
$C_{\varepsilon 1}, C_{\varepsilon 2}$	Constants in the ε transport equation
C_μ	Eddy viscosity constant
D	Diameter, additional term of the k transport equation
D_h	Hydraulic diameter, m
D_k	Original destruction term of the k transport equation in SST model
D_ω	Destruction term of the ω transport equation in SST model
d	Probe diameter, μm
d_{PIV}	Length of interrogation areas, mm
E	Additional term in the ε transport equation
E_γ	Dissipation term of the γ transport equation
F	Flatness, m^4/s^4
F_1, F_2	Blending functions in the ω transport and ν_t equation
$F_{1\,org}$	Blending function in the ω transport equation of SST model
f_1, f_2	Functions in the ε transport equation
f_μ	Damping function
H	Channel full-height, shape factor
h	Channel half-height, m
k	Height of roughness, turbulent kinetic energy
L	Length, m
M	Magnification factor
P_k	Production of the turbulent kinetic energy

$P_{\gamma 1}, P_{\gamma 2}$	Intermittency production terms
Q	Volumetric flow rate, m^3/hr
R	Diameter
Re	Reynolds number
Re_b	Reynolds number based on channel half-height and bulk velocity
Re_{bH}	Bulk Reynolds number based on channel full height and bulk velocity
Re_{cr}	Critical Reynolds number
Re_{turb}	Turbulent Reynolds number
Re_θ	Momentum thickness Reynolds number
Re_τ	Friction Reynolds number
$\widetilde{Re}_{\theta t}$	Local transition onset momentum thickness Reynolds number
S	Skewness, m^3/s^3; Absolute value of strain rate, $\left(2S_{ij}S_{ij}\right)^{-1/2}$
t	Time, sec
Tu	Free-stream turbulence intensity
U, V, W	Streamwise, wall-normal and spanwise velocities, m/s
U_b	Bulk velocity, m/s
U_c	Centreline velocity, m/s
U_t	Effective centreline velocity, m/s
u', v', w'	Fluctuating streamwise, wall-normal and spanwise velocities, m/s
${u'}_{rms}, {v'}_{rms}, {w'}_{rms}$	Streamwise, wall-normal and spanwise rms fluctuating velocities, m/s
$\overline{u'^2}$, $\overline{v'^2}$, $\overline{w'^2}$	Streamwise, wall-normal and spanwise normal Reynolds stresses, m^2/s^2
$\overline{u'v'}$	Reynolds shear stress, m^2/s^2
u_τ	Friction velocity, m/s
W	Channel width
x, y, z	Streamwise, wall-normal and spanwise directions
α, β	Constants
γ	Intermittency
$\Delta Re_{t,cr}$	Period of transition
Δt	Duration of flow excursion, sec
ΔU^+	Roughness function
δ	Boundary layer thickness, m
δ_t	Effective channel half-height, m
$\varepsilon, \tilde{\varepsilon}$	Dissipation rate, m^2/s^3

η	Stokes similarity parameter
θ	Momentum thickness, m
κ	von Kármán constant
ν	Kinematic viscosity, m^2/s
ν_t	Eddy viscosity, m^2/s
ρ	Density, kg/m^3
σ	Repeatability
$\sigma_{\theta t}, \sigma_k$	Prandtl number
τ_w	Wall shear stress, Pa
Φ	Representative velocity

Subscripts:

$0, 1$	Initial and final states
b	Bulk
c	Centreline
cr	Critical state
du	Differential flow
i, j, k	Dummy variables
$meas$	Measured component
s	Sand grain
t	Effective parameter in rough flows
$true$	True value of a velocity component
$turb$	Fully turbulent state

Superscripts:

$+$	Inner scaling
$*$	Outer scaling
^	Perturbing velocity component

Abbreviations:

BR	Background Removed
CCD	Charge-Coupled Device
CFD	Computational Fluid Dynamics
CNC	Computer Numerical Control
CONV	Convection
DAQ	Data Acquisition

DNS	Direct Numerical Simulation
DOF	Depth of Field
EPSRC	Engineering and Physical Sciences Research Council
FOV	Field of View
FST	Free-stream Turbulence
IA	Interrogation Area
LDV	Laser Doppler Velocimetry
MCV	Measuring Control Volume
PDF	Probability Density Function
PIV	Particle Image Velocimetry
PVC	Polyvinyl Chloride
RANS	Reynolds-Averaged Navier-Stokes
RMS	Root Mean Square
T-S	Tollmien - Schlichting
ZPG	Zero Pressure Gradient

Chapter 1. Introduction

1.1 Background

The research reported in this thesis is a collaboration between the University of Sheffield, University of Aberdeen and the University of Dundee and is funded by the Engineering and Physical Sciences Research Council (EPSRC). The overall project involves both numerical and experimental investigations of unsteady turbulent channel flows over smooth and rough surfaces. Direct Numerical Simulation (DNS) technique is used for the numerical analysis, which is undertaken by a post-doctoral research assistant, while this author is responsible for the experimental investigations as well as numerical modelling of the unsteady flows using Reynolds-Averaged Navier-Stokes (RANS) framework.

Unsteady turbulent flows are present in many engineering systems such as pipe networks, railway tunnels and biological circulatory systems. Our understanding of such flows can potentially lead to better predictions of flow conditions in many engineering applications.

The ultimate goal of the present research is to contribute to the development of new analytical or semi-empirical end-user formulations to model unsteady flows in pipe networks; to improve our understanding of the fundamental behaviour of turbulence which can be of great importance to turbulence modeller's community; and to shed light on the new development in transient channel flow transition.

A water flow loop facility with advanced instrumentation and flow control is designed and built in the Department of Mechanical Engineering at the University of Sheffield to examine the behaviour of flow and turbulence under unsteady conditions in smooth and rough channel flows. Furthermore, numerical simulations through the RANS framework are conducted to assess the performance of various turbulence models under unsteady conditions.

1.2 Aims and objectives

The aim of this research is to further develop our understanding of unsteady turbulent flows using advanced measurement techniques. The main attention of this research is devoted to *temporal accelerating* flows that consist of an initial fully developed turbulent flow at a specific flow rate, followed by a rapid acceleration to a higher one. This excursion of flow rate with respect to time is investigated at various final to initial conditions. The experimental results are used to validate numerical simulations and support the new findings from DNS of He and Seddighi (2013). The specific objectives of the research covered by this thesis are:

i. To develop a flow facility instrumented with advanced measuring equipment for fundamental research on turbulence in unsteady flows.
ii. To produce experimental evidence and provide benchmark data for new understanding of transient channel flow by performing systematic measurements of accelerating flows over smooth and rough surfaces.
iii. To evaluate the performance of RANS turbulence models in simulating unsteady flows against DNS data.

1.3 Thesis outline

This thesis consists of eight chapters. The Second Chapter summarises the recent developments in various related topics to this research. These topics consist of experimental and numerical investigations of unsteady channel and pipe flows, laminar to turbulence transition, flows over rough surfaces as well as RANS modelling of unsteady flows. The third Chapter discusses in detail the design and construction of the rig, the measurement campaign and methodology behind each of the applied techniques. Chapter Four presents and discusses data obtained from steady flows over smooth and rough surfaces. Chapters Five and Six present and discuss the results on the unsteady flows over smooth and rough surfaces, respectively. Chapter Seven presents and discusses the results obtained from numerical simulations of unsteady flows over smooth surfaces obtained from the Reynolds-Averaged Navier-Stokes (RANS) simulation framework. The last Chapter provides a conclusion from the present investigations and discusses future works.

Chapter 2. Literature Review

Unsteady turbulent flows occur in many engineering applications. Apart from the practical perspective, detailed study of unsteady turbulent flow structures leads to a profound understanding of the complex mechanisms that are generally absent in steady flows. This chapter describes the studies of the unsteady turbulent flows over both smooth and rough surfaces.

Research on unsteady turbulent flows is generally conducted through two main categories; periodic and non-periodic. The periodic flows can further be divided into pulsating and oscillatory. A periodic unsteady flow with a non-zero mean value is referred to as pulsating flow, whereas for oscillatory flows, the variation of flow rate occurs over a zero mean value. Pulsating flows are usually examined for a range of amplitudes and frequencies of the imposed flow rate as well as the mean Reynolds number of the flow. Non-periodic transient flows are characterised by the acceleration rate, ranging from very high rates which can be characterised as a step change to slow changes which in the limit become steady flow.

Factors that influence turbulent flows, which are encountered in many engineering applications, include wall temperature, wall blowing/suction, curvature and surface roughness. This project focuses on the effects of surface roughness on unsteady flows.

2.1 Unsteady flows over smooth surfaces

This section reviews the earlier experimental and numerical investigations of unsteady turbulent flows.

As mentioned earlier, unsteadiness can be imposed on the flow as periodic or non-periodic. Effects of flow unsteadiness on the generated boundary layer over the solid surface can be examined in different geometries. However, due to simplicity and wide applicability, the most

commonly examined geometries are flat plates, pipes and channels. The main focus of this research is on the channel flows.

As Uchida (1956) shows, laminar solution to the pulsating/oscillating boundary layer flow leads to a length scale l_s ($=\sqrt{2\nu/\omega}$) based on ν the kinematic viscosity and ω the frequency of the oscillation, describing the depth of oscillation. Due to the imposed oscillation, shear waves generated at the wall (caused by no slip condition) are propagated outwards. Beyond l_s the generated vorticity waves are attenuated and a uniform modulation imposes a "plug flow" manner. l_s is usually referred to as the Stokes layer thickness. It is apparent that by increasing the oscillation frequency ω, Stokes layer will become thinner. As a result, vorticity waves will be confined to a thinner layer of the entire flow field.

Three parameters characterise pulsating flows, the mean flow, the frequency of the oscillations and the ratio between oscillating and mean centreline velocity (the amplitude). Experimental studies (for instance Binder et al. (1995) and He and Jackson (2009)) have shown that for oscillation amplitudes of less than unity (sometimes referred to as current dominated flow), forcing frequency (ω) is a more influencing parameter on velocity and turbulent structures than the amplitude of oscillations.

Analogous to laminar pulsating flows, turbulent Stokes length $2l_t$ defines the extent to which the generated shear waves attenuate in turbulent flows. Turbulent Stokes length splits the flow into inner and outer regions analogous to the steady boundary layer regions. The interactions of these two layers have been the scope of many studies. This length scale has been first introduced by Tu and Ramaprian (1983). Scotti and Piomelli (2001) have shown that l_t can be defined, on the basis of eddy viscosity ν_t, as ($\sqrt{2(\nu+\nu_t)/\omega}$). The eddy viscosity was defined as $\nu_t = \kappa u_\tau l_t$, where κ is the von Kármán constant and u_τ is the friction velocity ($u_\tau = \sqrt{\tau_w/\rho}$). They have shown that the wall normalised turbulent Stokes length l_t^+ has the following relation to its laminar counterpart.

$$l_t^+ = l_s^+\left(\frac{\kappa\, l_s^+}{2} + \sqrt{1+\left(\frac{\kappa\, l_s^+}{2}\right)^2}\right) \tag{2.1}$$

As mentioned earlier the important role of forcing frequency on the flow field is undeniable in current dominated pulsating flows. Such flows can therefore be categorised into quasi-steady, low, intermediate, relatively and very high frequency regimes due to Scotti and Piomelli (2001). When the forcing frequency is very low, l_t^+ becomes much larger than the channel half height

(h) or pipe radius ($l_t^+ >> h^+,\ h^+ = h\,u_\tau/\nu$), in such a situation, the phases of turbulence quantities are independent of the wall distance. This regime is called quasi-steady.

The low-frequency regime begins where l_t^+ has the same order as h^+. In this regime, as one moves towards the wall region, production and dissipation of turbulence become out of phase and therefore equilibrium condition no longer prevails. In addition, turbulent kinetic energy production shows a significant phase asymmetry between the acceleration and deceleration cycles.

Within the intermediate frequency regime, $2l_t^+$ is smaller than h^+ and hence the inner and outer layers, as introduced earlier, exist simultaneously. Under such circumstances, the outer region experiences a frozen turbulence in a plug flow manner. Stokes solution yields a normalised speed $c^+ \sim \omega^+ l_t^+$ ($\omega^+ = \omega\nu/u_\tau^2$) representing the speed at which the generated shear waves propagate across the flow. At relatively large forcing frequencies, where Stokes length is thick, equation (2.1) can be rewritten as $l_t^+ = \kappa {l_s^+}^2$. Therefore c^+can be considered to be constant, leaving the speed *c* to be obtained from the friction velocity. By further increasing the forcing frequency within the relatively high frequency regime ($0.2 \geq \omega^+ \geq 0.04$), the propagation of shear waves is sustained beyond the viscous sublayer, further reducing the interaction between the inner and outer regions.

Further enhancement of forcing frequency leads to a complete detachment of the inner and outer layers, where the turbulence in the outer region would no longer be affected by the pulsation within the inner region. Therefore for very high frequency regime, flow patterns in the outer region can be seen as a steady state flow with a uniform modulation, demonstrating a plug flow. Turbulence in the inner region is attenuated rapidly inside the viscous sublayer while exhibiting a frozen pattern in the outer region. Such a situation is analogous to laminar Stokes flow, since ($\kappa\, l_s^+/2 \ll 1$) so from equation (2.1) $l_t^+ = l_s^+$, where eddy viscosity is no longer influential. Under such circumstances the amplitude of the modulation component of turbulence quantities should vanish in the outer region while the amplitude of modulation and phase lag of the wall shear should approach Stokes laminar values.

The mechanisms of turbulence production, redistribution of turbulence energy and diffusion associated with the acceleration and deceleration cycles of pulsating flows are analogous to ramp type excursions discussed next. As He and Jackson (2009) explains, pulsation of flow rate can be considered as a series of small perturbations initially felt in the wall region due to the no-slip condition. The turbulence field remains unaffected until the change in the mean flow causes

a turbulence production in the wall region. Therefore the relationship between the Stokes layer thickness and the location where the turbulence production is occurred becomes of significant importance in characterising the behaviour of turbulence.

The redistribution of turbulence from the axial component to the transverse and circumferential components due to the action of pressure results in further delays of these two components. This process also results in the attenuation of the amplitude of the modulation of transverse and circumferential fluctuating velocities in pulsating flows.

Propagation of turbulence from the wall to the core region introduces a delay in the turbulence field. The speed of turbulence propagation was shown to be independent of the frequency of the modulation and sensitive to the mean flow, specifically the friction velocity (He and Jackson, 2009).

In addition to the studies on unsteady periodic flows, there has been an interest in non-periodic unsteady flows as well. Experimental studies of Kataoka et al. (1975), Maruyama et al. (1976), Lefebvre (1987), He and Jackson (2000), Greenblatt and Moss (1999), Greenblatt and Moss (2004) and He et al. (2011) are some examples of research on non-periodic flows. Numerical investigations of Moin et al. (1990), Chung (2005), He et al. (2008), Ariyaratne et al. (2010), Seddighi et al. (2011), Di Liberto and Ciofalo (2011), Jung and Chung (2012), He and Seddighi (2013), Gorji et al. (2014) and Seddighi et al. (2014) examined sudden changes of pressure gradients or linear ramp up/down flow rates.

Kataoka et al. (1975) investigated a step change of flow rate from rest in pipe flows. They observed that the transition from laminar to turbulent flow was postponed as the final Reynolds number was increased. Maruyama et al. (1976) conducted a similar type of experiment, where response of turbulence was found to be slower in the core region than other locations. Moin et al. (1990) investigated the flow behaviour using Direct Numerical Simulation (DNS) in a channel flow subjected to sudden spanwise pressure gradients. It was shown in their investigations that the spanwise pressure gradient resulted in a suppressed turbulent activity. Chung (2005) also employed DNS to investigate the effects of sudden change in the streamwise pressure gradients in a decelerating turbulent channel flow. It was observed that there was no significant deviation from the log law during the excursion. Rate of response to the imposed pressure gradient is seen to differ between the three normal Reynolds stress components which is a sign of significant anisotropic behaviour. Seddighi et al. (2011) examined the flow behaviour under step increase and decrease of streamwise pressure gradient in a channel geometry. It was noticed that the

deviations of turbulent quantities from the quasi-steady values are more significant in accelerating than decelerating flows of similar magnitudes. A step increase of pressure gradient was shown to have similar effects on the turbulence field as in ramp-up flow excursions. The main distinction between the step-up and step-down changes of pressure gradient on the turbulence pattern was shown to be the length of the delay and the effect of the redistribution process of turbulence.

He and Jackson (2000) focused their experimental research on linearly increasing and decreasing flow rate in a fully developed pipe flow. They identified three delays associated with the response of turbulence. Delays in turbulence production, turbulence energy redistribution and its radial propagation were found to be the key features of such unsteady turbulent flows. It was found that the first response to the imposed flow rate was initiated from a region close to the wall with highest turbulence production (buffer layer). The axial component of Reynolds stress was found to be the first responding to the excursion while the other two normal components were still experiencing a period of delay. It was concluded that due to the action of turbulent diffusion the response of turbulence to the flow excursion propagates towards the centre. The situation in the ramp down (decelerating) case was found to be somehow similar. However, delays associated with the flow excursion were found to be smaller than in the accelerating case. The wall-normal stress component was shown to be responding later than the streamwise component. Turbulence intensity was shown to be increasing in the decelerating flows.

He et al. (2008) have identified three stages in the development of wall shear stress in ramp-type flow rate excursions through numerical studies. The first stage is due to the delays of turbulence and the dominance of the inertial forces. This stage covers the duration where the wall shear stress overshoots and then decreases and undershoots the values of the quasi-steady shear stress. They have also shown that a non-dimensional parameter involving inner turbulence time scales associated with the turbulence production correlates the unsteady wall shear stress components very well. It is shown by He and Ariyaratne (2011) that in this stage the unsteady component of the wall shear stress behaves in a laminar-like manner. Second stage begins with the generation of new turbulence that causes the wall shear stress to escalate. It is shown by He et al. (2011) that a correlation exists involving outer turbulence time scales that can be applied to determine the critical Reynolds number where transition from stage one to two occurs. The third stage includes the wall shear stress asymptotically approaching the quasi-steady value.

He and Seddighi (2013) have introduced a new concept in the study of unsteady flows. They have found striking similarities between the fully turbulent channel flows subjected to a step

increase of flow rate and boundary layer bypass transition due to free-stream turbulence (FST). They have shown that the initial flow structures undergo a process that involves three distinctive phases before reaching the final turbulent state. These phases consist of pre-transition, transition and fully turbulent stages that are equivalent to those seen in boundary layer bypass transition that are known as buffeted laminar flow, the intermittent flow and fully turbulent flow regions. They have shown that in transient channel flows, the initial streaky structures are elongated in the streamwise direction that are later disturbed by isolated turbulent spots. The generation of new turbulent packets due to instability eventually leads to a complete breakdown of the initial structures. This process is shown in Figure 2.1. These findings introduce a new analogy between the unsteady channel flows and FST induced transition.

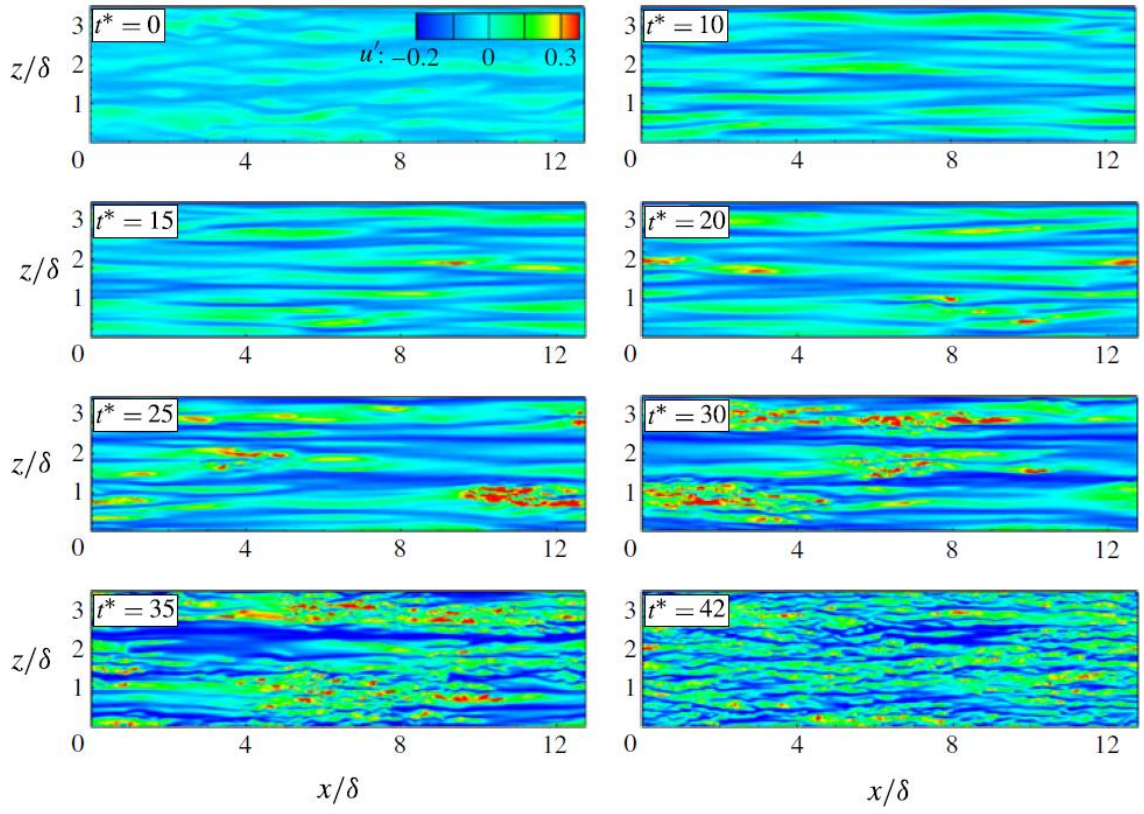

Figure 2.1 Temporal evolution of streamwise fluctuations in a plane adjacent to the wall (He and Seddighi (2013)).

Seddighi et al. (2014) have performed DNS to investigate the behaviour of unsteady turbulent flows with linearly accelerating flow rate. They have shown that the fundamental behaviour of turbulence during the transition process is similar to the step change flow conditions and consequently bypass transition. It was shown that in step-change of flow rate, a new boundary layer is generated instantly over the walls while ramp flow excursions produces a gradually-developing boundary layer.

He and Seddighi (2015) investigated various initial to final step-increase of flow rate ratios with DNS. They detected distinct differences between high and low final-to-initial Reynolds number ratios. Transition process during high ratio step-increases of flow rate was shown to be mainly characterised by the elongated streaks during the initial period that are followed by the generation and propagation of isolated turbulent spots. Whereas, flow structures under lower Re ratios show more progressive evolution. However, despite the distinctions in the flow structures, the behaviour of transient flow under both low and high final-to-initial Re was shown to be similar to laminar to turbulent transition. It was shown that during the pre-transition period, development of boundary layer under various final to initial Re had similar behaviour, closely following the Stokes solution. They also showed that a power-law correlates the critical time, where the transition process is initiated, to the unsteady-equivalent free-stream turbulence intensity. The unsteady-equivalent free-stream turbulence intensity was defined in such way to provide a measure for the rate of temporal acceleration.

It must be mentioned that there are similarities between the temporal and spatial accelerating/decelerating flows. In the flows subjected to streamwise pressure gradients it was found that spatially decelerating flows result in an amplification of turbulence intensity contrary to accelerating flows where the turbulence is shown to be attenuated. Comprehensive reviews on spatial accelerating and decelerating flows are provided by Smits and Wood (1985) and Bushnell and McGinley (1989).

2.2 Bypass transition

It has been a long time since researchers and engineers first devoted their interest to a phenomenon which is present in many thermofluid systems, transition to turbulence. There has been a great deal of research in the past centuries to study the processes involved in a laminar flow undergoing transition to a fully turbulent state. Identification of the characteristics in transitional flows leads to prediction and therefore control of such flows that have direct applications in many engineering design problems, such as improvement of mixing processes, skin-friction drag and heat transfer. These studies have mainly been conducted through various distinctive methods such as linear and non-linear stability theories, turbulence modelling, non-homogenous rapid distortion theory, experiments and direct numerical simulation.

The evolution of laminar to turbulent flow can take various forms. Transition to turbulence in a flat plate boundary layer occurs through either orderly (natural) or bypass transitions. The natural transition is a slow process occurring at high Reynolds numbers (order of 10^6). During this process two-dimensional Tollmien-Schlichting (T-S) waves are initially generated that are

only weakly unstable due to viscous processes. This specific route to turbulence can only be maintained if the free-stream turbulence intensity (Tu) remains less than 1%. These waves are then followed by secondary instabilities and eventually complete breakdown to turbulence. Arnal and Juillen (1978) have shown that for higher levels of free-stream turbulence intensity (>0.5-1%), T-S waves will no longer be generated. Under these circumstances, juxtaposed high and low streamwise velocity fluctuations appear, that are termed Klebanoff modes. This type of transition is referred to as bypass transition (Morkovin (1969)).

During the process of bypass transition, flow goes through three different stages (Jacobs and Durbin (2001)):

i. Buffeted laminar boundary layer
ii. Intermittent turbulent spot formation
iii. Fully turbulent boundary layer

In the first region, the boundary layer remains stable while elongated low and high streamwise velocity fluctuations begin to develop. Amplification of the streaks can be explained by rapid distortion theory (Phillips (1969)). Landahl (1980) explains the lift-up mechanism of mean momentum under these circumstances. DNS of zero-pressure-gradient (ZPG) boundary layer beneath grid turbulence of Jacobs and Durbin (2001) shows that the free-stream fluctuating streamwise velocity decays as flow reaches downstream, while flow within the boundary layer experiences a bypass transition. Contours of streamwise fluctuating velocity within the boundary layer clearly shows the elongation of streaks in the streamwise direction. These elongated streaks inside the boundary layer can reach very high amplitudes such as 20% of mean free-stream velocity with FST of only 3% (Zaki (2013)). However, these jets are only visible in the streamwise and not in the wall-normal direction.

During the second stage, localised perturbations trigger the instabilities which then cause turbulent spots. Two sources of secondary instabilities are identified which are of inner and outer nature (Vaughan and Zaki (2011)). The outer type of instability is one that is commonly seen in various experimental and numerical studies such as works of Jacobs and Durbin (2001) and Matsubara and Alfredsson (2001). The stability theory can be applied to detect a particular streak that is likely to transform to a secondary stability. Theoretical results of Reddy et al. (1998) suggest that this type of instability is mainly due to the inflection of the spanwise profiles of the streaky structures. However, the role of the Klebanoff modes that lead to the generation of secondary instabilities is still unknown. Durbin and Wu (2007) depict how an instability of Kelvin-

Helmholtz at the edge of the boundary layer evolves all the way down through the boundary layer to create a turbulent spot. The inner type of instability is first discovered by Nagarajan et al. (2007). They observed a wave-packet type of instability that emerged from the wall in their simulations of ZPG boundary layers with blunt leading edge. The theoretical work of Vaughan and Zaki (2011) investigates the nature of the inner and outer instabilities. It was found that the inner mode is connected with T-S waves and its growth rate is directly dependent on the amplitude and frequency of the base streaks.

The final stage of bypass transition is the complete breakdown of the flow structures to form a fully turbulent region that covers the entire span of the boundary layer. This process is highly nonlinear and therefore this region of the boundary layer can only be effectively studied by means of computer simulations.

Very limited information is available on the formation mechanisms of turbulent spots also known as bursts. The Orr-Sommerfeld theory can shed light on the difference of patterns inside and outside the boundary layer during the initial stages of transition. The formation of streaks (Klebanoff modes) can be explained by means of rapid distortion theory. Moffatt (1967) showed that the streamwise fluctuations grow linearly with time ($\overline{u^2} \propto t$). Gustavsson (1991) showed theoretically that the viscous processes diminish the maximum growth of streaks resulting in the decay of disturbances. He showed that in channel flows, Reynolds number is a suitable parameter to scale the growth rate. Therefore, according to his findings, a required time to achieve a certain growth is proportional to Re^{-1} ($Re = \frac{U_c h}{\nu}$, U_c being the centreline velocity, h is the channel half-height and ν being the viscosity). Luchini (1996) showed theoretically that in a boundary layer flow with three-dimensional disturbances, the streamwise disturbance velocities grow as $x^{0.213}$. The streamwise velocity profiles predicted from his investigations were in excellent agreement with experimental results. Luchini (2000) showed that by applying optimal perturbations (perturbations that maximise the energy growth) energy growth is proportional to x only.

Andersson et al. (1999) showed that the growth of disturbance energy is almost linear at a fixed spanwise wavenumber. Their results were in excellent agreement with the experimentally obtained fluctuating profiles of a boundary layer subjected to FST. They also proposed a simple relationship between the critical Reynolds number where the transition takes place and the free-stream turbulence intensity. This relationship correlates extremely well with the experimental results. This correlation is later confirmed by the experiments of Fransson et al. (2005).

Matsubara and Alfredsson (2001) experimentally examined boundary layer flows beneath grid turbulence with different levels of FST ranging from 1-6%. They found a form of scaling that collapses the energy spectra of streamwise disturbances at different locations along the boundary layer. Therefore, it was concluded that the streamwise length of these disturbances are proportional to the boundary layer thickness and that they grow linearly with downstream distance.

Ovchinnikov et al. (2008) performed a DNS study of bypass transition in high amplitude FST over a flat plate. The influence of FST's length scale on the mechanism of transition was found to be profound. FST with smaller length scales, results in outer source of instability while larger FST length scale, results in the formation of wavepacket type of instabilities.

Wu and Moin (2009) performed a DNS study of ZPG flat plate boundary layer with intermittent localised disturbances arising from patches of isotropic turbulence. Their results elucidate the role of Λ-shaped vortices that transform into hairpin shapes in the creation and breakdown of streaks.

2.3 Flows over rough surfaces

The characteristics of boundary layers produced over rough surfaces have always been of a huge interest in design applications such as aeroplanes, ships, fluid transport or even sports. Laboratory experiments were the first efforts to understand the effects of roughness on the fluid flow. Nikuradse (1933) was the first researcher who did extensive investigations on the flows inside circular sand-roughened pipes. By measuring the flow rate and the pressure drop along the pipe, he managed to plot the friction factor of different roughness sizes versus the Reynolds number. It was then observed that the friction factor in laminar flows was not affected by the roughness sizes while there was a huge difference of values in the turbulent regime. Years later, Moody (1944) plotted friction factor of the pipe to the relative roughness (that is the ratio of the roughness height to the pipe diameter) versus the Reynolds number on the basis of the results of Colebrook (1939) for the smooth and rough pipes. It should however be noted that the friction factors of the Moody diagram in the transitional rough flows were found to be overestimated for honed and commercial steel pipes (Allen et al. (2005) and Langelandsvik et al. (2008)). The Moody diagram was developed on the basis of sand roughness height k_s (sometimes called effective sand grain roughness). Therefore caution must be paid when applying Moody diagram to a generic roughness, since k_s should be determined experimentally as k_s contrary to the roughness height k is a flow property.

Flows over rough surfaces can be categorised into three regimes, hydrodynamically smooth $0 \leq k_s^+ \leq 5$, transitionally rough $5 \leq k_s^+ \leq 70$ and fully rough $70 \leq k_s^+$, where k_s^+ is the roughness Reynolds number, $k_s^+ = k_s u_\tau / \nu$. The presence of rough surface leads to a defect in velocity profile. The effect of roughness is generally incorporated to the smooth log-law velocity profile by an additional negative term called the roughness function (ΔU^+). This defect leads to a downward shift in the log-law profile. k_s^+ or ΔU^+both indicate the extent to which roughness interacts with the inner or outer regions of the flow.

If the roughness elements are confined to the viscous sublayer, the flow field is no different from that over a smooth surface. However, if the roughness penetrates out of the viscous sublayer region, deviations from the flows over smooth surfaces would be noticeable. By further growth of the roughness to the overlap region, the flow shall reside in the fully rough regime, where the flow is independent of the Reynolds number.

In the fully rough regime, viscosity dominancy is diminished. Therefore k_s becomes proportional to k and is dependent on the roughness geometry. It is worthy to note that Jiménez (2004) defines a well-characterised rough-wall flow, where $\delta/k > 40$, δ being the boundary layer thickness. In such a situation, effects of roughness on the flow field are usually examined through two characterising dimensions. One is the roughness height k and the other is the solidity λ which, as Schlichting (1936) defines, is the total projected frontal roughness area per unit wall-parallel projected area (this parameter represents the density of the roughness). Jiménez (2004) showed that there is a strong correlation between the ratio $k_s/C_D k$ (C_D being the drag coefficient) and λ obtained from the results of Schlichting (1936) and other researchers (Webb et al. (1971), Tani (1987), Bandyopadhyay (1987)). It is shown that the roughness effects (proportionality factor between k_s and k) rises as λ increases. However a critical solidity value exists where beyond it a reduction of this proportionality is seen. This reduction is due to the sheltering of the roughness elements leading to a weaker effect of roughness on the flow and hence a reduction of k_s. It should be mentioned that the power of λ is one of the major contributing factors for obtaining better correlations of roughness parameters.

d-type geometry refers to a surface with cavities of unit aspect ratio (width to height ratio), whereas the spacing between roughness elements is much larger in a *k*-type roughness. The geometrical difference between *d* and *k* type geometries is shown in Figure 2.2. Perry et al. (1969) found no correlation between the effective roughness k_s and roughness height k in ZPG boundary layer with *d*-type geometry. They observed that the effective roughness for a *d*-type roughness was proportional to the boundary layer thickness. This might be due to the isolation

of the flow inside the cavities and therefore a weak interaction between the inner and outer regions of the flow.

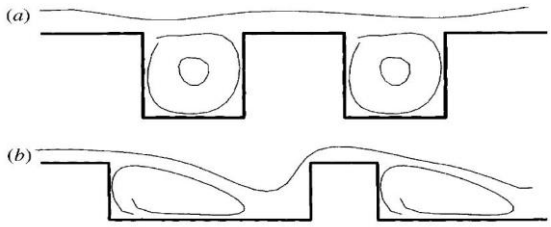

Figure 2.2 (a) *d*-type and (b) *k*-type roughness

Regarding the turbulence structure above the roughness sublayer, as Raupach et al. (1991) explains, three complementary hypotheses exist. These hypotheses lead to a better understanding of the flow and its correlating length and velocity scales. (1) Wall similarity hypothesis: Townsend (1976) noticed a flow similarity between different types of rough surfaces provided that the flow is in the fully rough regime. Wall similarity hypothesis postulates that the turbulent motions outside the roughness sublayer of the boundary layer are independent of the wall roughness and viscosity, while wall roughness is only affecting the flow by manipulating the friction velocity u_τ ($u_\tau = \sqrt{\tau_w/\rho}$), the displacement of the zero plane and the boundary layer thickness. (2) Equilibrium-layer hypothesis: Townsend (1976) states that the local rates of turbulent kinetic energy production and dissipation inside the inner layer (and still out of roughness sublayer) are so large that the aspects of the turbulent motions involved in these processes are independent of the flow conditions elsewhere. (3) Attached-eddy hypothesis: Townsend (1976) claims that the fully turbulent part of the boundary layer consists of eddies which are geometrically similar to each other, yet sharing a similar geometrical relationship with the wall.

Examples of the experimental studies of flows over rough surfaces within the fully turbulent regime include those of Perry et al. (1969), Ligrani and Moffat (1986), Flack et al. (2005), McKeon et al. (2005), Allen et al. (2005), Schultz and Flack (2009), Birch and Morrison (2011), Hong et al. (2011) and Hong et al. (2012). On the other hand, some of the numerical studies are those of Krogstad et al. (2005), Singh et al. (2007), Flores et al. (2007), Lee and Sung (2007) .

Perry et al. (1969) investigated the flow field over the *k* and *d* type roughness for a zero and adverse pressure gradient boundary layer, where, the role of solidity on the flow structure was further elucidated. Ligrani and Moffat (1986) studied the structure of flow over spherical roughness boundary layer in the transitional and fully rough regimes. The peak of turbulent

kinetic energy production in the transition regime was shown to diminish as the roughness Reynolds number was increased towards the fully rough regime. It was also shown that the friction velocity u_τ is suitable for normalising the streamwise normal Reynolds stress component in the outer region of a fully rough flow, while the wall-normal and spanwise components would collapse on the same pattern when the free-stream velocity is used for normalisation. Birch and Morrison (2011) examined the flow field in a range of Reynolds numbers within fully rough regime over two different roughness patterns, one a mesh of diamond shape and the other a grit type roughness in a fully developed channel flow. Hong et al. (2011) also investigated the flow patterns in a fully rough regime of fully developed channel flow roughened by pyramids using the Particle Image Velocimetry (PIV) technique. They observed that the roughness scale eddies generated in the wall region were transported to the outer region by means of large scale turbulent structures. With the help of PIV, measurements were also made in the roughness sublayer, demonstrating a continual increase of streamwise normal Reynolds stress component, as one approaches the crest, peaking at the height of the pyramids while wall-normal component was only increased slightly at the crest of the roughness. Contrary to these two components was the shear stress that decreases as the wall is approached. All the studies mentioned so far support the wall similarity hypothesis of Townsend (1976), while the measurements of Krogstad et al. (1992) showed a deviation of turbulence field in the outer layer of the rough surface from the smooth in fully rough flow. Jiménez (2004) stated that the reason for such deviation was due to the relatively high blockage ratio (k/δ) of the roughness. Since the flow around a rough element is affected within $4-5\ k$, for high blockage ratios the element would no longer be considered as rough wall but as an array of obstacles. On the other hand, studies of Djenidi et al. (1999), Leonardi et al. (2004) and Krogstad et al. (2005) on the *d*-type geometries reveal that the effects of roughness might extend to the outer region as well.

For $5 \leq k_s^+ \leq 70$ flow regime is transitionally rough, where both viscous shear stresses and form drag on the roughness are active simultaneously. The interaction between these two constituents leads to a further complicated flow behaviour. As shown by Tani (1987), variations of roughness function versus roughness Reynolds number in this regime are non-linear and depend on the roughness geometry.

The role of roughness on the flow pattern of steady flows has been considered so far. However, relatively less attention has been paid to unsteady flows over rough surfaces. Among these, studies of Toit and Sleath (1981), Sleath (1987), Shih et al. (1993), Chen et al. (2007) and

Fornarelli and Vittori (2009) were focused on oscillatory flows over rough surfaces, whilst Bhaganagar (2008) investigated the flow field over rough surfaces in a pulsatile channel flow.

Fornarelli and Vittori (2009) investigated the flow field obtained from an oscillating pressure gradient boundary condition on a semi-sphere roughness elements using DNS. It was shown that the secondary peak in the streamwise velocity component, close to the flow reversal, is generated by the horse-shoe coherent vortex structures that shed from the base of the roughness elements.

Bhaganagar (2008) applied DNS to investigate the characteristics of a pulsating channel flow over “egg carton” roughness elements. Various forcing frequencies were applied to study the flow dynamics in the low-, intermediate-, and high-frequencies. The long-time average of mean velocity for the low and intermediate frequencies were shown to be close to that of steady flow over rough wall. Similarly, the long-time averages of fluctuating velocities are independent from the forcing frequencies and hence can well be represented by the steady channel flows over rough walls.

Higher forcing frequencies result in deviations of the long-time averages of mean velocity from the steady rough-wall flows. The oscillatory boundary layer is shown to be confined to the inner layer while the mean velocity has a phase difference with respect to the centreline velocity. Turbulence intensity of various components were shown to be out of phase with each other as well as the shear stress and centreline velocity. In the outer layer a plug flow behaviour was seen with negligible modulation of turbulence intensities.

2.4 RANS modelling of unsteady channel flows

The ability of Reynolds Averaged Navier-Stokes (RANS) models to predict the flow behaviour of steady/unsteady channel/pipe flows has been investigated by a number of researchers. The studies of Patel et al. (1985), Myong and Kasagi (1990) and (Chang et al., 1995) are some good examples of application of RANS models to steady pipe/channel flows. Sarkar and So (1997) investigated the performance of different turbulence models for steady channel flows (along with Couette, boundary layer and back-step flows). They examined ten different low-Reynolds number turbulence models, comparing their results with the available DNS and experimental data. They observed that models with asymptotically consistent near wall behaviour generally return better predictions of flow features. Asymptotic behaviour of the turbulent kinetic energy, its dissipation rate and the Reynolds shear stress near a wall is explained by Launder (1986).

Performance of RANS models in unsteady flows have been studied by Cotton et al. (2001), Scotti and Piomelli (2002), Tardu and Da Costa (2005), Al-Sharif et al. (2010), Khaleghi et al. (2010) and Revell et al. (2011). The performance of turbulence models in predicting features of unsteady flows differ according to the turbulence model formulations. In most cases researchers compare the performance of different models against the available experimental or DNS data. Cotton et al. (2001) examined the performance of the second-moment closure model of Shima (1989) and the $k-\varepsilon$ model of (Launder and Sharma, 1974) for both oscillatory flat-plate boundary layer and pulsatile pipe flow. It was found that the second-moment closure schemes generally performed better in comparison with the $k-\varepsilon$ model examined. Scotti and Piomelli (2002) assessed the performance of five turbulence models against their own DNS data on pulsating flows (Scotti and Piomelli (2001)) while Khaleghi et al. (2010) investigated the performance of four turbulence models for a ramp-up pipe flow, comparing their results with the experimental data of (He and Jackson, 2000). In each of these two studies, the performance of an algebraic one-equation model, a $k-\varepsilon$ model, a $k-\omega$ model and a $k-\varepsilon-v^2$ model were examined. It was concluded from both studies that $k-\varepsilon-v^2$ model outperforms the rest. However, these conclusions were based on investigations of only a limited number of models among the various formulations. Furthermore, new turbulence models have recently been developed which were not considered by previous researchers.

2.5 Summary

This chapter has examined the relevant literature on the steady/unsteady flows over smooth and rough surfaces. First features and behaviour of channel flows subjected to periodic and non-periodic unsteadiness have been discussed in detail. A general picture of the characteristics of bypass transition over smooth surfaces is then depicted. The behaviour of flows over rough surfaces has been discussed next. Finally a brief introduction on the relevant RANS studies of unsteady flows is given. This chapter provides an essential background for the study of unsteady channel and pipe flows over smooth and rough surfaces.

Chapter 3. Experimental setup and measurement techniques

3.1 Introduction

In order to investigate the effects of flow unsteadiness on a fully developed channel flow, the accuracy and repeatability of the measurement and control systems are of great importance. During this study a water flow loop system has been designed and constructed that enables the user to investigate various flow features of unsteady turbulent channel flows through detailed measurement of local and bulk instantaneous velocities, wall shear stress and streamwise pressure gradient. Furthermore a sophisticated control valve is employed to manipulate the flow rate of water in the system. This chapter discusses in detail on the water flow loop facility design, data acquisition and automation and non-intrusive measurement techniques.

3.2 Channel flow facility

A water flow loop facility is designed to study unsteady flows over smooth and rough channel surfaces. Figure 3.1 shows a schematic view of the channel with the corresponding coordinate system applied throughout this thesis. Table 3.1 summarises the characteristics of some of the test facilities employed for similar purposes and their working conditions in the literature. Dean (1978) analysed the data obtained from various channel flow facilities and suggested the minimal width to full height ratio (W/H, referred to as aspect ratio) of 7 to avoid secondary flows at the midspan plane. This suggestion is later confirmed by others such as Hanjalic and Launder (1972), Monty (2005), Birch and Morrison (2011) as well as Hong et al. (2011). Regarding the length needed for obtaining a fully developed flow, Monty (2005) performed a comprehensive investigation of the effects of length to height ratio on the development of the flows in smooth pipes and channels. He eventually concluded that the length to height ratio of

130 is enough to produce a fully developed mean and turbulence profiles in channels. This length is however considered to be even shorter in flows over rough surfaces. The present facility complies with these proposals. The length of the closed rectangular channel is 160 length to full-height (L/H) with width to full-height (W/H) ratio of 7, where the total length, width and full-height physical sizes are 8, 0.35 and 0.05 metres, respectively.

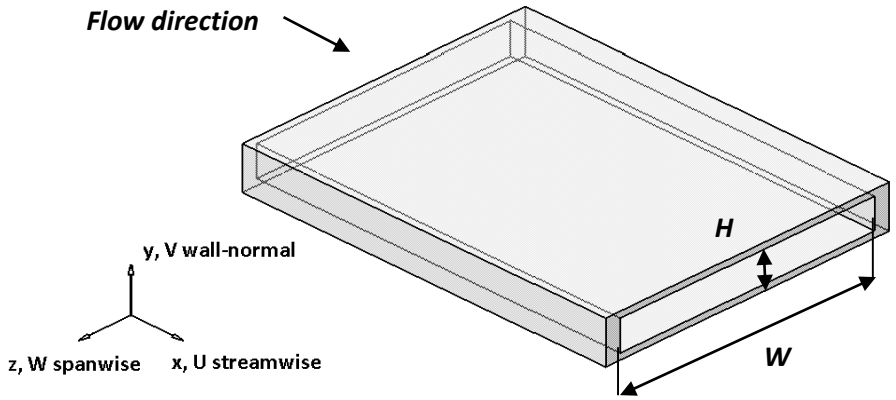

Figure 3.1 Schematic view of a channel flow.

Researcher(s)	Flow Type	Boundary Type	$Re_b = 2HU_b/\nu$	W/H	L/H (L/D)
Hanjalic and Launder (1972)	Channel	Rough	73K-306K	6	69
Perry and Abell (1975)	Pipe	Smooth	80K-260K	N/A	(90)
Dean and Bradshaw (1976)	Channel	Smooth	200 K	12	67
Zagarola and Smits (1998)	Pipe	Smooth	32K-35000K	N/A	(196)
He and Jackson (2000)	Pipe	Smooth	7K-45K	N/A	(178)
Zanoun et al. (2003)	Channel	Smooth	27K-300K	12	115
Monty (2005)	Channel	Smooth	76K-362K	11.7	205
Krogstad et al. (2005)	Channel	Rough	24K	13.5	50
Birch and Morrison (2011)	Channel	Rough	120K	7.5	67
Hong et al. (2011)	Channel	Rough	250K-387K	4	50

Table 3.1 Apparatus dimensions employed for studying fully developed two dimensional flows in pipes or channels.

3.3 Water flow loop

A water flow loop facility consisting of three main pipelines has been designed, built and commissioned in the Department of Mechanical Engineering at the University of Sheffield. This flow loop facility is capable of generating flow rates up to 60 m^3/h (Re = 23,700, based on half-height and bulk flow at T =20°C). It consists of an 8 metre rectangular cross section as the test

section. The test section is fed through a 4” PVC pipeline from the header tank located 4.5 metres above the test section’s outlet. PVC pipe is connected to the channel test section by means of a half a metre long stainless steel adaptor. Water flows from the top tank through a ball valve (fully open during operation), two sets of adaptors, PVC pipelines, a honeycomb, channel test section, control valve and a magnetic flow meter in series and is discharged to the bottom tank. Care has been taken to fully submerge the test section outlet pipe into the bottom tank to avoid further insertion of bubbles into the system. The capacity of the bottom tank is 3,000 litres (3x1 metres) which is considered to be sufficient to (i) reduce the possibility of cavitation at the pump by providing a half metre of water column on the suction side (ii) provide a long distance from the supply and discharge pipelines. The latter was of great importance since one of the supply pipes (overflow) had significant volume of trapped air that required aeration. A four inch bore 2.4 kW, 3 phase, 4 pole centrifugal in-line pump delivers the discharged water from the bottom tank to the header. This pipeline is also fully submerged into the header tank to reduce the splash. The capacity of the header tank is 400 litres. An overflow pipeline provides a constant head on the system by removing the excessive water from the header tank back into the bottom tank. Figure 3.2 depicts the arrangement of the water flow loop facility.

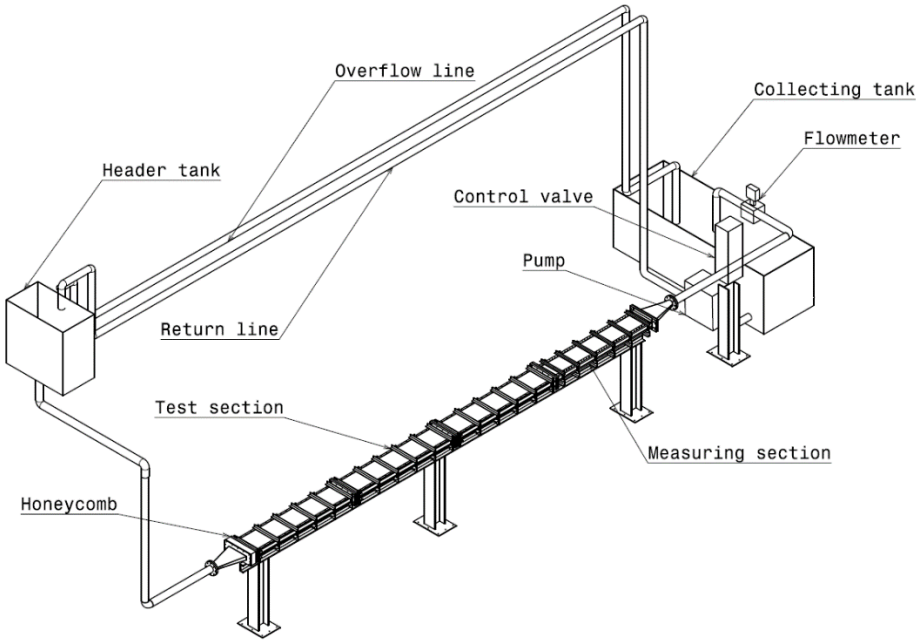

Figure 3.2 Drawing of the water flow loop facility.

In order to remove the possible swirls and to enhance the flow development through the test section, a honeycomb unit is placed before the test section and after the adaptor (Figure 3.2). Honeycombs are useful in mitigating the undesirable levels of turbulence, provided that the

ratio of length to cell diameters is 5-10 (Mehta and Bradshaw (1979)). The honeycomb unit is made by drilling and machining a PVC block of 100 mm length with 10 and 6 mm holes. This configuration of holes provides the sufficient condition for swirl removal with minimum pressure loss.

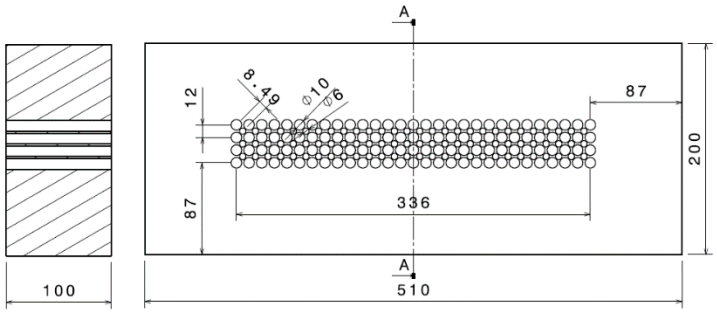

Figure 3.3 Honeycomb unit (dimensions in mm).

One of the challenges in the present design was the entrapment of significant amount of air into the water that results in formation of bubbles in the test section. This phenomena has two major adverse effects on the quality of the measurements. First, these bubbles can affect the fully developed, two-dimensional flow that is expected to be achieved further downstream. Second, these bubbles which were mainly flowing beneath the top surface of the channel limit the view from the top of the Particle Image Velocimetry (PIV) system. Therefore, great care was devoted to reduce the possibility of bubble formation in the system.

There were two main sources of bubble formation in the system (i) cavitation and (ii) air entrainment. Cavitation onsets in a system wherever the pressure of the liquid falls beneath its vapour pressure. In the present system, this was more likely to happen at the pump, control valve and honeycomb. As mentioned earlier, sufficient pressure was provided at the suction inlet of the pump to assure its optimum performance. On the other hand, no bubbles were expected at the honeycomb or the control valve due to relatively high pressure on the system.

As discussed earlier, the overflow pipe is responsible for the removal of the excessive water from the header tank. Therefore, this pipe is never fully filled with water providing constant air suction at its inlet. This mixture of air and water is returned to the collecting tank to be delivered to the test section. Due to lack of space at the header level of the lab, only a small tank of 400 litres could be accommodated, resulting in relatively small settling time. Such a configuration provides a loop of constant air injection into the system without a space for water to settle and air to escape. Two potential solutions were identified to reduce the adverse effect of the overflow on the system. These were either to divert the overflow to a separate tank or to reduce the delivery

of the pump. The second approach was implemented in the present system by mounting a carefully-trimmed mesh screen at the outlet of the pump's delivery line. This approach significantly reduced the volume of bubbles in the test section.

3.3.1 Test section

The test section is designed to have the capacity for studying a fully-turbulent, two-dimensional channel flow over smooth and rough surfaces. The length to height ratio (L/H) and width to height ratio (W/H) are 160 and 7, respectively. The channel facility is constructed out of four transparent Perspex sections, each two metres long, providing full optical access throughout its length. Each section consists of four Perspex plates that were first glued with Tensol 12 acrylic glue and then bolted together at every 100 mm. Four bars of 3 mm thickness stainless steel run along the length of the sections to enhance the strength of the bolted joints. Top and bottom plates are distanced 60 mm away from each other, providing space for 10 mm inserts. Rough inserts are only implemented in the last two sections of the flow facility (i.e. from $L/H = 80 - 160$).The thickness of the bottom/top and side plates are 20 and 30 mm, respectively. This configuration was kept throughout the first three sections (i.e. 6 metres). Figure 3.4 shows various elements of a single panel of the test section.

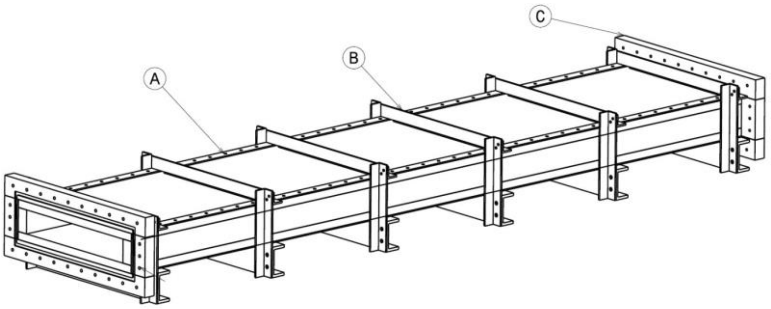

Figure 3.4 Single panel of the test section (a) Perspex channel (b) Supporting fixtures (c) Flanges.

A glass window is designed and mounted onto one side of the final section (measurement section), in order to improve the optical access to the measurement section. The edge of the window is located 6.8 metres downstream from the inlet. The window is 700 mm long with 500 mm distance from the outlet. The window consists of an aluminium frame and a 6 mm thick glass. Black Polyurethane adhesive was used to seal the glass plate onto the aluminium frame. A combination of 0.5 mm paper gasket and 4 mm O-ring chord was used to seal the window on the Perspex edges of the measurement section. The gap between the glass window and Perspex

sides is estimated to be less than 0.5 mm. The aluminium frame was pushed towards the Perspex test section by means of 8 clamps as shown on Figure 3.5.

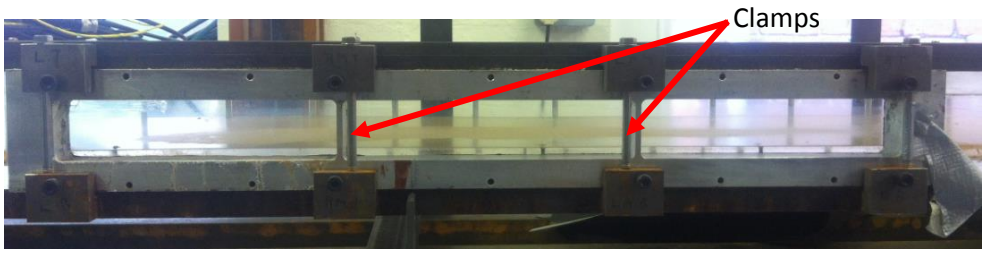

Figure 3.5 Glass window configuration

Bottom inserts of the test section are removable allowing the user to mount and study any surface topology of interest. These 10 mm inserts are bolted on top of the bottom plate of the test section. These bolts are located on the sides to have the minimum adverse influence on the flow. An effort was made to make these connections as flush as possible by using countersink screws. These screws are sealed and bolted from the outside. Due to further optical access complexities, inserts are only available at the bottom of the channel.

Each section is connected to the next by means of Perspex flanges (Figure 3.4). Each flange is glued to the test section and bolted to its counterpart. Only one face of each flange is grooved to accommodate the O-rings. Figure 3.6 illustrates the design and relevant dimensions. The nominal thickness of the O-ring chord is 5.33 mm.

The test section is mounted onto the longitudinal main support beams by means of fixtures (Figure 3.4). Three fixtures are in place for every section. These fixtures prevent the top and bottom plates of the test section from bending due to exerted hydrostatic pressure in the test section. It was shown by PIV measurements that the top and bottom plates were only displaced for ~ 120 and 80 μm, respectively, during the most severe unsteady conditions. Additionally, these fixtures are adjustable to level the test section.

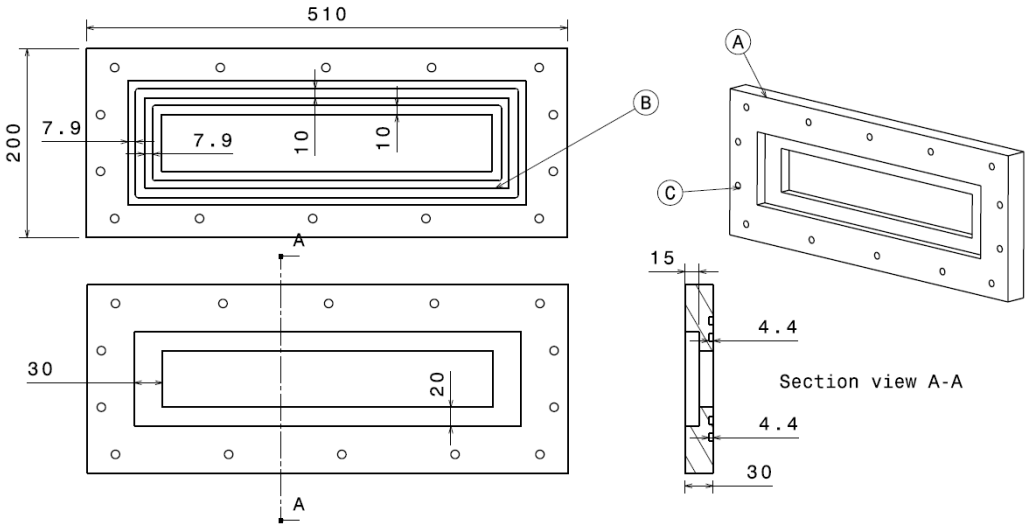

Figure 3.6 Flange dimensions. A: The flange; B: O-ring grooves; C: Holes for bolts (dimensions in mm)

3.3.2 **Flow control**

A 4" pneumatically operated globe valve is located one metre downstream of the outlet adaptor. This distance is considered to be sufficient for efficient performance of the valve. Equal percentage flow-lift characteristic was chosen for the valve. In such trim configurations, changes in the flow are an equal percentage of the existing flow for equal increment of the valve travel. This characteristic is of significant interest in cases where high control over the pressure changes is required. It should be stressed that the inherent characteristic of the valve is obtained by applying different valve opening percentages while the pressure loss through the valve is kept constant. This is obviously different from an arbitrary operational condition that stems from the configuration of any hydraulic system. Figure 3.7 depicts the opening versus flow rate for the inherent and operational scenarios.

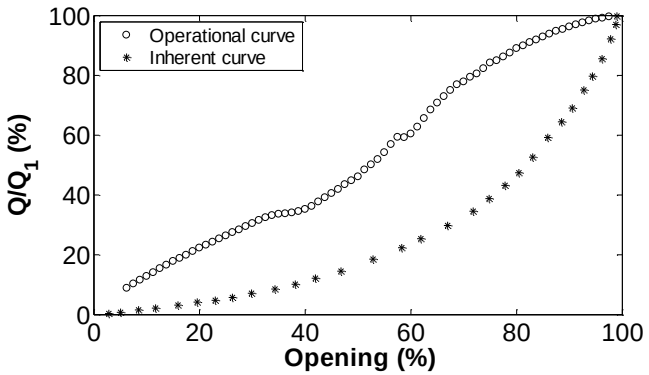

Figure 3.7 Operational versus inherent valve characteristics.

The custom made control valve consists of four main parts, the body of the valve, actuator, positioner and volume boosters. The cylinder actuator type provides a high level of accuracy in stem positioning. Two sets of boosters were mounted on the system to improve the stroking speed of the actuator in both directions. Precise Siemens PS2 positioner enables the user to control the position of the trim by means of a 4-20 mA signal (4 mA: fully shut – 20 mA: fully open).

Figure 3.8 shows the setup of the control valve. The positioner and boosters are supplied with compressed air at 4 bar. The positioner operates solely on a 4-20 mA current signal and therefore no extra power supply is required. The current signal is generated through a Phoenix Contact 3-way isolating amplifier supplied with the 0-10 volts signal from the Data Acquisition (DAQ) device.

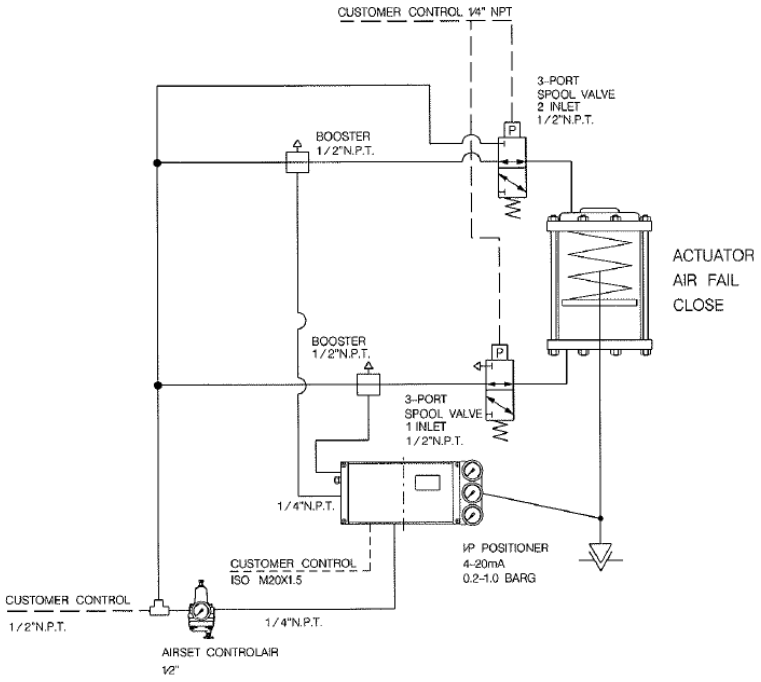

Figure 3.8 Sketch of valve actuator, booster and positioner.

The volume boosters are comprised of three ports, signal and pressure inlet-outlet. The signal ports are directly connected to the positioner outlet signal ports. In the case of steady operation of the valve, these boosters are bypassed, whilst variations in the signal port above the deadband limits result in activation of the booster and hence injection of high pressure air into the actuator. The boosters are connected to the actuator through spool valves. The spool valves are supplied with 4 bar compressed air from the main compressor. In the case of air supply

failure, high pressure air inside the lower chamber of the cylinder is evacuated through its corresponding spool valve, resulting in the closure of the system.

Repeatability of the flow (σ) is defined as the standard deviation of the streamwise mean velocity from various realisations measured by LDV at the centre of the channel.

Figure 3.9 shows the variation of centreline velocity's repeatability under steady conditions at different Reynolds numbers (based on half-height and bulk velocity). It can be seen from the figure that the valve's performance reduces significantly as the plug reaches its maximum opening.

During the experiments, it was noticed that the repeatability of the valve for sudden opening scenarios was further reduced. This resulted in slight difference between the opening times for individual ensembles, mainly affecting the streamwise velocity component. As shown in Chapters 5 and 6, this slight misalignment of the ensembles resulted in a scatter of the streamwise mean and rms velocity profiles, for a short duration, right after the valve's opening time ($t = 0$). Repeatability of the valve under severe transient conditions such as sudden-opening (e.g. 6.25 to 100 % opening) was measured to be better than 3%.

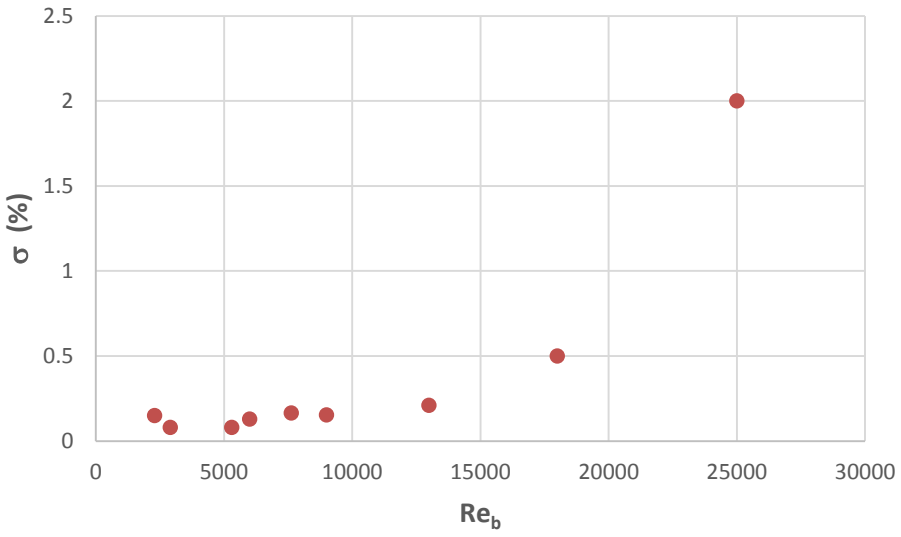

Figure 3.9 Repeatability of the flow versus Reynolds number.

3.3.3 Data acquisition system and measurement devices

The data acquisition system is provided by the National Instruments (NI USB-6211). This system consists of 16 analogue inputs and 2 analogue outputs both at signal resolution of 16 bits with

maximum sampling capability of 250,000 per second. The system is powered and connected to a PC through a USB port.

The analogue output ports are capable of generating voltages within the range of -10 - 10 volts with a maximum current drive of 2 mA. The first port is used to control the pneumatically operated valve, while the second is reserved for triggering and synchronisation purposes.

The analogue input ports are capable of measuring -10 - 10 volts. They are wired up to various measurement devices such as magnetic flow meter, hotfilm sensors and pressure transducer differentially in order to minimise the noise.

The variations in the bulk flow are measured by a 4" ISOMAG magnetic flow meter which is located further downstream of the control valve. According to manufacturer's report, levels of uncertainty in the measurements was recorded to be less than 0.2 % for velocities higher than 0.5 m/s and better than 0.3 % for small velocities of 0.173 m/s. Sufficient length of pipe ($> 10D$) is reserved before and after the flow meter to optimise its performance. Online filtering (time constant) of the measurement signal is disabled during the measurements in order to improve the response time of the flow meter. The full scale measurement of the device is set to 70 m^3/hr. The output signals from the magnetic flow meter are within 4-20 mA, which is converted to 0-10 volts by means of a 250 Ω resistance. The flow rate data obtained from the flow meter are recorded at 1 kHz throughout the measurements.

A silicon differential pressure transducer (0-10" H_2O, ¼" NPT) is used to measure the pressure drop across a fully developed section of the channel. The distance between the pressure taps is 4 metres. It is shown by Shaw (1960) that the associated errors in the pressure measurement highly depend on the d_p^+ ($d_p u_\tau/\nu$, d_p is the pressure tap diameter) values. Levels of error inside the tappings are mainly due to vortices that form inside the pressure tap. Figure 3.10 shows the dimensions of the pressure taps applied to the rig. Threaded section shows where the fittings are attached. It should however be mentioned that since the main purpose of this study is to measure pressure drops in unsteady flows, measurements from the pressure transducer are found to be inaccurate within small ranges of flow rates and therefore neglected.

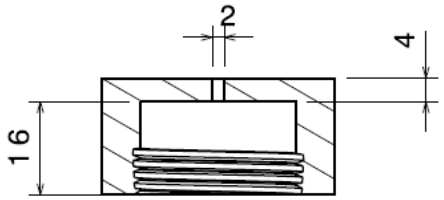

Figure 3.10 Pressure tapping dimensions in millimetre.

Furthermore, a pocket is created in the midspan of the top Perspex plate further downstream of the measurement section, providing a bed for glue-on hotfilms (depicted in Figure 3.11). Three hotfilms are mounted on this bed at a distance of 50 mm from each other and almost 15*H* from the outlet of the test section to measure the instantaneous wall shear stress. This distance is considered to be sufficient to diminish the outlet effects (Birch and Morrison (2011)). Sensors are grounded by 108 mm long brass tube which is machined off to be placed in a 2x1 mm groove. Hotfilms were glued onto the surface by means of Loctite 495. Fine wires of these sensors were soldered to an electrical joint and then soldered to RG59 BNC cables. The hotfilms are connected to the DAQ through a miniCTA box. However, these sensors only worked for a short time recording high variations of voltage under steady conditions that eventually decayed to a constant voltage. The defect in the hotfilms was mainly prone to the sealing of the fine signal wires.

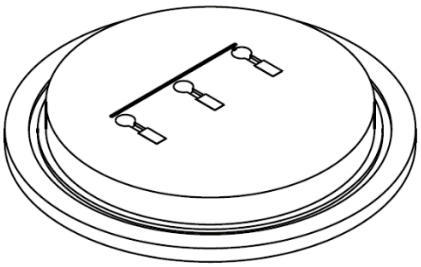

Figure 3.11 Hotfilm sensor bed.

Three different LabVIEW codes were developed to facilitate the control, data logging and synchronisation of the various sensors, control valve, LDV and PIV systems. In order to obtain the operational curve of the valve (Figure 3.7), small piecewise increments of voltage were supplied to the valve while the flow rate was constantly monitored and recorded. This curve was later used to generate different linear type of flow excursion signals. The other two codes are mainly used to produce unsteady flows with either sudden or linear flow excursions.

3.4 Data Processing

The ensemble averaged statistical quantities for PIV measurements are obtained from the temporal and streamwise spatial averages. A representative velocity Φ is averaged as follows

$$\overline{\Phi}(t) = \frac{1}{NP}\sum_{i=1}^{N}\sum_{j=1}^{P}\Phi_{i,j} \tag{3.1}$$

Reynolds stresses are calculated in a similar fashion

$$\overline{\varphi'^2}(t) = \frac{1}{NP}\sum_{i=1}^{N}\sum_{j=1}^{P}(\varphi_{i,j} - \overline{\Phi}(t))^2 \tag{3.2}$$

where N is the number of repeated runs and P is the number of data points in the streamwise direction.

The ensemble averages of the instantaneous data from flow meter, hotfilm sensors, pressure transducer and LDV are calculated in the following "windowing" procedure as initially introduced by He and Jackson (2000) in the study of transient flows. In the equations below u and v represent the instantaneous streamwise and wall-normal component of velocity. Ensemble averages can be defined as

$$\overline{U}_k = \frac{1}{NM}\sum_{i=1}^{N}\sum_{j=1}^{M}U_{i,j+(k-1)M} \tag{3.3}$$

and the Reynolds normal and shear stresses reintroduced as

$$\overline{u'^2_k} = \frac{1}{NM}\sum_{i=1}^{N}\sum_{j=1}^{M}(u_{i,j+(k-1)M} - U_k)^2 \tag{3.4}$$

$$\overline{v'^2_k} = \frac{1}{NM}\sum_{i=1}^{N}\sum_{j=1}^{M}v^2_{i,j+(k-1)M} \tag{3.5}$$

$$\overline{u'v'}_k = \frac{1}{NM}\sum_{i=1}^{N}\sum_{j=1}^{M}(u_{i,j+(k-1)M} - U_k)v_{i,j+(k-1)M} \tag{3.6}$$

where $k = 1, 2, \ldots, L$ and L is the number of windows in a single realisation of the transient. M and N are the number of samples in each window and the number of repeats of the transient, respectively. Quantities in equations (3.3) and (3.4) can be replaced with flow rate, wall shear stress or pressure to calculate the mean and variance of these flow properties.

3.5 LDV system

A TSI FSA3500 two-component LDV system is employed to measure the instantaneous velocity in streamwise and wall-normal directions. Figure 3.12 shows the different components of the LDV system. This system consists of a CVI Melles Griot argon-ion laser generating device that is capable of generating lasers of wavelengths of 488 (blue) and 514.5 (green) nm with maximum output power of 300 mW. The power of each beam at the outlet of the transmitter probe was later measured to be approximately 30 mW. The beam is then directed into the beam separator device to be split, where one single beam of each component shifts by 40 MHz in the Bragg Cell unit. This shift allows the system to measure the direction of the flow. Each single beam is then reflected through the fibre couplers to be directed to the transmitting probe through fibre optic cables. In order to maintain the transmitted energy of the beams, the couplers should be precisely aligned with the incoming reflected beams in the splitter box. This process results in four sets of beams being fired from the transmitting probe, each two measuring one component of the flow.

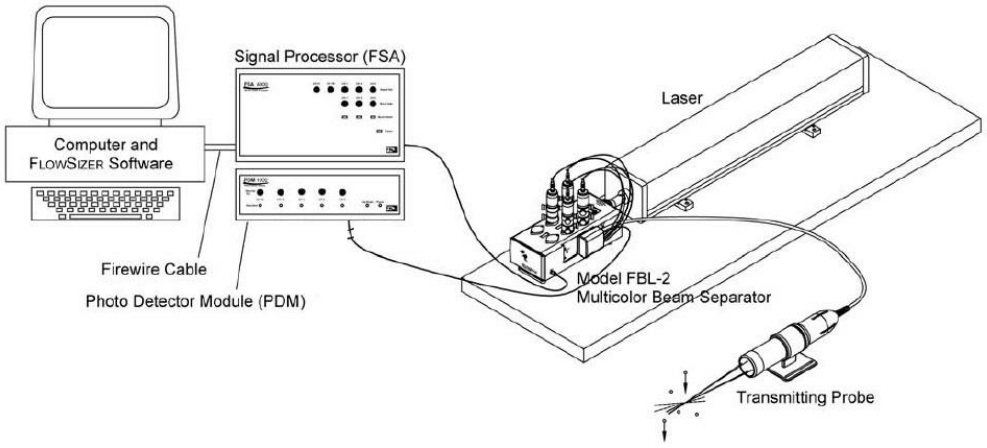

Figure 3.12 Sample LDV system.

Each two beams cross each other at the focal length of the probe lens creating the measuring control volume (MCV). MCV of each component is an ellipsoid with Gaussian intensity distribution in all three dimensions. Two intersecting waves create fringes at the MCV as shown on Figure 3.13. Fringe spacing is a function of intersection angle and wavelength. The properties of the employed lens are tabulated in Table 3.2.

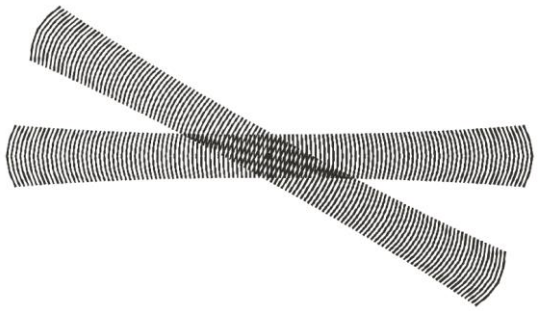

Figure 3.13 Fringes created at the measuring control volume.

	Lens focal length (mm)	Beam spacing (mm)	Fringe spacing (μm)	MCV diameter (μm)	MCV length (mm)
LDV TR260	363	50	3.7	90	1.3

Table 3.2 Lens Properties.

As a particle crosses the bright fringes, scatters light in the bright fringe and scatters no light in the dark one. This results in a fluctuating pattern of scattered light intensity with a frequency proportional to the particle velocity. Since the distance between the fringes as well as the time required for a particle to travel from one fringe to another is known (from the frequency content), velocity of the particle can be calculated. The scattered light from the fringes is collected by the optics, a backscatter system in the present study, and transmitted to the Photomultiplier Tubes through the fibre optic cables, where it can be converted to electrical signals. Series of low, high and band pass filtering processes are then applied to these signals to improve the signal to noise ratio and to allow the user to measure zero or reversing flows. Seed's arrival times is shown to have a Poisson distribution as reported by Britz and Antonia (1996) (Figure 3.14).

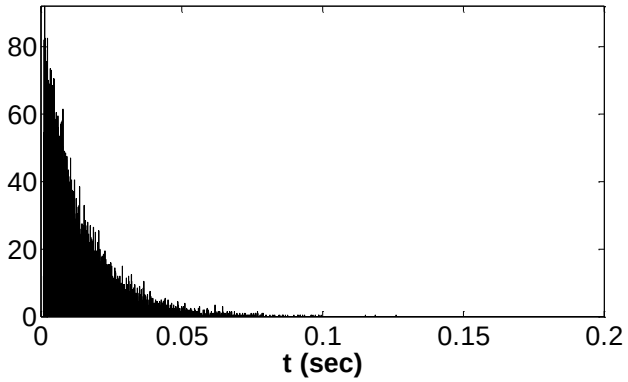

Figure 3.14 Distribution of seed's arrival times measured at the centre of the channel.

Throughout the measurements, transmitting probe was mounted on an Isel-Automation three dimensional traversing system capable of travelling 1450x1000x890 mm in streamwise, spanwise and wall-normal directions, respectively, with precision better than 0.01 mm. It is also important to mention that due to different refractive indices of water and air the actual displacement of the laser in the spanwise direction is affected. For this reason, the actual displacement of the laser in the spanwise direction is calculated by multiplying the displacement by 1.34.

Hollow glass spheres with silver coating are used for seeding purposes in this study. The mean diameter of the seeds is 10 microns with unit specific gravity allowing it to follow the fluid path with high levels of fidelity. It was noticed that this specific type of seeding had superior optical properties which resulted in achieving higher data rates in comparison to the plain hollow Polyamide sphere seeds with similar physical properties.

As shown by Durst et al. (1998), non-dimensional probe volume diameter d^+ (du_τ/ν, d is the probe diameter) is one of the most critical quantities in describing the spatial resolution of LDV systems in wall shear flows. The mean velocity gradient in the wall-normal direction produces different velocities at the edges of the MCV, resulting in velocity gradient bias. This gradient causes a bias in the measurement of fluctuating velocity components where their mean profiles are affected (for instance in our case u'_{rms} and its higher order statistics). The velocity gradient bias causes an overestimation of Reynolds stresses in LDV measurements (Schultz and Flack (2013)).

It is shown by Durst et al. (1995) that by writing the Taylor expansion series around the centre of a MCV, one can obtain an explicit relationship between the measured and true local velocity values. Streamwise mean and normal Reynolds stress reads

$$\overline{U}_{i\,meas} = \overline{U}_{i\,true} + \frac{d^2}{32}\left(\frac{d^2\overline{U}_{i\,true}}{dy^2}\right) + \cdots \tag{3.7}$$

$$\overline{u'^2}_{i\,meas} = \overline{u^2}_{i\,true} + \frac{d^2}{16}\left(\frac{d\overline{U}_{i\,true}}{dy}\right)^2 + \cdots \tag{3.8}$$

where $\overline{U}_{i\,true}$ and $\overline{u^2}_{i\,true}$ are the true mean and turbulent components of the measured ones ($\overline{U}_{i\,meas}$ and $\overline{u^2}_{i\,meas}$) and d is the diameter of the MCV. These corrections were only applied to the steady cases investigated throughout these investigations and are not applicable to unsteady ones.

Velocity bias as introduced by Buchhave et al. (1979) was corrected by applying Gatetime Weighting function from the FlowSizer v3.0 software menu. Velocity bias stems from the fact that more of the faster particles go through the measuring volume at each instant of time resulting in a bias towards faster particles in the sampled velocities. This causes the velocity mean values to be higher than their actual values. Gatetime Weighting function normalises each velocity data of particles with their respective gate times. For instance, slower particles have longer gate times and therefore more weight. This function was enabled throughout the measurements of steady and unsteady velocity measurements.

In the case of Reynolds shear stress measurements in both steady and unsteady scenarios, it was of great importance to measure two components of a similar particle at an instant of time. For this reason, coincident mode was activated in the software to measure an identical burst. There are two methods available to identify similar bursts on each channel, one by means of a Gate Scale percentage and the other by the actual coincident interval time. Gate Scale controls how many gate widths in the forward and backward directions are required to synchronise the bursts. Two Gate Scale percentages are shown in Figure 3.15 to further elucidate the concept. Each channel in the figure represents a component of velocity. Smaller Gate Scales results in a stricter control on the passing seeds and hence less data rate. This scale can also be defined as a fixed coincident interval time. In this method, the actual time between two consecutive bursts on each channel should fall within a certain time band unless to be rejected. The former method was applied throughout the measurements herein where the Gate Scale was reduced to 200%.

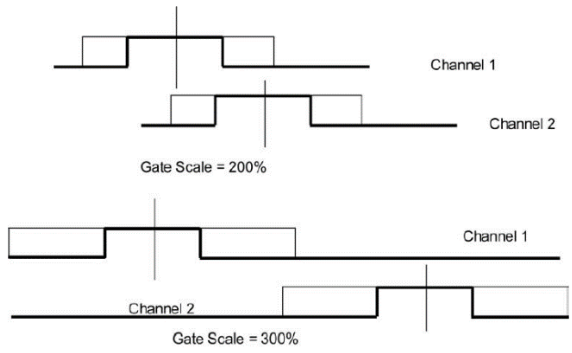

Figure 3.15 Coincident mode measurement.

During the steady measurements, spurious data were identified by removing the individual samples of ± 7 times the rms values as suggested by Den Toonder and Nieuwstadt (1997).

Another source of uncertainty in the LDV measurements is the location of the wall. There are different approaches introduced in the literature regarding this issue. Oldengarm et al. (1975)

measured a sine wave as the measuring volume reached the particles attached to the surface. Wei and Willmarth (1989) explain that they have assumed the location of the wall to be where no LDV signal is attainable. On the other hand, Durst et al. (1995) and DeGraaff and Eaton (2001) have assumed the wall to be located at a position where the signal due to light scattering by the particles attached to the surface is maximum. In the investigations reported herein, it was noticed that a location exists somewhere close to the wall that a strong signal with normal distribution and almost zero magnitude (order of -4) is attainable. This location was assumed to be the wall. Figure 3.16 shows the velocity signal at the wall measured by LDV.

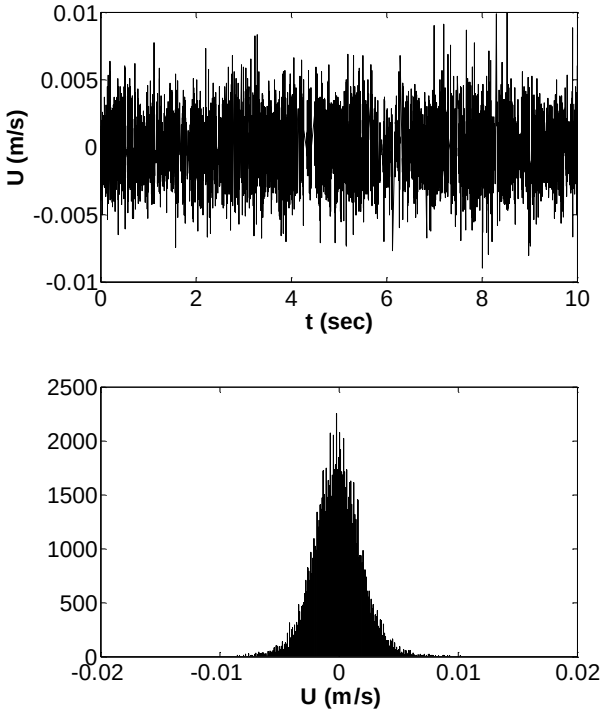

Figure 3.16 Streamwise instantaneous velocity signal and its distribution measured at the wall.

For the steady cases, ensemble averages are computed from 20,000 samples at each point. In order to assure that the acquired data are independent from each other the interval time between the samples (reverse of sampling frequency) was maintained twice the integral length scales ($h/\overline{U}$) of the flow. Mean and higher order statistics obtained from LDV measurements were collected at 30 points in wall normal locations.

Ideally, measurements have to be taken at the midspan of the channel where a two-dimensional flow is expected. However, it was noticed during the initial measurements, that the v' component of the flow is not realisable at most of the wall-normal direction due to the configuration of the beams and the channel i.e. the top beam being blocked by the lower plate

of the channel facility. For this reason and the major role that this components plays in unsteady flows, it was decided to traverse the measurement location in the spanwise direction towards the glass window where three-dimensional effects are insignificant. This location is later shown in §4.4 to be at 3.5h from the glass window.

3.6 PIV system

Particle Image Velocimetry (PIV), contrary to LDV, provides an instantaneous flow field. A PIV system consists of three main components, laser pulse generator, CCD (Charge-Coupled Device) camera and a post-processing software. Figure 3.17 illustrates the procedures involved in obtaining a velocity field by using PIV. A double-pulsed laser generates two consecutive sheets of light to be fired at Δt seconds from each other. A CCD camera, preferably located perpendicular to the sheet of light, records the two consecutive frames. These two frames are then required to be image processed by using advanced cross-correlation algorithms to yield a single instantaneous velocity field.

Three inherent assumptions are the building blocks of a PIV system: first, the tracer particles follow the fluid motion; second, the tracer particles are distributed homogenously and finally the particles have uniform displacement within the interrogation regions.

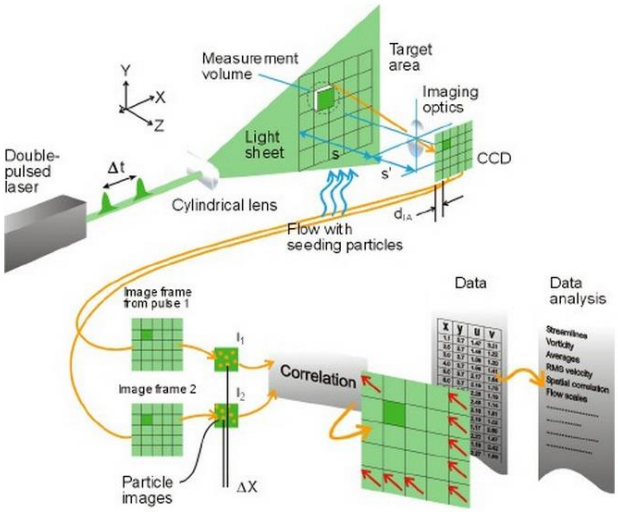

Figure 3.17 PIV system components (Dantec Inc.).

A Dantec Dynamics integrated planar PIV system was employed for these investigations. Laser generator device was a Litron Nano-S-65 Nd:YAG (Yttrium Aluminium Garnet) laser capable of generating pulsed laser at wavelength of 520 nm (green) with maximum energy of 65 mJ per pulse. A Dantec Dynamics FlowSense 12-bit 4M CCD camera with the resolution of 2048x2048 pixels was used to capture the images from the flow field. A 60 mm focal length Nikon AF Micro-

Nikkor lens with maximum aperture number of f/2.8D was mounted on the CCD camera. Dantec DynamicStudio v3.31 software was used for image and data processing purposes. Synchronisation of the laser, camera and the computer was performed by a NI PCI-E 1427 DAQ card and a Dantec Dynamics timer box which was controlled by a NI PCI 6602 timer board.

Two sets of camera - laser orientations were used throughout the measurements reported herein. Figure 3.18 (a) depicts the orientation where the laser is firing from the side (horizontal direction) to perform measurements in the xz plane while the second configuration facilitates the measurements in the xy plane (Figure 3.18 (b), vertical direction).

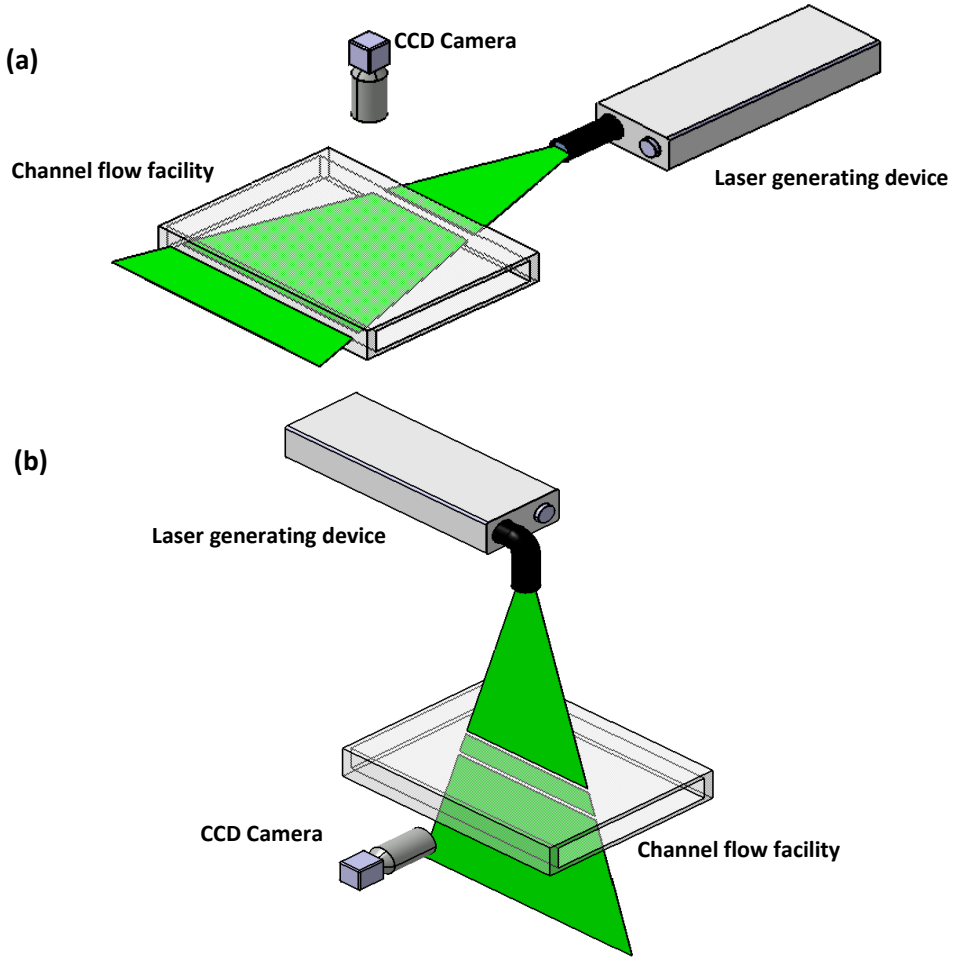

Figure 3.18 Different camera-laser orientations for planes at (a) xz and (b) xy directions.

Velocity fields in planar PIV systems are calculated from the seed displacement and the time between the laser pulses (Δt). Statistical cross-correlation algorithms are applied to find the displacement of each set of particles. This process requires each image to be divided into a number of interrogation areas (IA). Group of particles in each IA create a unique fingerprint in the first frame. A search area needs to be defined so that each particle can be traced within the search range. The search area is the combination of IA and overlapping zones. Ideally, the unique

finger print detected in the first image should be traceable in the second image within the overlapping zone. A cross-correlation value needs to be calculated at each position within the overlapping zone resulting in a correlation function. The maximum cross-correlation is obtained when the fingerprint is detected in the second frame. Displacement vector can then be identified by the offset of the interrogation regions. Now that the displacement is known, velocity can be calculated with reference to Δt. This process is then repeated throughout the FOV.

A number of PIV rules of thumb have been suggested upon the investigations of Keane and Adrian (1990) and Keane and Adrian (1991). The diameter of seed particles are suggested to be more than 2 pixels to reduce the peak locking (Raffel et al. (2007)). Peak locking occurs when the PIV correlation algorithm is locked in to integer pixel displacement. For instance, if a particle's diameter is confined into one single pixel, the displacement of that particle is assumed to be the displacement of that single pixel. This conjecture however requires sub-pixel accuracy to be validated. Peak locking can stem from both experimental and numerical shortcomings. 5-15 particles are generally required to produce strong cross-correlation within the IA and the searching area. Maximum displacement of the particles between the laser pulses is suggested not to exceed 25% of the IA width. This improves the detection process of the fingerprints.

Effort has been made in these investigations to comply with the general guidelines introduced above. However, the major challenge in the measurement of unsteady flows stems from the fact that the optimal displacement of the particles between the pluses can be hugely different for the initial and final flows. Furthermore, the measurement of velocity gradients of the streamwise component of the flow with rather large FOV sizes applies a constraint on the applicability of the final general guideline.

During the investigations reported herein, the adaptive correlation technique has been applied to calculate the velocity field. In this method, velocity vectors with an initial larger IA size are iteratively calculated, narrowing down to the final IA size. Three iterations are performed in the investigations reported herein to reduce the final interrogation size to 32x32 pixels. Spurious velocity vectors were detected and removed by performing two validation approaches in series and parallel:

i. Peak validation: According to Keane and Adrian (1992), the ratio of the two highest consecutive correlation peaks should not exceed 1.2 otherwise this results in their rejection and a moving averaged value is replaced.

ii. Moving average: A moving average is performed in an 8x8 neighbourhood with 3 iterations and acceptance factor of 0.12. The gradient of velocity vectors exceeding the acceptance factor are removed and a moving averaged value is replaced.

Velocity vectors are estimated from mean particle displacement inside the IA. Throughout the investigations reported herein, a second order central differencing scheme is employed to estimate the derivative of the displacement with respect to time.

The high accuracy sub-pixel algorithm, independent of the particle image shape and correlation peak shape, is applied throughout these investigations to reduce the peak-locking effect. Furthermore, deforming windows option was enabled to improve the measurement in wall shear flow applications.

The accuracy of PIV measurements is affected by a variety of factors such as sub-pixel interpolation of the displacement correlation peak, the particle's fidelity to the flow, light pulse timing, light sheet positioning, depth of field (DOF) as well as the size of the interrogation area. As mentioned earlier in this section, uniform displacement of particles within the interrogation area is an ideal situation and is violated in wall shear flows. In order to achieve an acceptable valid detection probability of 95%, Keane and Adrian (1992) suggest the gradients in the flow to obey the following expression:

$$\frac{M\Delta U_y \Delta t}{d_{PIV}} < 0.03 \tag{3.9}$$

where M is the magnification factor, $\Delta U_y = (\partial U/\partial y) * d_{PIV}/2$, Δt is the time between the pulses and d_{PIV} is the length of the IA. The inequality above has a significant impact on the validity of the measurements at locations with high velocity gradients, such as those in the wall region. For instance, it can be shown that the measurement of a flow at Reynolds number of 18,000 can only be considered to be valid above the $y^+ = 34$ providing the magnification factor, Δt and IA size are 1.812, 350 μs and 32 pixels, respectively. The above criteria was used throughout the steady wall shear flow investigations in this study to determine the light pulse timing (Δt).

3.7 Summary

The characteristics of the water flow facility, data processing, measurement equipment as well as data logging and control systems are discussed in this chapter. Limitations and advantages of each measurement technique is discussed in detail to provide us with an overview towards the measurement of steady and unsteady turbulent channel flows in the next chapters.

Chapter 4. Characterisation of the test facility and instrumentation

4.1 Introduction

This chapter reports the data obtained from LDV and PIV measurements in the channel under steady conditions at various Reynolds number flows. These investigations are of great importance since they reveal the characteristics of the test facility and, by comparing the results with the benchmark data of conventional channel flows, they provide a thorough validation of the system. Development of streamwise velocity, two dimensionality of the flow, configurations of the PIV system and comparison of the measurements to the benchmark data in channel flows over smooth and rough surfaces are discussed in detail in the present chapter. The streamwise, wall-normal and spanwise directions are shown as x, y and z as depicted in Figure 3.1.

4.2 Streamwise flow development

In order to demonstrate that the fully developed condition prevails in the measurement section, a number of measurements are performed in the streamwise direction along the glass window at the centre of the channel.

Figure 4.1 shows the variations of the mean and higher order statistics of velocity in the streamwise direction. The measurements are performed at the spanwise centre of the channel ($z/h = 7$) with a flow rate of 42.8 m^3/h equivalent to a Reynolds number of 17,000. Ensemble averages have been performed on 40,000 samples. These quantities are normalised with the bulk velocity (U_b) and channel full-height (H).

It can be seen from Figure 4.1 that the streamwise mean and fluctuating velocity components are clearly fully developed and the variation is within 99.9% in the designated region, whilst the

streamwise and the wall-normal skewness (S_u, S_v) and flatness (F_u, F_v) also show a fully developed feature with no systematic variation in x direction, albeit with the relatively higher levels of scatter up to 99.2 and 98.7 %, respectively. It can therefore be concluded from the statistics that the flow is very well developed in the measurement section. Therefore, the cross sectional and spanwise measurements of the flow mainly performed at $x = 143\,H$ unless otherwise stated.

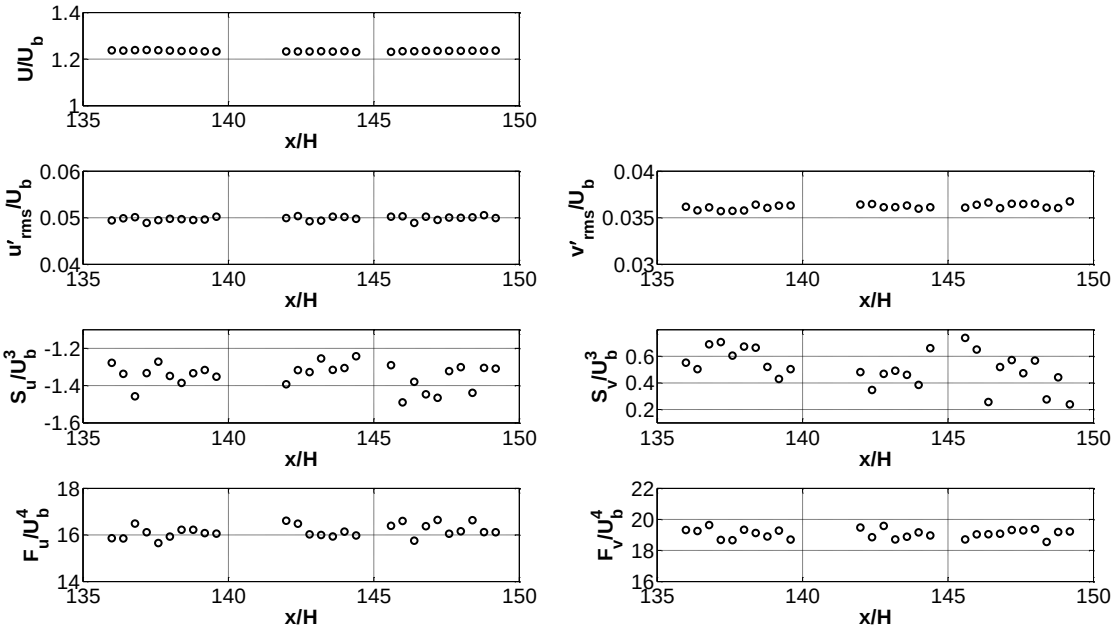

Figure 4.1 Variations of mean and higher order statistics at the centre of the channel in the streamwise direction at Re = 17,000.

4.3 Two dimensionality

A series of measurements are performed in the spanwise direction of the flow at various Reynolds numbers. The measurements are taken at the centre of the channel with both LDV and PIV systems. These measurements help to understand the behaviour of the flow and to identify the region in which a two-dimensional flow assumption is valid.

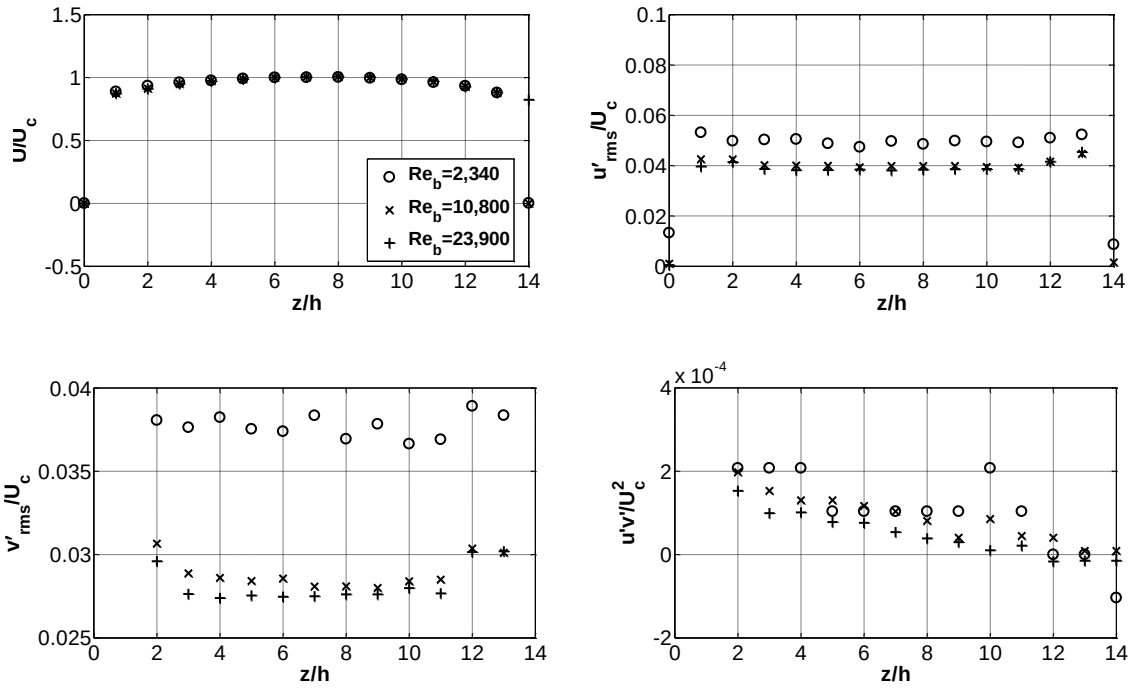

Figure 4.2 LDV measurements of mean, fluctuating and shear stress profiles at various Reynolds numbers at the plane $y/h = 1$.

The ensemble averaged mean and turbulent statistics shown in Figure 4.2 are obtained from 30,000 samples and normalised by the maximum centreline velocity (at $z/h \sim 7$) and channel half-height (h). It can be seen that the Reynolds shear stress is very low as expected and the rest of the profiles demonstrate good two-dimensional behaviour in the range of $z/h \sim 3.5 - 10.5$. All profiles, except the Reynolds shear stress, show high levels of symmetry in the spanwise direction. It is should be noted that the fluctuating velocity components obtained from the low Reynolds number flow do not collapse with the high Reynolds number ones.

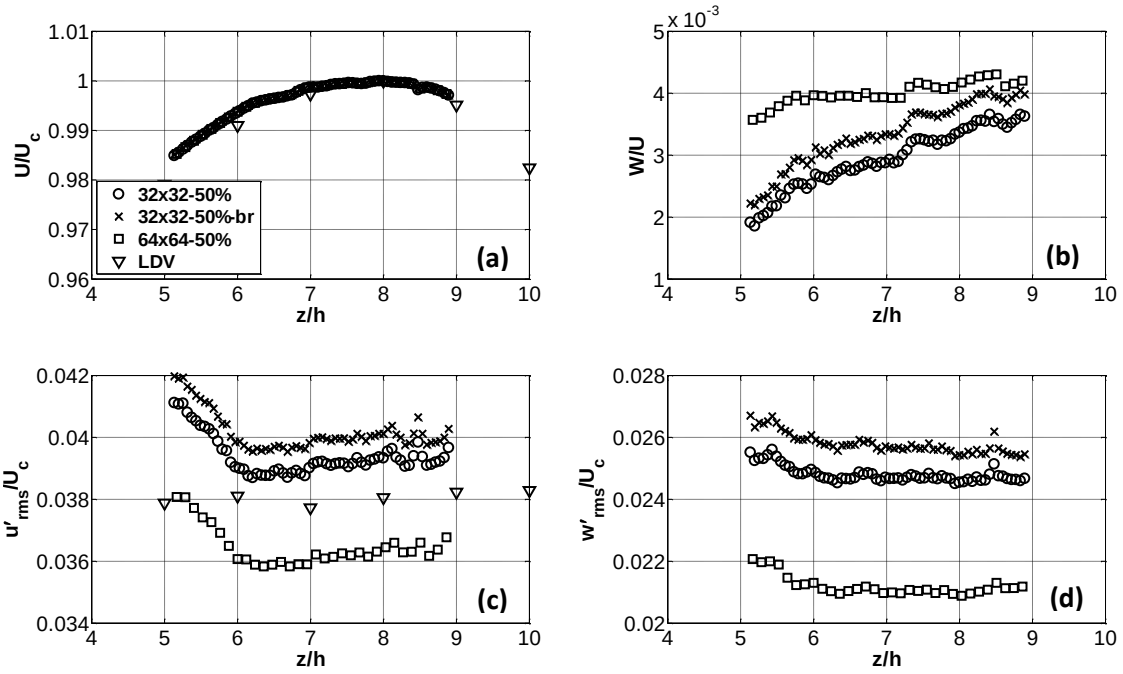

Figure 4.3 PIV measurements of streamwise and spanwise velocity components at the centre of the channel at $Re_b = 24{,}800$.

Figure 4.3 compares velocity profiles obtained from different PIV techniques with those of LDV at the centre of the channel with $Re_b = 24{,}800$. The two component LDV system does not allow for the measurement of spanwise velocity component and neither planar PIV for the wall-normal component. Therefore relevant comparisons are only made for the streamwise mean and fluctuating quantities (Figure 4.3 a & c). The FOV of the PIV images is 94x94 mm. The ensemble averages are calculated from 2,500 image pairs. Data obtained from the temporal averages are then spatially averaged in the streamwise direction. Adaptive correlation technique is applied to the PIV images in three different approaches to assess their effectiveness in the measurement of flow statistics. In the first approach, images are processed with 32x32 pixel interrogation areas with 50% overlapping. In the second approach, similar interrogation areas and overlapping percentage are applied to images that are initially filtered by removing the background noise, these data are shown with '-br' legend in Figure 4.3. Background noise removal is performed by subtraction of the averaged intensity over the ensembles from each individual image. Therefore, images yielded from this process are expected to be free from the background noises. The final approach was to apply a coarser grid of 64x64 pixel of interrogation areas with 50% overlapping.

The measured mean and fluctuating velocities from different PIV post-data processing approaches are in agreement with the LDV, whilst some discrepancies are noticeable between the different PIV processing approaches. Among these, the 32x32 pixel interrogation area with

no background noise removal measures rms values closest to the LDV profile. It is also interesting to see a sharp fall in the PIV streamwise rms data between $z/h = 5 - 6$ that is not evident in the LDV profiles.

It is worth noting that the ratio W/U is considered to show the two dimensional effects. It can be seen from Figure 4.3 (b) that this ratio remains small throughout the FOV. Figure 4.3 shows that the mean and turbulence quantities within the measured range are weakly sensitive to the spanwise location which verifies the spanwise spatial averaging in analysing unsteady flows over smooth and rough surfaces in chapters 5 and 6, respectively.

4.4 Steady smooth channel flows

Figure 4.4 shows the mean and fluctuating profiles of streamwise velocity at different Reynolds numbers measured at the centre of the channel with LDV. These figures show the inner (a-b) and outer (c-d) scaled profiles of mean and fluctuating values. It can be seen from the figures that the measurements are in close agreement with the DNS data. The levels of statistical uncertainties for 20,000 samples based on 95% confidence level were estimated to be better than 0.17% for mean and 2.6% for rms fluctuating velocities.

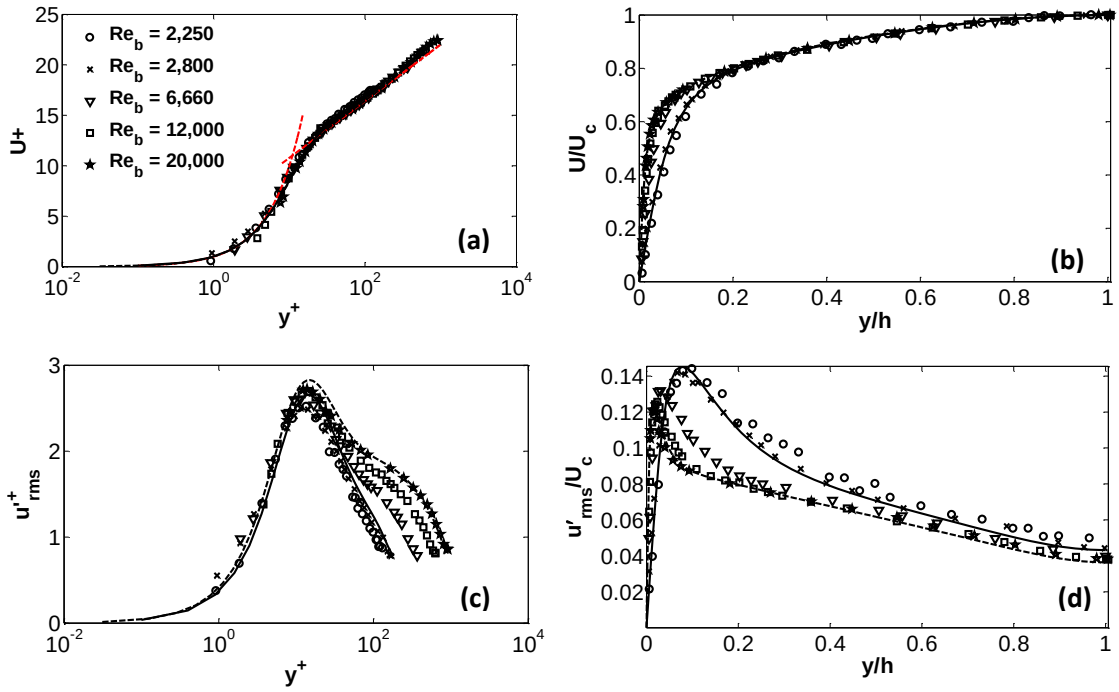

Figure 4.4 LDV measurements of mean and fluctuating streamwise velocity component at various Reynolds numbers. (Dash line: DNS data of Hoyas and Jiménez (2008) $Re_b = 21{,}300$; Solid line: DNS data of He and Seddighi (2013) $Re_b = 2{,}800$; Red straight line: log-law)

There are a number of different methods suggested in the literature for indirectly calculating the wall shear stress in channel flows. This parameter is particularly useful in non-dimensionalasing various flow quantities (as shown in Figure 4.4 (a-c)).

One of these methods is to use the Blasius' friction law which is defined as follows:

$$C_f = 0.079(4Re_b)^{-0.25} \tag{4.1}$$

where C_f is the friction coefficient, Re_b is the Reynolds number based on bulk velocity and half-height of the channel. Friction coefficient has the following relationship with the wall shear stress:

$$C_f = \frac{2\tau_w}{\rho U_b^2} \tag{4.2}$$

where τ_w is the wall shear stress and ρ is the density of the fluid. There are however other empirical correlations such as the one suggested by Dean (1978):

$$C_f = 0.073(2Re_b)^{-0.25} \tag{4.3}$$

Alternative methods for calculating the wall shear stress in channel and pipe flows are based on log-law fitting to the fully turbulent region of velocity profile, or the polynomial-fitting to the buffer region proposed by Durst et al. (1996), or line-fitting to the Reynolds shear stress curve in the core region.

For smooth walls, the standard logarithmic profile is obtained from dimensional analysis and the Reynolds number invariance principle as follows (Townsend (1976)):

$$U^+ = \frac{1}{\kappa}\ln(y^+) + B \tag{4.4}$$

where U^+ is the mean streamwise velocity, non-dimensionalised with friction velocity ($u_\tau = \sqrt{\tau_w/\rho}$), $y^+(= yu_\tau/\nu)$ is the non-dimensional distance from the wall and κ and B are the von Kármán constant, and an empirical constant, respectively. It is shown by Nagib and Chauhan (2008) that the von Kármán constant cannot be considered to be universal and it depends on the geometry, pressure gradients and Reynolds number. Specifically in the case of channel flows, the aspect ratio of the facility is believed to be a factor in determination of the von Kármán constant (Marusic et al. (2010)). On the other hand, there are different constants proposed for B in the literature (such as Kim et al. (1987) and Durst et al. (1996)). For all these uncertainties as well as the controversy over the onset of the log-law region, wall shear stress in the present unsteady smooth investigations are mainly calculated from the Blasius' friction law (4.1) unless otherwise stated. This method is applied to non-dimensionalise the results shown in Figure 4.4.

The log-law dash line plotted in Figure 4.4 (a) has the constants of $\kappa = 0.41$ and $B = 5.17$. It is noteworthy to mention that the rms component of velocity for flows of Reynolds number 2,250 and 2,800 do not collapse with the relatively higher Reynolds number flows in the centre. Figure 4.5 show that the mean streamwise component of the velocity is subjected to mixed inner-outer scaling. It can be seen from the figure that this scaling provides a better collapse of data in the core region of the flow.

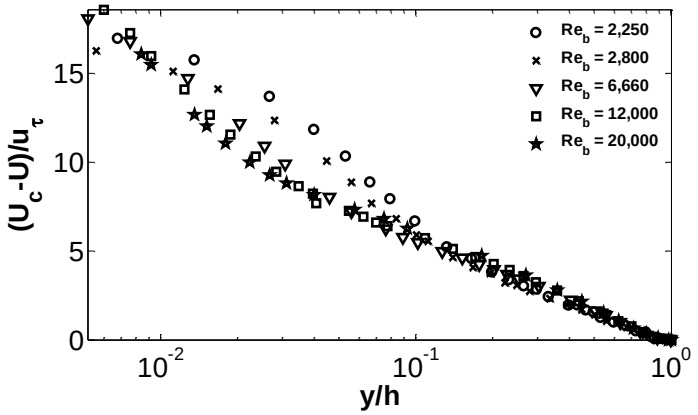

Figure 4.5 Mixed scaling of mean velocity component at various Reynolds numbers.

As mentioned earlier, due to the configuration of the laser beams, the access of the second LDV component was limited in the midspan of the channel. For this reason, most of the measurements of unsteady flows discussed in chapters 5 and 6 are taken at a location 3.5h away from the edge in the spanwise direction. This allowed the laser to measure the wall-normal component of the flow as close as 4.17 mm from the wall.

Figure 4.6 shows the LDV measurements at $z = 3.5h$ of the streamwise mean component along with the shear and normal Reynolds stresses at two different Reynolds numbers, streamwise components measured at the midspan and DNS data in a similar range of Reynolds numbers are also shown in the figure for comparison. Very close agreement can be seen between the statistics of the streamwise velocity component in the midspan and the side measurements. On the other hand, comparisons of ${v'}_{rms}$ and $\overline{u'v'}$ obtained from the experiments at Reynolds number 26,000 are in good agreement with the DNS data while the lower Reynolds number flow shows higher discrepancy. This difference might be due to the low Reynolds number effects between the DNS and experiments or might be an indication of relatively higher three-dimensional effects at low Reynolds number flows.

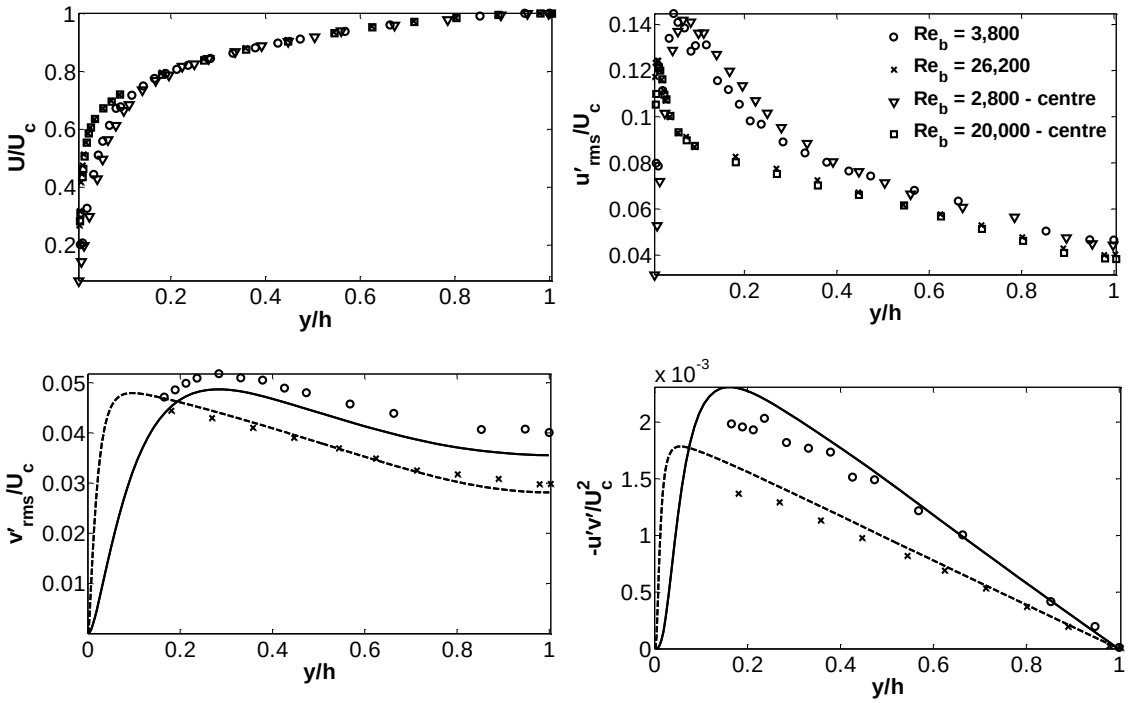

Figure 4.6 LDV measurements of mean and turbulence at 3.5h from the side window. (Dash line: DNS data of Hoyas and Jiménez (2008) $Re_b = 21{,}300$; Solid line: DNS data of Gilbert and Kleiser (1991)$Re_b = 3{,}835$)

4.4.1 PIV configuration

PIV was also used to measure the mean and turbulent statistics under various flow conditions. Comparison of these investigations with DNS allows the user to quantify the quality of PIV measurements. A series of steady measurements with different light pulse timings (Δt) have been conducted with a priori setup, so that these results can be used to optimise the measurements for unsteady flows. These measurements are carried out at both the midspan and 3.5h from the side wall.

Table 4.1 tabulates the PIV sensitivity tests of light pulse timings at various Reynolds numbers and different midspan locations. During these measurements, 2,500 image pairs were acquired at a sampling frequency of 7 Hz. The first set of measurements with FOV size of 24x50 mm were taken at the midspan of the channel providing full channel height measurements, while the second set with a smaller FOV size of 20x27 mm measured at 3.5h to provide a higher resolution close to the bottom wall of the channel. The latter is the smallest FOV size that could have been achieved with the provided PIV configuration. Light sheet was masked to narrow down its thickness to 2 mm at both locations.

Re_b ($U_b h/\nu$)	Δt (μsec)	z/h	FOV (mm x mm)
2,450	300, 800, 1000, 1200	7	24x50
2,700	1200	3.5	20x27
3,000	300, 900, 1000	7	24x50
3,400	1000	3.5	20x27
10,000	400, 900	3.5	20x27
25,000	300, 500	7	24x50
26,300	200, 300, 400	3.5	20x27

Table 4.1 PIV measurements at various Reynolds numbers, spanwise locations and light pulse timings.

For the sake of brevity, sensitivity of PIV measurements to the light pulse timing are only presented at two very different Reynolds numbers in Figure 4.7 and Figure 4.8. For the low Reynolds cases (Figure 4.7), the fastest light pulse timing ($\Delta t = 300\,\mu sec$) resulted in an overestimation of all rms components in both wall and core regions. A longer interval between the pulses has improved the measurements of the mean, fluctuating and shear stress components. However, even for Δt as high as 900 μsec measurements of rms components in the core region are not satisfactory. This is while 1000 μsec seem to return more realistic measurements in comparison to DNS. It must be mentioned that the levels of Reynolds shear stress component in the wall region are measured to be lower than DNS with both 900 and 1000 μsec configurations. Figure 4.8 shows the measurements of PIV at the final Reynolds number (~25,000) with two different light pulse timings of 300 and 500 μsec. It is interesting that within the investigated range of light pulse timings, v'_{rms} is the only sensitive component to the choice of Δt while $\overline{U}$, u'_{rms} and $\overline{u'v'}$ show only slight differences in the wall region.

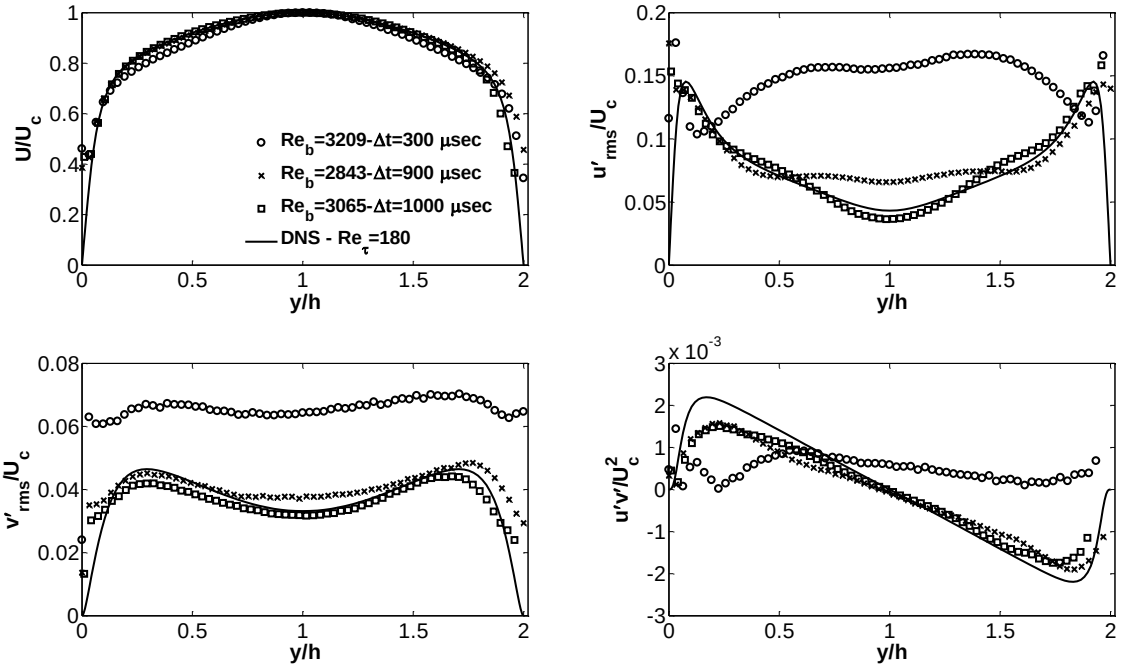

Figure 4.7 PIV measurements of streamwise and wall-normal velocity statistics with different light pulse timings at $Re_b \approx 3000$.

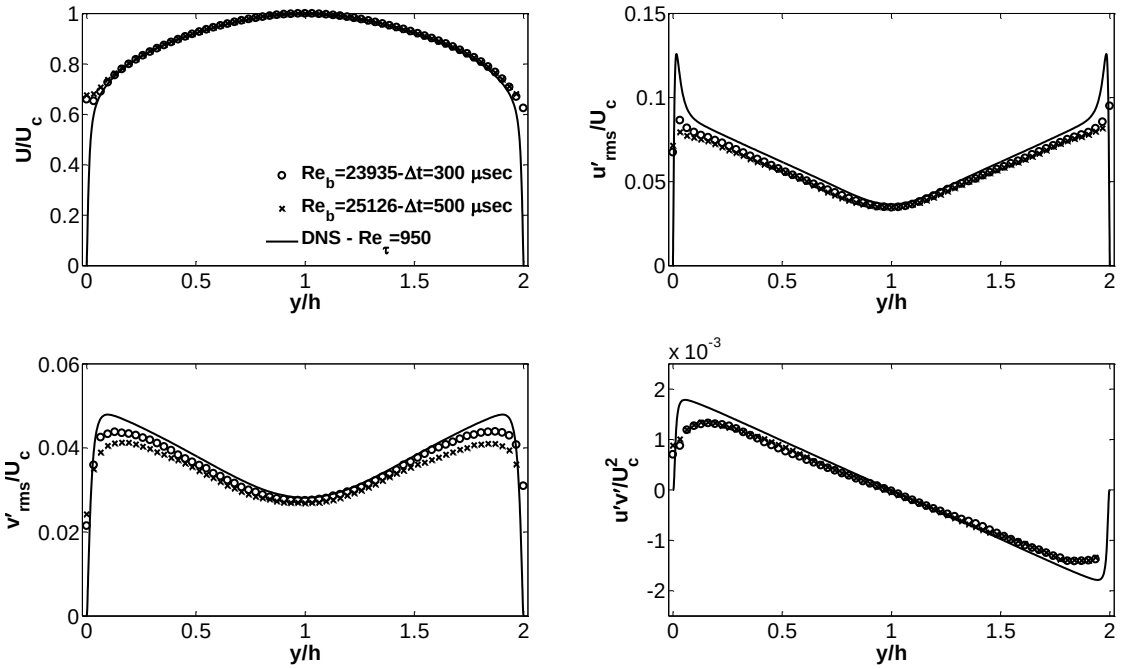

Figure 4.8 PIV measurements of streamwise and wall-normal velocity statistics with different light pulse timings at $Re_b \approx 25{,}000$.

The choice of Δt can play a major role in the measurements of PIV and therefore should be optimised according to the flow characteristics. This specifically becomes a challenge in the study of unsteady flows where the initial and final Reynolds numbers are very different from each other. In order to improve the resolution of the measurements, the laser sheet is moved

to 3.5h from the edge of the channel in the spanwise direction, where the flow shows a good two-dimensional behaviour (Figure 4.2).

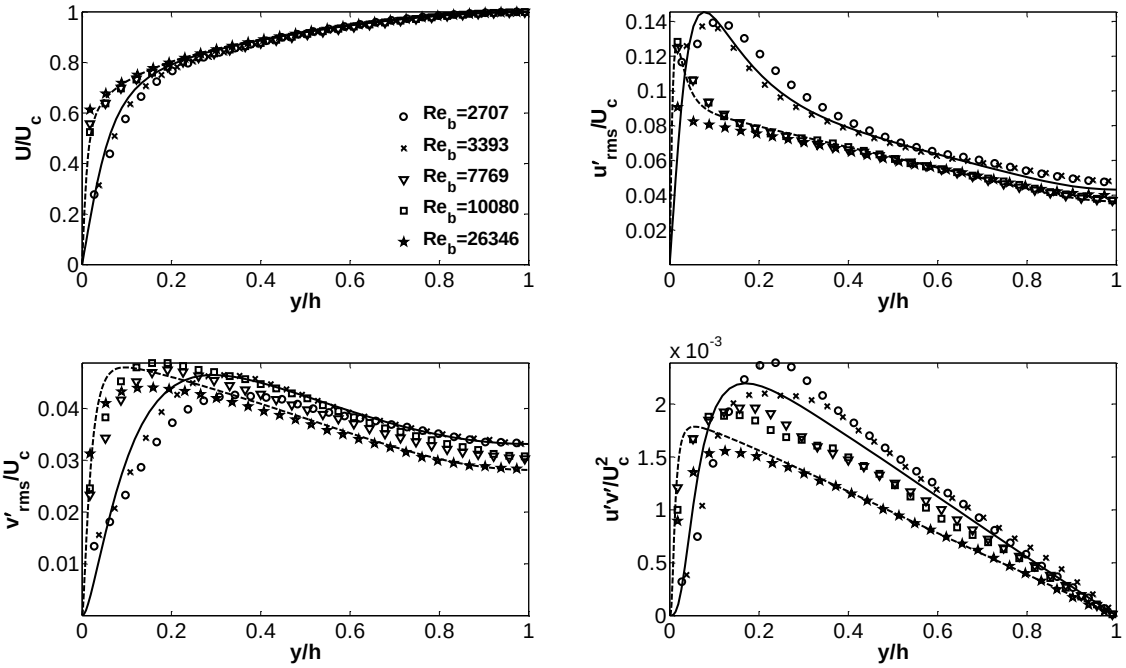

Figure 4.9 Outer scaled PIV measurements of mean, fluctuating and shear stress components at various Reynolds numbers at 3.5h in spanwise direction (Dash line: DNS data of Hoyas and Jiménez (2008) $Re_\tau = 21{,}300$; Solid line: DNS data of He and Seddighi (2013) $Re_b = 2{,}800$).

4.4.2 **Results**

Figure 4.9 shows a comparison between the PIV measurements and DNS data at $z = 3.5h$. Measurements are in good agreement with the DNS data. Large velocity gradients at the wall region, reflections from the surface as well as the finite pixel resolution of the camera made the measurements of flow components in the wall region extremely difficult.

The agreement between the PIV data and DNS is also confirmed in Figure 4.10 through the inner scaling of statistics, U^+ and y^+ where u_τ is obtained from the $\overline{u'v'}$ curve.

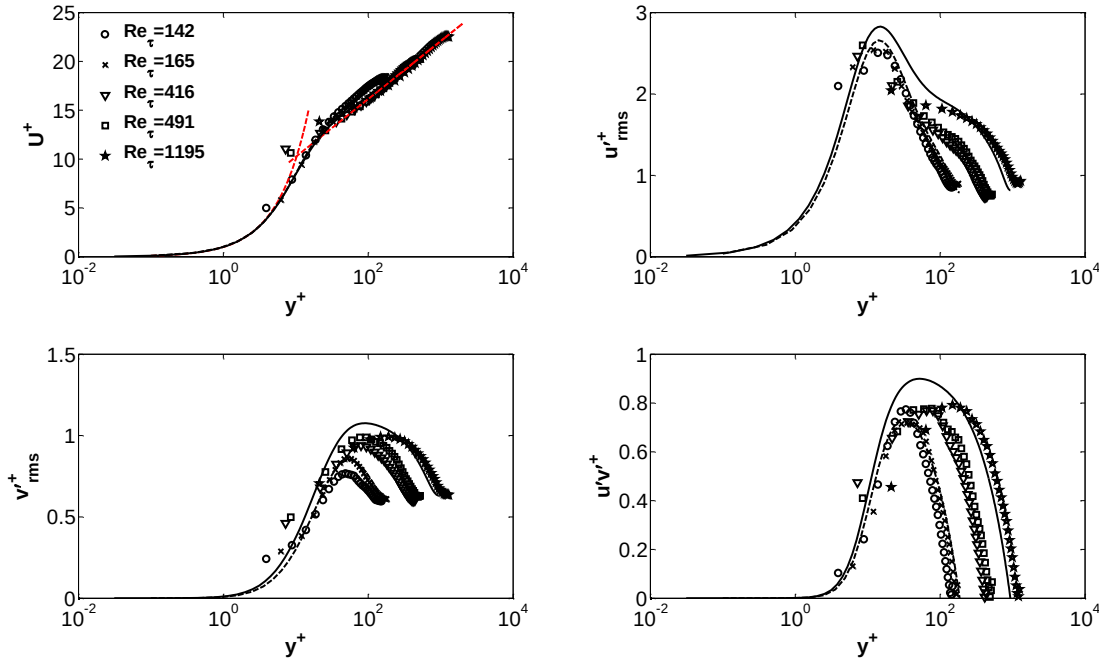

Figure 4.10 Inner scaled PIV measurements of mean, fluctuating and shear stress components of flow at various Reynolds numbers at 3.5h in spanwise direction (Dash line: DNS data of Hoyas and Jiménez (2008) $Re_\tau = 950$; Solid line: DNS data of He and Seddighi (2013) $Re_\tau = 180$).

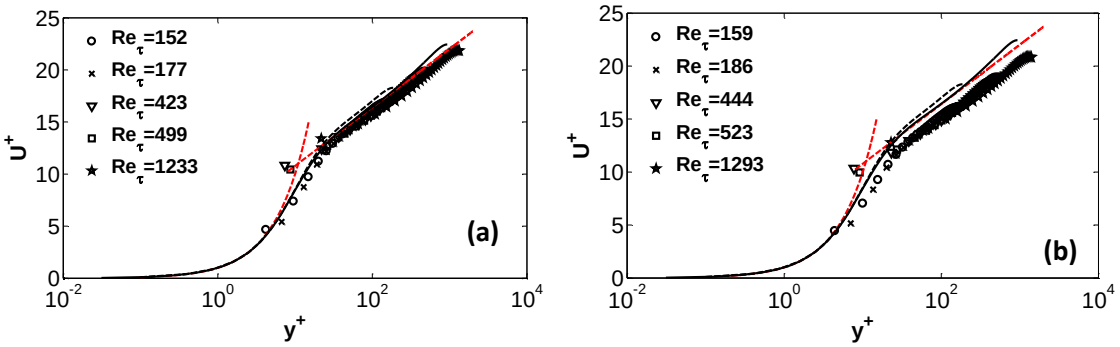

Figure 4.11 Inner scaled streamwise velocity at various Reynolds numbers calculated from (a) Blasius and (b) Dean.

Correlations of Blasius (4.1) and Dean (4.3) are also applied to calculate u_τ for comparison. Figure 4.11 shows the differences between Blasius and Dean estimation of u_τ. It can be seen from the plots that Blasius slightly and Dean significantly overestimate the values of u_τ within the range of present investigations. Therefore, from now on, Blasius correlation is applied wherever direct calculation of wall shear stress was not available. The log-law constants plotted in the figures have values of $\kappa = 0.389$ and $B = 4.31$, fitting well to higher Reynolds number flows (from $Re_\tau = 416$ shown in Figure 4.10).

4.5 Steady rough channel flows

This section presents and discusses the results obtained from PIV measurements of steady flows in a channel with a smooth surface on the top and a rough surface on the bottom.

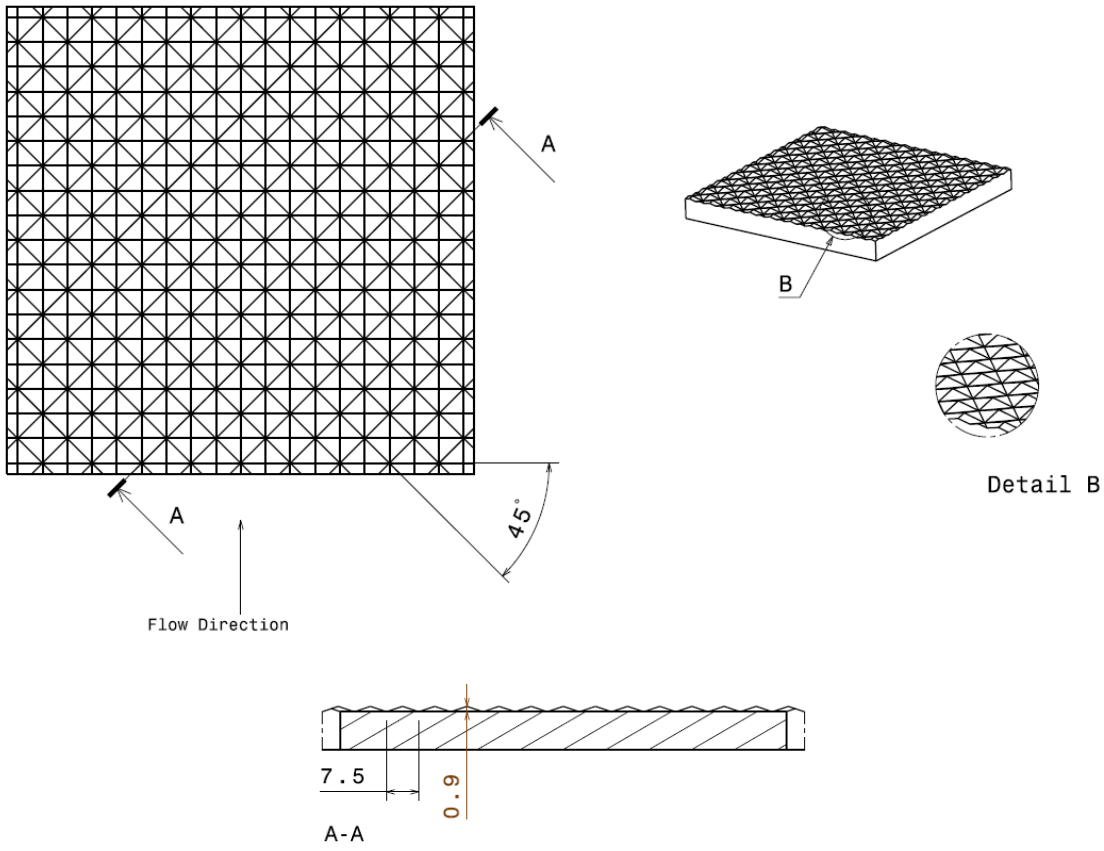

Figure 4.12 Geometry of roughness plate at the bottom surface of the channel.

Figure 4.12 depicts the geometry and size of the rough plate installed at the bottom of the channel facility. The roughness geometry consists of a series of square based pyramids with the wavelength of 7.5 mm and height (k) of 0.90 mm. These plates are installed in the final 4 metres of the channel facility. The pattern of the pyramids shown in Figure 4.12 is machined with a precision CNC milling machine on a Perspex plate of thickness 10 mm. The length of each plate is 1 metre. The plates are fixed to the channel bottom wall by using uniformly distributed bolts of a 400 mm spacing. These bolts are carefully drilled halfway through the plate. The last two plates are made of black Perspex to mitigate the possible light reflections from the rough surface. The direction of the flow is shown in Figure 4.12.

Table 4.2 summarises the details of the investigated cases over rough plates. The bulk Reynolds number (Re_b) is based on the channel half-height (h) and the bulk velocity (U_b). Friction Reynolds number is based on the friction velocity (u_τ) and effective channel half-height (δ_t).

Friction velocity is obtained by extrapolating a linear fit to the wall from the total shear stress profile. The location of the wall ($y = 0$) is assumed to be on the crest of the pyramids. The effective channel half-height is where the Reynolds shear stress approaches zero in the core region of the flow. In other words, the effective channel half-height of a smooth surface channel flow is equal to the geometrical channel half-height. k_s and k_s^+ are the equivalent sand-grain roughness height and roughness Reynolds number, respectively.

Re_b	Re_τ	δ_t/k	k^+	k_s^+	δ_t/h
2,836	166	28.6	5.8	8.7	1.03
3,489	211	29.3	7.2	10.8	1.05
5,041	311	29.7	10.5	15.7	1.07
7,736	506	30.9	16.4	24.6	1.11
9,932	663	31.8	20.9	31.3	1.15
18,218	1355	33.9	39.9	58.8	1.22
24,569	1894	34.2	55.5	83.2	1.23

Table 4.2 Details of the investigated flow conditions over the rough surface.

The measurements presented and discussed in this section are obtained from the vertical configuration of the laser sheet, shown in Figure 3.18 (b), located at 3.5h from the side walls. The size of the FOV was fixed at 33 x 33 mm with a sampling frequency of 7 Hz. The ensemble and streamwise spatial averaging are applied to 4,000 image pairs to obtain mean and turbulence quantities. The thickness of the laser sheet was maintained at 2 mm throughout the measurements. The PIV settings such as light time pulsing and image processing algorithms were similar to those used for the smooth flows discussed in §4.4.1.

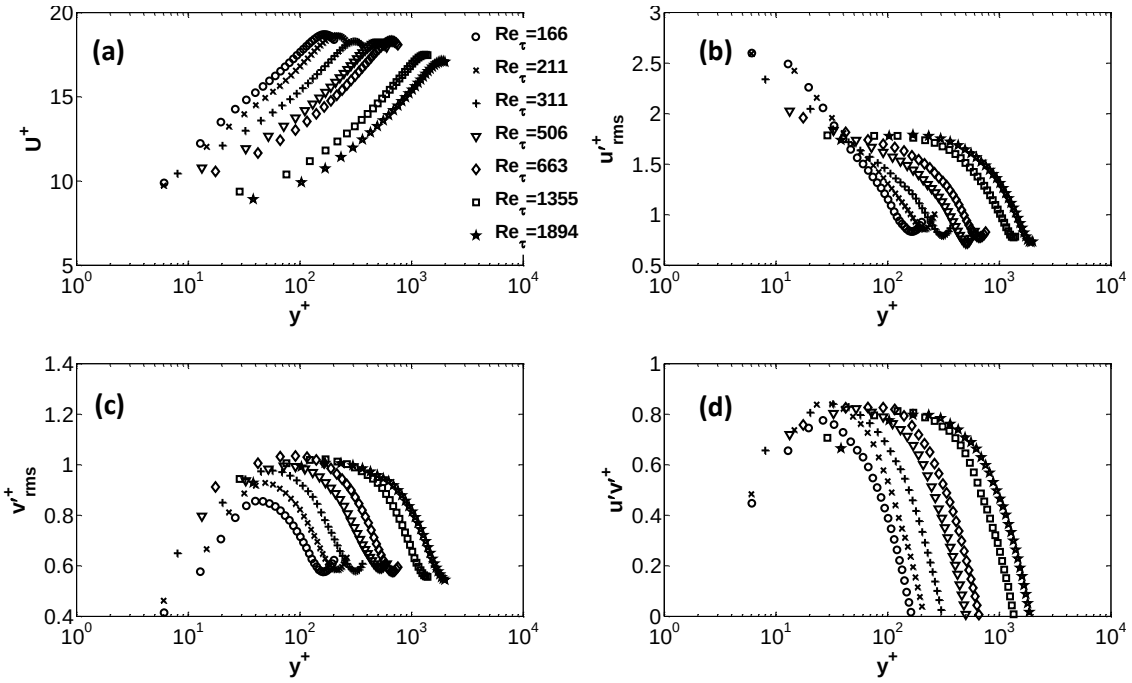

Figure 4.13 Inner-scaled mean and fluctuating components of streamwise and wall-normal velocities at different Reynolds numbers.

Figure 4.13 shows the measurements of the mean and rms components of the velocity along with the Reynolds shear stress at various Reynolds numbers. Inner scaling parameters are used in this figure to normalise the various components. Wall shear stress used for normalising these components is obtained from the slope of the Reynolds shear stress profile.

Figure 4.14 shows various components of mean and fluctuating velocities normalised by the outer scaling parameters, such as effective centreline velocity (U_t) and effective channel height (δ_t). It should be noted that the effective centreline velocity in these measurements is equal to the centreline velocity of the smooth channel flows. Filled symbols in this and the next figure, show the measurements from the smooth flow at similar bulk Reynolds number. These trends facilitate the comparison between the flows over rough and smooth surfaces.

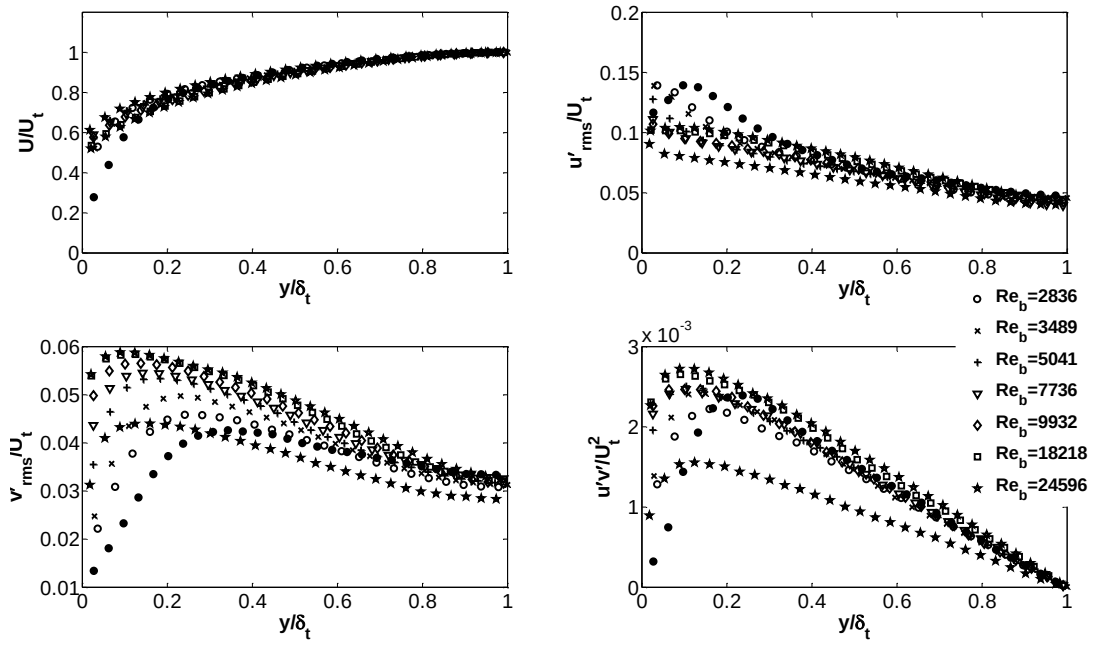

Figure 4.14 Outer-scaled mean and rms components of velocity at different Reynolds numbers (filled symbols show corresponding smooth flow measurements).

Figure 4.15 shows (a) the velocity deficit profiles, (b) normal streamwise and (c) wall-normal Reynolds stresses as well as (d) the Reynolds shear stress normalised by the friction velocity (u_τ). The wall-normal locations are normalised by the effective channel half-height (δ_t). It can be seen from this figure that the mean and turbulent components of the flow completely collapse on each other in the outer region of the flow, regardless of the surface or flow conditions. The normal streamwise stress component ($\overline{u'^2}$) obtained from the lower Reynolds flows ($Re_b = 2{,}836, 3{,}489$) show lower degree of similarity in comparison to the relatively higher bulk flow conditions. A similar trend is also evident in the behaviour of wall-normal stress component ($\overline{v'^2}$). This behaviour can mainly be attributed to the relatively low roughness Reynolds number (k_s^+). The profiles of Reynolds shear stress ($\overline{u'v'}$) show excellent collapse for all the flow and surface conditions. These plots provide a strong support for the Townsend's hypothesis of Reynolds number similarity and its extension wall similarity (Raupach et al. (1991)).

This similarity is rather surprising considering that the flows investigated herein lie on the transitionally rough regime (shown in Figure 4.16 (a)). In addition, most of the investigated flows in this study do not comply with the well-characterised flow conditions of Jiménez (2004), as the blockage ratio (δ/k) in these investigations are well below 40.

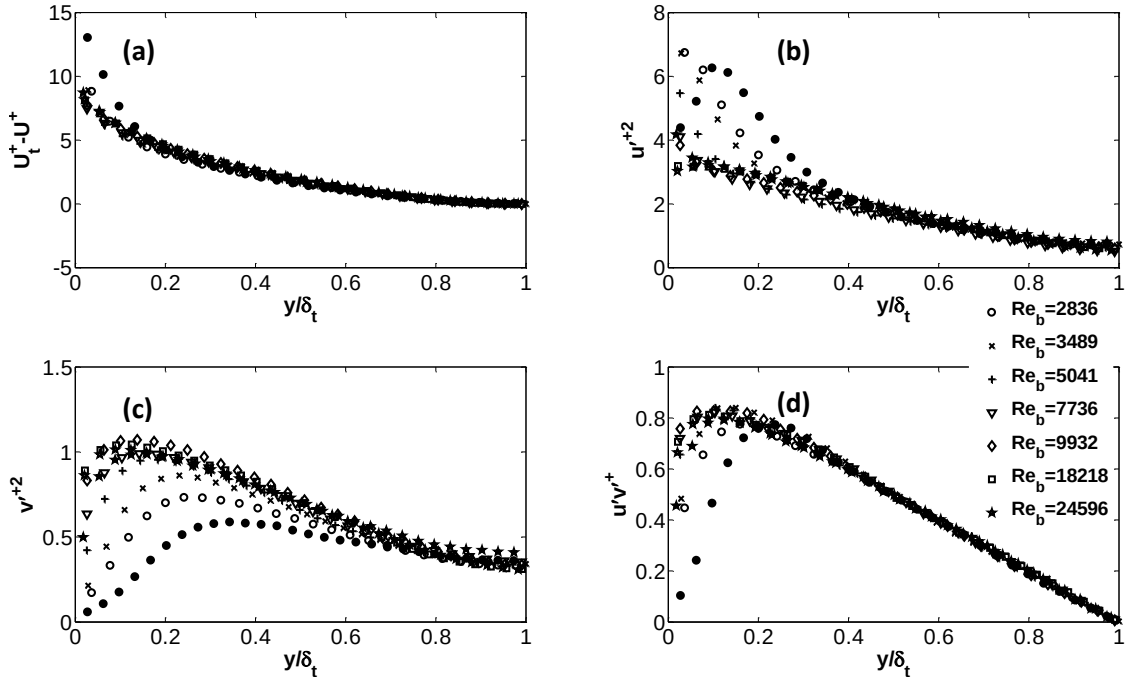

Figure 4.15 Mean and Reynolds stresses at different Reynolds numbers (filled symbols show corresponding smooth flow measurements).

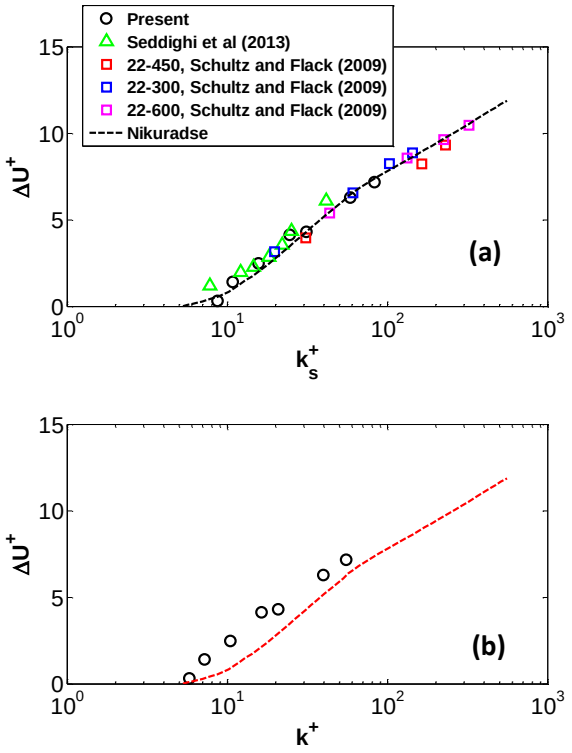

Figure 4.16 Roughness function versus (a) k_s^+(b)$k = k_s$. Dash line: Nikuradse

Figure 4.16 shows the variation of the roughness function (ΔU^+) versus the roughness Reynolds number (k_s^+, k^+) obtained from present investigations as well as others. The roughness function is the amount of the downward shift in the log region of the velocity profile in comparison to

the smooth curves, therefore, being a measure of the momentum deficit due to roughness elements. In the present investigations, this value is obtained by curve fitting to the log region of the smooth and rough inner-scaled velocity curves (Figure 4.13 (a)). The method of Österlund et al. (2000) was applied herein to calculate the log-law constants. The equivalent roughness height (k_s) for the fully rough flows was obtained from the following relationship:

$$\Delta U^+ = \frac{1}{\kappa}\ln(k_s^+) + B - C \tag{4.5}$$

where C is the roughness function intercept for uniform sand grain equal to 8.5. B and κ are obtained from the smooth flow and in these investigations are equal to 4.31 and 0.389, respectively. k_s was found to be $\approx 1.49k$ which is similar to the findings of (Schultz and Flack, 2009) and Seddighi et al. (2013) who investigated similar pyramid geometries.

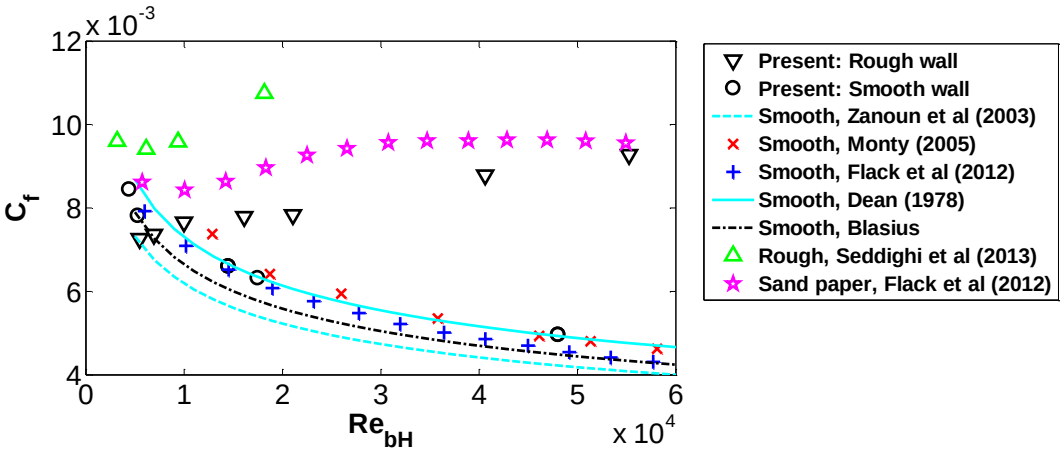

Figure 4.17 Friction coefficient at different Reynolds numbers.

Figure 4.17 compares the variations of the friction factor over smooth and rough surfaces at various Reynolds numbers (based on full channel height, H and bulk velocity) from the present and other investigations. The bulk velocity used for calculation of the friction factor and Reynolds number shown in Figure 4.17 is obtained from averaging the mean streamwise velocity obtained from PIV measurements. The friction coefficient over smooth surface is shown to be in agreement with the correlation of Dean (1978) for higher Reynolds number flows, whilst correlating better with those of Blasius at smaller Reynolds number flows. The friction coefficient and bulk Reynolds number curves calculated on the basis of flow meter measurements were shown to have an offset from the Dean's curve, correlating better with those of Blasius and Zanoun et al. (2003) (not shown here). For the sake of simplicity, bulk flow measurements of flow meter were applied to the Blasius' correlation to calculate the steady initial and final wall shear stresses for unsteady smooth-wall flows throughout this thesis.

Similarly, rough-wall flows with smaller Reynolds numbers are shown to be correlating well with the Blasius' correlation.

4.6 Summary

This chapter presents and discusses results obtained from the smooth and rough surfaces under steady conditions. LDV and PIV are used to measure the flow characteristics under various Reynolds numbers. These measurements are conducted at either midspan or $z = 3.5h$ from the near side wall for various steady flow scenarios.

Measurements under steady smooth flow conditions are in good agreement with the available benchmark data confirming minimal two dimensional effects at the midspan and the offset plane of 3.5h.

Results obtained from the rough surface flow conditions provide a strong support for Townsend's wall and Reynolds number similarity. According to Raupach et al. (1991), turbulent motions outside the roughness sublayer at high Reynolds numbers are independent of the wall roughness and viscosity. In the present investigations, the streamwise, wall-normal and shear Reynolds stresses at even relatively low roughness Reynolds numbers of $k_s^+ = 15.7$ and a blockage ratio (δ_t/k) of 34.2 also exhibit strong similarities.

In the present investigations, friction coefficient for smooth and hydrodynamically smooth surfaces is found to be in a better agreement with the correlations of Blasius and Dean (1978) for low and high Reynolds number flows, respectively.

The equivalent sand grain roughness height (k_s) obtained from the present investigations is in close agreement with the previous investigations of similar geometrical roughness. Contrary to the actual roughness height (k), equivalent sand grain roughness height correlates well with the roughness function following that of Nikuradse.

Chapter 5. Unsteady flows over smooth surfaces

5.1 Introduction

In this chapter, the behaviour of flow mean and turbulence characteristics under transient conditions over smooth surfaces are investigated in detail. During the experiments, the flow rate is accelerated from a lower Reynolds number turbulent flow to one at a higher Reynolds number (Re). The acceleration is generated by either a sudden opening of the control valve or a slowly but better controlled valve opening operation. PIV (Particle Image Velocimetry) and LDV (Laser Doppler Velocimetry) are used to measure the mean and turbulence characteristics of the flow.

In Section 5.2, details of the case studies are introduced. The instantaneous flow fields are discussed in Section 5.3. In order to provide a quantitative approach to the study of turbulence in unsteady flows, ensemble-averaged parameters are used in the consequent sections to study the time-developing boundary layers, auto-correlations, the behaviour of mean and fluctuating components and finally the critical Reynolds number and the period of transition.

5.2 Cases studied

A range of initial and final transient flow conditions are investigated to elucidate the underlying mechanisms involved in transient flows. Measurement conditions are tabulated in Table 5.1. Two type of accelerating flows have been investigated herein. In the first set, the flow temporal acceleration from a lower flow Re to the higher Re takes place in response to a sudden opening of the valve. Therefore, the required time for the transition in this scenario depends solely on the initial and final states as well as the operational curve of the control valve (Figure 3.7). Figure 5.1 shows the variation of bulk flow against time for some main sudden opening cases

studied herein. These variations are measured by the magnetic flow meter. In the second scenario, the flow acceleration from the first stage to the next occurs through a fully controlled routine. In other words, the valve's plug movement is manipulated in such a way to generate a pre-defined ramp type excursion of flow rate between the two states (cases S29-76R4 and S29-76R6). The latter scenario is mainly performed for validation and verification purposes while the main focus of this research remains on the sudden opening scenarios.

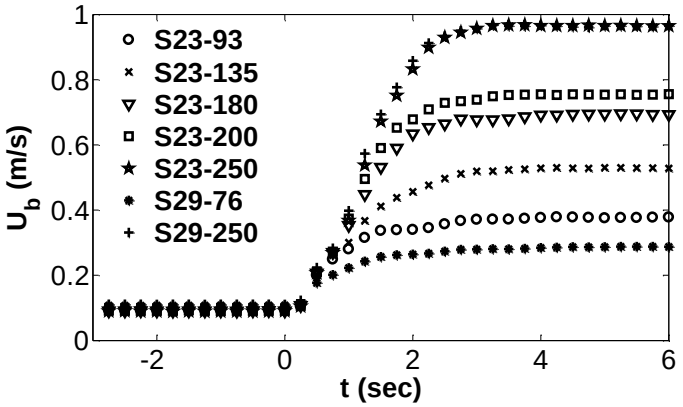

Figure 5.1 Variation of bulk velocity for selected sudden opening unsteady flows.

Table 5.1 summarises the features of unsteady flows investigated herein. Subscripts of 0 and 1 are used to designate the initial and final states, respectively. Δt is defined as the time required for the initial bulk velocity to reach 90% of the final state. Bulk Reynolds number (Re_b) is based on the bulk velocity (U_b) and channel half-height (h). Calculation of the friction Reynolds number (Re_τ) requires a priori knowledge of the friction velocity (u_τ) and hence wall shear stress (τ_w). As shown in §4.4.2, Blasius predictions of wall shear stress is the closest estimation among those investigated herein, therefore it has been applied here to calculate the friction Reynolds number for the steady flows. Δt^* $(= \Delta t U_{b1}/h)$ is the normalised acceleration time on the basis of the channel half-height and the final bulk velocity (U_{b1}). Alternatively, t_0^+ $(= {u_{\tau 0}}^2 t/\nu)$ is also used in the subsequent sections of this chapter as another non-dimensional time-scale.

PIV and LDV are both applied to measure mean and turbulence components of the flow. Two laser-camera configurations are used for the PIV measurements. The first configuration is to produce measurement of the flow field over a horizontal plane. This configuration requires the camera to be located at the top while the laser is fired from the side, perpendicular to the camera (Figure 3.18 (a)). The second configuration is applied to provide wall-normal measurements (Figure 3.18 (b)). The PIV wall-normal measurements are performed at two spanwise locations, midspan (7h) and quarter-span (3.5h). As discussed in §4.4, the quarter-span

measurements provide a better resolution in the wall region. Such measurements were only taken at the bottom plate in order to avoid occasional flow of air bubbles during the transients.

LDV measurements are made only at the quarter-span to facilitate measurements of the streamwise (u'_{rms}) and wall-normal (v'_{rms}) velocity components in the wall region. For cases S23-250, S29-76 and S29-250, eleven points were traversed in the wall-normal direction. For the rest of the cases shown in Table 5.1 measurements were only made at three wall-normal locations.

The main objective of these experiments is to examine the effects of various Re_{b1}/Re_{b0} ratios on the characteristics of transient flows. In order to facilitate the identification of the cases, following nomenclature is employed in Table 5.1;

- The first letter designates the type of surface topology (e.g. S for smooth, R for rough).
- The first and second numbers correspond to the initial and final Re, respectively (e.g.23-250 for 2,300-25,000).
- The last alphabet designates the type and duration of flow excursion (e.g. R3 for a 3 seconds ramp), for sudden opening cases, this is left blank.

Case No.	$U_{b0}-U_{b1}$ (m/s)	Δt (sec)	$Re_{b0}-Re_{b1}$	$Re_{\tau 0}-Re_{\tau 1}$	Δt^*	Comments
S23-250	0.09-0.96	1.9	2,300-25,000	150-1160	73.2	11 points LDV & PIV†
S23-230R3	0.09-0.94	3.3	2,300-23,400	150-1115	124.5	PIV†‡
S23-200	0.09-0.76	1.9	2,300-20,000	150-970	57.5	3 points LDV & PIV†
S23-180	0.09-0.69	1.85	2,300-18,000	150-890	51.4	3 points LDV & PIV†
S23-135	0.09-0.53	2	2,300-13,500	150-680	42.3	3 points LDV & PIV†
S23-93	0.09-0.38	1.4	2,300-9,300	150-500	21.1	3 points LDV & PIV†
S29-250	0.11-0.96	1.85	2,913-25,000	180-1190	71.4	11 points LDV & PIV†
S29-76	0.11-0.29	1.35	2,913-7,625	180-420	15.6	11 points LDV & PIV†‡
S29-76R4	0.11-0.29	4	2,913-7,625	180-420	47.2	PIV†
S29-76R6	0.12-0.29	6.1	2,913-7,625	180-420	70.76	PIV†
S29-54	0.09-0.19	3.4	2,913-5,450	180-311	25.9	3 points LDV
S35-250	0.14-0.98	1.9	3,500-25,000	220-1238	74.7	3 points LDV
S33-40	0.12-0.15	6.7	3,300-4000	200-236	40.1	3 points LDV
S60-250	0.24-0.98	1.3	6,000-25,000	384-1326	51.1	3 points LDV
S90-250	0.37-0.97	1.35	9,000-25,000	562-1313	52.6	3 points LDV

Table 5.1 Initial and final flow conditions of the unsteady measurements. †: PIV measurements at 3.5h, ‡: PIV measurements at 7h.

5.3 Instantaneous flow behaviour

In this section, the focus of the discussions is devoted to the instantaneous behaviour of the flow under transient conditions.

In order to facilitate the discussions, a previously examined unsteady flow case by He and Seddighi (2013) (indicated as HS13 herein) is revisited through experimental observations. This case consists of a step change of flow rate with initial and final friction Reynolds numbers of 178-418. The imposed acceleration time scale in terms of non-dimensional time is $\Delta t^* = 0.22$ which is equivalent to $t = 0.019$ seconds in the experimental facility described in Section 3.2. Due to experimental limitations, the fastest acceleration rate in the described range is 1.35 seconds as shown in Table 5.1 (case S29-76).

In case S29-76, the bulk velocity is increased from 0.11 to 0.29 m/s in 1.35 seconds due to a sudden opening of the valve. The history of the ensemble-averaged bulk flow and friction

coefficient is shown in Figure 5.2, where t and t^* are the dimensional and normalised time. Dash lines, designate the time stamps shown in the streamwise fluctuating contours presented next (Figure 5.3).

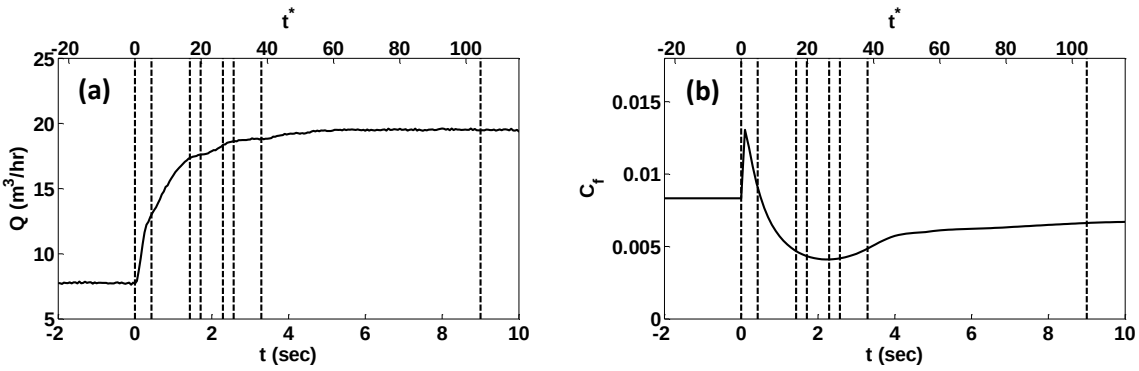

Figure 5.2 Temporal evolution of (a) bulk flow; and (b) friction coefficient for case S29-76.

Due to technical difficulties in the implementation of hot-film sensors, friction coefficient ($C_f = 2\tau_w/\rho U_b^2$) for all the cases reported herein was calculated by means of RANS CFD simulations of channel flow under corresponding experimental flow conditions. The actual flow variation shown in Figure 5.2 (a) is used to calculate C_f. Therefore, the C_f values are only indicative and the timescales might differ from the actual flow conditions, readers are referred to Chapter 7 for further information on the modelling procedures and results.

Figure 5.3 shows the contours of the fluctuating streamwise velocity (u') of case S29-76 measured at a horizontal plane adjacent to the wall. This velocity is obtained from subtraction of the mean velocity averaged in both streamwise and spanwise directions of the FOV from the instantaneous velocity ($u' = u - \overline{U}$). The fluctuating velocity was then normalised using final bulk velocity (u'/U_{b1}).

The distance of the measurement plane was 1 mm above the bed which is equivalent to $y_0^+ (= yu_{\tau 0}/\nu) = 7$ and $y/h = 0.04$. y_0^+ is based on the initial flow friction velocity obtained from the Blasius' friction law.

The initial steady flow consists of low magnitude fluctuations with limited streamwise streaky structures ($t^* = 0$). The formation, development and enhancement of the elongated streaks of positive and negative u' is the main characteristic of the early stages of the transient flow ($t^* < 15$). It can be seen that these structures become stronger in magnitude as time proceeds until around $t^* \sim 20$ where the first signs of high magnitude fluctuations appear (e.g. Figure 5.3, $t^* =$

16.6). These turbulent spots initially appear as isolated bursts which later spread throughout the domain as time proceeds (e.g. Figure 5.3, $t^* = 104.4$).

The above process is typical of that observed in the boundary layer bypass transition, see for example Jacobs and Durbin (2001). The dark blue regions in the contours of streamwise fluctuating velocity at the early stages of transition are the negative jets which are known as the primary instability (also known as Klebanoff modes) in the boundary layer bypass transition due free-stream-turbulence. This stage of the transient flow is referred to as the pre-transition due to He and Seddighi (2013) which is equivalent to the buffeted laminar boundary layer in bypass transition studies. The progressive amplification and elongation of the jets are followed by the appearance of the first turbulent spots. These spots result in juxtaposed layers of elongated positive and negative streamwise fluctuating velocities that eventually breakdown to form a new fully turbulent state. DNS study of He and Seddighi (2013) has shown that this process progresses independently on the top and bottom walls of the channel.

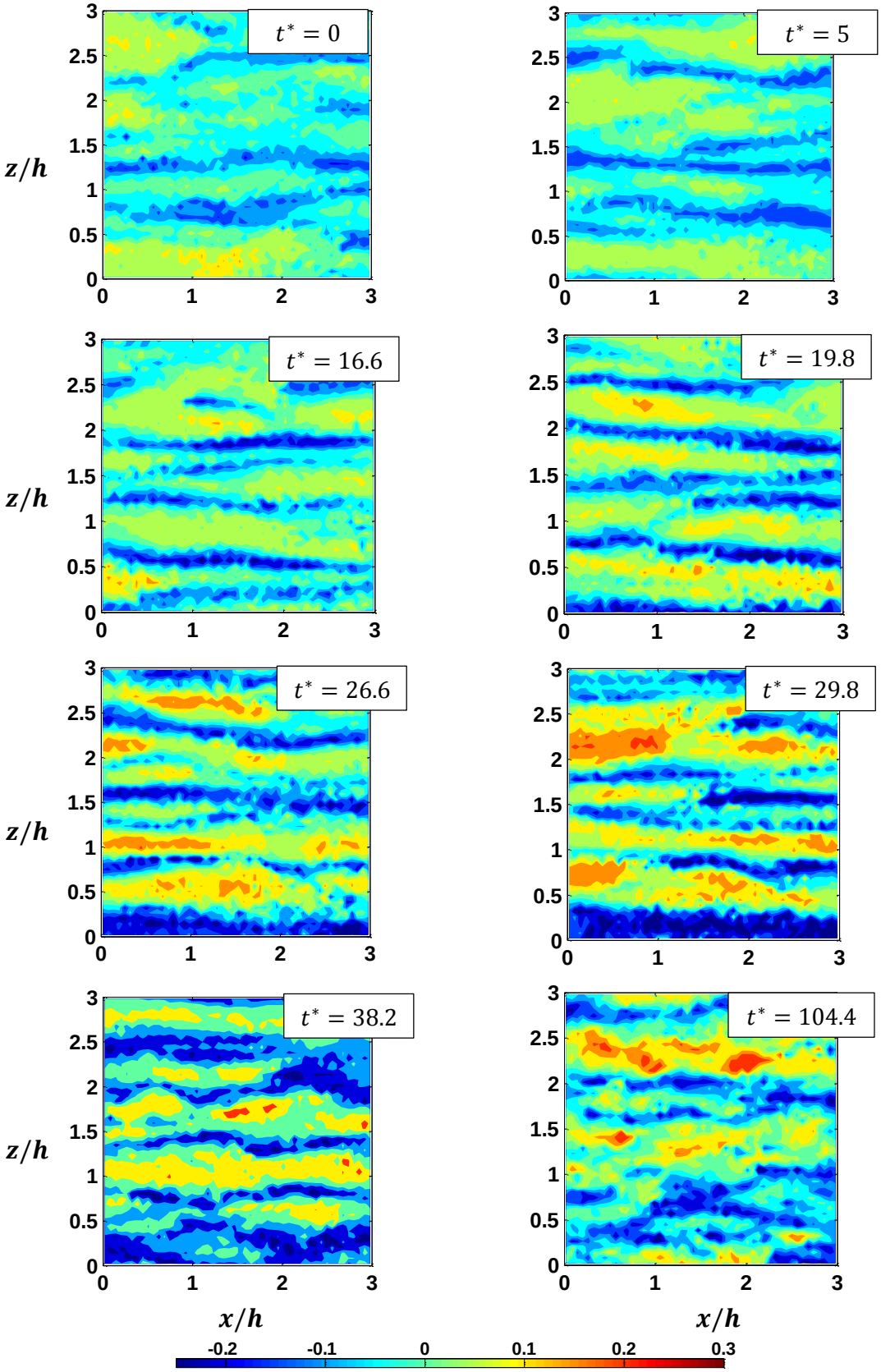

Figure 5.3 Temporal evolution of contour plots of streamwise fluctuating velocity (u'/U_{b1}) for case S29-76 at a plane 1 mm ($y_0^+ = 7, y/h = 0.04$) above the bed.

In order to further elucidate the concept, we shall look into the instantaneous velocity fluctuations of the streamwise and wall-normal components. Figure 5.4 shows the fluctuating streamwise and wall-normal velocity components obtained from case S29-76 measured by the LDV at various wall-normal locations of $y_0^+ = 2{,}9{,}31$ and 189.

Distinct differences can be seen in the response of u' and v' velocity components as previously shown by He and Seddighi (2013) . For instance, in Figure 5.4 (c) and (d), the high amplitude but rather low frequency response of u' following the valve opening is attributed to the existence of the streaky structures which are not perceivable in the trends of v'. The response of the v' component corresponds to the onset of transition. Since the initial transition is limited to the wall region, the response of u' and v' in the core region is delayed. Propagation of turbulence from the wall to the core region of the channel results in the increase of the amplitude of fluctuating signals (subplots (e) and (f)).

Similar trends to that of Figure 5.4 are provided from the PIV measurements in the spanwise direction. These measurements are shown in Figure 5.5 at the centreline of the FOV in the spanwise direction. The variation of w' during and after the transition can be seen to be similar to that of v', that is to have an initial calm state followed by abrupt fluctuations after the onset of transition.

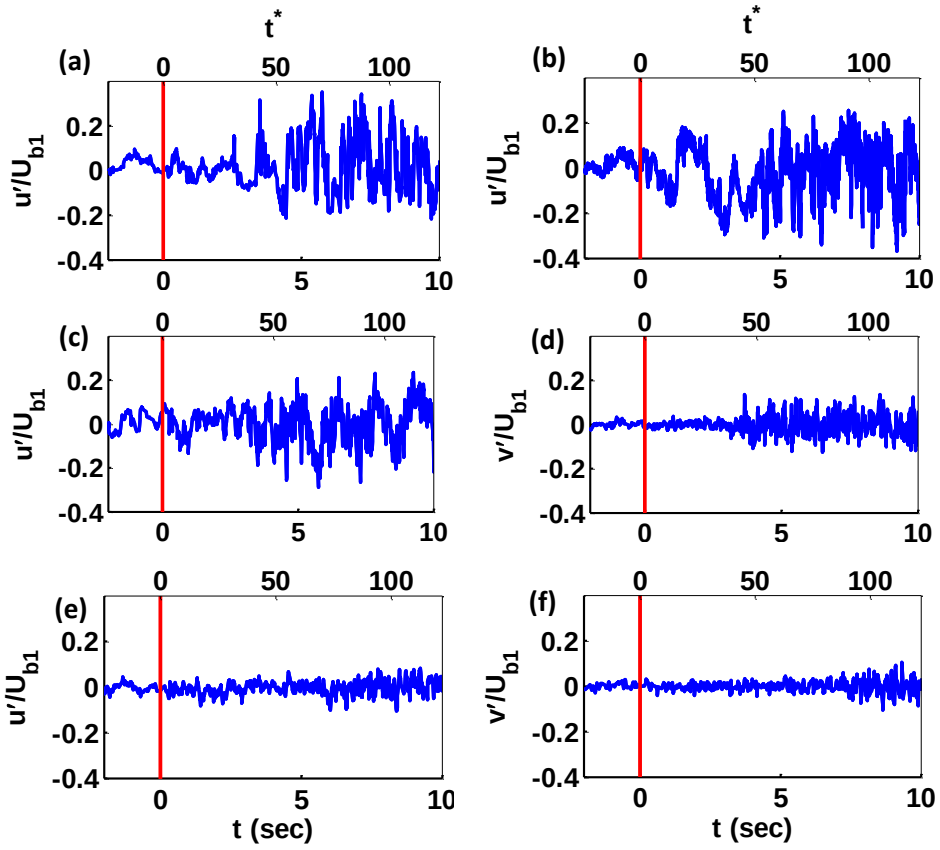

Figure 5.4 LDV measurements of fluctuating velocity of streamwise and wall-normal components at (a) $y_0^+ = 2$; (b) $y_0^+ = 9$; (c) and (d) $y_0^+ = 31$; (e) and (f) $y_0^+ = 189$ for case S29-76.

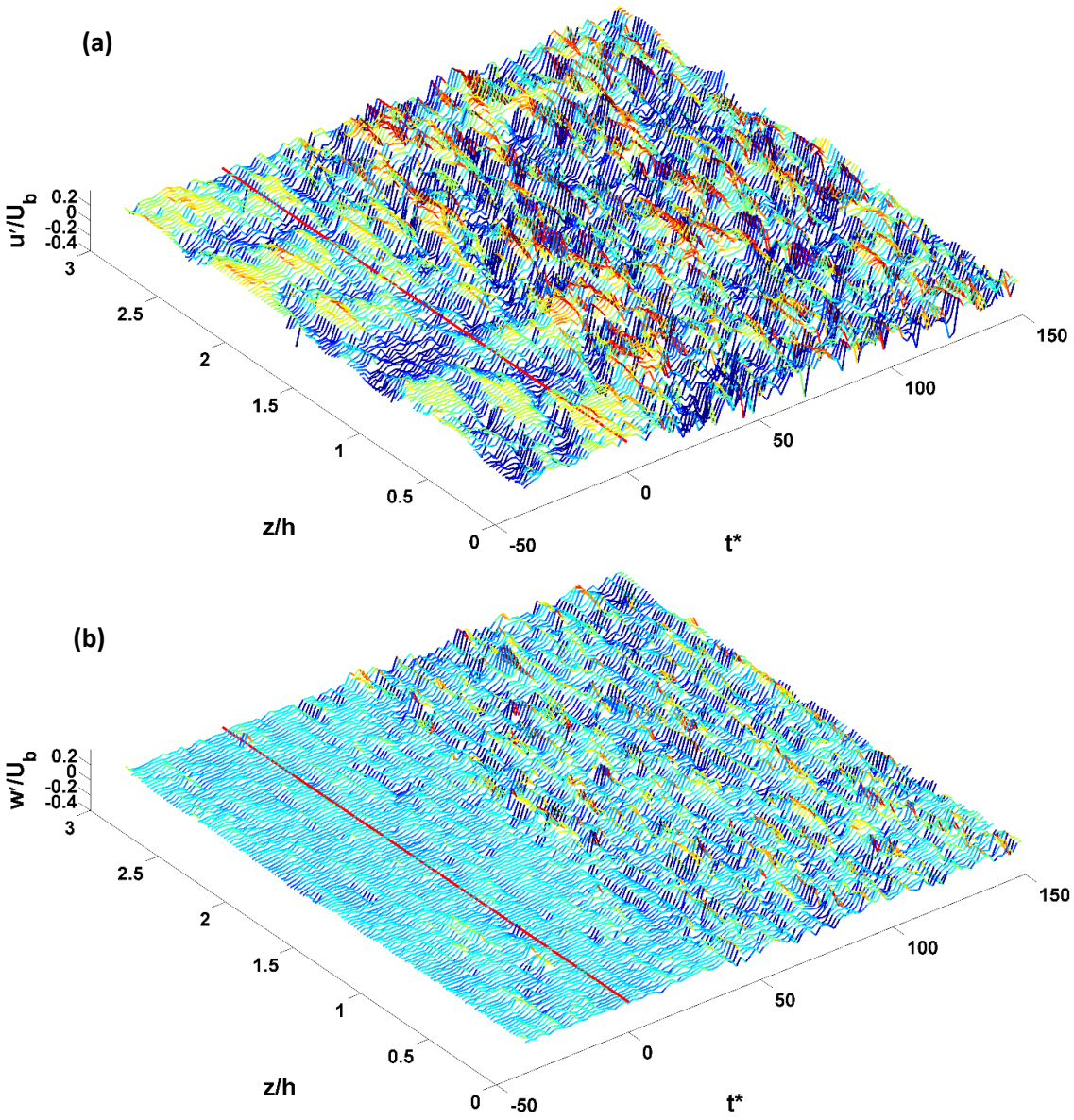

Figure 5.5 Temporal variation of normalised fluctuating velocities in (a) streamwise (u'/U_{b1}) and (b) spanwise directions (w'/U_{b1}) at $y_0^+ = 7$, $y/h = 0.04$ in the midsection of the FOV for case S29-76.

Case S23-230R3 is the highest final to initial Reynolds number ratio producible with the present water flow facility that is 2,300-25,000 in 3.3 seconds. In order to improve the repeatability of the valve opening in the mentioned range of the trim travel, this case adopts a slower ramp with an improved valve movement control. Figure 5.6 shows the variation of ensemble-averaged flow rate along with friction coefficient, calculated from CFD. It should be noted that the development of C_f shown in the figure is only indicative and the time scales are not necessarily the same as those of the actual flows. Contour plots of streamwise fluctuating velocity at various times are shown next with the corresponding times designated as dash lines in Figure 5.6.

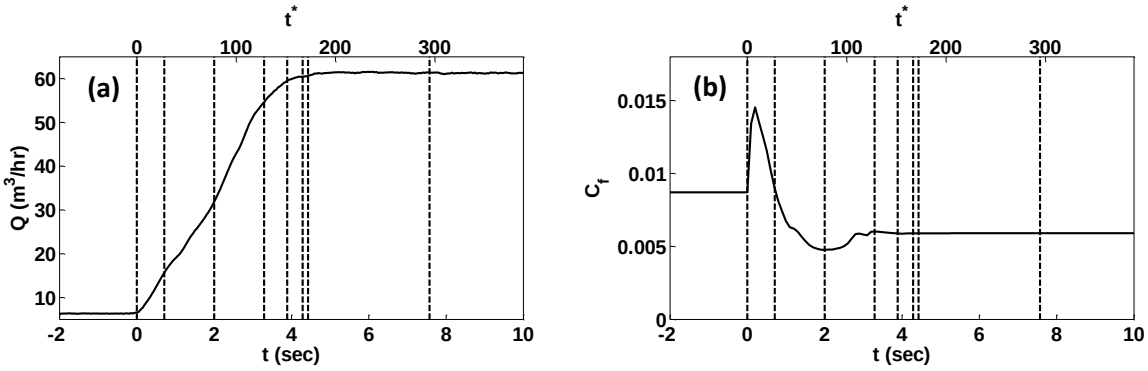

Figure 5.6 Temporal evolution of (a) bulk flow; and (b) friction coefficient for case S23-230R3.

The instantaneous u' contours in the xz plane at a distance of 1 mm from the bottom surface are shown at various times in Figure 5.7. The process is very similar to the smaller final to initial Re case described earlier, except that the streaks during the pre-transition phase are much stronger in magnitude. It is also interesting to note that the streaky structures are mitigated in a short duration after the valve's opening (e.g. Figure 5.7, $t = 0.71\ sec$, $t^* = 27.79$) before their amplification, burst generation and final break down. Figure 5.8 shows the fluctuating streamwise and wall-normal velocity components obtained from the case S23-250 measured by the LDV at the wall-normal locations of $y_0^+ = 2,12,33$ and 152. Fluctuations of streamwise and spanwise velocities are shown in Figure 5.9.

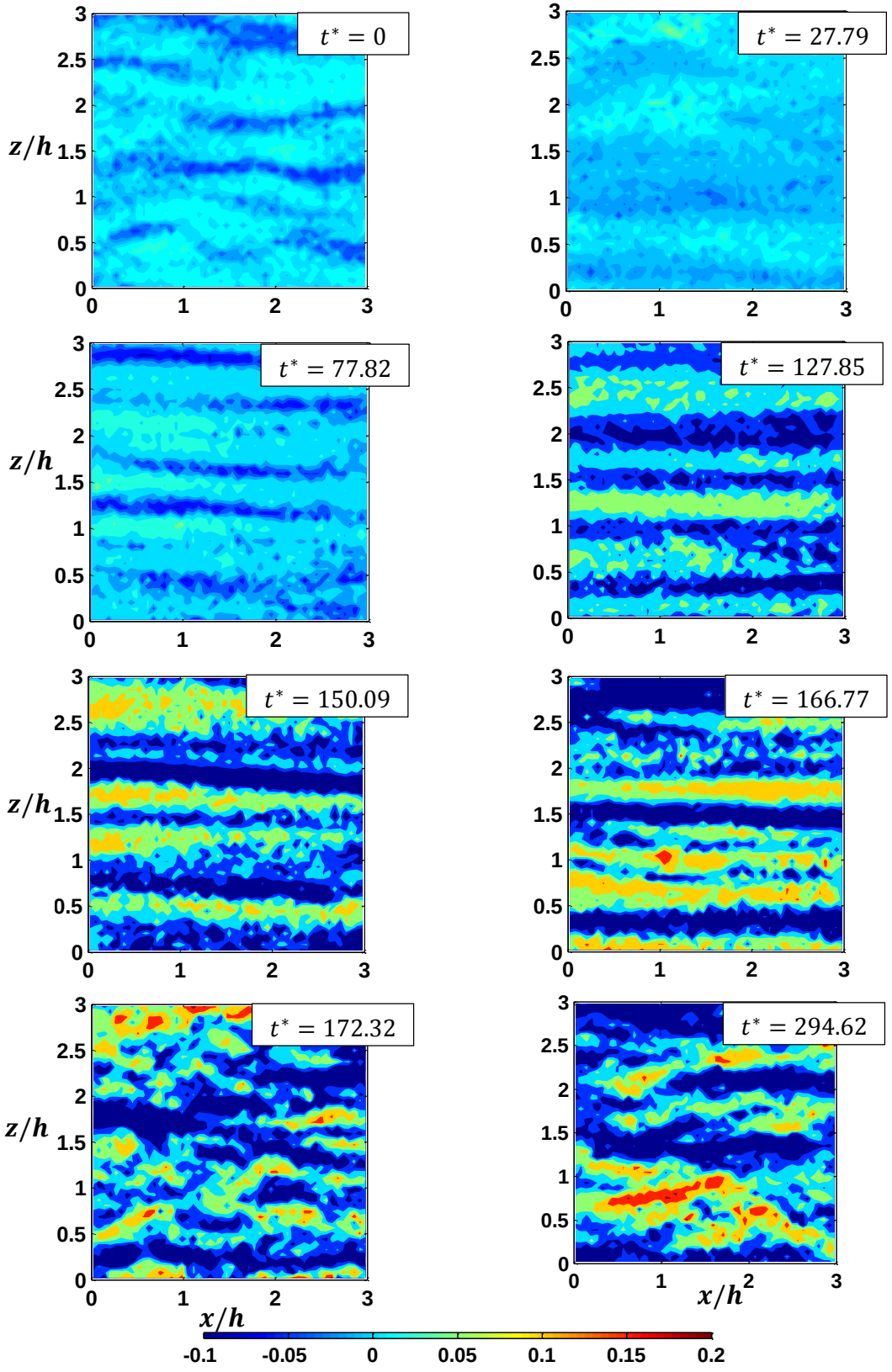

Figure 5.7 Temporal evolution of contour plots of streamwise fluctuating velocity (u'/U_{b1}) for case S23-230R3 at a plane 1 mm $(y_0^+ = 6, y/h = 0.04)$ above the bed.

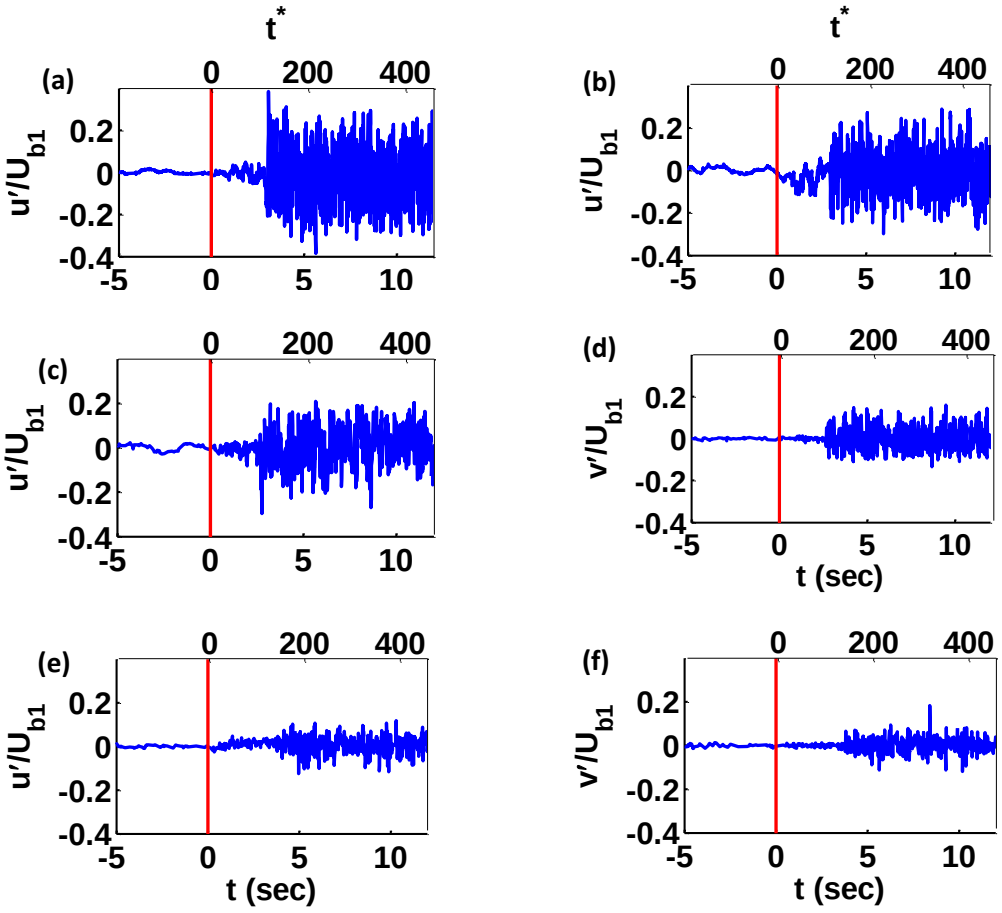

Figure 5.8 LDV measurements of fluctuating velocity of streamwise and wall-normal components at (a) $y_0^+ = 2$; (b) $y_0^+ = 12$; (c) and (d) $y_0^+ = 33$; (e) and (f) $y_0^+ = 152$ for case S23-250.

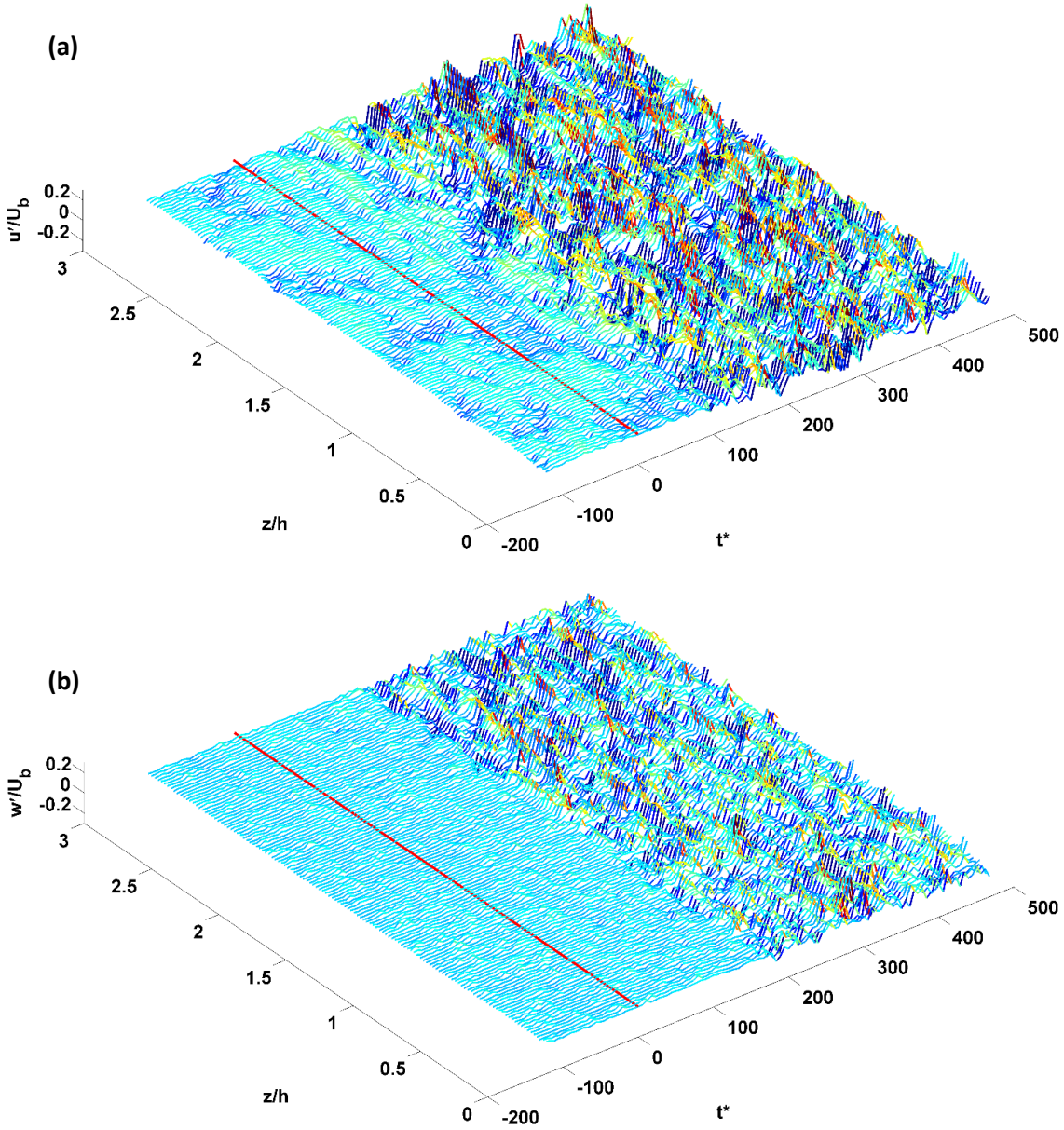

Figure 5.9 Temporal variation of normalised fluctuating velocities in (a) streamwise (u'/U_{b1}) and (b) spanwise directions (w'/U_{b1}) at $y_0^+ = 6$, $y/h = 0.04$ in the midsection of the FOV for case S23-230R3.

5.4 Ensemble-averaged flow behaviour

In this section, the behaviour of the flow under transient conditions is examined on the basis of ensemble-averaged flow statistics. This section can shed light on the quantitative aspect of the phenomenon emerged from the instantaneous flow fields in the previous section. Statistics obtained from PIV measurements are obtained from both temporal and spatial averages, where the detail of the spatial averaging approach depends on the plane of measurement. Spatial averaging takes place in both x and z direction in xz planes, while only streamwise spatial

averaging takes place in xy plane. Ensemble-averaged statistics for unsteady LDV measurements were calculated by means of the windowing approach discussed in §3.4.

It will be shown in this section that the quantitative behaviour of flow and turbulence under unsteady conditions are directly comparable to bypass transition flows due to free-stream-turbulence. The parameters to be discussed include perturbing velocities, momentum-thickness Reynolds number and shape factor.

5.4.1 The time-developing boundary layer

It has previously been shown by DNS studies that a step-change of flow rate from an initially turbulent flow results in a three-stage flow development, named pre-transition, transition and fully turbulence. During the pre-transition phase, a newly formed boundary layer on the wall begins to expand into the core region of the flow. As shown previously by DNS investigations, and to be confirmed here through experiments, the development of the velocity profiles during the pre-transition phase show strong correlations if normalised by the similarity parameter $\eta(= y/2\sqrt{\nu t})$.

In order to facilitate the comparisons between the unsteady channel flow and boundary layers, perturbing velocity is introduced as follows (He and Seddighi (2013))

$$\overline{U}^{\wedge}(y/h, t^*) = \frac{\overline{U}(y/h, t^*) - \overline{U}(y/h, 0)}{\overline{U}_c(t^*) - \overline{U}_c(0)} \tag{5.1}$$

where $\overline{U}_c(t^*)$ is the ensemble-averaged centreline velocity at t^*.

The first Stokes problem deals with a laminar flow over a flat plate that is subjected to a sudden movement at constant velocity. Solution to this problem is identical to the heat conduction equation for one-dimensional unsteady temperature variations (Schlichting et al. (2000)). A dimensionless similarity variable can be defined as $\eta = y/2\sqrt{\nu t}$ with a solution of

$$U(\eta) = 1 - \mathrm{erf}(\eta) \tag{5.2}$$

where $\mathrm{erf}(\eta) = \frac{2}{\sqrt{\pi}} \int_0^{\eta} e^{-\eta^2} d\eta$. Non-dimensional parameters of $\overline{U}^{\wedge}, y_0^+$ and t_0^+ can be implemented into the Stokes solution.

Stokes first problem is concerned about the sudden movement of a solid boundary and therefore requires a modification for relatively slower evolving boundaries. Applying a factor of 0.75 to η was shown to collapse and scale the Stokes solution on the results obtained from all the unsteady cases investigated herein (Figure 5.10).

Table 5.2 summarises the actual and normalised timescales describing the onset of transition and fully turbulent regimes in various cases investigated herein. Friction coefficient or v'_{rms} history plots can be used to find the critical time. The critical time marks the end of the pre-transition zone and the onset of transition. On the other hand, the u'_{rms} history plots in the wall region can be used to designate the commencement of the fully turbulent regime. The method these quantities are derived herein is discussed in §5.4.3 with further details. The "*cr*" and "*turb*" subscripts in Table 5.2 are used to designate the onset of transition and fully turbulent states, respectively. (He and Seddighi, 2015) suggest that t_0^+ is a useful quantity to specifically detect the period of the pre-transition phase. This period is in the range of $80 < t^+_{0,\ cr} < 130$ in most of the examined cases herein.

Cases	$t_{cr}(sec)$	$t_{turb}(sec)$	t^*_{cr}	t^*_{turb}	$t^+_{0,\ cr}$	$t^+_{0,\ turb}$
S23-250	2.4	4.2	94.3	165.1	87.5	153.1
S23-200	2.6	5	82.7	159.0	81.3	156.3
S23-180	2.8	4.8	80.9	138.6	94.5	162.0
S23-135	2.4	4.7	50.6	99.1	87.7	171.7
S23-93	2.8	6.1	40.6	88.4	98.4	214.3
S29-76	2.4	5.3	28.9	63.9	126.3	279.0
S29-54	2.4	6.1	18.4	46.6	110.8	281.7
S29-250	1.9	3.5	74.2	136.8	96.1	177.1
S35-250	1.4	2.8	54.9	109.9	98.8	197.6
S33-40	2.5	8	15.3	49.0	152.5	488.1

Table 5.2 Dimensional and normalised critical and fully turbulent timescales for various unsteady cases.

Figure 5.10 shows the development of perturbing velocity profiles with time for four different unsteady cases, S29-76, S23-250, S23-93 and S23-135. In these figures, the perturbing velocity is plotted versus a modified similarity parameter $\eta = y/2\sqrt{\nu t}$. The Stokes solution (equation (5.2)) is also provided for direct comparisons. It can be seen that the perturbing velocity remains more or less unchanged during the pre-transition regime collapsing on the scaled Stokes solution at all four cases. It can be seen from these figures that the development of the perturbing velocity is very similar for all four cases, despite the fact that these four cases are very different in terms of final and initial flow conditions. It is noticeable that the detection of the onset of transition is not feasible from the perturbing velocity profiles.

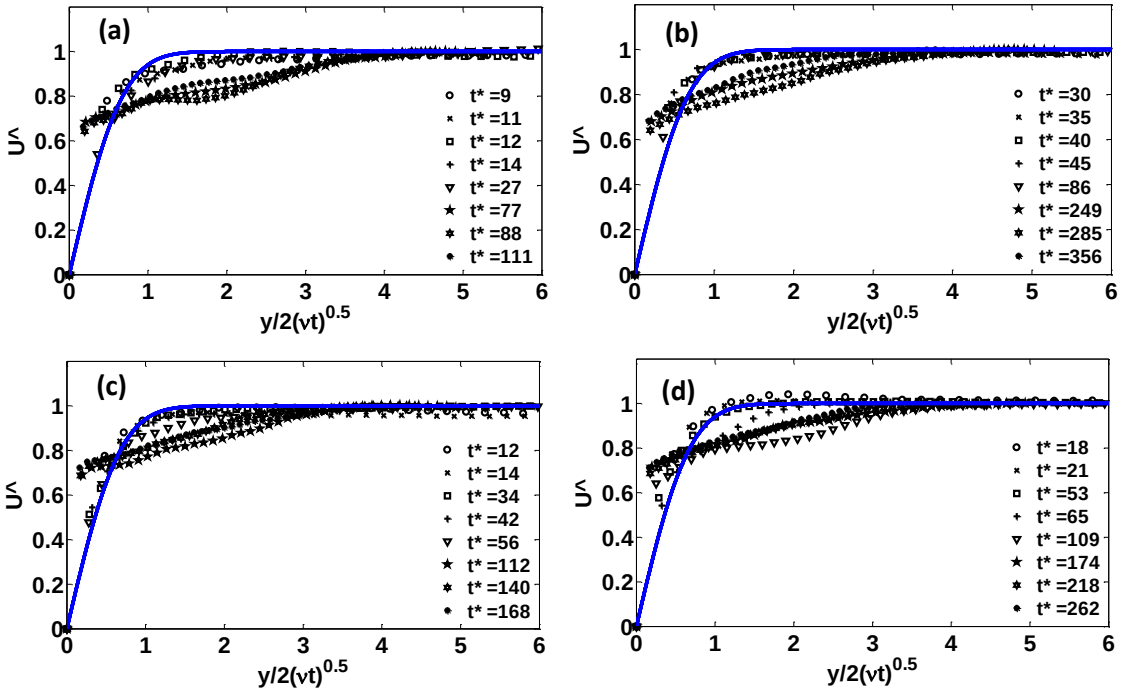

Figure 5.10 Development of perturbing velocity profiles with time for four different cases: (a) S29-76; (b) S23-250; (c) S23-93; (d) S23-135; Line: scaled Stokes solution.

The displacement thickness (δ_{du}), momentum thickness (θ) and shape factor (H) of the boundary layers in unsteady internal flows are re-introduced as follows by He and Seddighi (2013)

$$\delta_{du}(t^*) = \int_0^1 \left(1 - \overline{U}^{\wedge}(y/h, t^*)\right) d(y/h) \tag{5.3}$$

$$\theta(t^*) = \int_0^1 \overline{U}^{\wedge}(y/h, t^*)\left(1 - \overline{U}^{\wedge}(y/h, t^*)\right) d(y/h) \tag{5.4}$$

$$H(t^*) = \delta_{du}(t^*)/\theta(t^*) \tag{5.5}$$

Figure 5.11 shows the development of momentum-thickness Reynolds number ($Re_\theta = \theta h\overline{U_c}/\nu$) and shape factor for two unsteady cases calculated from equations (5.4) and (5.5). Direct comparisons with transitional flows (Roach and Brierley (1992)) are also provided for case S29-76. In these comparisons, $Re_x (= U_\infty x/\nu)$ needs to be linked to a temporal Reynolds number. One of the feasible methods to provide the link is to replace x with $U_{conv}t$. Convective velocity of $0.74U_b$ is shown by He and Seddighi (2013) to correlate their data very well. Similar convective velocity shows a good correlation with the data obtained from case S29-76, bearing in mind that the HS13 case study had a similar final to initial Reynolds number ratio with a much shorter acceleration time (0.019 seconds). It should however be mentioned that the convective velocity introduced above was specifically curve-fitted to the friction coefficient trend of HS13 and hence cannot be considered to be universal. Furthermore, the results of case S23-250 are

also included for comparisons. As can be seen from these curves, the general behaviour of the two cases are very similar, although the final to initial Reynolds number ratios are very different. It should be emphasised that the low-resolution PIV measurements in the wall region can affect the quality of the displacement and momentum thickness calculations.

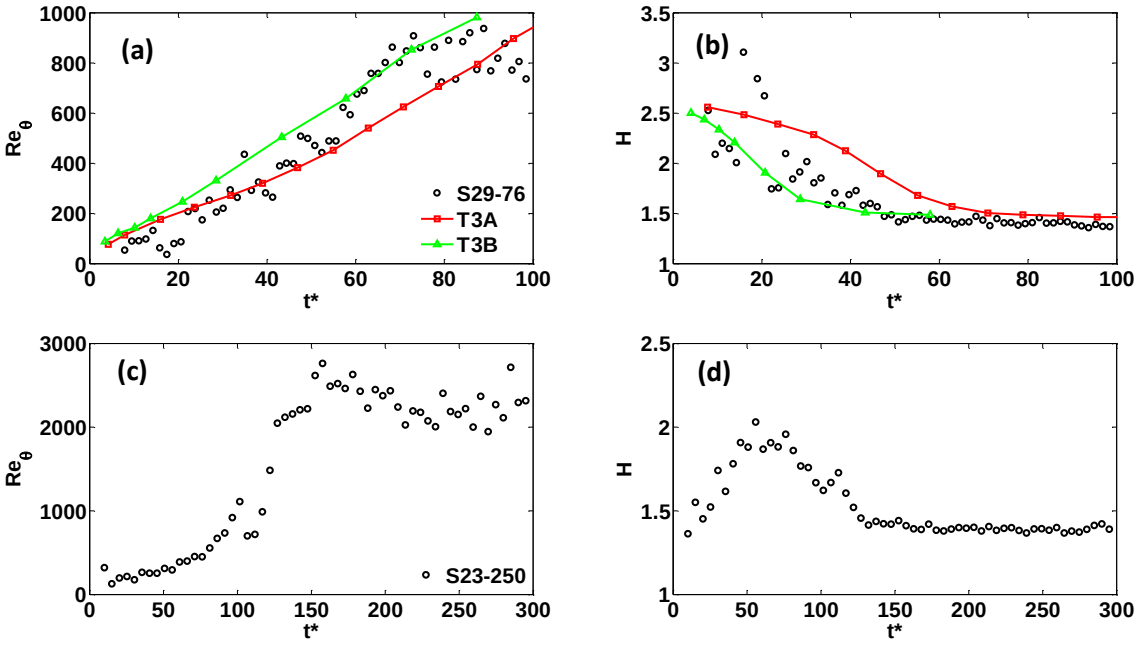

Figure 5.11 Development of momentum-thickness Reynolds number and shape factor for unsteady boundary layers for cases S29-76 (a, b) and S23-250 (c, d).

The temporal development of $\overline{\hat{U}}$ profiles from different cases can be compared with each other. In order to facilitate these comparisons, time can be normalised by means of inner-scaling parameters such as $u_{\tau 0}$ and ν. Figure 5.12 shows the temporal development of perturbing velocity obtained from different cases versus $t_0^+ = tu_{\tau 0}^2/\nu$. Despite the chaotic early behaviour of the flow, the perturbing velocity in the various cases collapse with each other up to $t_0^+ = 90$ covering the whole range of pre-transition phase, regardless of the initial, final and acceleration conditions of the transient flow. It can be seen from Figure 5.12 that the scaled Stokes profile represents the flow during this phase reasonably well. This kind of velocity development is strikingly similar to the behaviour of laminar flows and the role of the Stokes similarity solution in governing the flow characteristics. It is the most extreme unsteady cases (i.e. S23-250 and S29-250) that first begin to deviate more rapidly from the others during the early stages of the transition phase.

It should however be noted that during the early stages of the flow rate excursion (i.e. $t_0^+ = 10$), scatters are seen in the profiles that can mainly be attributed to the finite repeatability of the flow at the very early stages of sudden opening scenarios.

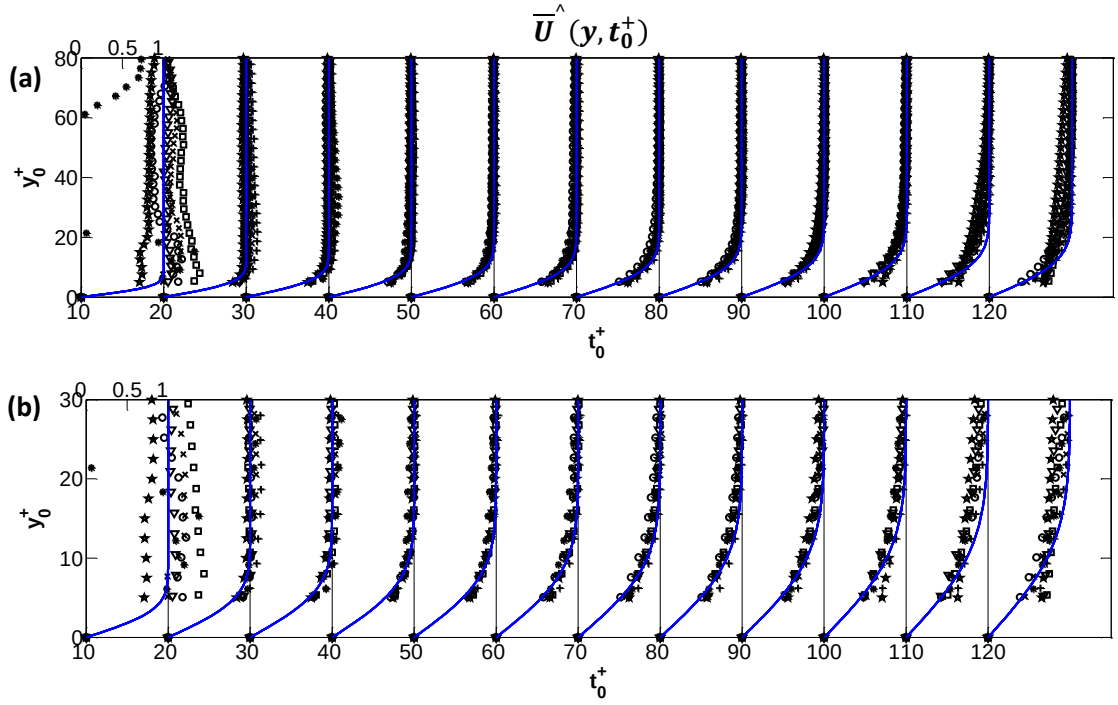

Figure 5.12 Development of perturbing velocity profiles at various Reynolds numbers; (a) actual profiles; (b) zoomed profiles; Line: scaled Stokes solution.

Similar behaviour is evident in the trends of perturbing streamwise and wall-normal rms velocity profiles shown in Figure 5.13. Perturbing rms velocity profiles are obtained as following:

$$\overline{u'}^{\wedge} = \frac{u'_{rms} - u'_{rms,0}}{U_{b1} - U_{b0}} \tag{5.6}$$

$$\overline{v'}^{\wedge} = \frac{v'_{rms} - v'_{rms,0}}{U_{b1} - U_{b0}} \tag{5.7}$$

It can be seen in Figure 5.13 that the fluctuating velocities of streamwise and wall-normal components collapse throughout the pre-transition phase up to $t_0^+ = 90$, while $\overline{v'}^{\wedge}$ of the S29-250 is the first to deviate from the rest in the early stages of transition. $\overline{u'}^{\wedge}$ profiles show a sensitivity to the flow excursion during the pre-transition regime due to the streaks dynamics in the wall region. Contrary to $\overline{v'}^{\wedge}$ that is frozen throughout the pre-transition zone, marking the onset of transition by its response. Flow features presented herein are in general agreement with the DNS data of He and Seddighi (2015).

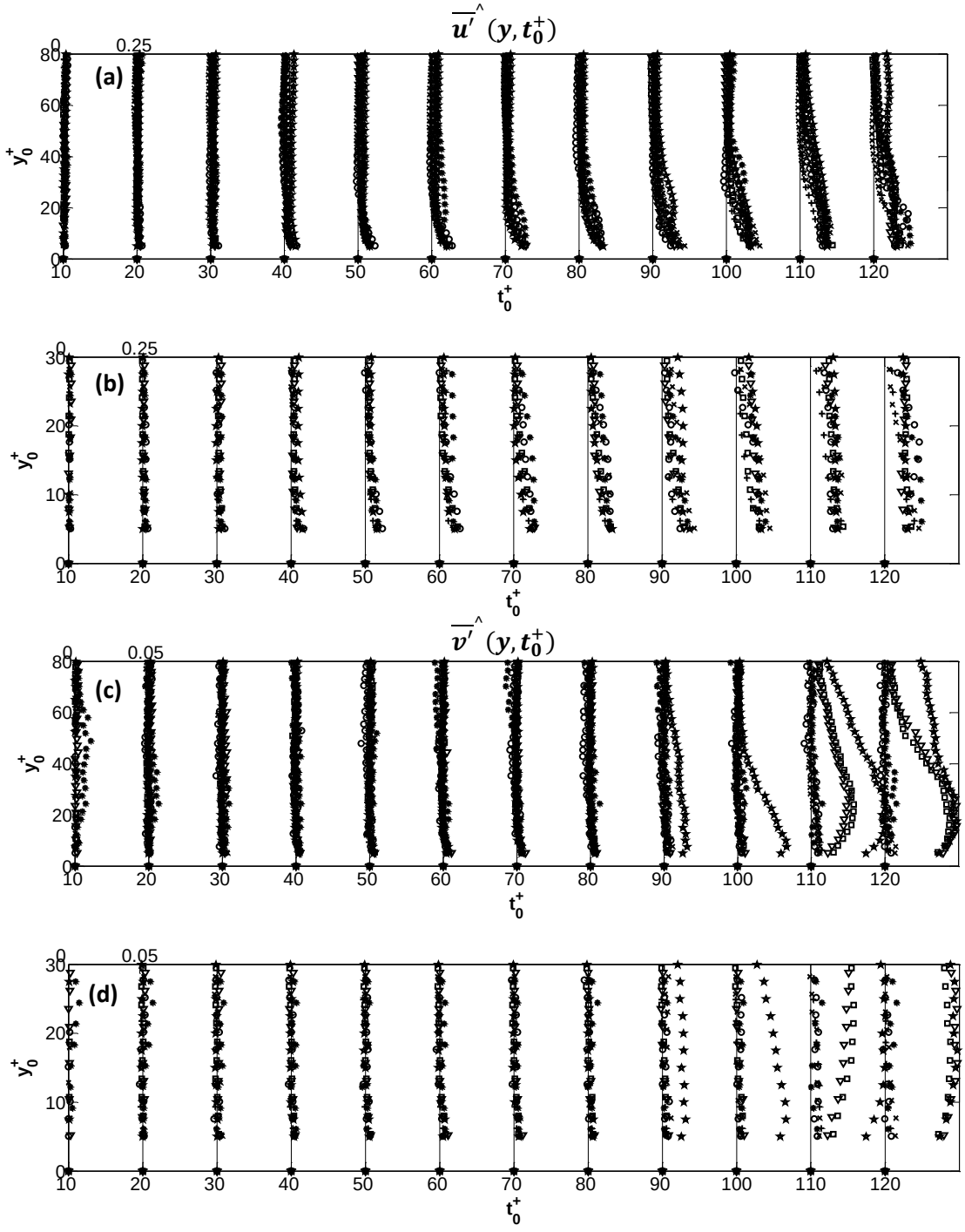

Figure 5.13 Development of perturbing streamwise (a) actual profiles; (b) zoomed profiles and wall-normal; (c) actual profiles; (d) zoomed profiles of fluctuating velocities at various Reynolds numbers.

5.4.2 **Correlations**

Correlations are used to facilitate the discussions on the structures of the flow. In particular, correlations can be used to quantify the distribution of the streaky structures. Spatial correlations of the streamwise velocity in different directions are calculated as follows:

$$R_{11}(x_i, t) = \frac{\overline{u'(x_i, t)u'(x_i + dx_i, t)}}{\overline{u'(x_i, t)^2}} \tag{5.8}$$

where $R_{11}(x_i, t)$ is the auto-correlation of the streamwise fluctuating velocity at specific time t and along the direction x_i (here, $i = 1 \equiv x$ and $3 \equiv z$).

Contrary to many other measurement devices, PIV allows for direct calculation of spatial auto-correlations of the fluctuating velocities with no inherited implications from the Taylor hypothesis (Taylor (1938)). Figure 5.14 shows the ensemble-averaged spatial correlations of velocity in the spanwise (a, c) and streamwise (b, d) directions at various times. These measurements are taken at the plane of $y/h \approx 0.04$. In general, correlations at the spanwise direction (a, c) indicate only slight changes in the spanwise size of the streaks due to the imposed acceleration. On the other hand, correlations in the streamwise direction, show a small increase mainly during the pre-transition period. This increase at the early stages of the flow excursion is due to the elongation of the streaks during the pre-transition period. This state is then followed by a reduction in the correlation at the final steady flow, resembling the breakdown of the elongated structures. As mentioned earlier, the elongation of streaks is seen as a primary instability in the bypass transition due to free-stream turbulence. This feature is weakly recognisable through the correlation plots of unsteady flows examined herein. As mentioned earlier in this chapter, transition features are not as striking as the DNS investigations of He and Seddighi (2013) since the rate of acceleration is much lower (e.g. 67.5 times lower for case S29-76).

Figure 5.15 facilitates the visualisation of the streaks in the two examined cases S29-76 (a) and S23-230R3 (b). Positive spanwise correlation values of the streamwise velocity are set to zero in this figure, while the negative values are shown as contours. It can be seen from these figures, that the initial spanwise distribution of the streaky structures is diminished slightly as the acceleration is imposed. R_{11} remains more or less constant throughout the pre-transition phase. These streaks become narrower as time proceeds.

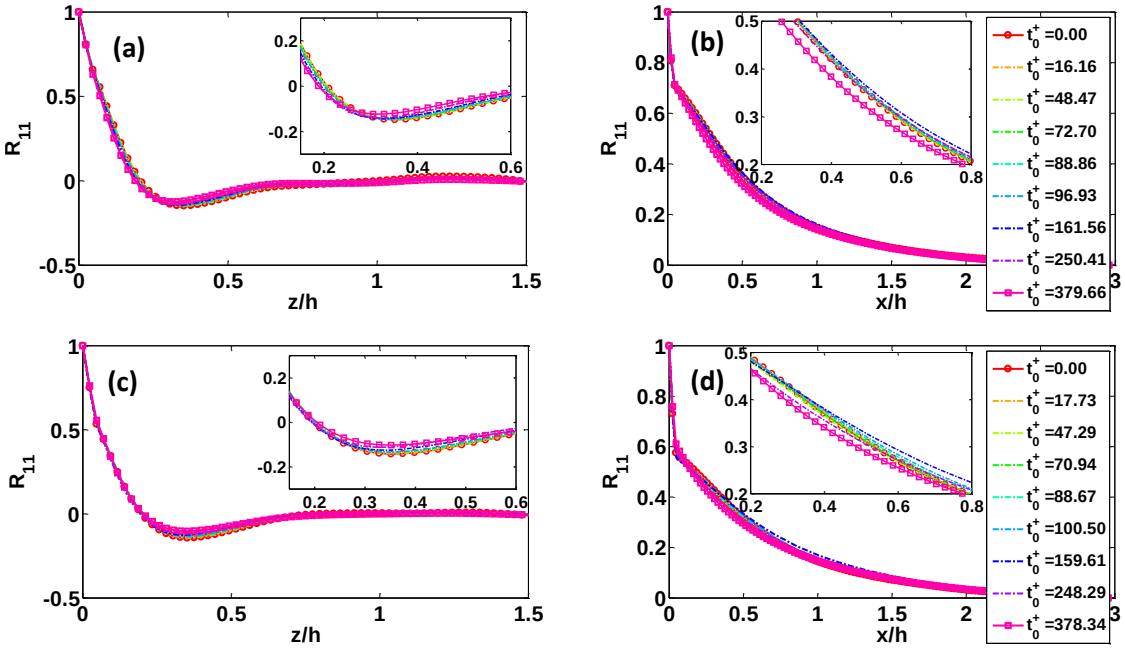

Figure 5.14 Temporal development of streamwise velocity correlations of cases (a-b) S29-76, $y_0^+ = 7$; (c-d) S23-230R3, $y_0^+ = 6$; insets: Zoomed correlations.

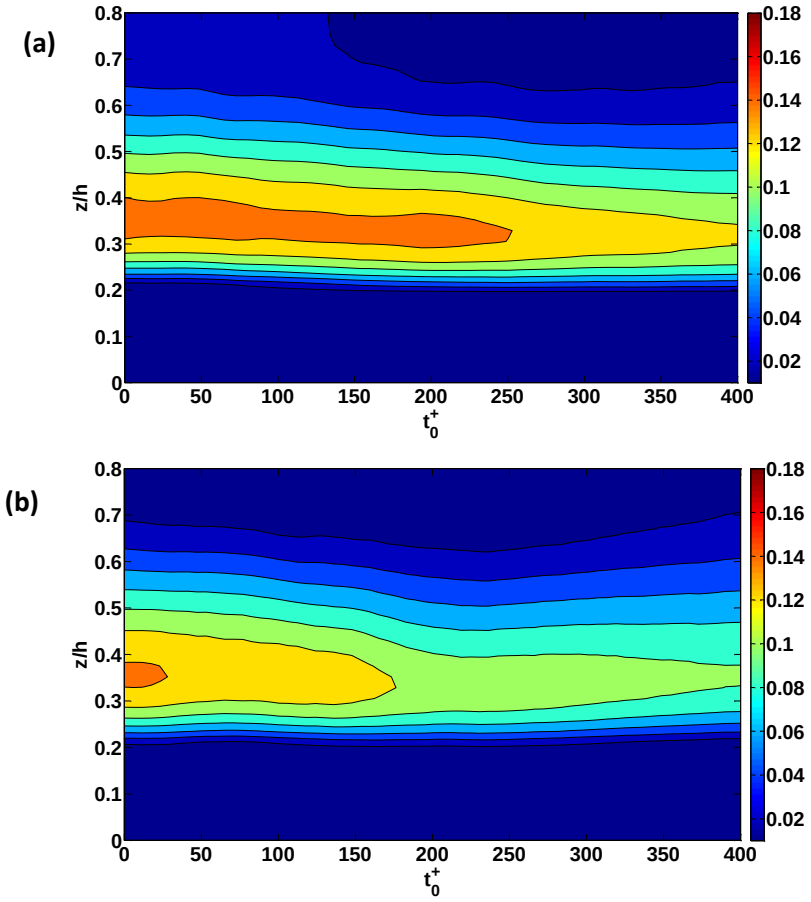

Figure 5.15 Temporal development of the streamwise fluctuating velocity correlation in the spanwise direction; (a) S29-76, $y_0^+ = 7$; (b) S23-230R3, $y_0^+ = 6$

5.4.3 Behaviour of mean and rms fluctuating velocities

This section discusses the behaviour of mean and turbulent stresses in temporal accelerating turbulent channel flows. The main discussion of this section will be on cases S23-250, S29-76 and S29-250, where most data points are collected from the LDV measurements, however, other cases will be used throughout this text to facilitate the discussion.

Figure 5.16 shows the variation of the bulk velocity, measured by the flow meter, with time for case S29-76. Such a trend of flow variation is achieved by a sudden opening of the control valve from the initial Reynolds number of 2,913 equivalent to friction Reynolds number of 180. The ensemble-averaged statistics shown in Figure 5.17 are obtained from 80-100 repeats for LDV and 20 repeats for PIV. The modified ensemble-averaging technique of He and Jackson (2000) for transient flows is applied to the data obtained from the LDV and flow meter. Details of this method are discussed in §3.4. PIV data are initially spatially averaged in the streamwise direction and then temporally averaged through 20 ensembles.

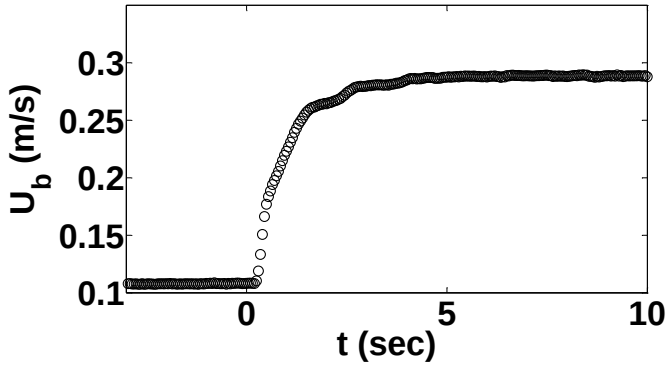

Figure 5.16 Temporal variation of flow rate for case S29-76 ($Re_b = 2{,}913 - 7{,}625$).

The statistics presented in Figure 5.17 are normalised with the bulk velocity of the final state (U_{b1}). Top and bottom abscissae of these figures show the statistics variations with actual (t) and normalised (t^*) time. Note that every four consecutive subplots are sharing the same legends. It can be seen from Figure 5.17 that PIV measurements (black symbols) of mean and streamwise fluctuating velocities along with the Reynolds shear stresses are in close agreement with LDV (red symbols) at various locations across the channel. However, at locations very close to the wall, discrepancy between the two increases due to relatively low spatial resolution of PIV. The rms component of wall-normal velocities measured by the two techniques show a small shift of magnitude at initial and final Reynolds number. As discussed in Chapter 3, LDV measurements of ${v'}_{rms}$ and therefore $\overline{u'v'}$ component were not available at distances close to the wall (i.e. for $y/h < 0.17$) and hence are not compared to PIV in Figure 5.17 (c and d).

It can be seen from Figure 5.17 (b) that ${u'}_{rms}$ responds immediately to the flow excursion in the wall region, while the ${v'}_{rms}$ and $\overline{u'v'}$ components are still frozen (c, d). This is a well-known feature of unsteady flows subjected to temporal accelerations. The pipe flow investigations of He and Jackson (2000) have revealed a diffusion mechanism that results in propagation of turbulence from the wall to the core region.

The early responses of the ${u'}_{rms}$ component can be directly linked to the instantaneous behaviour of the flow shown earlier in §5.3. Elongation of the initial streaky structures during the pre-transition phase results in an immediate response of the ${u'}_{rms}$ component at the wall region, leading to the conclusion that the stretching of the pre-existing streaks first commence in the wall region. ${v'}_{rms}$ component experiences a delay during the pre-transition regime, showing no response to neither the flow acceleration nor the immediate response of the ${u'}_{rms}$ component. This behaviour is clearly seen in the studies of bypass transition (for instance Durbin and Wu (2007)).

The v'_{rms} component remains largely unchanged during the pre-transition regime in the wall region ($y_0^+ < 50$), making it a very important component in terms determining the onset of transition (Figure 5.17 (c, g)).

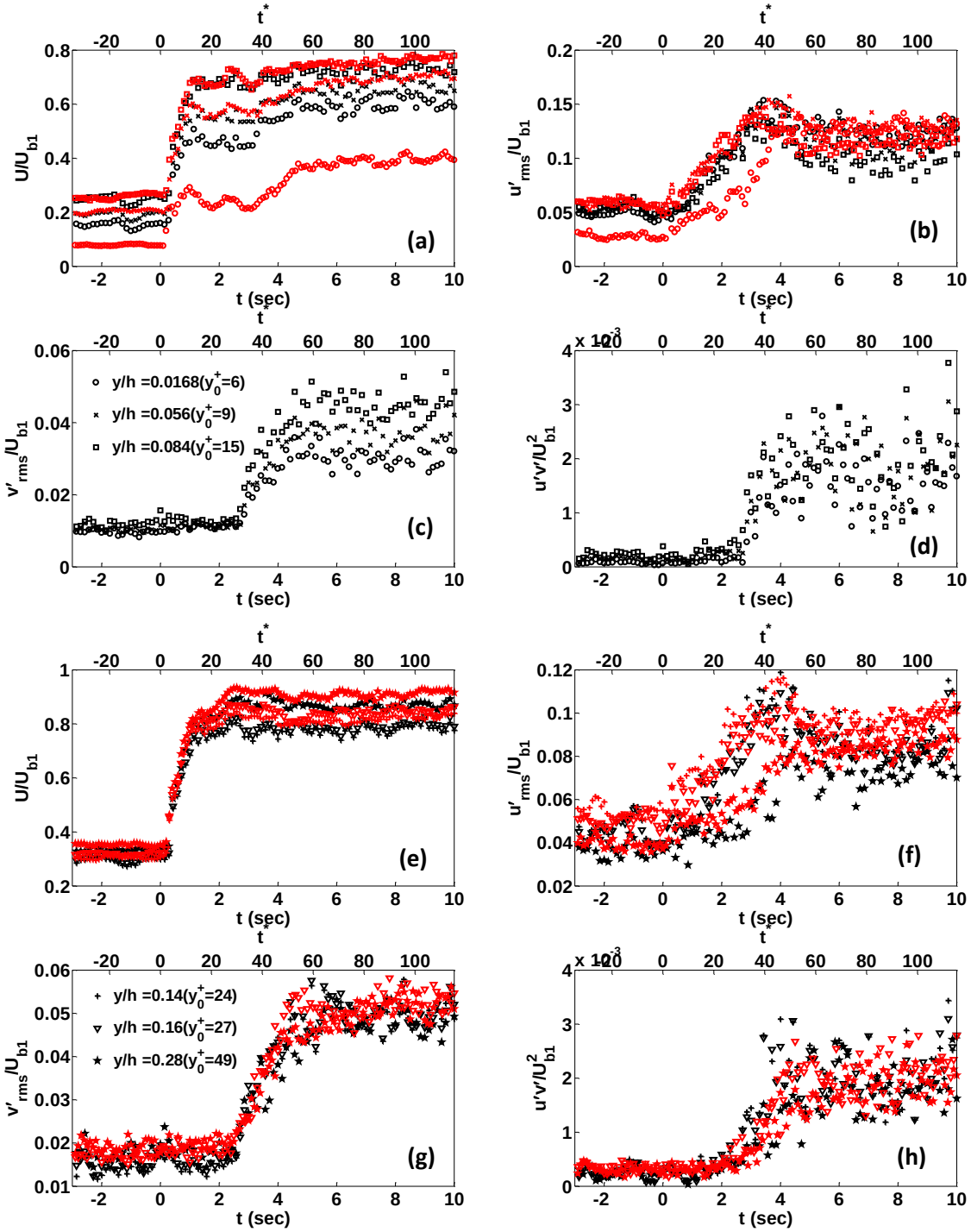

Figure 5.17 continued on next page.

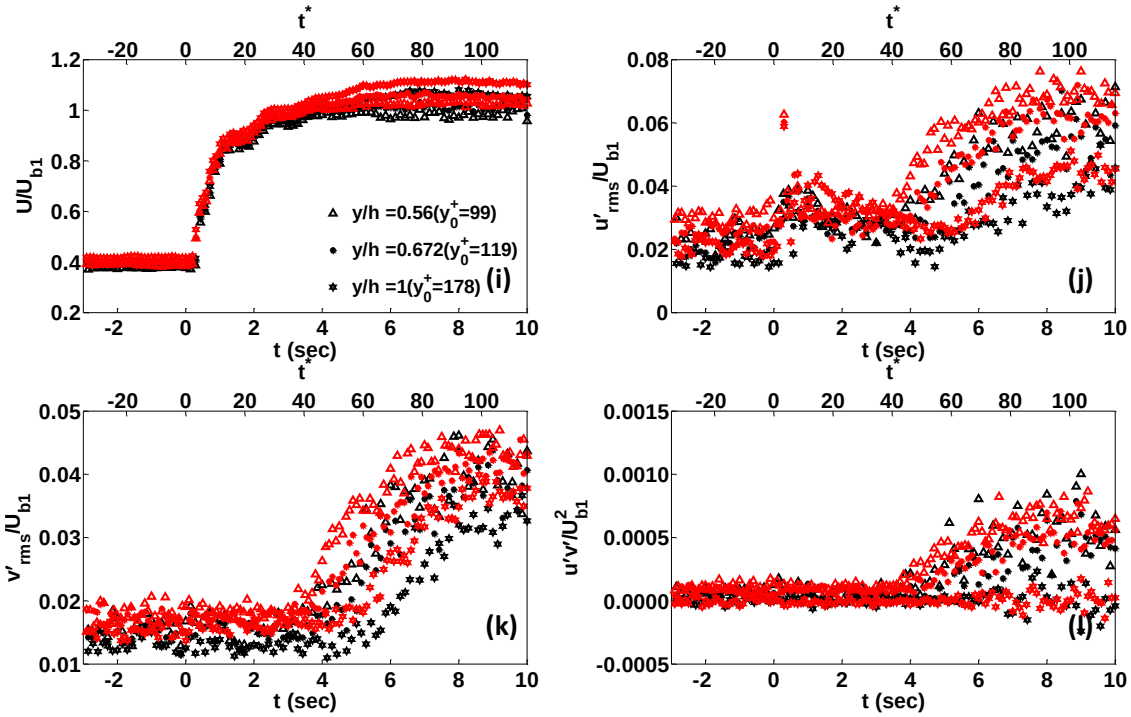

Figure 5.17 Temporal development of mean, fluctuating velocities and Reynolds shear stresses for case S29-76 ($Re_b = 2{,}913 - 7{,}625$); Red symbols: LDV, Black symbols: PIV. Note: Every four subplots share a same legend.

The behaviour of the mean, fluctuating and Reynolds shear stress, as measured by PIV, is shown separately in Figure 5.18 at selected locations. The process of turbulent diffusion from the wall to the core region can clearly be identified in Figure 5.18 (b), where the response of u'_{rms} component in the wall region is almost immediate after the valve opening. A small jump of u'_{rms} component in the core region right after the valve opening is attributed to the finite repeatability of the valve at sudden opening scenarios. It will be shown later in this section that the "controlled" valve openings do not suffer from this shortcoming. This early response of u'_{rms} at the core region is not reflected in the wall-normal fluctuating component, since it is only the mean velocity of the streamwise component that is affected by the poor repeatability of the valve opening.

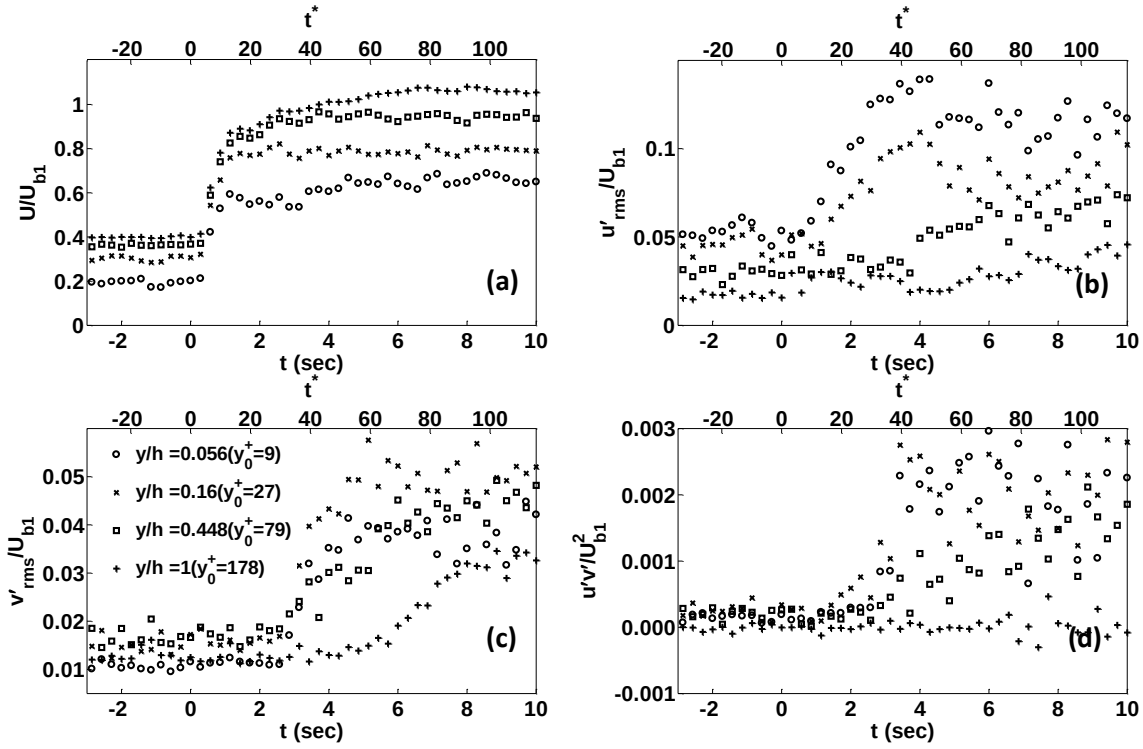

Figure 5.18 Temporal development of mean, fluctuating and Reynolds shear stress components for case S29-76 ($Re_b = 2{,}913 - 7{,}625$).

Tests have been carried out with various initial and final Reynolds number scenarios. The temporal variation of the bulk flow for case S23-250 is shown in Figure 5.19. The history of the statistics measured at various locations with PIV and LDV for this case are shown in Figure 5.20, whilst Figure 5.21 shows the response of various flow quantities due to PIV at selected wall-normal locations.

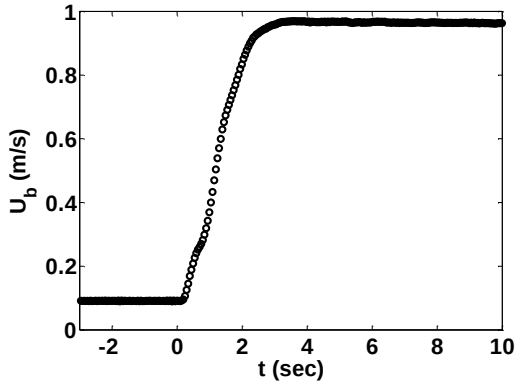

Figure 5.19 Temporal variation of flow rate for case S23-250 ($Re_b = 2{,}300 - 25{,}000$).

Similar trends of mean and turbulence behaviour to the previous case are observed for case S23-250. It can be seen from Figure 5.20 (a and b) that the streamwise velocity measurements of LDV close to the wall are not reproducible with the PIV due to the large gradients of velocity,

finite resolution of the camera as well as the surface reflections. The discrepancy between the two techniques decreases significantly as the distance from the wall is increased. It is noticeable from the subplots (g) and (k) that the response of the v'_{rms} component is measured to be slightly longer in PIV in comparison to LDV.

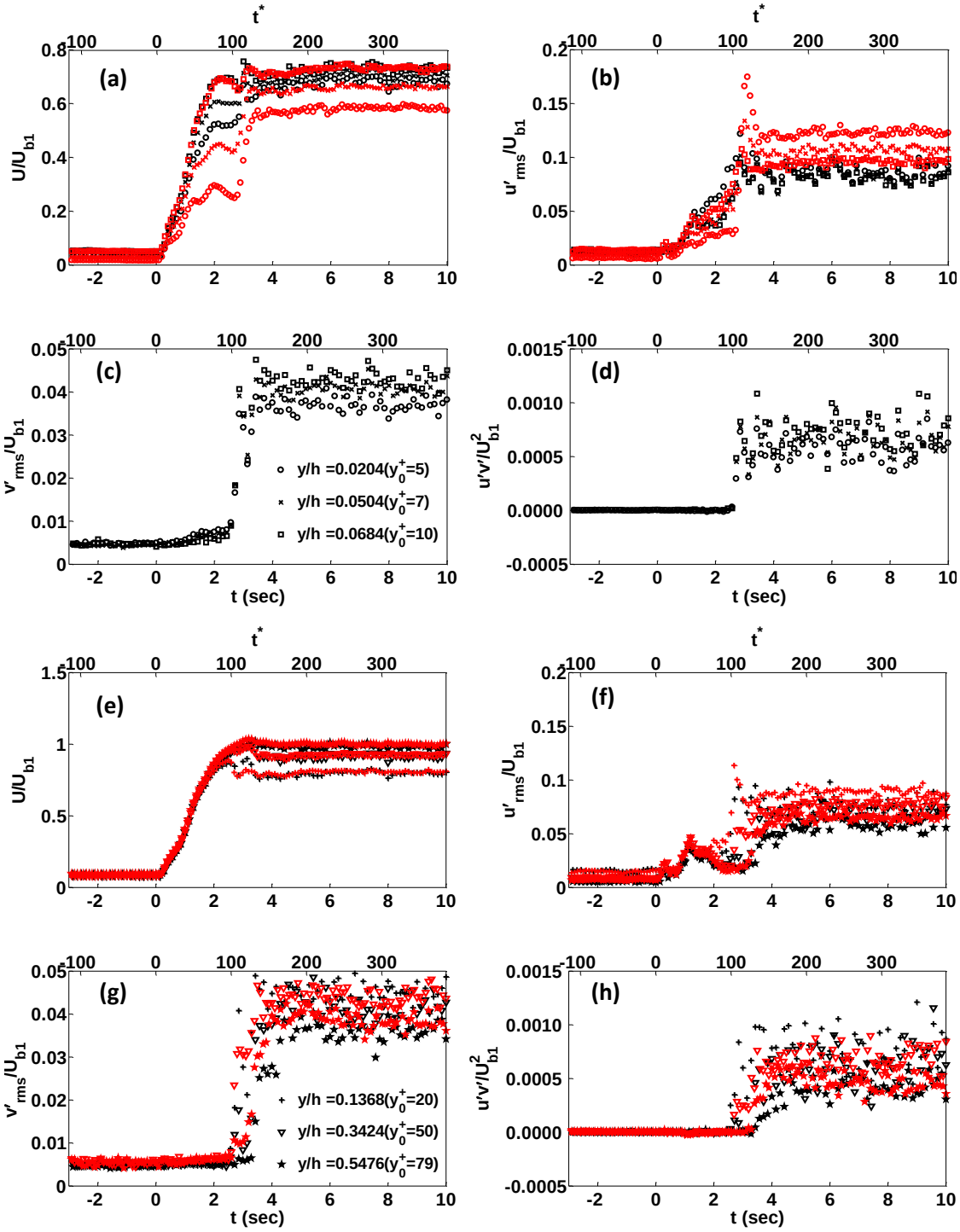

Figure 5.20 continued on next page.

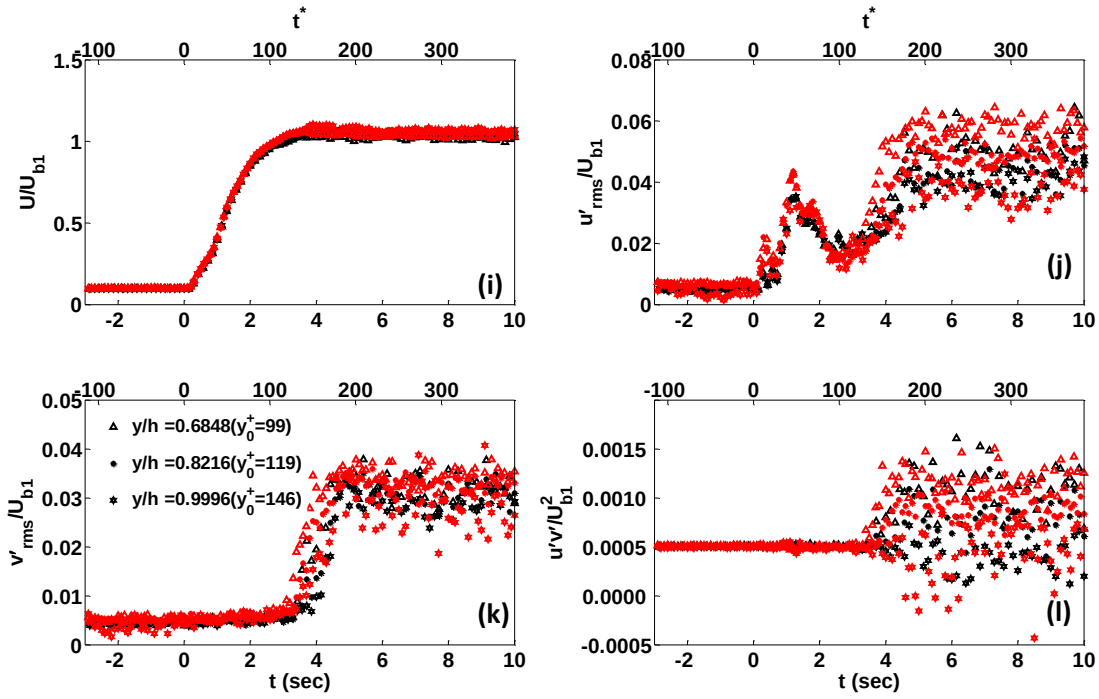

Figure 5.20 Temporal development of mean, fluctuating velocities and Reynolds shear stresses for case S23-250 ($Re_b = 2{,}300 - 25{,}000$); Red symbols: LDV, Black symbols: PIV. Note: Every four subplots share a same legend.

Figure 5.21 shows the plots of mean, rms fluctuating velocities and shear stresses obtained from PIV measurements. As mentioned earlier, the early response of the u'_{rms} component in the centre is caused due to poor repeatability of the control valve in sudden opening scenarios. Once more it can be seen from these figures that the period of v'_{rms} delays are similar in the wall region, with a transition time of $t = 2.4\ sec$ or $t^* = 87.5$.

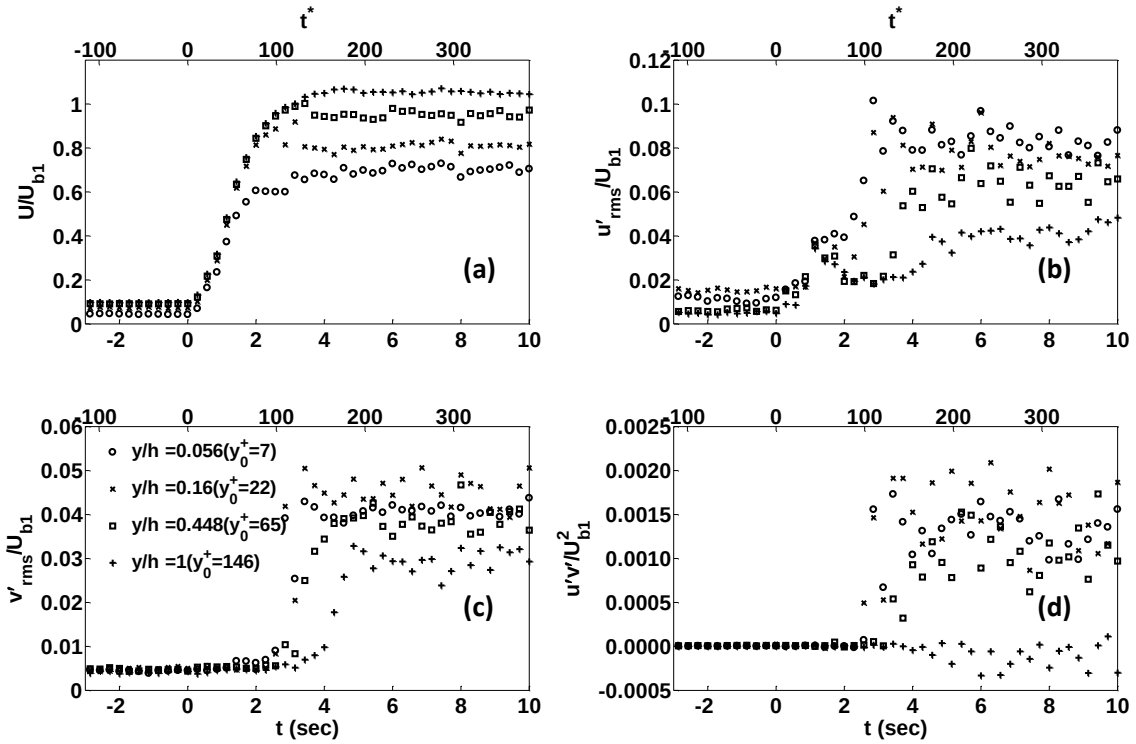

Figure 5.21 Temporal development of mean, fluctuating and Reynolds shear stress components for case S23-250 ($Re_b = 2{,}300 - 25{,}000$).

For the sake of generality of the discussions, a slow ramp unsteady case is presented as well. Figure 5.22 shows the linear variation of the mean flow rate with initial and final Reynolds numbers of 2,913 and 7,625, respectively, where the flow excursion lasts for almost 6 seconds.

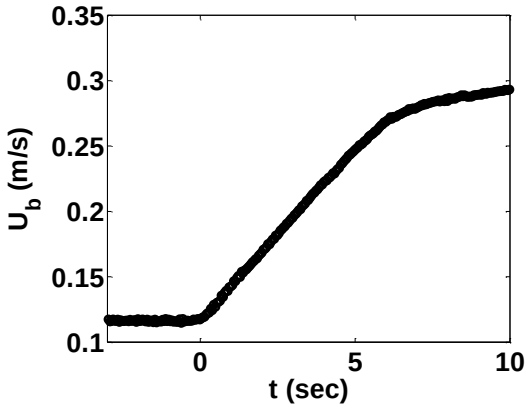

Figure 5.22 Temporal variation of flow rate for case S29-76R6 ($Re_b = 2{,}913 - 7{,}625$).

The statistics obtained from PIV measurements are plotted versus actual and normalised time in Figure 5.23. As can be expected, similar flow features to the previous cases are identifiable for this flow condition. It can be seen that the mean velocity escalates in a linear fashion, while the normal and shear stresses are experiencing longer delays in comparison with the sudden opening case (S29-76). The propagation of turbulence towards the core region of the channel

can clearly be seen in the trends of u'_{rms} component, whilst, the v'_{rms} and $\overline{u'v'}$ components are experiencing longer delays in the entire cross-section of the flow. Contrary to sudden opening scenarios, carefully controlled flow rate excursion in this case resulted in higher levels of flow repeatability. Consequently, and as expected, smooth delays of u'_{rms} components are noticeable in the core region.

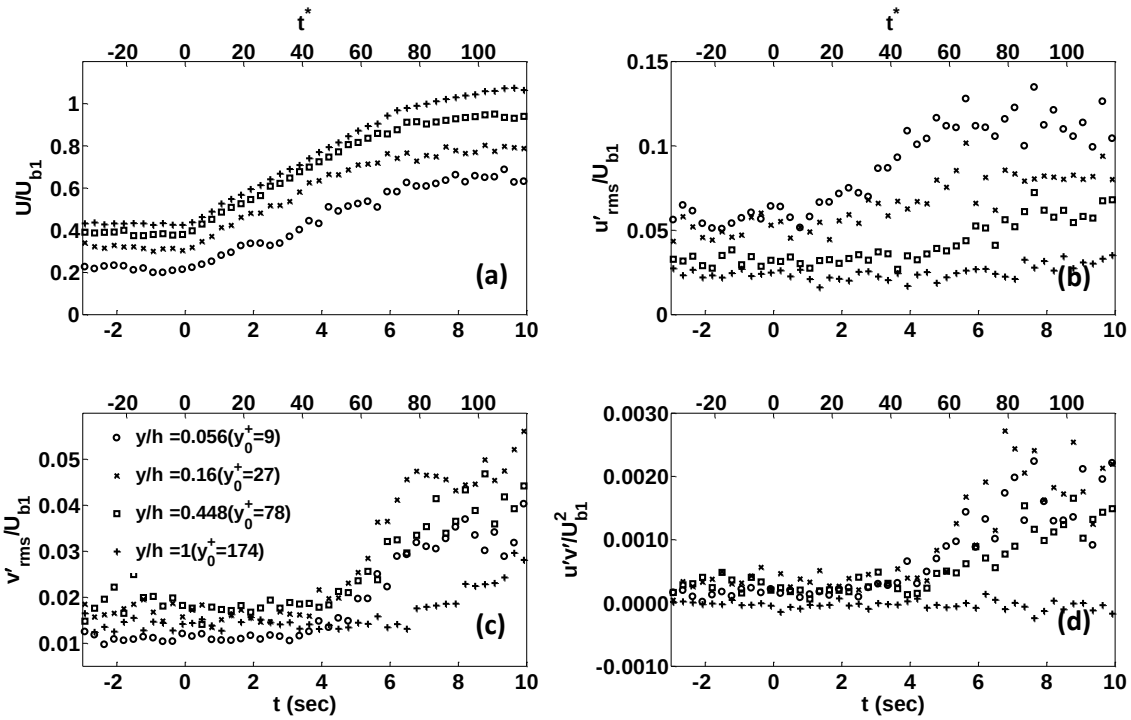

Figure 5.23 Temporal development of mean, fluctuating and Reynolds shear stress components for case S29-76R6 ($Re_b = 2{,}913 - 7{,}625$).

In order to facilitate the examination of temporal responses in different cases, the normalised perturbing rms values, that is $(u'_{rms} - u'_{rms,0})/(u'_{rms,1} - u'_{rms,0})$, $(v'_{rms} - v'_{rms,0})/(v'_{rms,1} - v'_{rms,0})$ and $(\overline{u'v'} - \overline{u'v'_0})/(\overline{u'v'_1} - \overline{u'v'_0})$ versus t_0^+ as well as $\widehat{\overline{v'}}$ versus t^* are shown to remove the effects of initial and final conditions. These quantities facilitate the identification of the response time and consequently detection of t_{cr} based on the response of wall-normal fluctuating velocities (v'_{rms}) at the wall region. Figures 5.24-5.26 show the variations of the normalised streamwise, wall-normal and shear stresses for all sudden opening cases. These measurements are obtained from the LDV.

Figure 5.24 shows the development of normalised u'_{rms} component obtained from various cases at three different wall-normal locations. It can be seen from the subplot (a) that there is a good collapse of data throughout the transition process with no regards to the acceleration ratio. The discrepancy between the data is increased at further distances from the wall. It can

be seen from the subplot (b) and (c) that higher acceleration ratios result in sharper responses of turbulence.

Figure 5.25 shows the development of normalised v'_{rms} component obtained from various cases at $y/h = 0.17$ and the channel's centreline versus t_0^+ in subplots (a) and (b) and versus t^* in subplots (c) and (d). It is evident from these figures that how final-initial Reynolds number can affect the transition process. Higher final-initial ratios result in a sharper response of the v'_{rms} while lower ratios provide smoother path of transition.

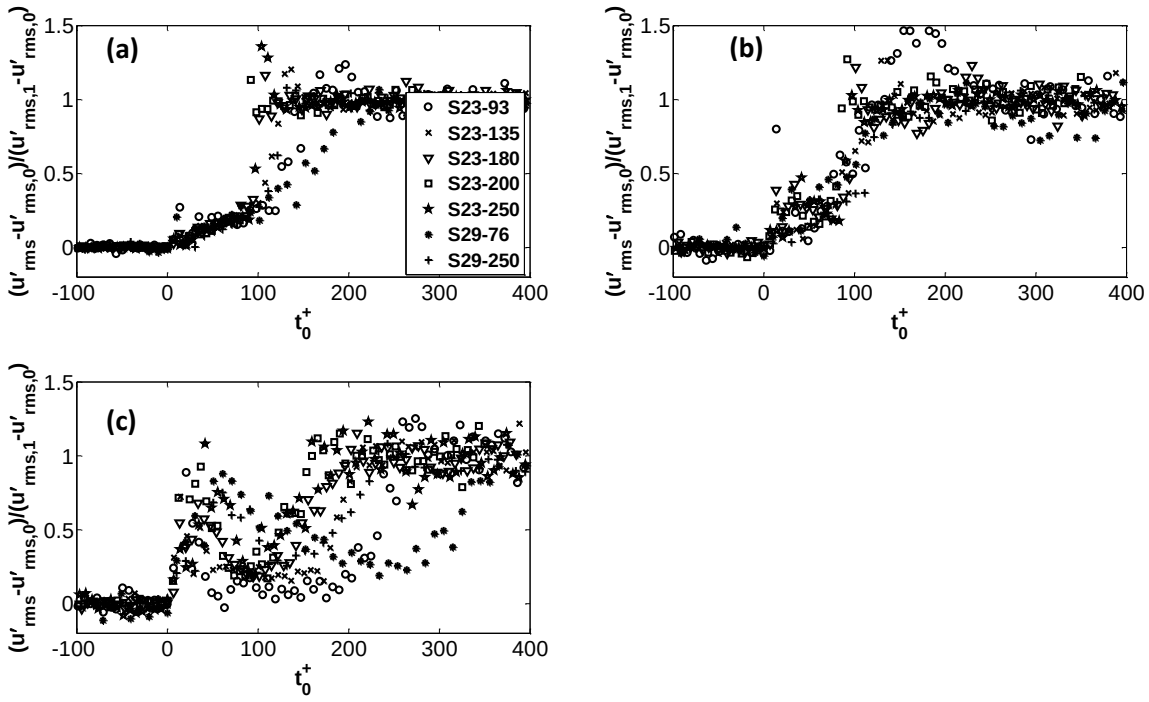

Figure 5.24 LDV measurement of u'_{rms} velocities for different transients at (a) $y/h = 0.02$, $y_0^+ = 3$; (b) $y/h = 0.17$, $y_0^+ = 25$; (c) $y/h = 1$, $y_0^+ = 150$.

Figure 5.26 shows the development of the normalised $\overline{u'v'}$ at $y/h = 0.17$. The response trends of shear stress are very similar to that of v'_{rms}, demonstrating a sharper response for a higher final-initial scenario.

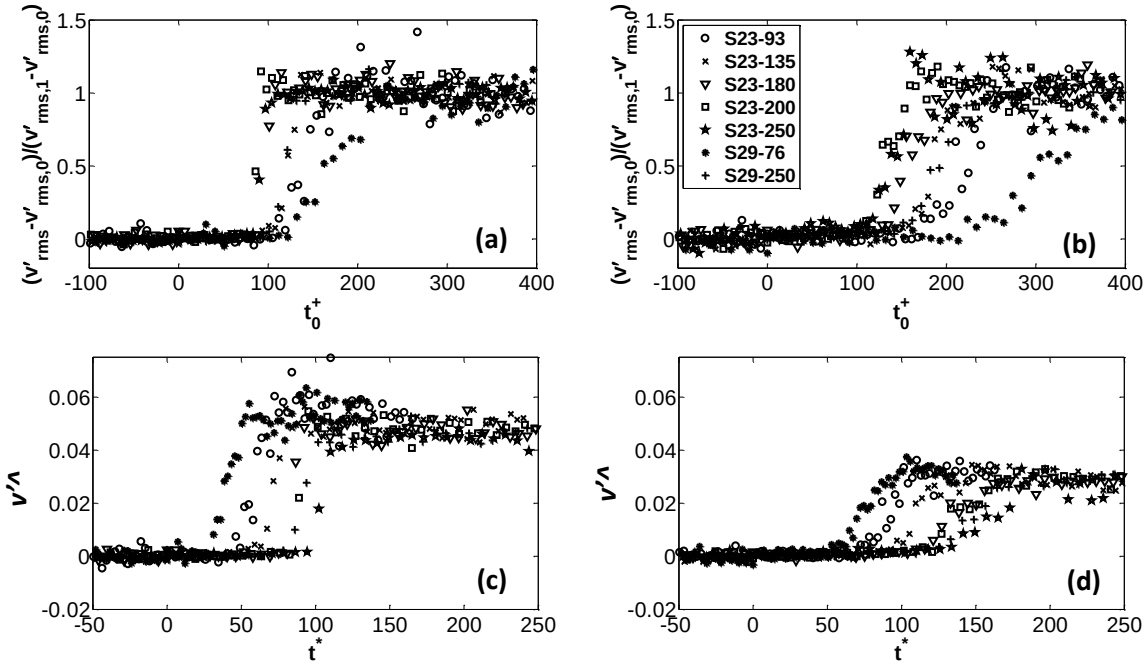

Figure 5.25 LDV measurement of v'_{rms} velocities for different transients at (a) and (c) $y/h = 0.17$, $y_0^+ = 25$; (b) and (d) $y/h = 1$, $y_0^+ = 150$.

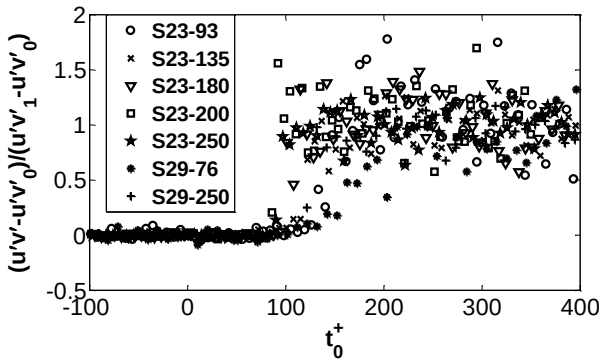

Figure 5.26 LDV measurement of $\overline{u'v'}$ velocities for different transients at (a)$y/h = 0.17$, $y_0^+ = 25$.

The history profiles of various statistics obtained from all cases introduced in Table 5.1 are presented in the Appendix A.

5.4.4 Correlations of critical Reynolds number in smooth flows

It has been shown by (He and Seddighi, 2013) and (He and Seddighi, 2015)(hereafter HS15) that the final-initial Reynolds number ratio is of significant importance due to its effect on the initial or "free-stream" turbulence intensity. Since the concept of free-stream turbulence is mainly used in external boundary layer flows, a re-definition of this parameter in unsteady fully-developed channel flows is of interest. He and Seddighi have re-defined the initial turbulence intensity as follows:

$$Tu_0 \approx 1.8\left(\frac{u_{\tau 0}}{U_{b1}}\right) \tag{5.9}$$

Derivation of this parameter was based on the peak values of the initial normalised fluctuating velocities $u'^{+}_{rms,0}, v'^{+}_{rms,0}$ and $w'^{+}_{rms,0}$ of 2.7, 1.2 and 0.9 in streamwise, wall-normal and spanwise directions, respectively.

Another concept which is of equal importance in transition of external flows over flat surfaces is the Reynolds number defined as $Re_x = \frac{xU_\infty}{\nu}$, where x is the distance from the leading edge and U_∞ the free-stream velocity. In order to re-write the Reynolds number in a fully developed channel flow, a characteristic length-scale is needed to replace the distance from the leading edge. This can be defined as a convection velocity equal to the final bulk velocity, U_{b1}, giving $x = tU_{b1}$. Therefore, an equivalent Reynolds number can be defined as follows (He and Seddighi (2015)):

$$Re_t = \frac{tU_{b1}^2}{\nu} \tag{5.10}$$

In order to study the sensitivity of the transition process to the initial and final Reynolds numbers, a critical Reynolds number needs to be defined. In spatially developing boundary layers, transition from laminar to turbulent state initiates where the friction coefficient deviates from the Blasius solution. Similar to boundary layer bypass transition flows, DNS study of He and Seddighi (2015) has shown that the first bursts of turbulence are generated where the friction coefficient (C_f) is at its minimum. The time required for the friction coefficient to reach its minimum state is called the critical time. Therefore, critical Reynolds number is defined as $Re_{t,cr} = t_{cr}U_{b1}^2/\nu$. Due to technical complications, direct measurement of friction coefficient was not possible in the present investigations. However, as shown earlier, the response of the v'_{rms} component can be a good measure of the state of the flow. It was shown in this chapter that the response of v'_{rms} component is very similar at the wall-normal locations smaller than $y_0^+ \approx 50$. Therefore, in the present investigations, the response of the v'_{rms} component in this region is used to determine the critical time (Table 5.2).

As mentioned earlier in §2.2, theoretical and experimental studies of spatially developing boundary layers suggest a parabolic relationship between the critical Reynolds number and the free-stream turbulence intensity (such as theoretical work of Andersson et al. (1999)). Figure 5.27 depicts the relationship between these modified parameters in unsteady flows. It also provides a comparison with the DNS of unsteady flows, correlations and theoretical models of Blumer and van Driest (1963) and Andersson et al. (1999) for bypass transition flows. Blumer

and van Driest have proposed the following empirical relationship between the critical Reynolds number and free-stream turbulence intensity for boundary layer bypass transition flows:

$$\frac{1}{\sqrt{Re_{t,cr}}} = a + b\sqrt{Re_{t,cr}}Tu_0^2 \tag{5.11}$$

where $a = 10^{-4}$ and $b = 62.5 \times 10^{-8}$.

Andersson et al. (1999) have proposed the following model to predict the critical Reynolds number in bypass transition boundary layer flows, which can be considered to be a modification to Blumer and van Driest empirical correlation:

$$\sqrt{Re_{t,cr}}Tu_0 = K \tag{5.12}$$

where K is considered to be a constant for free-stream turbulence levels at 1-5%. $K$is suggested to be 1200 by Andersson et al. (1999), noting that, the choice of this constant is subjected to several parameters. The definition of the transition Reynolds number in boundary layer flows is an influencing factor. Other factors are considered to be the degree of anisotropy, the leading edge suction peaks, pressure gradients and obviously scales and degree of the free-stream turbulence.

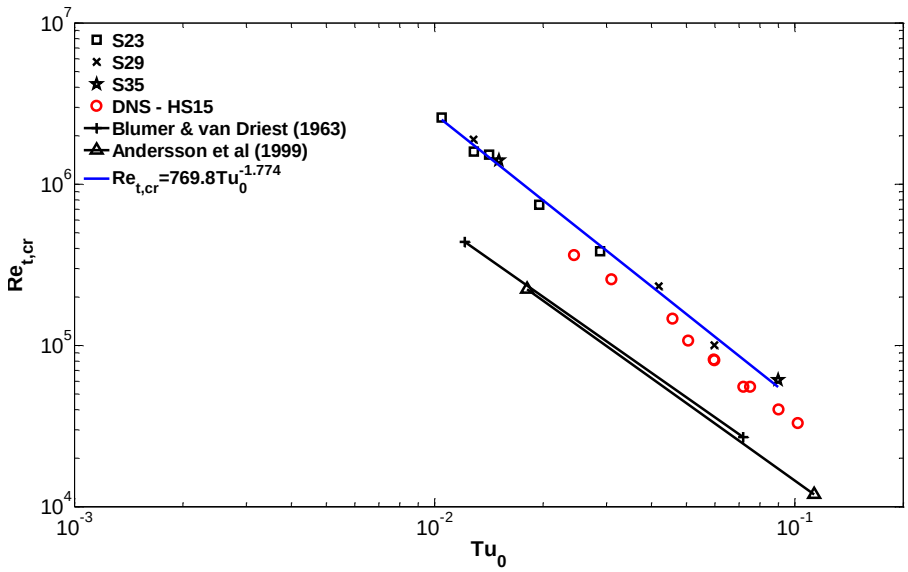

Figure 5.27 Critical Reynolds number as a function of equivalent turbulence intensity for various flow conditions.

He and Seddighi (2015) were the first to correlate the modified critical Reynolds number and free-stream turbulence intensity for unsteady flows. They have proposed the following best-fit

to their data obtained from ten different unsteady flows with Reynolds number ratios ranging from 1.1-4.5.

$$Re_{t,cr} = 565Tu_0^{-1.71} \tag{5.13}$$

It can be noticed that the constants of the power law are different from the proposal of Andersson et al. This difference is of no surprise, since the nature of these two flows are quite different. These differences can emerge from various reasons, such as the definition of the initial turbulence intensity as well as the actual flow patterns in a fully developed turbulent flow and a spatially developing boundary layer.

The experiments carried out in the present investigations are performed to cover a wider range of Reynolds number ratios, where Re_{b1}/Re_{b0} varies from 1.2-10.8. Best-fit curve to these data is found to be:

$$Re_{t,cr} = 770Tu_0^{-1.77} \tag{5.14}$$

which is very close to the findings of He and Seddighi (2015). On the other hand, the general behaviour of the trend is very close to findings of other researchers of boundary layer bypass transition with differences in the constants. The difference between the equations (5.14) and (5.13) (present data and HS15) is likely due to the flow acceleration, which is a step change in HS15 but a much slower ramp in the present experiments. This might also arise from the uncertainties involved in the determination of the friction factor from the experiments.

The length of the transition is another important feature of bypass transition flows. This length is of particular importance in terms of modelling and correlating various types of transitional flows. The length is defined as the difference between the initial and final states of a transitional flow. For instance, Fransson et al. (2005) have defined this difference as follows:

$$\Delta Re_{t,cr} = Re_{x,\gamma=0.9} - Re_{x,\gamma=0.1} \tag{5.15}$$

where x is the downstream distance from the edge and γ is the level of intermittency, where $\gamma = 1$, resembles a fully turbulent flow and $\gamma = 0$ is a laminar state. This parameter is usually plotted versus $Re_{x,\gamma=0.5}$, which represents the flow at the middle of the transition process ($\gamma = 0.5$). By assuming a linear relationship between the two, the following relation between the length of transition and $Re_{x,\gamma=0.5}$ were obtained from the examination of various experimental data by Fransson et al. (2005):

$$\Delta Re_{t,cr} = A + BRe_{x,\gamma=0.5} \tag{5.16}$$

where constants A and B are 3.9x10^4 and 0.33, respectively.

There are other empirical formulations based on the experimental data, proposed to predict the length of transition, such as those of Dhawan and Narasimha (1958), Abu-Ghannam and Shaw (1980) and Narasimha (1985).

Narasimha (1985) has proposed the following power-law correlation between the length of transition and the critical Reynolds number:

$$\Delta Re_{t,cr} = \alpha Re^{\beta}_{x,\gamma=0.5} \tag{5.17}$$

where α and β are 9.0 and 0.75, respectively. Narasimha has used a narrower levels of intermittency (i.e. $0.25 < \gamma < 0.75$) for calculation of $\Delta Re_{t,cr}$ in comparison to Fransson et al. (2005).

In the studies of unsteady flows the period of transition may be defined as follows:

$$\Delta Re_{t,cr} = Re_{t,turb} - Re_{t,cr} \tag{5.18}$$

where $Re_{t,turb}$is considered to be the final fully turbulent state, while the $Re_{t,cr}$ is the critical Reynolds number. He and Seddighi (2015) have used the friction coefficient curve to determine the termination of transition. They have used the first maxima peak of the friction coefficient after the departure from the Stokes solution to indicate the fully turbulent state. In the experiments, however, u'_{rms} curve is used as a feasible measure to determine the end of transition. Transition is considered to be finished when the u'_{rms} response to the excursion of flow rate in the wall region ($y_0^+ \approx 3$) has reached its final state. This is consistent with the observations of instantaneous signal of the u'_{rms}, since this component is the first experiencing the final turbulence levels in the wall region, while other components are undergoing a frozen state (for instance the signals shown in Figure 5.4). The period of u'_{rms} response is shown to be very similar up to the buffer layer ($y_0^+ \approx 20$), see Figure 5.17 (b).

Figure 5.28 provides a comparison between the bypass transition and the unsteady flows. Equations (5.16) and (5.17) are provided to facilitate the comparisons with the bypass transition flows. However, as the definition of critical Reynolds number is different for unsteady flows, a modification to these equations is required. Implementation of this modification is performed

by replacing the $Re_{x,\gamma=0.5}$ in these two equations with its equivalent $Re_{t,cr} + 0.5\Delta Re_{t,cr}$ (He and Seddighi (2015)).

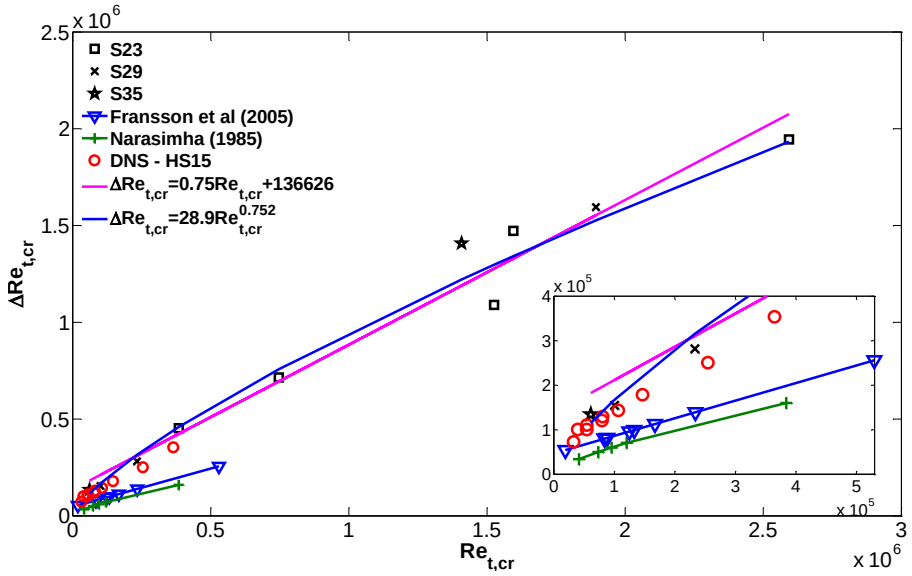

Figure 5.28 Period of transition as a function of critical Reynolds number for various flow condition.

It can be seen from Figure 5.28 that the range of unsteady flows investigated herein, goes much beyond the available DNS. It is shown in the inset figure, that there is a good consistency between the experiments and the DNS data. Whilst the general trend encompassing the whole available data from the experiments is shown to be more of a power-law type rather than a linear relationship which is more likely to prevail in flows with shorter period of transition. The power-law coefficients fitted to the experimental data are $\alpha = 28.9$ and $\beta = 0.752$, where β is similar to the proposal of Narasimha (1985) for boundary bypass transition flows.

5.5 Summary

Particle Image Velocimetry (PIV) and Laser Doppler Velocimetry (LDV) have been used to study the mean and turbulence behaviour in accelerating unsteady channel flows over smooth surfaces. These measurements comprise of different initial and final Reynolds numbers, all at fully turbulent state. Present investigations cover a variety of unsteady flows with various final to initial Reynolds number ratios.

Fluctuating streamwise velocity contours at the wall region reveal a new and interesting perspective towards the study of unsteady flows. It is shown in §5.3 that the fluctuating velocity patterns undergo a strikingly similar process that has previously been seen in bypass transition flows. Following the direct numerical simulations of He and Seddighi (2013), two sets of

experiments were performed at a spanwise plane at the $y/h = 0.04$. The first and second cases, S29-76 and S23-250R3, examine the flow excursion process from a steady flow at $Re_{b0} = 2{,}913$ and $2{,}300$ which is increased to $Re_{b1} = 7{,}625$ and $25{,}000$ due to opening of the control valve, respectively. During the initial stages of the flow excursion, pre-existing streaks, or backward-jets, are stretched in the streamwise direction, resembling the Klebanoff modes previously seen in the buffeted laminar regime of the bypass transition flows. Stretching of the streaks continues up to an instant $t^* \approx 16$ and 120 or $t_0^+ \approx 76$ and 128 for the S29-76 and S23-250R3, respectively, where the irregular instabilities appear, resembling the bursts of turbulence in transitional flows. These isolated packets of instability spread to other locations in the plane as time proceeds further, occupying the entire surface. Three distinct regimes are identifiable in these flows named pre-transition, transition and fully-turbulent due to He and Seddighi (2013).

The transition-like phenomena observed in the instantaneous flow fields can be quantitatively evaluated by examining the ensemble-averaged quantities. Perturbing velocity, which is a measure of the temporal development of the mean flow with respect to its initial state, was shown to behave similarly to the Stokes solution during the pre-transition phase when plotted versus the unsteady-equivalent similarity parameter, $\eta = y/2\sqrt{\nu t}$, regardless of the final-to-initial state of the flow. The momentum-thickness Reynolds number and the shape factor of the internal unsteady channel flows are shown to follow a similar trend as those of a boundary layer.

Interestingly, perturbing mean and fluctuating velocities obtained from various cases examined herein show to collapse extremely well during the pre-transition period regardless of the final-initial flow conditions. According to the ensemble-averaged data, the pre-transition period can extend up to $t_0^+ \approx 90$ for the cases examined herein. This is however an averaged estimation of the pre-transition duration and can be subjected to changes in the instantaneous flow visualisation. It should be emphasised that the degree of the flow response during the transition phase depends on the acceleration rate. For instance, considering the fluctuating velocities, the responses in cases with higher final-initial Reynolds number ratios seem to deviate more rigorously from those in other cases.

Streamwise and spanwise correlations of the streamwise velocity can provide quantitative information on the characteristics of the streaks. Measurements of the spanwise and streamwise auto-correlations of the streamwise velocity in a plane adjacent to the wall ($y/h = 0.04$) show a slight decrease in the width and elongation in length of the streaks during the pre-transition and transition processes.

The response of the ensemble-averaged mean and fluctuating velocities due to the excursion of flow rate provides useful information on the flow-field across the channel. It is shown that u' component is the first fluctuating velocity that responds to the acceleration in the wall region while other components (${v'}_{rms}$, $\overline{u'v'}$, and ${w'}_{rms}$) are experiencing longer delays. The early response of ${u'}_{rms}$ can be attributed to the elongation of the pre-existing coherent structures. The elongation process provides a flow field that is comparable in many ways with the buffeted laminar flow in bypass transition flows. The friction coefficient obtained from RANS simulations and previously through DNS studies, is shown to behave very similar to the Stokes solution for an unsteady laminar flow during the pre-transition phase. Formation of turbulent spots and their propagation across the flow-span results in the response of the ${v'}_{rms}$ and ${w'}_{rms}$ components, providing a good measure for the end of the pre-transition period.

A critical Reynolds number ($Re_{t,cr}$) can be defined to mark the start of transition. This parameter is equivalent to the critical Reynolds number of boundary layer flows. $Re_{t,cr}$ utilises an equivalent length-scale to x, which is defined on the basis of the final bulk velocity and the critical time (t_{cr}). Equivalently, free-stream turbulence intensity (Tu_0) can be defined to provide a measure of final-to-initial flow conditions. The flow-loop facility employed in the present investigations provides a capability for higher initial free-stream turbulence levels in comparison to what was previously examined by (He and Seddighi, 2015). Confirming the previous investigations, critical Reynolds number is found to have a power-law relationship with the initial free-stream turbulence levels. The constant of the power-law are higher than the proposal of He and Seddighi (2015). This relationship was found to be $Re_{t,cr} = 770Tu_0^{-1.77}$. However, it must be emphasized that the constants of this power-law are more likely to be a product of arbitrary assumptions and are dependent on the interpretation of the initial turbulence field.

The period of transition in unsteady flows has been defined as the difference between the time when the flow has reached a fully turbulent state and the critical time for transition. Unsteady flows with lower initial free-stream turbulence intensity are shown to have higher critical Reynolds numbers with longer period of transition. The period of transition is shown to have a power-law relationship with the critical Reynolds number with the power-law constant of 0.75 which is similar to the findings of Narasimha (1985) in spatially developing boundary layer flows.

Chapter 6. Unsteady flows over rough surfaces

6.1 Introduction

In this chapter the behaviour of mean and turbulence characteristics in an asymmetric rough channel flow are investigated in detail. The asymmetric rough channel flow investigated herein comprises of a smooth surface on the top of the channel and a rough surface at the bottom. The size, pattern and flow characteristics of the rough plates are discussed in detail in Section 4.5. During these investigations, the flow rate is increased from a lower Reynolds number turbulent flow to one with a higher Reynolds number. In order to facilitate the comparisons, the rate and magnitudes of the flow rate excursions investigated herein are similar to the previous investigations over smooth surfaces (described in Chapter 5). For these rough surface experiments, velocities are measured using PIV only.

In Section 6.2, details of the case studies are introduced. The instantaneous flow fields are discussed in Section 6.3. Ensemble-averaged results are then presented to shed light on the development of the flow mean and fluctuating velocities. Relevant comparisons to unsteady flows over smooth surfaces are made to highlight the effects of the roughness. Finally the effects of roughness on the initial free-stream turbulence intensity, critical Reynolds number and period of transition are investigated.

6.2 Cases studied

A range of initial-to-final Reynolds number unsteady flows are generated by sudden opening of the control valve. The duration as well as the initial and final bulk states of the flows investigated match those presented earlier in Table 5.1. The flows start from an initial bulk Reynolds number

of 2,300 or 2,900, i.e. essentially a hydrodynamically smooth flow, and end with much higher Re corresponding to either transitional or fully rough regime.

Table 6.1 summarises the flow conditions of the unsteady cases examined. The variation of the bulk flow conditions are maintained in a similar fashion to produce similar bulk Reynolds numbers and acceleration rates as for the smooth-wall experiments. The duration of the flow excursions (Δt) corresponds to the time to reach 90% of the final flow. Nomenclature of the cases is based on the initial and final bulk Reynolds numbers as well as the surface conditions of the channel (R indicates the measurements over rough plates). Temporal variations of the bulk velocities are shown in Figure 6.1.

Case No.	$U_{b0}-U_{b1}(m/s)$	$\Delta t\ (sec)$	$Re_{b0}-Re_{b1}$	Δt^*
R23-250	0.09-0.96	1.9	2,300-25,000	73.2
R23-230R3	0.09-0.94	3.3	2,300-23,400	124.5
R23-200	0.09-0.76	1.9	2,300-20,000	57.5
R23-180	0.09-0.66	1.85	2,300-18,000	51.4
R23-135	0.09-0.50	2	2,300-13,500	42.3
R23-93	0.09-0.35	1.4	2,300-9,300	21.1
R29-250	0.11-0.96	1.85	2,913-25,000	71.4
R29-76	0.11-0.27	1.35	2,913-7,625	15.6

Table 6.1 Initial and final flow conditions for the rough wall experiments.

PIV is used to measure streamwise, wall-normal/spanwise velocities over the rough wall, while the flow meter is used to measure the bulk flow condition. PIV measurements are performed over vertical (xy) and horizontal planes (xz) as shown in Figure 3.18. The vertical plane measurements are performed at a plane with $z = 3.5h$ distance from the near side wall. The horizontal plane measurements are performed at $y{\sim}0.75\ mm$ (${\sim}0.8k$) above the crest of the roughness elements. The horizontal plane measurements were made for cases R23-76, R23-250 and R23-230R3 only, in order to provide direct comparisons to the measurements over smooth surfaces. These measurements are performed with two different camera distances from the laser sheet: the first and second camera configurations provide a $77 \times 77\ mm$ and $19.7 \times 19.7\ mm$ of FOV, respectively. The vertical measurements provide a FOV of $33 \times 33\ mm$. All image pairs are collected at a sampling frequency of 7 Hz. The origin of the wall is assumed to be at the tip of the roughness crest throughout these investigations.

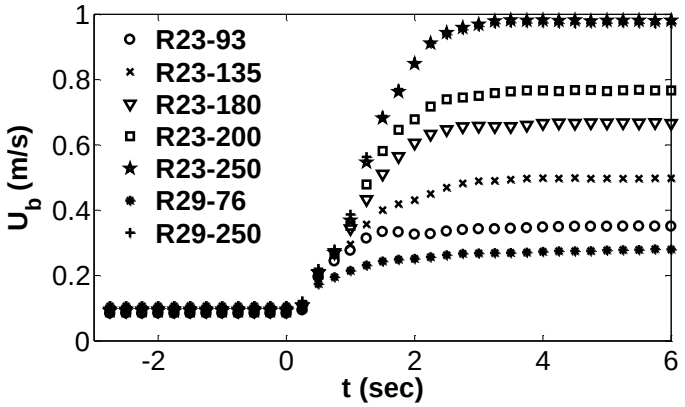

Figure 6.1 Variation of bulk velocity for all sudden opening flows over rough surfaces.

6.3 Instantaneous flow behaviour

This section will focus on the behaviour of the instantaneous flow field under unsteady conditions. Three main cases will be considered: R29-76, R23-230R3 and R23-250. The variation of the bulk flow in each of these cases along with the time stamps of certain events presented later in this section are shown in Figure 6.2. These measurements are obtained from the horizontal configuration of the laser sheet at a plane of $y = 0.75\ mm$. For the sake of brevity, results obtained from the smaller FOV size are not presented here.

The first case presented in this section is the R29-76, which is equivalent to the S29-76 in terms of bulk Reynolds numbers and acceleration rate. As was shown earlier in §4.5, the initial flow conditions in the range of $Re_b \sim 2300 - 2800$ can be considered to be hydrodynamically smooth and therefore the initial wall shear stress can be obtained from the Blasius correlation.

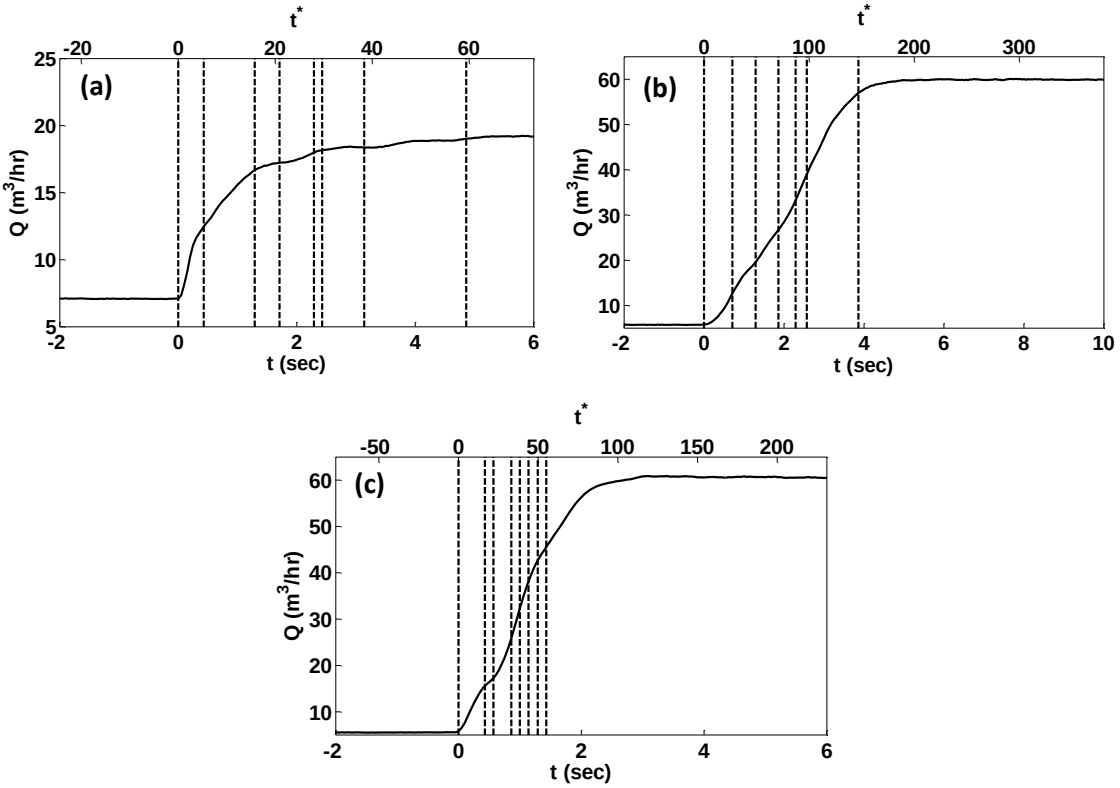

Figure 6.2 Variation of bulk flow with time for the cases (a) R29-76 (b) R23-230R3 (c) R23-250

Figure 6.3 shows the evolution of the normalised fluctuating streamwise velocity at different instances of time. It can be seen from the contour plots that the transition process is very similar to that of smooth flows and therefore similar to boundary layer bypass transition due to FST. The initial flow contains positive and negative streaky structures that experience elongation and amplification of magnitude in the streamwise directions during the early periods of the flow excursion (e.g. $t^* = 20.9$). This pattern is then disturbed by high amplitude bursts of turbulence that lead to complete breakdown of the structures. This observation is similar to the previous investigations over the smooth surfaces except the fact that the plane of measurement for the rough-wall flows is slightly closer to the wall. This shortcoming in exact adjustment of the laser plane is not of great importance as the flow features within the wall region are considered to be similar.

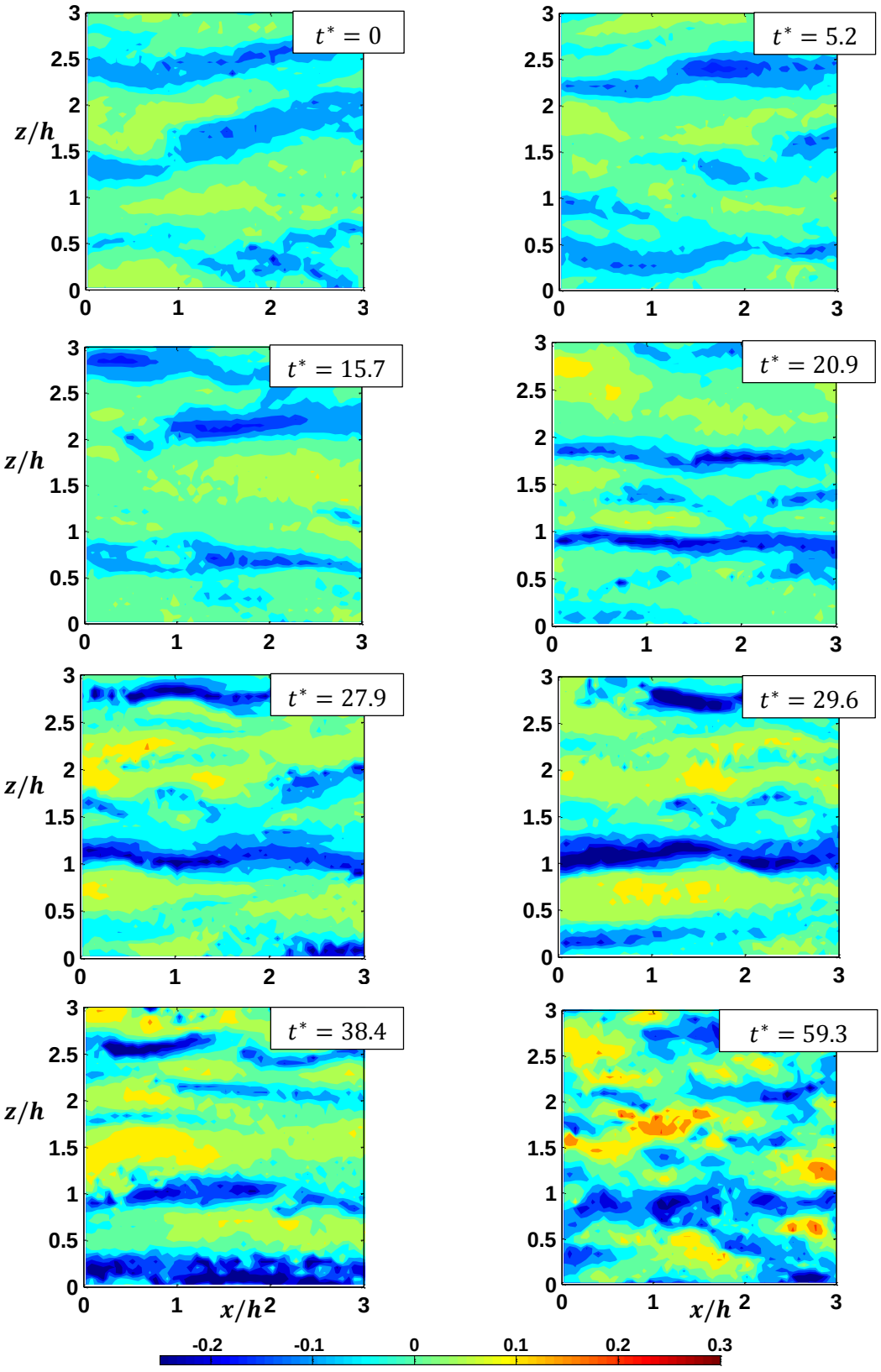

Figure 6.3 Temporal evolution of contour plots of normalised streamwise fluctuating velocity (u'/U_{b1}) for Case R29-76 at a plane 0.75 mm ($y_0^+ = 5.3$, $y/h = 0.03$) above the roughness.

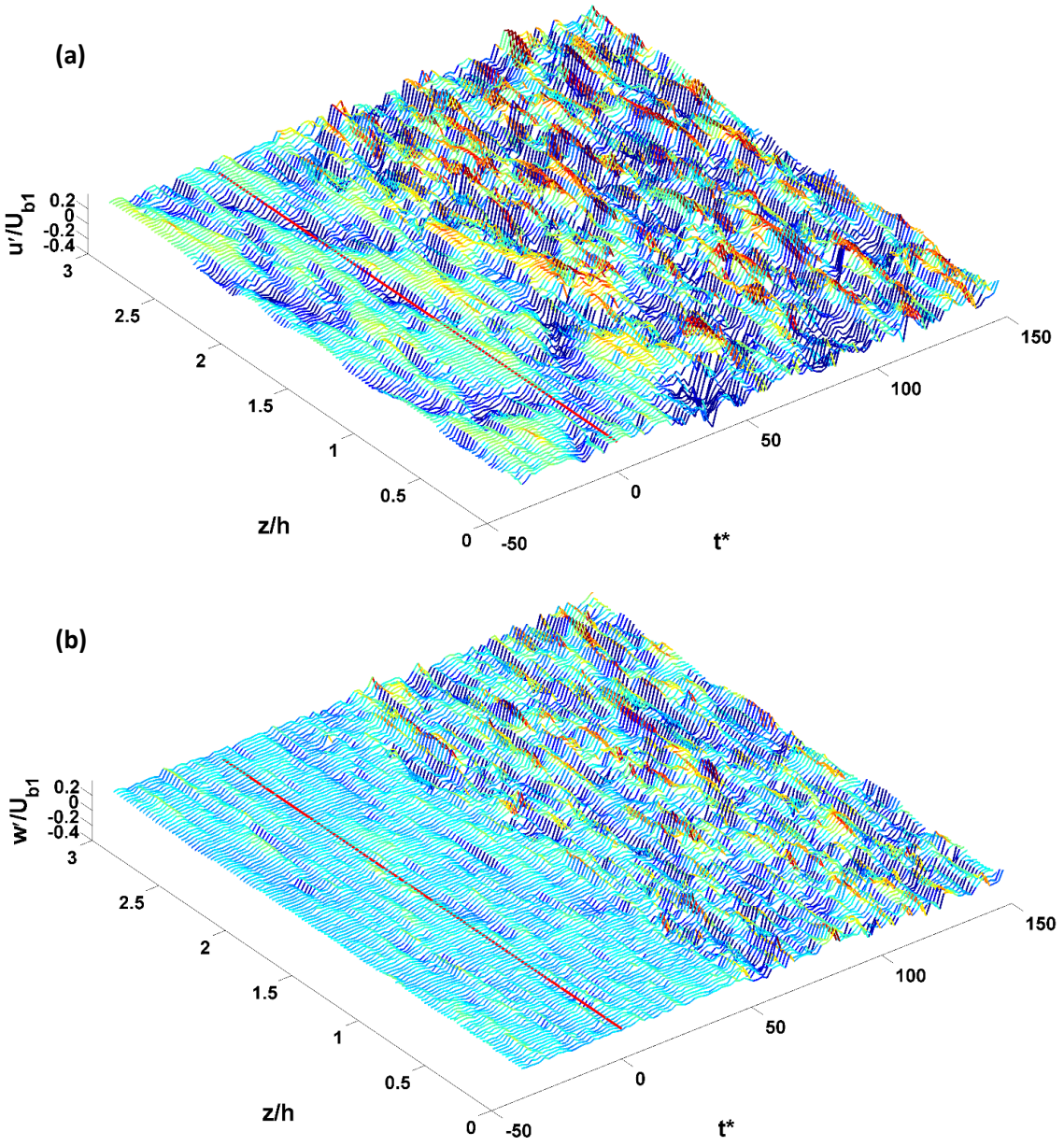

Figure 6.4 Temporal variation of normalised fluctuating velocities in (a) streamwise (u'/U_{b1}) and (b) spanwise directions (w'/U_{b1}) at $y_0^+ = 5.3$, $y/h = 0.03$ in the midsection of the FOV for case R29-76.

Figure 6.4 shows the fluctuating streamwise and spanwise velocities for case R29-76 at the midspan of the FOV at a similar plane presented earlier. These plots confirm the similarities observed between the smooth and rough flows more clearly. Despite the small differences in the magnitude of the fluctuations, the response of turbulence, as well as its structure, is similar to case S29-76. Figure 6.5 compares the instantaneous fluctuating signals at three different locations in the FOV from the smooth and rough flows. It can be seen from these figures that the response of tubrulence can be considered to be very similar in these two cases. This can mainly be attributed to the fact that both the intial and final Reynolds numbers of the unsteady

cases are relatively low and hence the surface is not far from a hydrodynamically smooth condition.

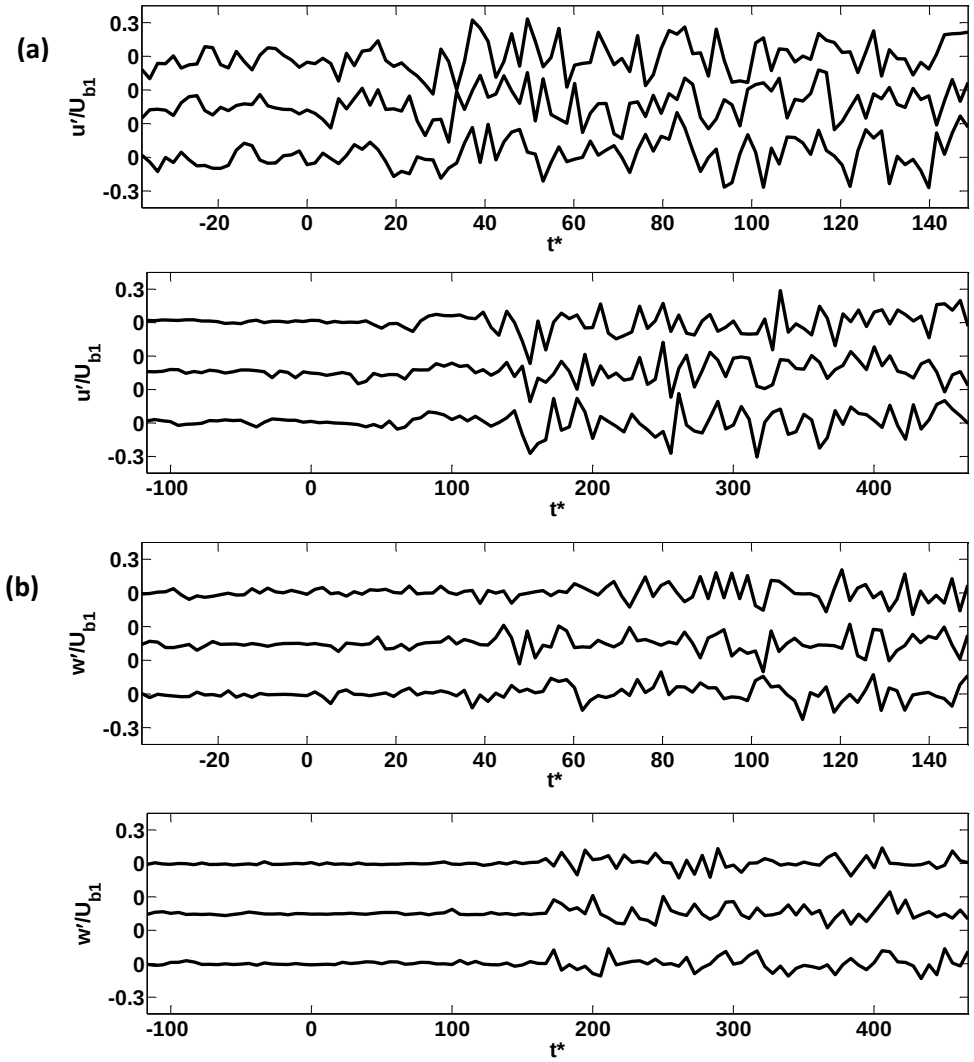

Figure 6.5 Temporal evolution of (a) streamwise and (b) spanwise fluctuating velocities over smooth (top) and rough surfaces (bottom) for the case R29-76 at $y_0^+ = 5.3$, $y/h = 0.03$.

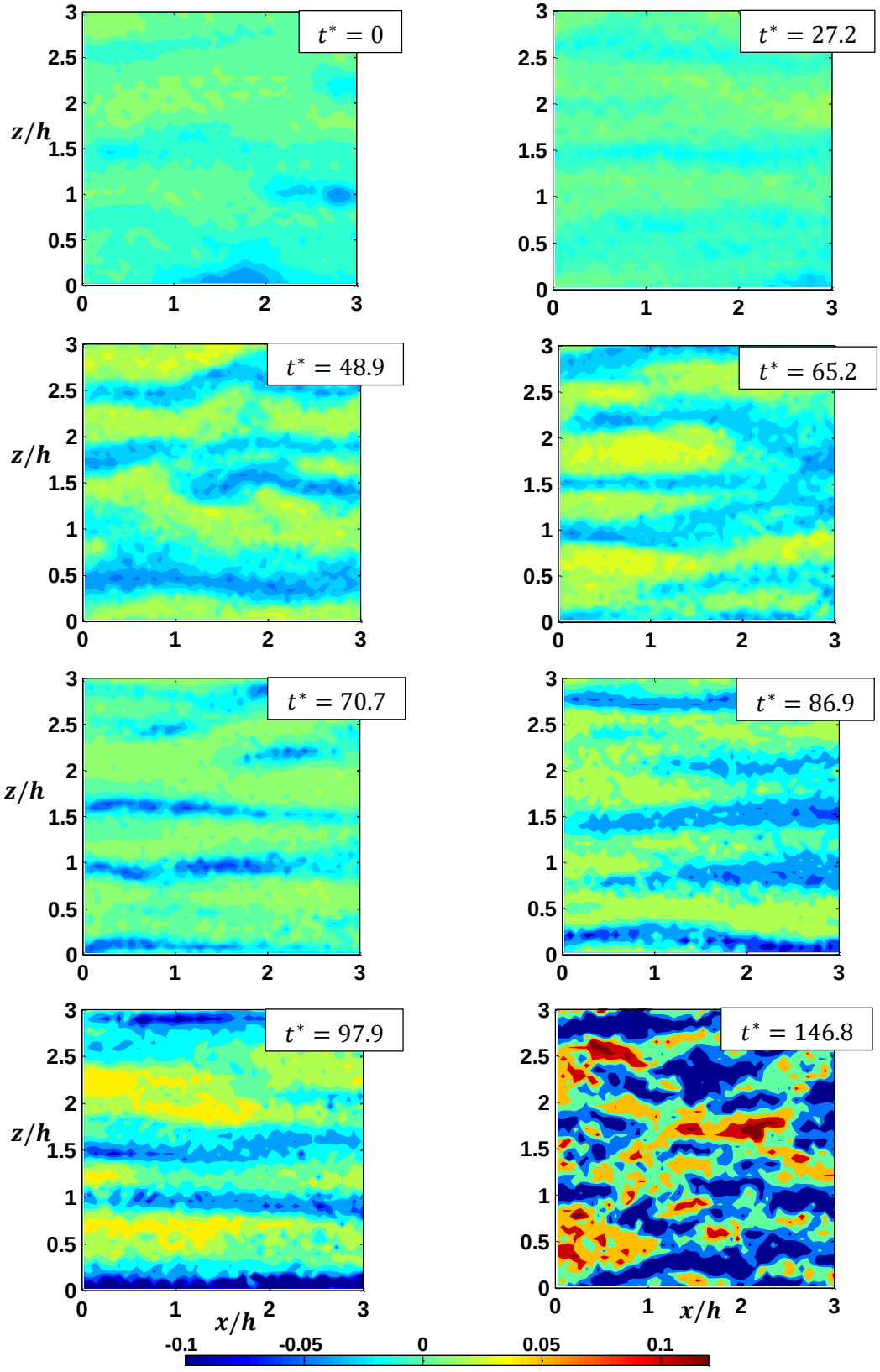

Figure 6.6 Temporal evolution of contour plots of normalised streamwise fluctuating velocity (u'/U_{b1}) for Case R23-230R3 at a plane 0.75 mm ($y_0^+ = 4.5$, $y/h = 0.03$) above the roughness.

Contours of streamwise fluctuating velocity for case R23-230R3 are shown in Figure 6.6. It can be seen from the contour plots that the acceleration of the flow results in an elongation of the initially existing streaky structures leading to their complete breakdown by $t^* \approx 150$, which is very similar to the smooth-wall measurements. Figure 6.7 shows the streamwise and spanwise fluctuating velocities obtained from case R23-230R3. These plots clearly show the so-called calm and turbulent states associated with the pre-transition and fully turbulent states introduced in Chapter 5. It should however be noted that the response of the fluctuating velocities is enhanced for the flows over the specific rough surface investigated herein. A direct comparison of the fluctuating velocities over smooth and rough surfaces for the R23-230R3 is provided in Figure 6.8 to further clarify the effect of the roughness. It is clear that the transition is earlier in the flow over a rough wall than over a smooth wall.

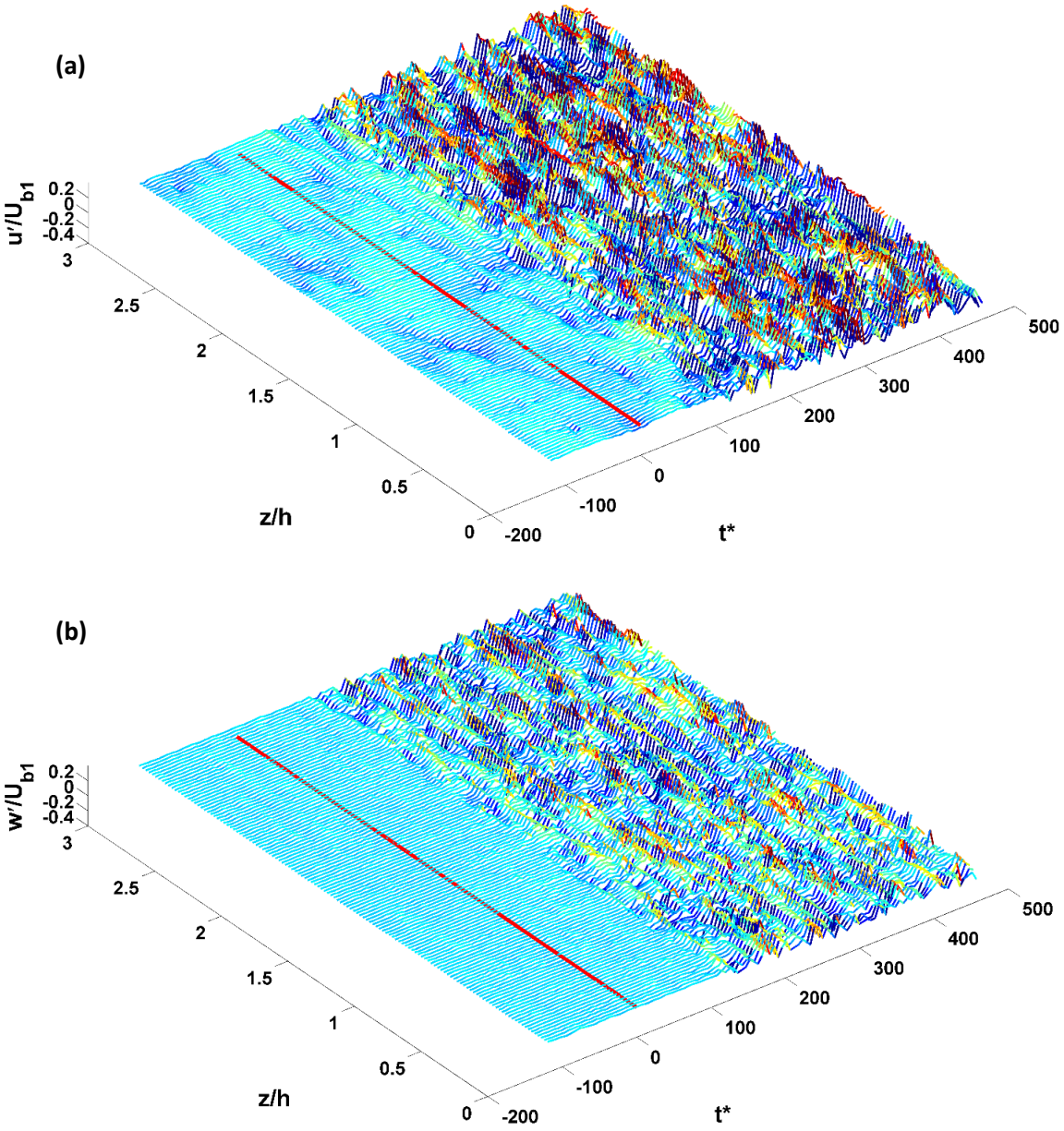

Figure 6.7 Temporal variation of normalised fluctuating velocities in (a) streamwise (u'/U_{b1}) and (b) spanwise directions (w'/U_{b1}) with time at $y_0^+ = 5.3$, $y/h = 0.03$ in the midsection of the FOV for case R23-230R3.

The last case to investigate is the R23-250, which comprises a sudden opening of the control valve to increase the bulk flow from $U_b = 0.09$ to $0.96\ m/s$ in 1.9 seconds. The evolution of the streamwise fluctuating velocity contours are shown in Figure 6.9. The initial process of this evolution is similar to the ramp case. The early stages ($t^* < 49.5$) consists of elongation of the juxtaposed high and low streaky structures. This is while the breakup process is much faster in comparison to the ramp case. It can be seen from the contour plots of the sudden opening case that the magnitude and size of the elongated jets before the breakup are much lower than the jets in the ramp case. A comparison of the fluctuating signals obtained from the PIV for the rough

case (Figure 6.11) with the LDV plots in Figure 5.8 reveals an enhancement in the process of transition, namely, an early transition in the former.

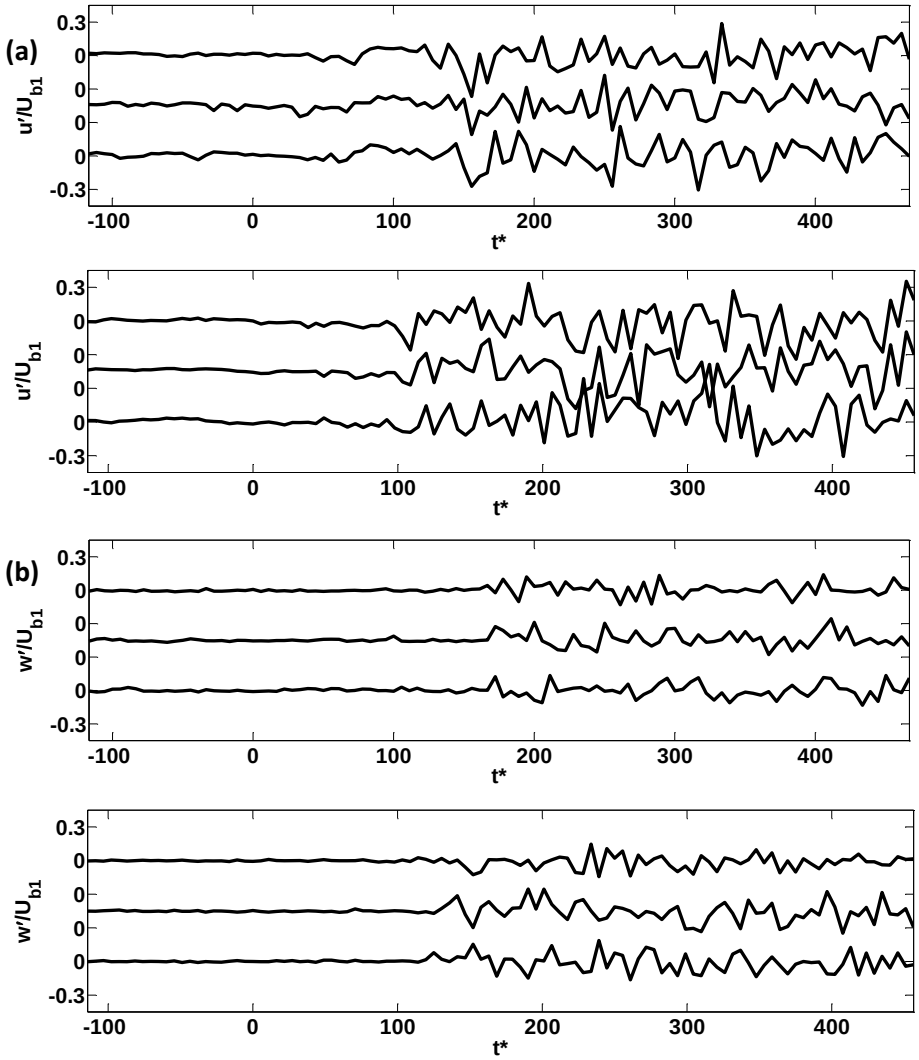

Figure 6.8 Temporal evolution of (a) streamwise and (b) spanwise fluctuating velocities over smooth (top) and rough surfaces (bottom) for the case R23-230R3 at $y_0^+ = 4.5$, $y/h = 0.03$.

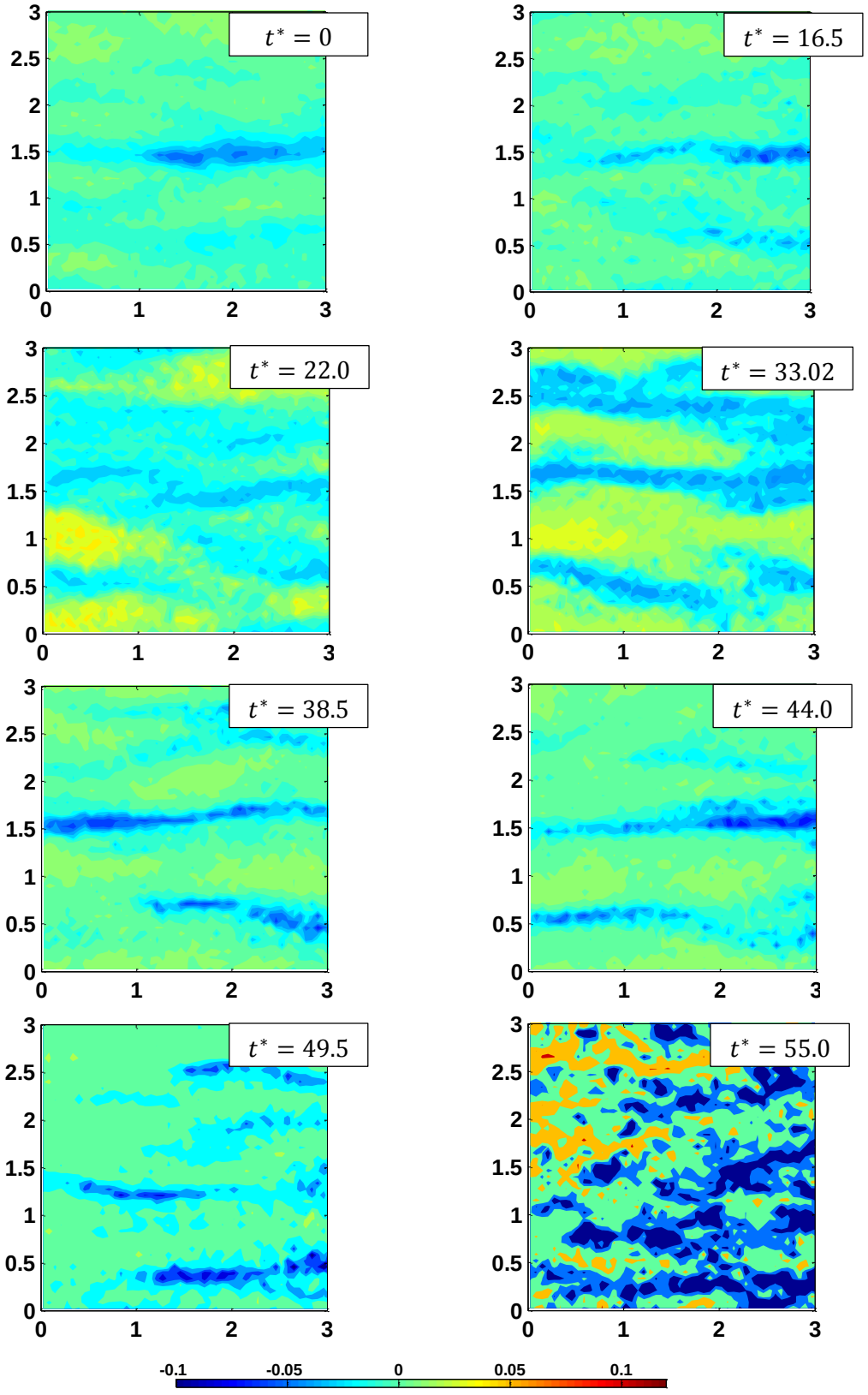

Figure 6.9 Temporal evolution of contour plots of normalised streamwise fluctuating velocity (u'/U_{b1}) for Case R23-250 at a plane 0.75 mm ($y_0^+ = 4.5$, $y/h = 0.03$) above the roughness.

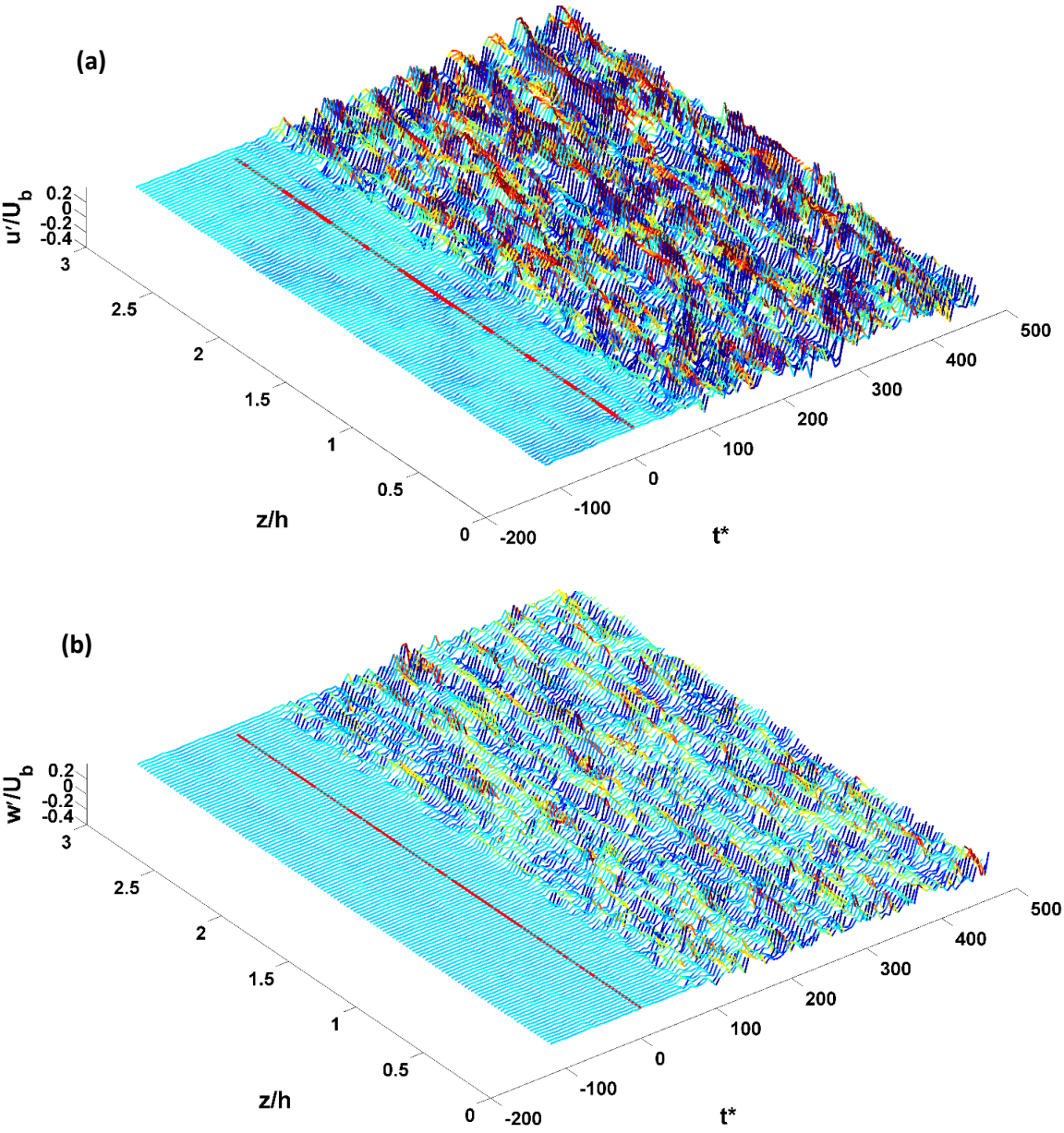

Figure 6.10 Temporal variation of normalised fluctuating velocities in (a) streamwise (u'/U_{b1}) and (b) spanwise directions (w'/U_{b1}) at $y_0^+ = 5.3$, $y/h = 0.03$ in the midsection of the FOV for case R23-250.

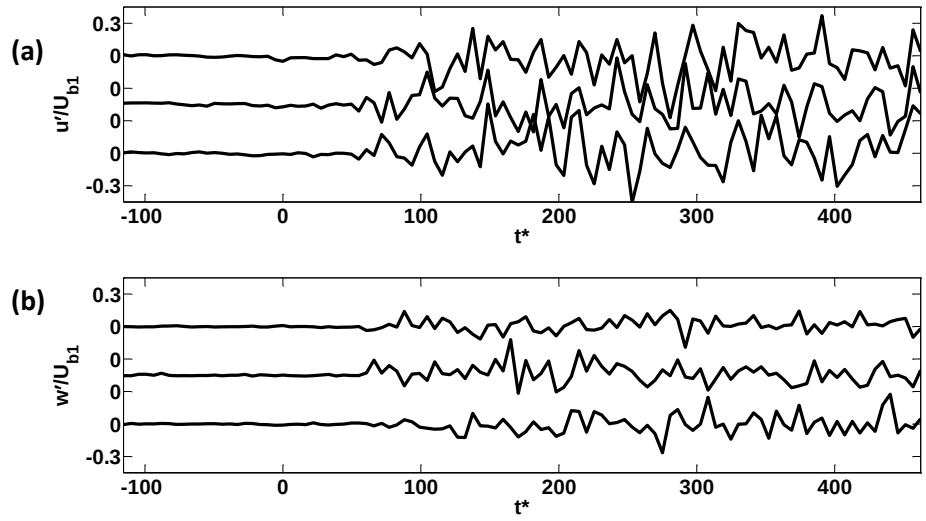

Figure 6.11 Temporal evolution of (a) streamwise and (b) spanwise fluctuating velocity over the rough surface at the plane of $y_0^+ = 5.3$, $y/h = 0.03$.

6.4 Ensemble-averaged flow behaviour

In this section the ensemble-averaged flow quantities are presented. Different cases of final-to-initial Reynolds numbers are investigated to measure the effect of roughness on various flow parameters in comparison to smooth flows. Statistics obtained from the PIV measurements are calculated from the spatial and temporal averaging similar to flows over the smooth surfaces described in the earlier chapters. These statistical calculations are performed on 30 ensembles.

6.4.1 The time developing boundary layer

This section focuses on the development of the boundary layer formed on the rough wall during and after the flow excursion. Measurements from the vertical laser sheet configuration (Figure 3.18 (b)) at the xy plane of $z = 3.5h$ from the near side wall are used for this analysis.

Perturbing velocity ($\widehat{\overline{U}}\,(y/\delta, t^*)$, equation (5.1)) was used in the previous chapter to show the development of the velocity profile during and after the transition process. Similar plots are presented in Figure 6.12 to show the development of the velocity profiles at various instances with respect to the Stokes similarity parameter η ($= y/2\sqrt{\nu t}$) over the rough surface of the channel for four selected cases with rather different acceleration rates and initial flow conditions. It can be seen from these plots that the general trend of velocity profile development is very similar regardless of the acceleration rate or the initial flow conditions. It should be noted that the perturbing velocity profiles nearly collapse on the Stokes solution in the early stages of all test cases with no scaling parameter required.

During the initial instances of the flow development, the perturbing velocity profiles nearly collapse on the Stokes solution. This behaviour is similar to the flow development shown earlier over smooth surfaces. Further temporal development results in deviations from the Stokes solution and steeper defections (in comparison to the smooth cases) in the wall region as a result of the roughness. These developments continue until a new boundary layer is formed.

Similarities observed in the development process of the boundary layer over smooth and rough surfaces show the existence of a pre-transition period, where flow behaves similar to the laminar buffeted regime of the transitional flows.

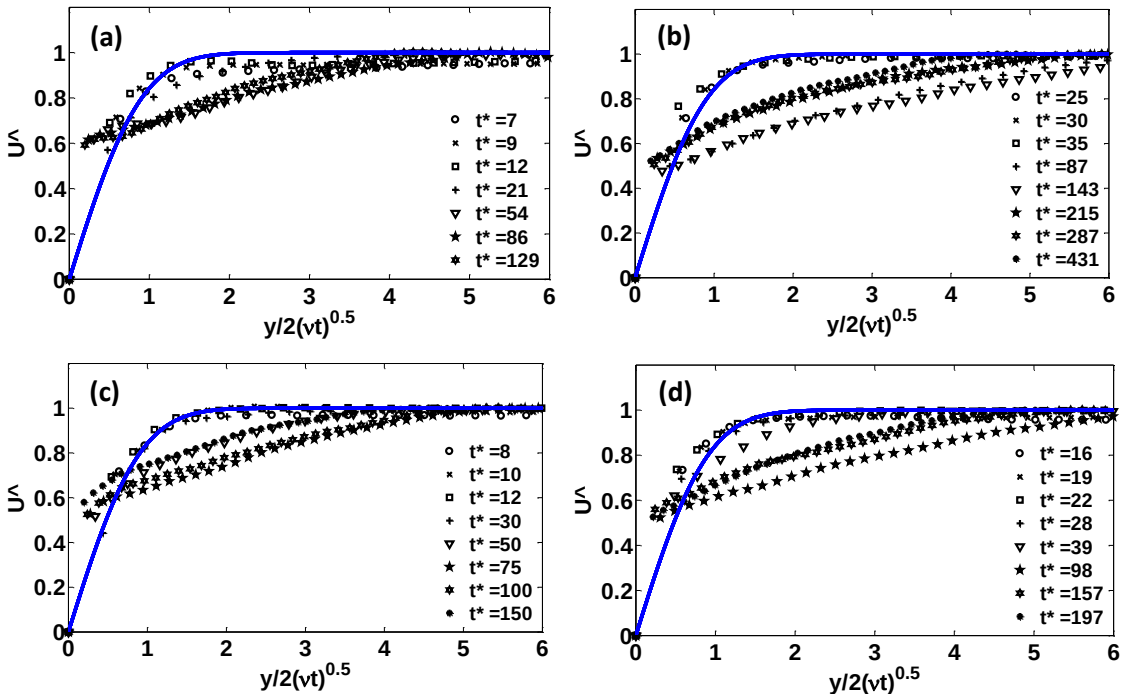

Figure 6.12 Development of perturbing velocity profiles with time for four different cases; (a) R29-76 (b) R23-250 (c) R23-93 and (d) R23-135; Line: Stokes solution

It can be seen from the instantaneous flow fields as well as the development of the perturbing velocity profiles that similarities exist between the unsteady flows over rough and smooth surfaces discussed in the previous chapter. It can be concluded that the features of the bypass transition due to free-stream turbulence are still evident over the rough surfaces in the flow conditions investigated herein. Table 6.2 summarises the actual and normalised critical and fully turbulent timescales for the rough-bed cases. Similar to smooth flows, the fully turbulent condition was defined as the time when the near-wall streamwise fluctuating velocity reaches its final value, while the critical time is when the wall-normal fluctuating velocity responses to the flow excursion in the wall region.

Cases	$t_{cr}(sec)$	$t_{turb}(sec)$	t^*_{cr}	t^*_{turb}	$t^+_{0,\ cr}$	$t^+_{0,\ turb}$
R23-250	1.14	2.57	44.86	100.93	39.20	88.20
R23-200	1.14	2.57	35.10	78.97	40.13	90.29
R23-180	1.43	3.14	38.17	83.98	51.14	112.50
R23-135	1.43	3.14	28.35	62.37	45.38	99.85
R23-93	2.29	4.86	32.04	68.09	70.55	149.92
R29-76	2.29	4.57	25.74	51.48	107.13	214.27
R29-250	1.14	2.57	44.46	100.04	53.44	120.24

Table 6.2 Dimensional and normalised critical and fully turbulent timescales for various unsteady cases over the rough wall.

Figure 6.13 shows the development and distribution of the perturbing velocity with respect to t_0^+ ($= u_{\tau 0}^2 t/\nu$) and y_0^+ ($= y u_{\tau 0}/\nu$). Despite the variation in the commencing curves, which can be mainly attributed to the finite repeatability of the flow, a good collapse of trends exists during the initial instances of the flow development ($t_0^+ < 40$). The deviation from the Stokes solution initiates from $t_0^+ \sim 50$ which marks the critical point of transition. This is significantly lower than the $t_0^+ \sim 90$ over smooth flows.

Difference in the development of the boundary layer velocity profile for lower and higher Reynolds number ratios is evident from the trends. It is clear that the development of R23-93 and R29-76 during the transition process is very different from the other cases. This can mainly be attributed to the relatively low final Reynolds numbers of these cases.

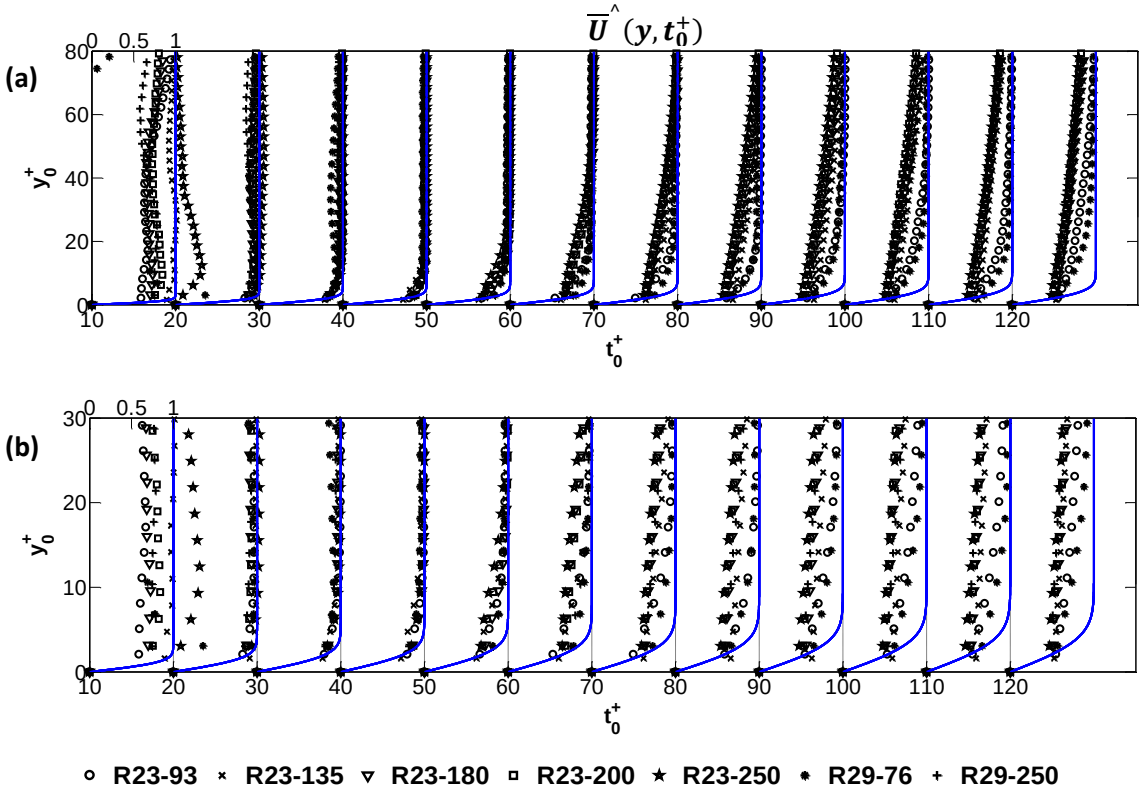

Figure 6.13 Development of perturbing velocity profiles at various Reynolds numbers; (a) actual profiles (b) zoomed profiles; Line: Stokes solution.

The streamwise and wall-normal perturbing rms velocities are plotted in Figure 6.14 and Figure 6.15, respectively. The profiles obtained from each of the components show good collapse up to $t_0^+ < 50$. Similar to smooth flows, the development of the $\overline{u'}^{\wedge}$ profile in the wall region during the pre-transition zone is attributed to the dynamics of the streaky structures, whilst the $\overline{v'}^{\wedge}$ profiles are almost frozen. It is noteworthy that similarities can be observed in the $\overline{u'}^{\wedge}$ development of R29-76 and R29-250 up to the critical time of the R29-250 ($t_0^+ \sim 50$).

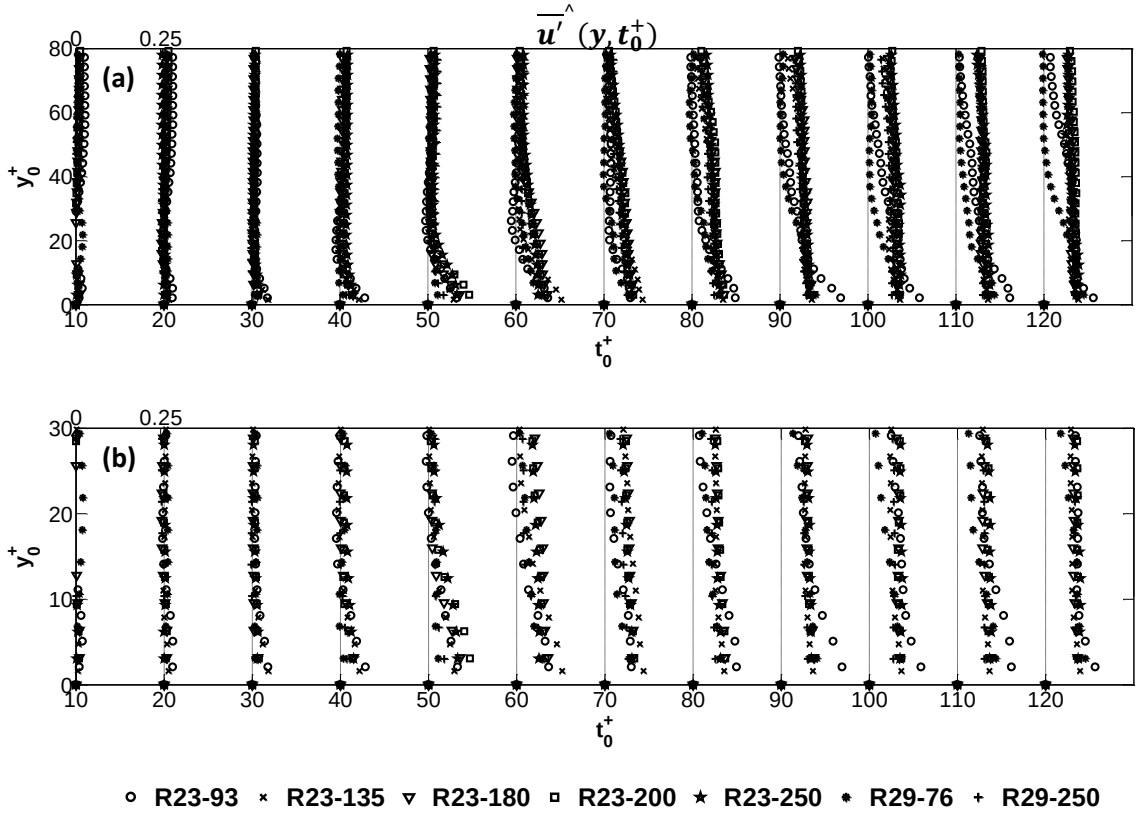

Figure 6.14 Development of perturbing streamwise fluctuating velocities at various Reynolds numbers; (a) actual profiles, (b) zoomed profiles.

Cases R23-200 and R23-250 are the first to show a $\overline{v'}^{\wedge}$ respond at the wall region (at $t_0^+ \sim 50$), while slower accelerating flows such as R23-93 and R29-76 experience a longer pre-transition zone, in comparison to others, requiring more time to build up to the final state.

It can be noticed, by comparing the developing plots of the unsteady flows over roughness presented here and the counterparts obtained from the flows over smooth surfaces discussed in §5.4.1, that the duration of the pre-transition phase is significantly reduced for flows over rough surfaces. The response of the $\overline{v'}^{\wedge}$ for the R29-76 is similar to the corresponding smooth case as both the initial and final Reynolds numbers are relatively low, inducing minimum roughness effects on the flow. However, case R23-93, which has a slightly higher final Reynolds number, responds faster in comparison to its equivalent smooth behaviour. The behaviour of the fluctuating velocities are further discussed in the next sections.

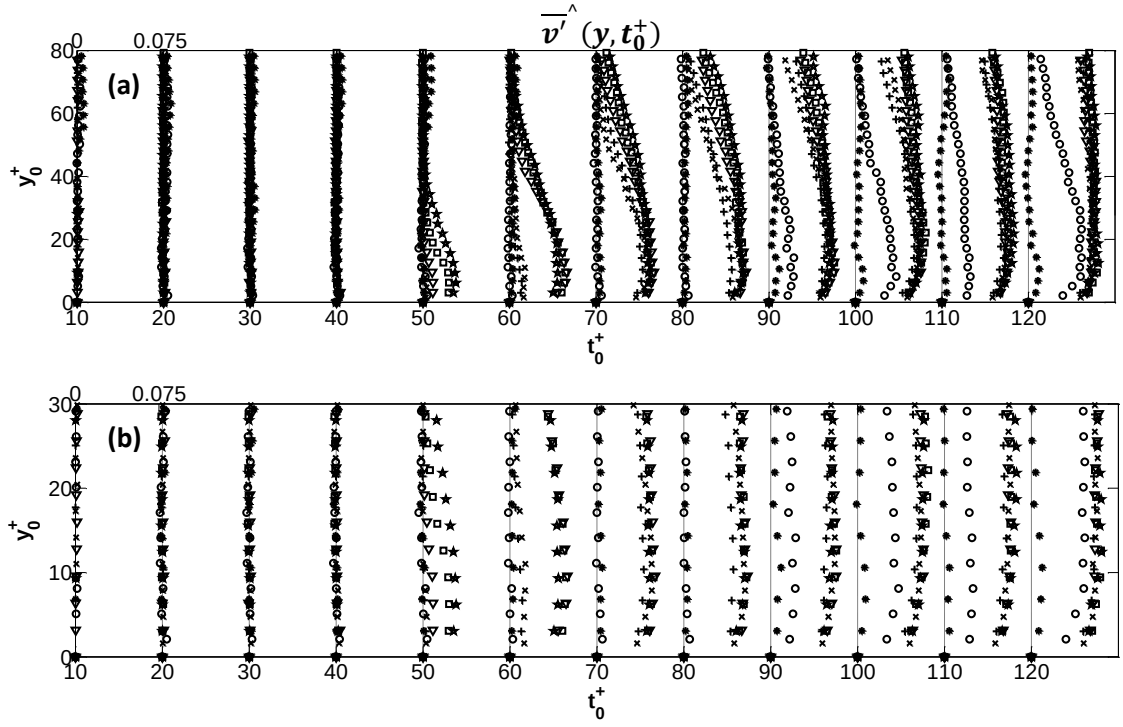

Figure 6.15 Development of perturbing wall-normal fluctuating velocities at various Reynolds numbers; (a) actual profiles, (b) zoomed profiles.

6.4.2 **Correlations**

This section discusses the behaviour of the streamwise auto-correlations (equation (5.8)) obtained from the three different unsteady scenarios in the streamwise and spanwise directions. The auto-correlation function can be used to quantify the distribution and behaviour of the streaky structures during the transition. These correlations are obtained from the streamwise/spanwise spatial and ensemble averaging over the entire 30 runs. The measurements used for this analysis are from a horizontal plane at $y/h = 0.03$ ($y/k = 0.8$).

Figure 6.16 shows the development of streamwise velocity auto-correlations for R29-76, R23-230R3 and R23-250 in the spanwise and streamwise directions. The trends obtained from the R29-76 show a slight stretch in the streamwise and a continuous mitigation in the spanwise size of the streaky structures during the pre-transition phase ($t_0^+ < 100$). More or less the same behaviour is observed in the other two cases. The main difference between the ramp and sudden opening scenarios of case R23-250 is the duration of the pre-transition phase. It can be seen that the stretching process of the streaks in the streamwise direction is much shorter for the sudden opening case (subplots c and e).

The effect of roughness on the initial ($t_0^+ = 0$) streamwise correlations in both streamwise and spanwise directions is shown to be more pronounced in the normalised wall-normal location of

4.5 for cases with lower initial Re flows as shown in Figure 6.16 (c to f). The existence of roughness has resulted in correlation waves of wavelengths equal to the wavelength of the roughness in the low wall-normal locations (such as $y_0^+ = 4.5$), whilst higher planes of $y_0^+ = 5.3$ for case R29 are not affected by the roughness (Figure 6.16 (b)).

Figure 6.17 shows the visualisation of the streaks during and after the flow excursion for cases R29-76, R23-230R3 and R23-250. Negative auto-correlation values designate the strength of the backward jets in a turbulent flow field. The magnitude of the negative correlation values in the spanwise direction are shown in the subsequent figures while the positive ones are set to zero (Figure 6.17). The correlation map of case R29-76 is very similar to that of its corresponding smooth case (Figure 5.15 (a)). Similar to smooth flows, the initial spacing between the streaks immediately after the valve opening reduces with the increase in the acceleration rate. The spacing remains more or less constant throughout the pre-transition phase. On the other hand, the onset of transition results in a reduction of the streaky structures reflecting the burst and generation of turbulent spots. This feature of transition is more apparent in the R23-230R3 and R23-250 contour plots (Figure 6.17 (b) and (c)). By comparing R23-230R3 to its smooth counterpart (Figure 5.15 (b)), an early transition due to the presence of roughness is noticeable.

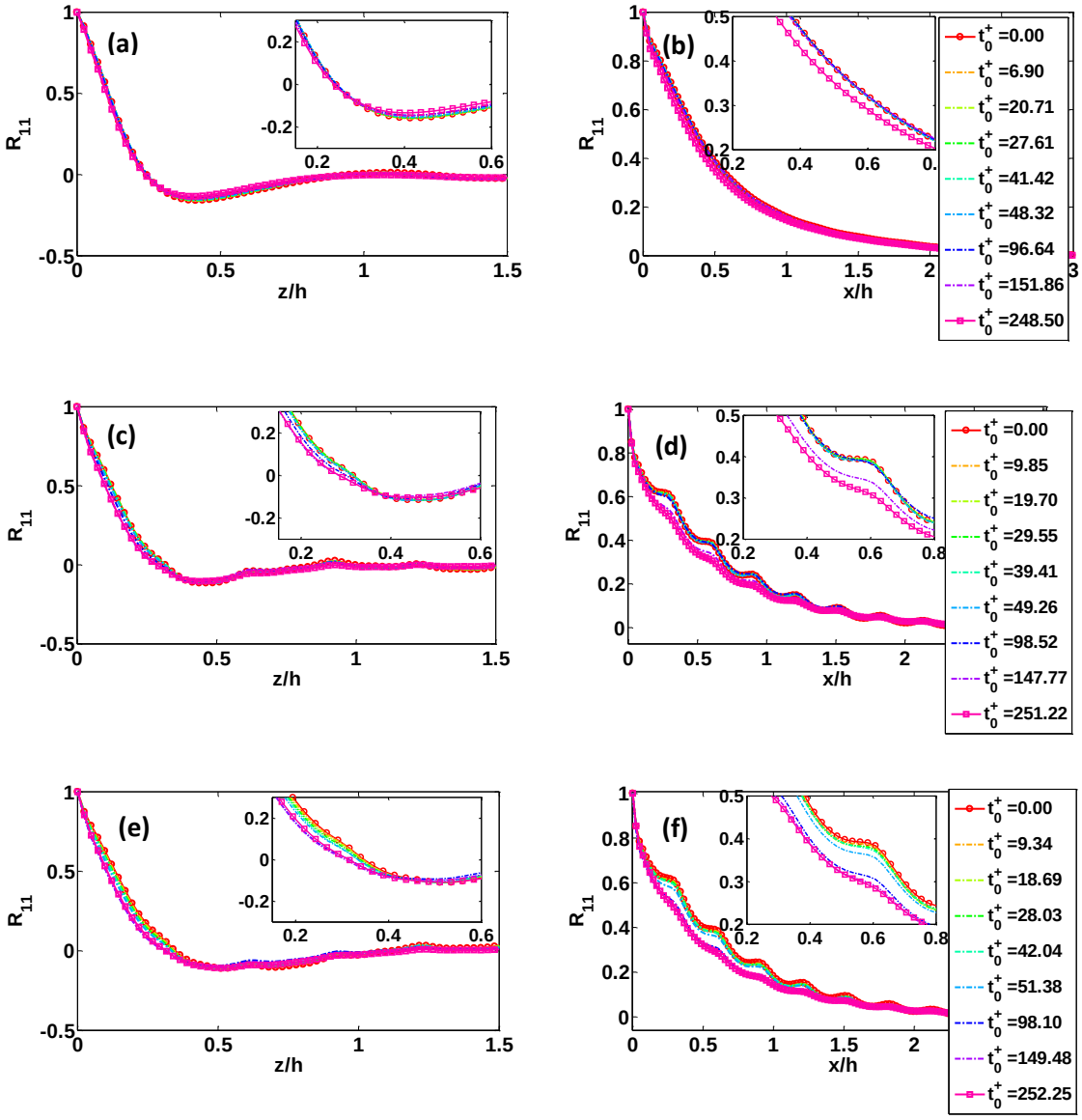

Figure 6.16 Temporal development of streamwise velocity correlations for cases (a-b) R29-76, $y_0^+ = 5.3$; (c-d) R23-230R3, $y_0^+ = 4.5$; (e-f) R23-250, $y_0^+ = 4.5$.

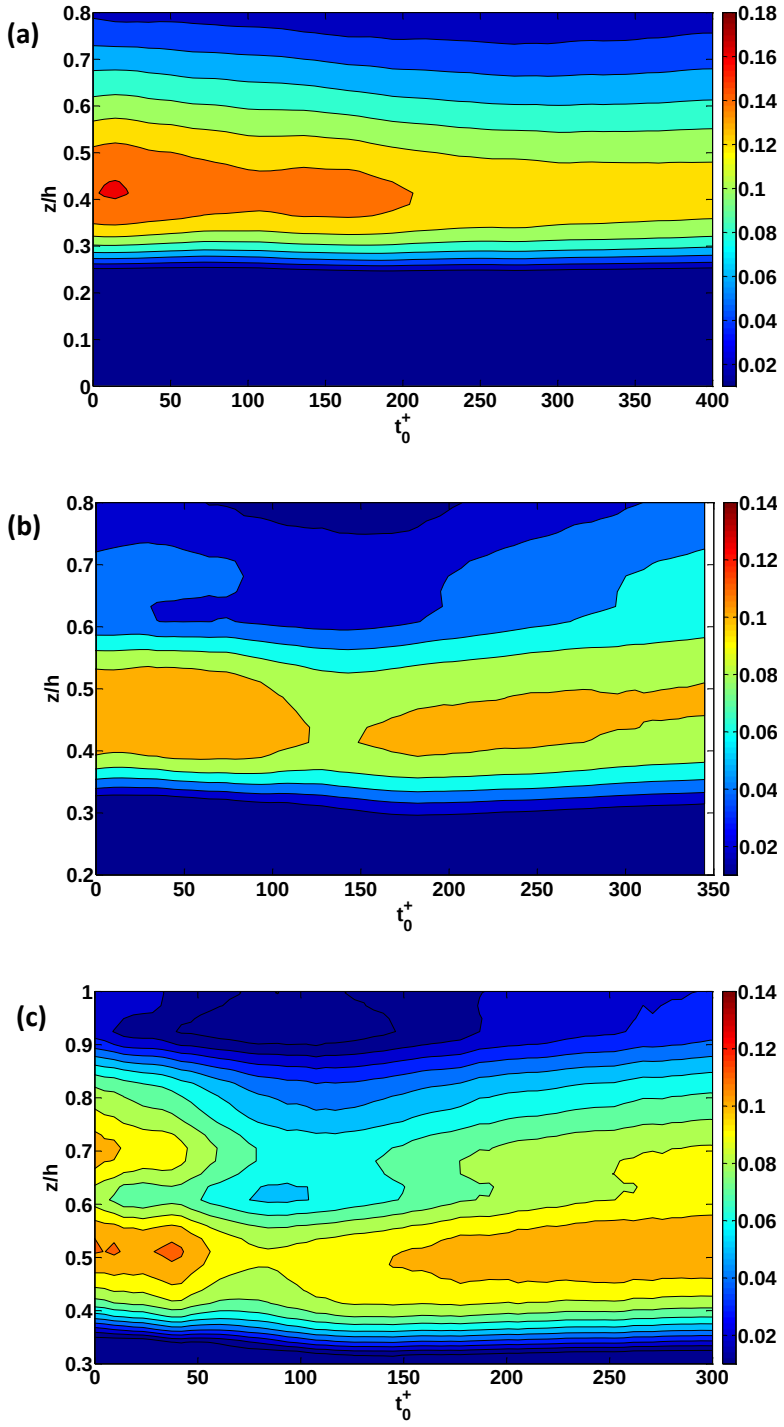

Figure 6.17 Temporal development of the streamwise fluctuating velocity correlation in the spanwise direction; (a) R29-76, $y_0^+ = 5.3$; (b) R23-230R3, $y_0^+ = 4.5$; (c) R23-250, $y_0^+ = 4.5$

6.4.3 **Behaviour of mean and rms fluctuating velocities**

This section discusses the behaviour of the mean and fluctuating velocities of unsteady flows over rough surfaces. The main discussion will be focused on the two cases of R29-76 and R23-

250. However, statistics obtained from other cases are provided in relevant discussions to facilitate the comparisons.

Figure 6.18 provides a comparison between the smooth (shown in red symbols) and rough (shown in black symbols) response of the normalised mean and turbulent quantities to the excursion of flow rate (Figure 6.1) for case R29-76. Final bulk velocity (U_{b1}) is used to normalise the velocity and time in the upper abscissae (t^*). It can clearly be seen from these figures that only a slight difference in the response of turbulence is observed between the smooth and rough surfaces.

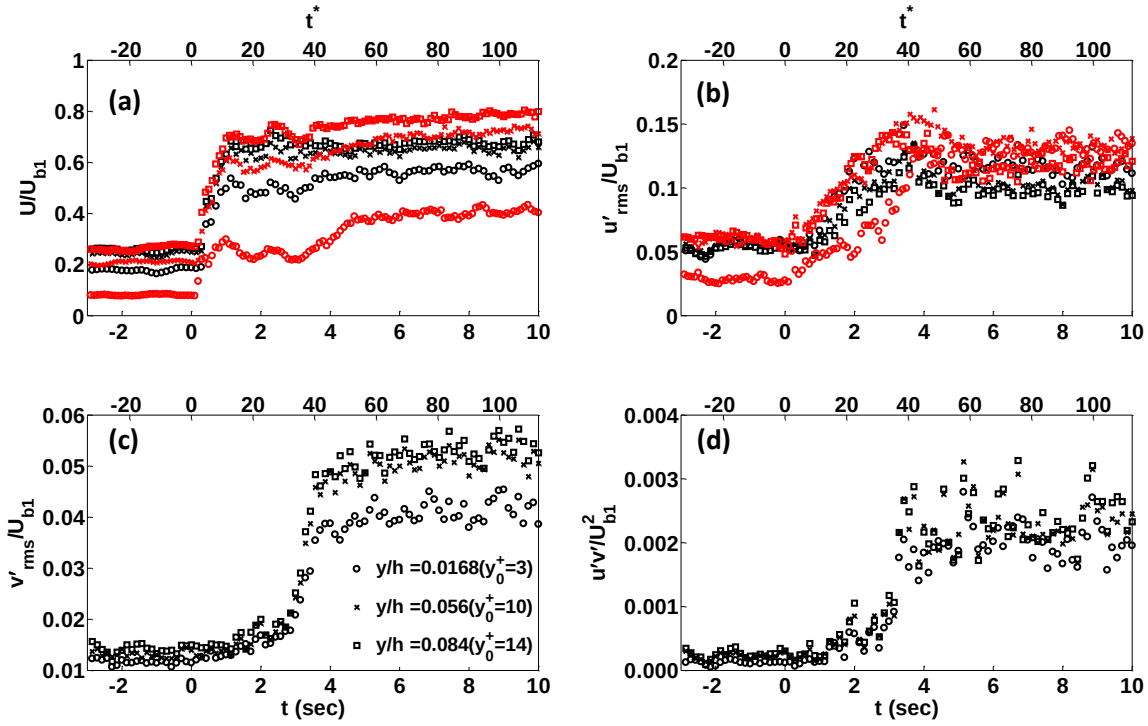

Figure 6.18 continued on next page.

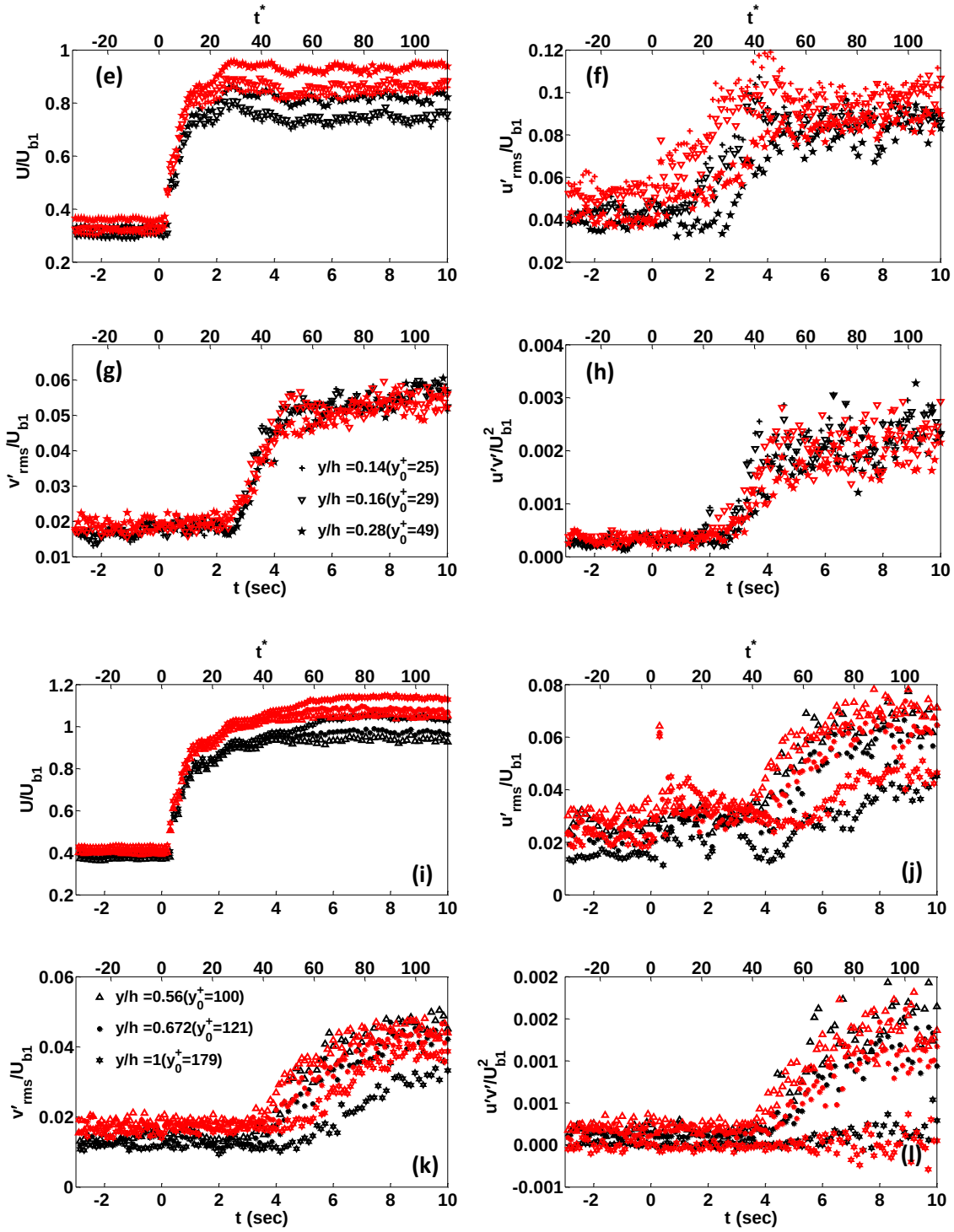

Figure 6.18 Temporal development of mean, fluctuating velocities and Reynolds shear stresses; Red symbols: S29-76 (LDV), Black symbols: R29-76 (PIV). Note: Every four subplots share a same legend.

The behaviour of the normalised mean and turbulent quantities are shown separately at selected wall-normal locations for case R29-76 in Figure 6.19. By comparing these with the

trends obtained from the smooth counterparts, insignificant differences can be seen in the temporal responses of the flow.

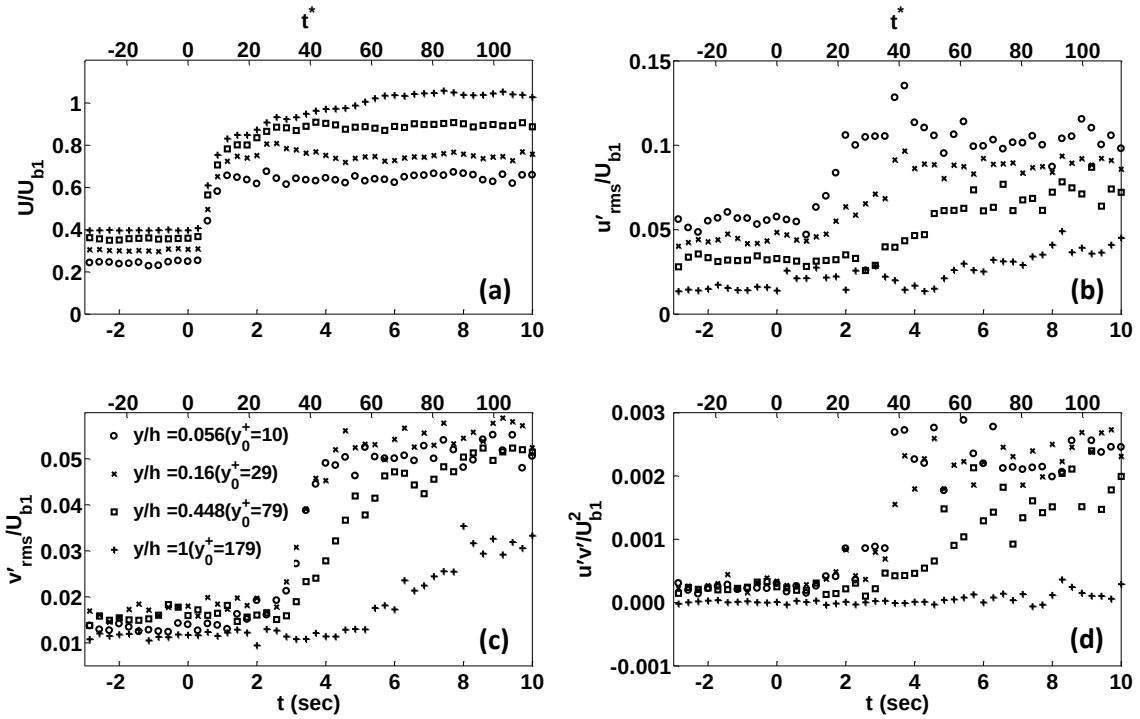

Figure 6.19 Temporal development of mean, fluctuating and Reynolds shear stress components for the case R29-76.

Figure 6.20 shows the temporal development of the mean and turbulent statistics subjected to a sudden opening of the valve for case R23-250. Similar to the previous plots of this kind, data obtained from the LDV measurements over the smooth surface are shown in red and the data obtained from the PIV measurements over the rough surface are shown in black.

It can be seen from the plots that the mechanisms governing the turbulence behaviour in smooth surfaces are still valid in rough flows. It is shown that the production of turbulence is first initiated in the wall region and is later propagated towards the centre. However, the main difference between the two flows is that the delays of the streamwise and wall-normal fluctuating velocities in the rough flows are much shorter than the smooth counterparts. Similar to the smooth flows, the duration of the delays in the response of v'_{rms}/U_{b1} in the wall region (Figure 6.20 (c)) is almost independent from the wall distance. It should be mentioned once more that the sudden response of the streamwise fluctuating velocity in the core region (subplot (j)) is attributed to the finite repeatability of the valve in sudden opening scenarios.

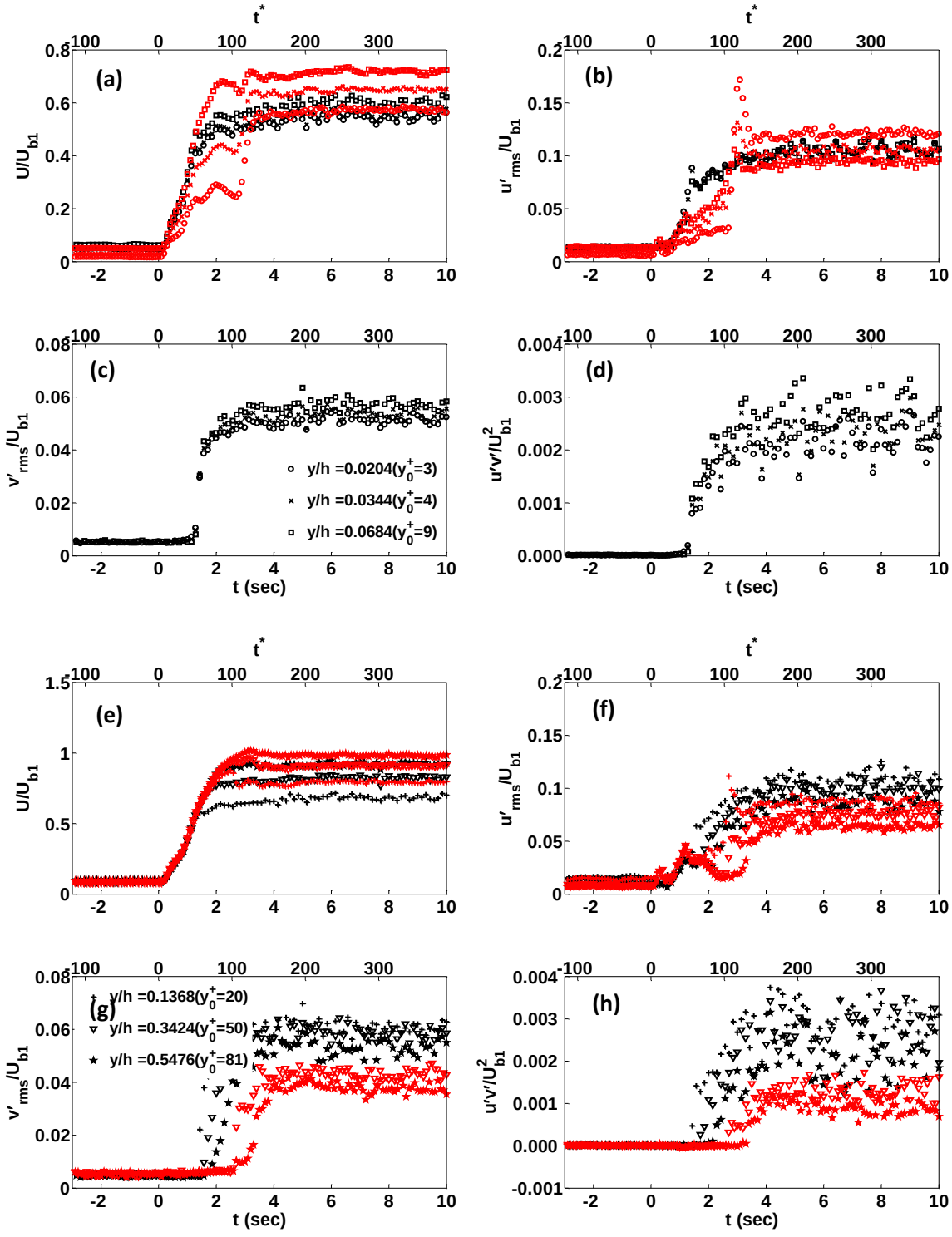

Figure 6.20 continued on next page.

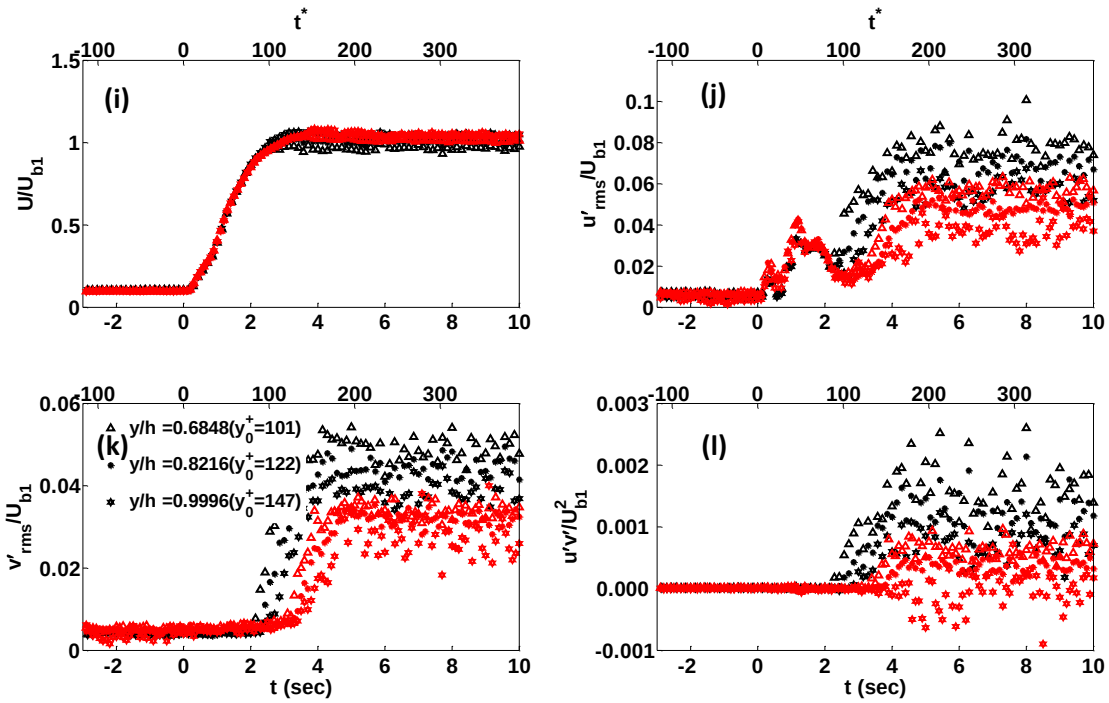

Figure 6.20 Temporal development of mean, fluctuating velocities and Reynolds shear stresses; Red symbols: LDV (S23-250), Black symbols: PIV (R23-250). Note: Every four subplots share a same legend.

Figure 6.21 shows the temporal development of the normalised mean, streamwise and wall-normal fluctuating velocities as well as the Reynolds shear stress at selected locations for R23-250. General features of the flow and turbulence are shown to be similar to those for the corresponding smooth-wall flows. It is mainly the duration of the delays that are significantly reduced for rough-wall flows.

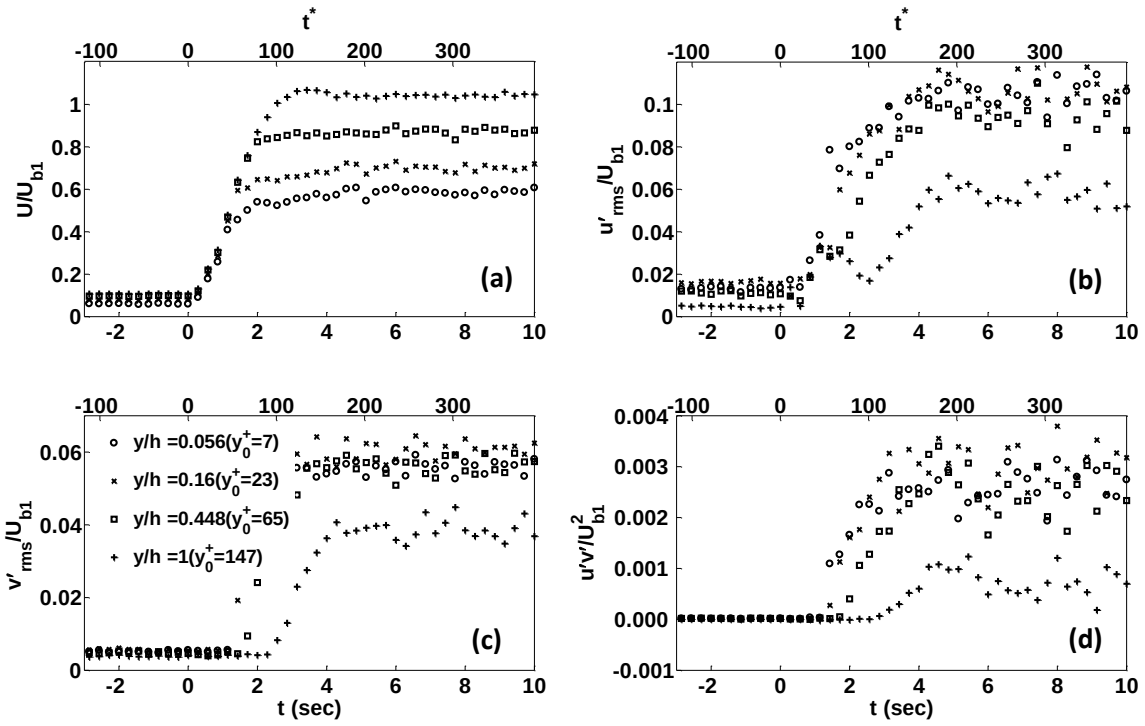

Figure 6.21 Temporal development of mean, fluctuating and Reynolds shear stress components for the case R23-250.

In order to further facilitate the comparisons between the smooth and rough unsteady flows, four sets of plots are provided in Figure 6.22-25 at four selected wall-normal locations. These plots show the response of the wall-normal fluctuating velocity versus time with different normalisation factors. The wall-normal fluctuating velocity is either presented as the increase from its initial value at the start of the excursion $(v'_{rms} - v'_{rms,0})/(v'_{rms,1} - v'_{rms,0})$ (Figure 6.22 and Figure 6.23) or perturbing rms velocity ($\widehat{\overline{v'}}$) (Figure 6.24 and Figure 6.25).

Normalisation of the wall-normal fluctuating velocity with its initial values and t_0^+ is shown in Figure 6.22-23 for smooth and rough walls, respectively. Direct comparison of S29-76 and R29-76, in Figure 6.22 and 6.23, shows no significant alteration in the response timescales. It is noticeable from Figure 6.23 that the trends obtained from the various Reynolds numbers with relatively high acceleration rates collapse very well in the wall region (subplots a and b). Whilst, the difference in the responses of this component becomes wider in the core of the flow (subplots c and d). Among the slow acceleration cases, R29-76 shows similar response behaviour to the S29-76 while the duration of the delays in the R23-93 is shorter than its smooth counterpart.

Figure 6.24 and 6.25 show the development of $\widehat{\overline{v'}}$ versus t^* at four different wall-normal locations for various Reynolds numbers over the smooth and rough surfaces, respectively. It can

be seen from Figure 6.25 (b) that the trends obtained from various Reynolds numbers collapse relatively well with respect to t^* regardless of their acceleration rates. This is contrary to the observations of flows over smooth surfaces that t_0^+ was a more suitable non-dimensional parameter in determining the time of transition. It should however be noted that except the two relatively slower accelerating cases of R23-93 and R29-76, the rest of the rough unsteady cases collapse on each other relatively well with respect to t_0^+ (Figure 6.23 (b)). Onset of transition for the cases examined herein occurs in $20 < t^* < 35$. Statistics obtained from all the cases introduced in Table 6.1 are presented in Appendix B.

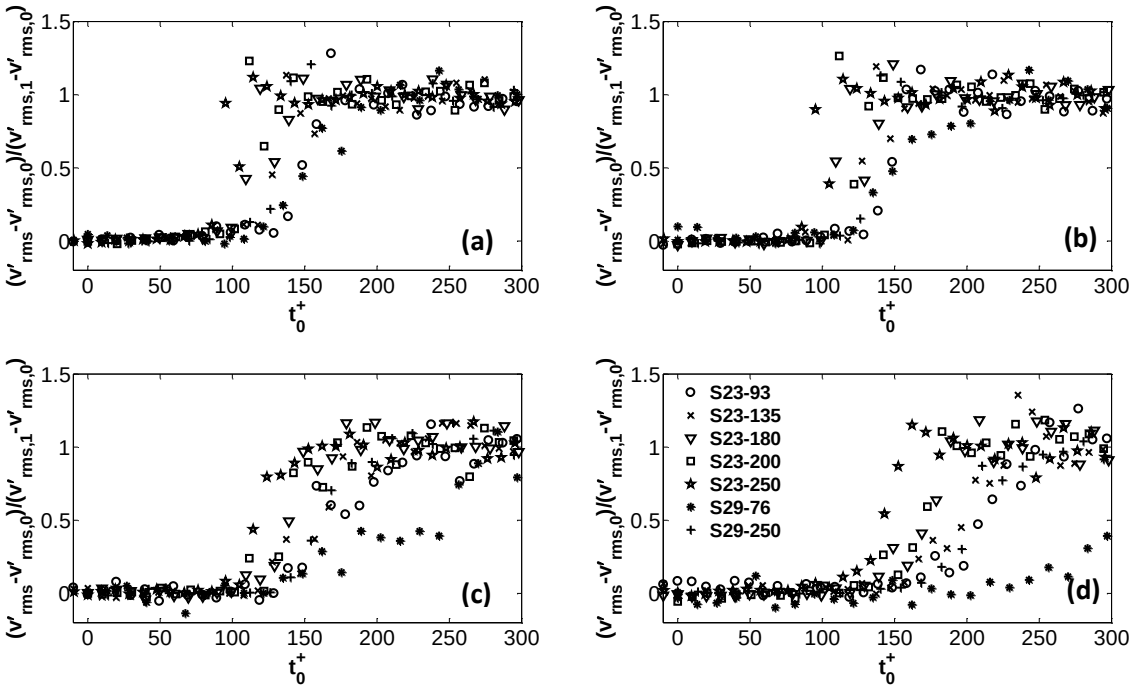

Figure 6.22 Variation of normalised wall-normal fluctuating velocity versus t_0^+at (a) $y/h = 0.07$; (b) $y/h = 0.15$; (c) $y/h = 0.5$; and (d) $y/h = 1$ for smooth flows.

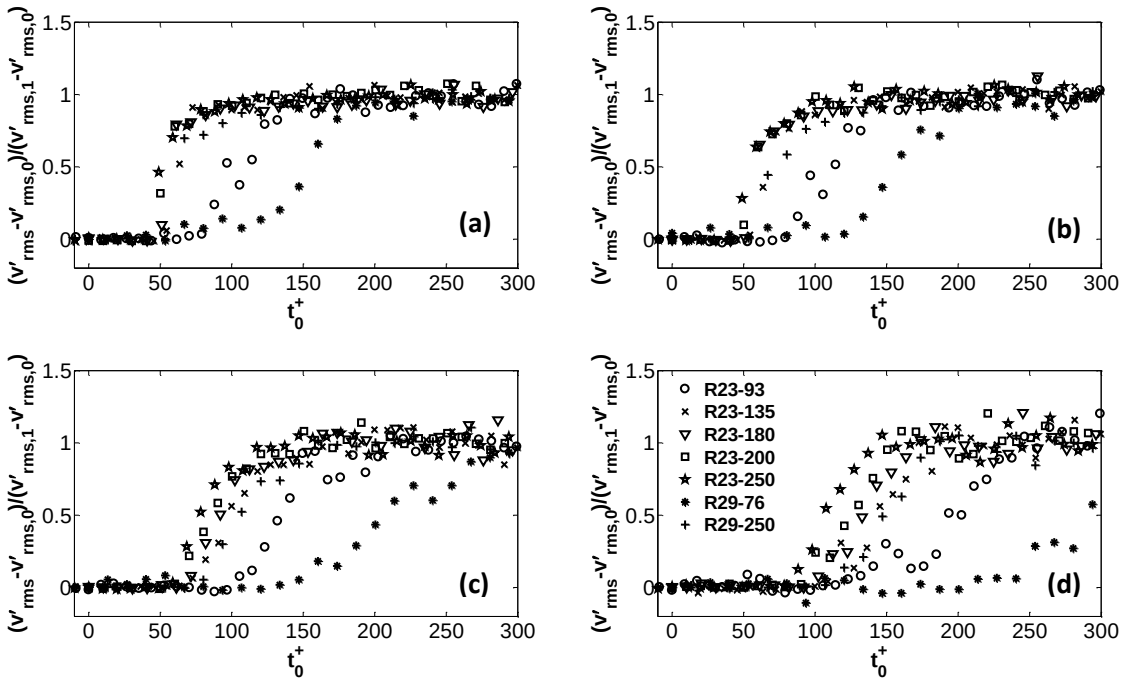

Figure 6.23 Variation of normalised wall-normal fluctuating velocity versus t_0^+at (a) $y/h = 0.07$; (b) $y/h = 0.15$; (c) $y/h = 0.5$; and (d) $y/h = 1$ for rough flows.

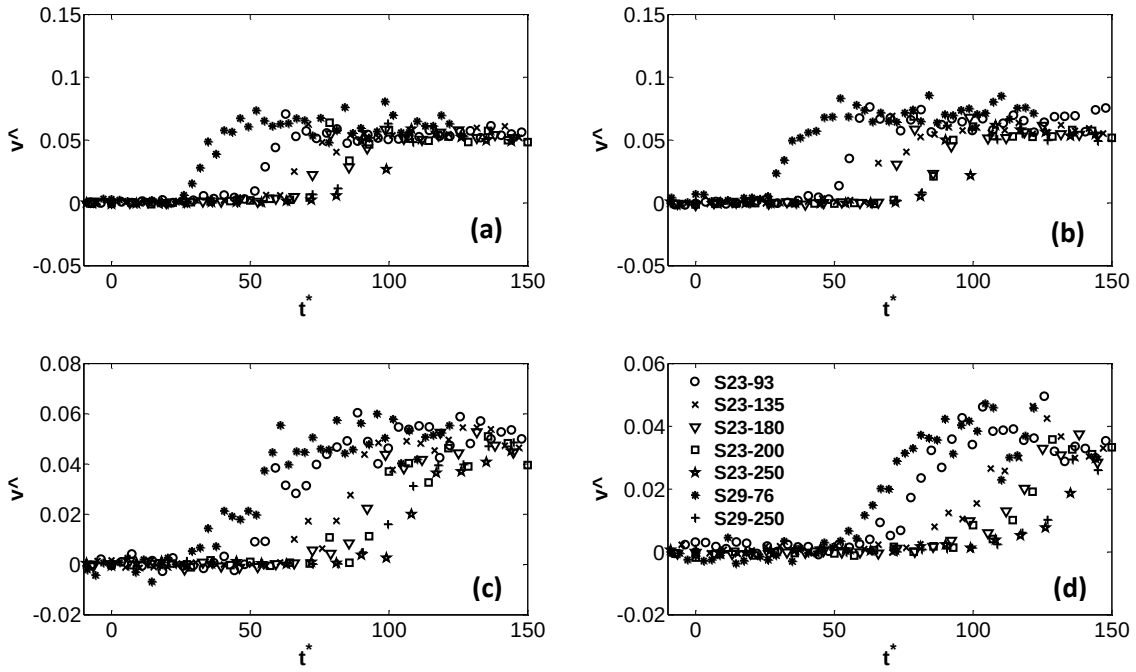

Figure 6.24 Variation of perturbing wall-normal rms velocity versus t^*at (a) $y/h = 0.07$; (b) $y/h = 0.15$; (c) $y/h = 0.5$; and (d) $y/h = 1$ for smooth flows.

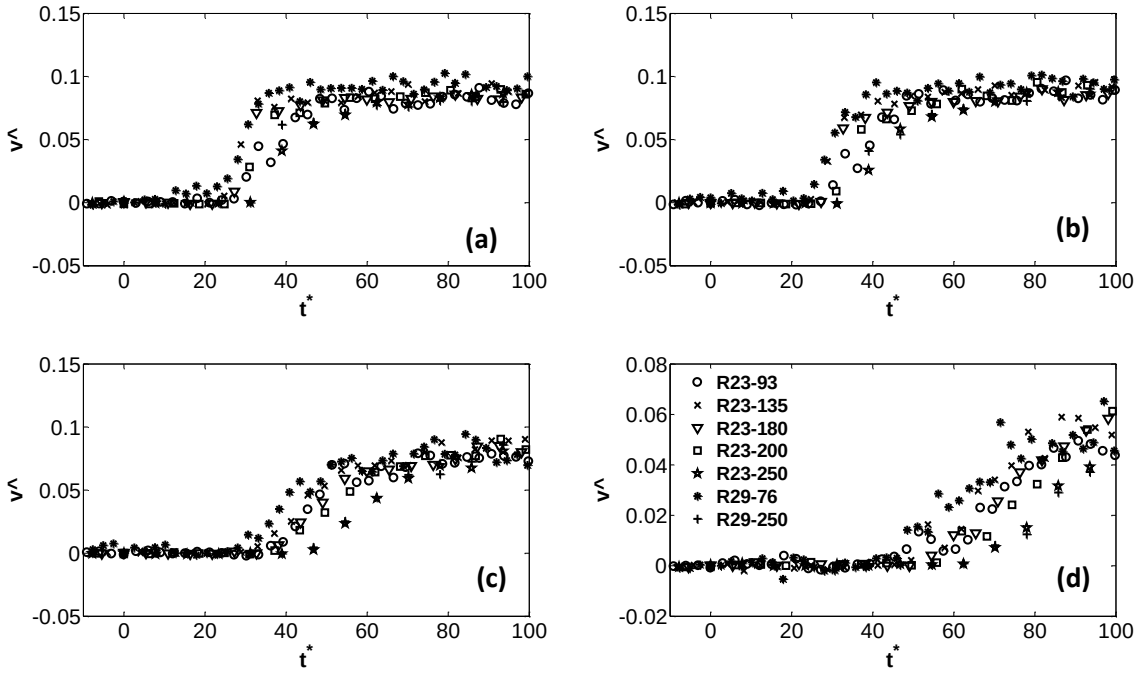

Figure 6.25 Variation of wall-normal rms perturbing velocity versus t^*at (a) $y/h = 0.07$; (b) $y/h = 0.15$; (c) $y/h = 0.5$; and (d) $y/h = 1$ for rough flows.

6.4.4 Correlations of critical Reynolds number in rough flows

This section discusses the effect of the rough surface on the critical transition Reynolds number as introduced by He and Seddighi (2013) and He and Seddighi (2015) for smooth flows. Definitions of the initial free-stream turbulence (Tu_0), critical Reynolds number ($Re_{t,cr}$) and the period of transition ($\Delta Re_{t,cr}$) are the same as for smooth-wall flows, introduced in §5.4.4. These quantities are calculated on the basis of critical and fully turbulent timescales introduced in Table 6.2. It was shown in §4.5 that the initial flow conditions for the unsteady rough-wall flows correspond to the hydrodynamically smooth regime. Therefore, the wall shear stress and consequently the friction velocity can be determined from the equivalent smooth correlations. This specifically becomes useful in the calculation of Tu_0.

Figure 6.26 shows the variation of the critical Reynolds number with the initial free-stream turbulence intensity. Smooth-wall results obtained from the experiments and DNS are also shown for comparison. Similar to unsteady smooth-wall flows and bypass transition, it is shown that a power law correlates the data for the unsteady flows over the rough wall. As Tu_0 decreases, the critical Reynolds number increases at a slower rate in comparison to its corresponding smooth-wall flows. Specifically, when $Tu_0 \sim 4.2 \times 10^{-2}$, the critical Reynolds number is similar in the rough and smooth wall flows. With the decrease of Tu_0, difference

between the critical Reynolds number in the two flows develops, approaching less than half of those obtained from smooth flows for lower Tu_0 values of 0.01.

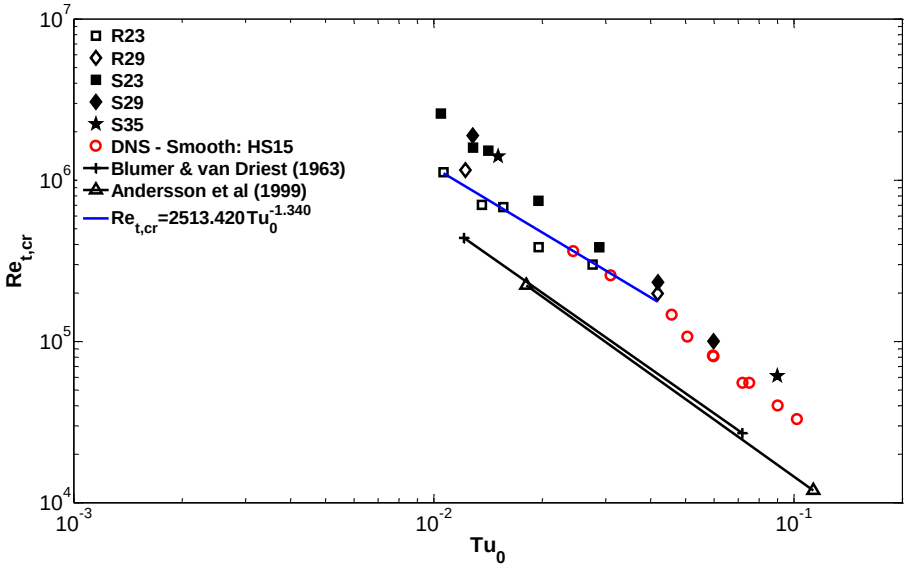

Figure 6.26 Critical Reynolds number as a function of equivalent turbulence intensity for various flow conditions over smooth and rough surfaces.

Figure 6.27 provides a measure between the period of transition and the critical Reynolds number obtained from the smooth and rough unsteady flows as well as the bypass transition correlations. It is evident from the trends that the period of the transition for a similar range of bulk Reynolds number is significantly decreased due to the effects of roughness. Best-fit curves are also shown in the figure, providing a linear relationship between the critical Reynolds number and the period of transition.

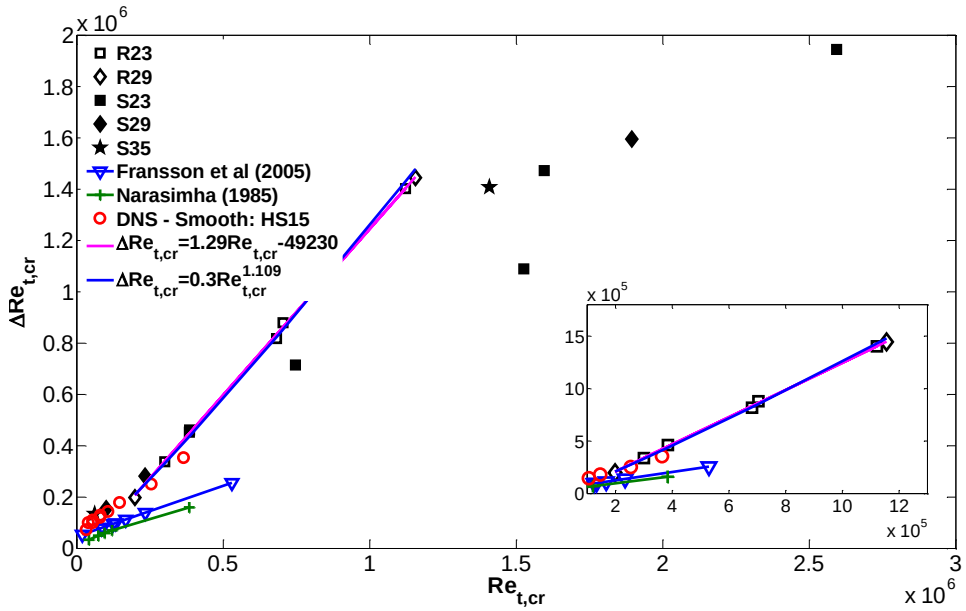

Figure 6.27 Period of transition as a function of the critical Reynolds number and duration for various flow conditions over smooth and rough surfaces.

6.5 Summary

A range of unsteady flows with mainly constant initial Reynolds number and a different higher final Reynolds number were investigated in an asymmetric channel with roughness at the bottom. PIV is used to measure the mean and turbulence quantities at different planes of motion. Vertical laser sheet measurements provided the statistics in the wall-normal direction for a wider range of cases. The horizontal laser sheet configuration was used to measure the flow properties in the spanwise and streamwise directions at a height of $y{\sim}0.03h$ (i.e. $y{\sim}0.8k$) for three of the flow excursion scenarios.

It was shown in §6.3 that the instantaneous fluctuating flow field under rough conditions is similar to smooth flows in terms of the transition behaviour. At the same time quantitative differences can be seen between the two bed types. It was shown that the streamwise fluctuating velocity undergoes a pre-transition phase similar to unsteady smooth flows with high and low amplitude juxtaposed streaks. These streaks are stretched in the streamwise and narrowed in the spanwise direction, resembling the Klebanoff modes present in the bypass transition due to free-stream turbulence. The first sign of secondary instability appears at a critical time, marking the start of transition. Similar to smooth-wall flows, the response of the wall-normal Reynolds stress component can accurately measure the start of transition. It was shown that the behaviour of streaky structures throughout the excursion are qualitatively similar to smooth flows. During the pre-transition phase the spacing of the streaks are almost

constant, with slight reduction after the commencement of the flow excursion. At the same time the quantitative behaviour of the streaks is highly sensitive to Reynolds number. For instance, the S29-76 and R29-76 behaviours are very similar as the roughness interaction with the flow can be considered insignificant. On the other hand, the transition is enhanced in accelerating flows encompassing larger Reynolds numbers, resulting in a diminished pre-transition period.

Evolving temporal boundary layer represented by the perturbing velocity profiles collapses on the Stokes solution during the pre-transition regime, providing similarities during and after the pre-transition for the unsteady cases examined herein. It should however be noted that the development rate of this temporal boundary layer depends on the initial and final Reynolds numbers. For instance, the pre-transition period is longer in the R23-93 and R29-76, while this range is relatively lower at around $t_0^+ \sim 50$ for the other cases. The perturbing rms velocities collapse reasonably well during the pre-transition phase, while the wall-normal component can specifically mark the critical time of transition. The development of the perturbing streamwise fluctuating velocity during the pre-transition regime reflects the dynamics of the streaky structures in the wall region while the wall-normal component remains unchanged.

The overall picture depicted from the instantaneous fluctuating velocities can be confirmed from the statistics. The rough-wall measurements performed herein confirm the previous findings of He and Jackson (2000) on the mechanisms of turbulence production, redistribution and radial propagation in unsteady turbulent flows. The geometrical properties of the roughness implemented in the present investigations, however, results in relatively shorter delays of streamwise, wall-normal and consequently shear stresses across the channel. As mentioned earlier, the critical time can be obtained from the response of the wall-normal fluctuating velocity v'_{rms}. The critical non-dimensional inner scaled time (t_0^+) is shown to be ~ 50 for all cases investigated, except for the relatively lower Re flows of R29-76 and R23-93. Whilst the scatter between the normalised critical time for similar cases over smooth surfaces is much wider and more sensitive to the levels of Tu_0. On the other hand, the critical time normalised with the outer-scaling parameters (t^*) appears to collapse the responses of various accelerating flows in the wall region, regardless of the Tu_0 levels.

Similar to smooth flows, the critical Reynolds number is shown to have a power-law dependence on Tu_0, with a reduced critical Reynolds number for small initial turbulence intensity levels. The period of transition ($\Delta Re_{t,cr}$) was shown to be significantly reduced due to the roughness. A linear relationship was shown to exist between the period of transition and the critical Reynolds number.

Chapter 7. Numerical simulation of channel flows over smooth surfaces

Note: This chapter is published in the Computers & Fluids, 2014, 89(0): 111-123.

7.1 Introduction

The present chapter reports a systematic assessment of the performance of a wide range of low-Reynolds number turbulence models used to predict the flow characteristics of ramp-up-type unsteady flows in a channel. Recent DNS results are used as benchmark data for the assessment. The DNS data used for the validation purposes are previously published in He and Seddighi (2013) and Seddighi et al. (2014).

7.2 Methodology

The study reported here involves the assessment of ten different turbulence models applied to three accelerating flow test cases. FLUENT 13.0 is used as the RANS solver for the numerical investigations.

The flow domain consists of a rectangular channel section with smooth wall boundaries and the working fluid is water ($\rho = 1000\ kg/m^3$, $\nu = 1 \times 10^{-6}\ m^2/s$). The channel is 8 metres long and 0.05 metres high, giving a length to height ratio of L/H=160 as shown in Figure 7.1. Because of symmetry, the computational domain covers half of the channel height. In this study, only spatially fully developed flow is of interest; hence, the results presented are taken at 7.5 metres from the inlet (L/H=150, AB line in Figure 7.1). Systematic mesh sensitivity tests were carried out

for each group of turbulence models to obtain mesh-independent solutions. These tests were conducted by distributing 70, 100 and 180 control volumes in the wall normal direction (*y* direction, shown in Figure 7.1). It was concluded that distributing 100 control volumes non-uniformly along the wall normal direction is adequate to achieve mesh independent solutions. The number of control volumes used in the axial direction (*x* direction, shown in Figure 7.1) is 30 but this is of no significance since only axially developed flow is of interest. This also means that the level of turbulence intensity at the inlet is of no relevance as long as it is set to a sufficiently high level to initiate turbulence in the channel. In this work, it is set to be 5% in all simulations. The non-dimensional distance of the first node from the wall is maintained within the range of y^+= 0.3 – 0.9 ($y^+ = yu_\tau/\nu$, u_τ representing friction velocity) during the excursion to ensure the low-Reynolds criterion for the models is satisfied.

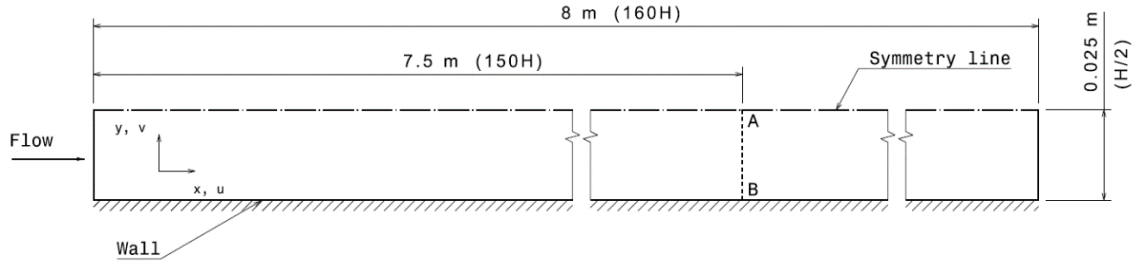

Figure 7.1 Sketch of the channel geometry.

In all test cases the flow rate is increased linearly from an initial steady state Reynolds number ($Re_0 = U_{b0}D_h/\nu$, U_{b0} representing the bulk velocity) of 9,308 to a final Reynolds number (Re_1) of 29,650. The length scale of the Reynolds number is based on the hydraulic diameter, i.e. $D_h = 2H$, where *H* is the full height of the channel. We consider three acceleration time periods (Δt): Case A, 8.16 seconds ("low" acceleration); Case B, 2.86 seconds ("intermediate" acceleration); Case C, 0.02 seconds ("high" acceleration). Table 7.1 summarises the initial and final flow conditions of the examined flow cases along with non-dimensional time scale ($\Delta t^* = \Delta t/(H/2)/U_{b1}$) and ramp rate ($dU/dt = (U_{b1} - U_{b0})/\Delta t$). Although these simulations are carried out for water, as long as the boundary conditions such as the initial and final Reynolds numbers and non-dimensional acceleration rate are consistent, the choice of fluid is of no significance to the outcome of the simulations.

Flow Case	Re_0	Re_1	Δt^*	$\Delta t\ (sec)$	$dU/dt\ (m/s^2)$
A	9,308	29,650	96.8	8.16	0.025
B	9,308	29,650	33.9	2.86	0.071
C	9,308	29,650	0.2	0.02	10.17

Note $\Delta t^* = \frac{\Delta t}{(H/2)/U_{b1}}$ $\frac{dU}{dt} = \frac{U_{b1}-U_{b0}}{\Delta t}$

Table 7.1 Test cases and flow conditions.

The continuity and momentum transport equations along with the Reynolds stress closure equations are solved for the computational domain. The flow is assumed to be two-dimensional and Cartesian coordinates are employed for the governing equations.

Continuity:

$$\frac{\partial U_i}{\partial x_i} = 0 \tag{7.1}$$

Momentum:

$$\frac{DU_i}{Dt} = -\frac{1}{\rho}\frac{\partial P}{\partial x_i} + \frac{\partial}{\partial x_j}\left(\nu\frac{\partial U_i}{\partial x_j} - \overline{u_i u_j}\right) \tag{7.2}$$

where linear eddy viscosity models employ a stress-strain relation as follows:

$$\overline{u_i u_j} = 2/3\, k\delta_{ij} - \nu_t\left(\frac{\partial U_i}{\partial x_j} + \frac{\partial U_j}{\partial x_i}\right) \tag{7.3}$$

where ν_t, the eddy viscosity, is obtained by solving a set of turbulence transport equations, the details of which are presented in the next sections.

Only low-Reynolds number turbulence models can potentially predict the features of unsteady flows. Here we consider ten low-Reynolds turbulence models, which can be categorised into four groups: $k-\varepsilon$ models, $k-\omega$ based models, the v^2-f model of Durbin (1995) and the $\gamma - Re_\theta$ transition model of Langtry and Menter (2009).

7.2.1 $k-\varepsilon$ models

Low-Reynolds number $k-\varepsilon$ turbulence models are based on solving transport equations for turbulent kinetic energy and its dissipation rate, as follow:

$$\frac{Dk}{Dt} = \frac{\partial}{\partial x_j}\left[\left(\nu + \frac{\nu_t}{\sigma_k}\right)\frac{\partial k}{\partial x_j}\right] + P_k - \tilde{\varepsilon} - D \tag{7.4}$$

$$\frac{D\tilde{\varepsilon}}{Dt} = \frac{\partial}{\partial x_j}\left[\left(\nu + \frac{\nu_t}{\sigma_\varepsilon}\right)\frac{\partial \tilde{\varepsilon}}{\partial x_j}\right] + C_{\varepsilon 1} f_1 \frac{1}{T_t} P_k - C_{\varepsilon 2} f_2 \frac{\tilde{\varepsilon}}{T_t} + E \tag{7.5}$$

where P_k is the production of turbulent kinetic energy given by

$$P_k = -\overline{u_i u_j}\frac{\partial U_i}{\partial x_j} \tag{7.6}$$

The eddy viscosity in $k-\varepsilon$ models is defined to be $\nu_t = C_\mu f_\mu k^2/\varepsilon$, C_μ being a constant and f_μ being the damping function. T_t in equation (7.5) is a turbulent time scale, $\tilde{\varepsilon}$ is the modified isotropic dissipation rate, *D* and *E* are near wall correction functions for k and ε equations, respectively.

The six $k-\varepsilon$ turbulence models examined in this study are designated as AB for Abid (1993), LB for Lam and Bremhorst (1981), LS for Launder and Sharma (1974), YS for Yang and Shih (1993), AKN for Abe et al. (1995) and CHC for Chang et al. (1995). Note that the performance of FLUENT's built-in LS model is found to be unexpectedly poor and therefore a User Defined Function (UDF) for LS developed by Mathur and He (2013) was also implemented. The FLUENT built-in implementation of LS is designated LS-FLUENT and the UDF implementations is designated LS-UDF in what follows.

A summary of the model constants, damping functions and near-wall correction functions are presented in Table 7.2-7.4.

Model	C_μ	$C_{\varepsilon 1}$	$C_{\varepsilon 2}$	σ_k	σ_ε
AB	0.09	1.45	1.83	1.0	1.4
LB	0.09	1.44	1.92	1.0	1.3
LS	0.09	1.44	1.92	1.0	1.3
YS	0.09	1.44	1.92	1.0	1.3
AKN	0.09	1.5	1.90	1.4	1.4
CHC	0.09	1.44	1.92	1.0	1.3

Table 7.2. Constants for the turbulence models.

Model	f_μ	f_1	f_2
AB	$\tanh(0.008Re_k) \times (1+\frac{4}{Re_t^{3/4}})$	1.0	$1-2/9\exp\left(-\frac{Re_t^2}{36}\right) \times (1-\exp(-\frac{Re_k}{12}))$
LB	$\left(1-\exp(-0.0165Re_y)\right)^2 \times\left(1+\frac{20.5}{Re_t}\right)$	1.0	$1-\exp(-Re_t^2)$
LS	$\exp\left(\frac{-3.4}{(1+Re_t/50)^2}\right)$	1.0	$1-0.3\exp(-Re_t^2)$
YS	$\left(1+1/\sqrt{Re_t}\right) \times\left[1-\exp\begin{pmatrix}-1.5\times10^{-4}Re_y\\-5.0\times10^{-7}Re_y^3\\-1.0\times10^{-10}Re_y^5\end{pmatrix}\right]^{0.5}$	$\frac{\sqrt{Re_t}}{1+\sqrt{Re_t}}$	$\frac{\sqrt{Re_t}}{1+\sqrt{Re_t}}$
AKN	$\left[1+\frac{5}{Re_t^{0.75}}\exp\left(-\left(\frac{Re_t}{200}\right)^2\right)\right] \times\left(1-\exp\left(-\frac{y^*}{14}\right)\right)^2$	1.0	$\left\{1-0.3\exp\left(-\left(\frac{Re_t}{6.5}\right)^2\right)\right\} \times\left(1-\exp\left(-\frac{y^*}{3.1}\right)\right)^2$
CHC	$\left[1-\exp(-0.0215Re_y)\right]^2 \times\left(1+\frac{31.66}{Re_t^{5/4}}\right)$	1.0	$[1-0.01\exp(-Re_t^2)] \times\left[1-\exp(-0.0631Re_y)\right]$

Table 7.3. Functions in the turbulence models.

Model	D	E	Wall BC
AB	0	0	$\varepsilon_w = \nu\left(\frac{\partial^2 k}{\partial y^2}\right)$
LB	0	0	$\varepsilon_w = \nu\left(\frac{\partial^2 k}{\partial y^2}\right)$
LS	$2\nu\left(\frac{\partial\sqrt{k}}{\partial y}\right)^2$	$2\nu\nu_t\left(\frac{\partial^2 U}{\partial y^2}\right)^2$	$\tilde{\varepsilon}_w = 0$
YS	0	$\nu\nu_t\left(\frac{\partial^2 U}{\partial y^2}\right)^2$	$\varepsilon_w = \nu\left(\frac{\partial^2 k}{\partial y^2}\right)$
AKN	0	0	$\varepsilon_w = \nu\left(\frac{\partial\sqrt{k}}{\partial y}\right)^2$
CHC	0	0	$\varepsilon_w = \nu\left(\frac{\partial^2 k}{\partial y^2}\right)$

Note $Re_t = \frac{k^2}{\nu\varepsilon}$ $Re_y = \frac{yk^{1/2}}{\nu}$ $y^* = \frac{yu_\varepsilon}{\nu}$ $u_\varepsilon = (\nu\varepsilon)^{0.25}$

Table 7.4. D and E terms along with the boundary conditions.

7.2.2 $k-\omega$ and shear stress transport (SST) $k-\omega$ models

FLUENT 13.0 employs the low-Reynolds number $k-\omega$ model of Wilcox (1994), which solves two transport equations, one for turbulent kinetic energy (same as for the $k-\varepsilon$ models) and one for its specific dissipation rate ($\omega \propto \varepsilon/k$). Further details of this model can be found in Wilcox (1994).

The $k-\omega$ Shear Stress Transport (SST) model developed by Menter (1994) employs a blending function, which retains the near-wall ω equation while switching to ε equivalent further from the wall. Further details of the model can be found in Menter (1994).

7.2.3 v^2-f model

Anisotropy of the turbulence stresses is not addressed in linear eddy viscosity turbulence models. Durbin (1991) replaced the *ad hoc* damping functions of the $k-\varepsilon$ models by introducing the wall-normal stress $\overline{vv}$ as the velocity scale in the eddy viscosity formulation. An elliptic relaxation function is also solved to model the redistribution process of wall-normal stress transport equation. However, due to difficulties of implementation of the original formulation, major commercial codes tend to use more numerically stable formulations. The

$v^2 - f$ version coded in FLUENT, which is examined in this study, is the due to Iaccarino (2001) but with default constants of those proposed by Lien and Kalitzin (2001).

7.2.4 $\gamma - Re_\theta$ transition model of Langtry and Menter (2009)

The performance of a correlation based transition turbulence model of $\gamma - Re_\theta$ Langtry and Menter (2009) available in FLUENT 13.0 is also considered. The model incorporates two extra transport equations into the SST model, one for the intermittency γ and the other for the transition onset momentum-thickness Reynolds number $\widetilde{Re}_{\theta t}$. Turbulent kinetic energy and its specific dissipation rate transport equations of the SST model are customised to include the additional transport equations.

The following are the transport equations for intermittency and momentum-thickness Reynolds number:

$$\frac{\partial \rho\gamma}{\partial t} + \frac{\partial \rho U_j \gamma}{\partial x_j} = P_\gamma - E_\gamma + \frac{\partial}{\partial x_j}\left[\left(\mu + \frac{\mu_t}{\sigma_f}\right)\frac{\partial \gamma}{\partial x_j}\right] \tag{7.7}$$

$$\frac{\partial \rho\widetilde{Re}_{\theta t}}{\partial t} + \frac{\partial \rho U_j \widetilde{Re}_{\theta t}}{\partial x_j} = P_{\theta t} + \frac{\partial}{\partial x_j}\left[\sigma_{\theta t}(\mu + \mu_t)\frac{\partial \widetilde{Re}_{\theta t}}{\partial x_j}\right] \tag{7.8}$$

where P_γ and E_γ are the production and dissipation terms of the intermittency transport equation, respectively. $P_{\theta t}$ is the production term of momentum-thickness in the Reynolds number transport equation. σ_f and $\sigma_{\theta t}$ are the constants of intermittency and momentum-thickness Reynolds number transport equations, respectively.

Intermittency is a measure of the regime of the flow. For instance, in a growing boundary layer over a flat plate, intermittency is zero before the transition onset and reaches a value of one when the flow is fully turbulent. In order to determine the condition of a developing boundary layer, correlations exist between the location of the transition onset and the free-stream turbulence intensity, pressure gradient and transition momentum-thickness Reynolds number (e.g. Abu-Ghannam and Shaw (1980) and Mayle (1991)). Both algebraic and transport equations have been developed by researchers to determine the intermittency factor. Langtry and Menter (2009) couples the transport equations for intermittency and transition onset momentum-thickness Reynolds number to Menter (1994) SST model. The production term in the turbulent kinetic energy transport equation is modified to account for the changes in the intermittency of the flow.

The transition onset momentum-thickness Reynolds number is mainly responsible for capturing the nonlocal effects of turbulence intensity and pressure gradient outside the boundary layer. Further details regarding the formulation of the model and its performance in different test cases can be found in Langtry and Menter (2009).

7.3 Comparisons for steady flow

DNS results for two steady flow scenarios, corresponding to the initial and final Reynolds numbers ($Re_0 = 9{,}308$ and $Re_1 = 29{,}650$) of the unsteady flow cases to be discussed in the next section, are used to assess the performance of the ten different low-Reynolds number turbulence models applied to two-dimensional, fully developed, steady channel flow.

Figure 7.2 shows the predications of the mean axial velocity, turbulent kinetic energy, turbulent shear stress and turbulent viscosity with the DNS results for the initial and final Reynolds number flows. Bulk velocity (U_b) which represents the ratio of flow rate to cross sectional area and kinematic viscosity (ν) are used to normalise the mean and turbulence quantities.

All turbulence models with the exception of LS-FLUENT give an acceptable prediction of the axial velocity profile across the channel. However, the performance of the various models is rather different for the predictions of turbulent kinetic energy, turbulent shear stress and turbulent viscosity.

Most models are successful in predicting the location of the peak of turbulent kinetic energy for both steady flow cases. The predictions of the turbulent kinetic energy of LB, $v^2 - f$ and $k - \omega$ are the closest to DNS in the wall region, whereas the kinetic energy predictions of AB, AKN, CHC, LS-UDF and $\gamma - Re_\theta$ match better the DNS data in the core region. The last three models significantly under-predict the peak of turbulent kinetic energy for both flows even though they show superior performance in predicting the unsteady flows (as discussed in §7.4).

The turbulent shear stress is well predicted by AKN, LB, YS and $\gamma - Re_\theta$. This contrasts with AB, CHC, LS-UDF and $v^2 - f$, which slightly under-predict, and LS-FLUENT, which significantly over-predicts the shear stress. The turbulent viscosity predictions of most of the $k - \varepsilon$ models are quite good in the wall region, with AKN, LB, YS and $k - \omega$ being the closest to DNS. In the core region, however, all models except AKN and $k - \omega$ predict a monotonic increase of eddy viscosity that is contrary to the DNS data. The over-prediction of eddy viscosity in this region is a known shortfall of many $k - \varepsilon$ models that results from the under-prediction of dissipation ((Billard and Laurence, 2012)). Myong and Kasagi (1990) argue that in most $k - \varepsilon$ models the chosen value of σ_k is too low in comparison to σ_ε and they therefore suggest using higher $\sigma_k/\sigma_\varepsilon$

ratios. In the absence of turbulent energy production in the core region, this ratio balances the diffusion and dissipation terms in the turbulent kinetic energy and its dissipation rate transport equations. Among the $k-\varepsilon$ models investigated, AKN utilises the highest $\sigma_k/\sigma_\varepsilon$ ratio improving its eddy viscosity predictions in the core region.

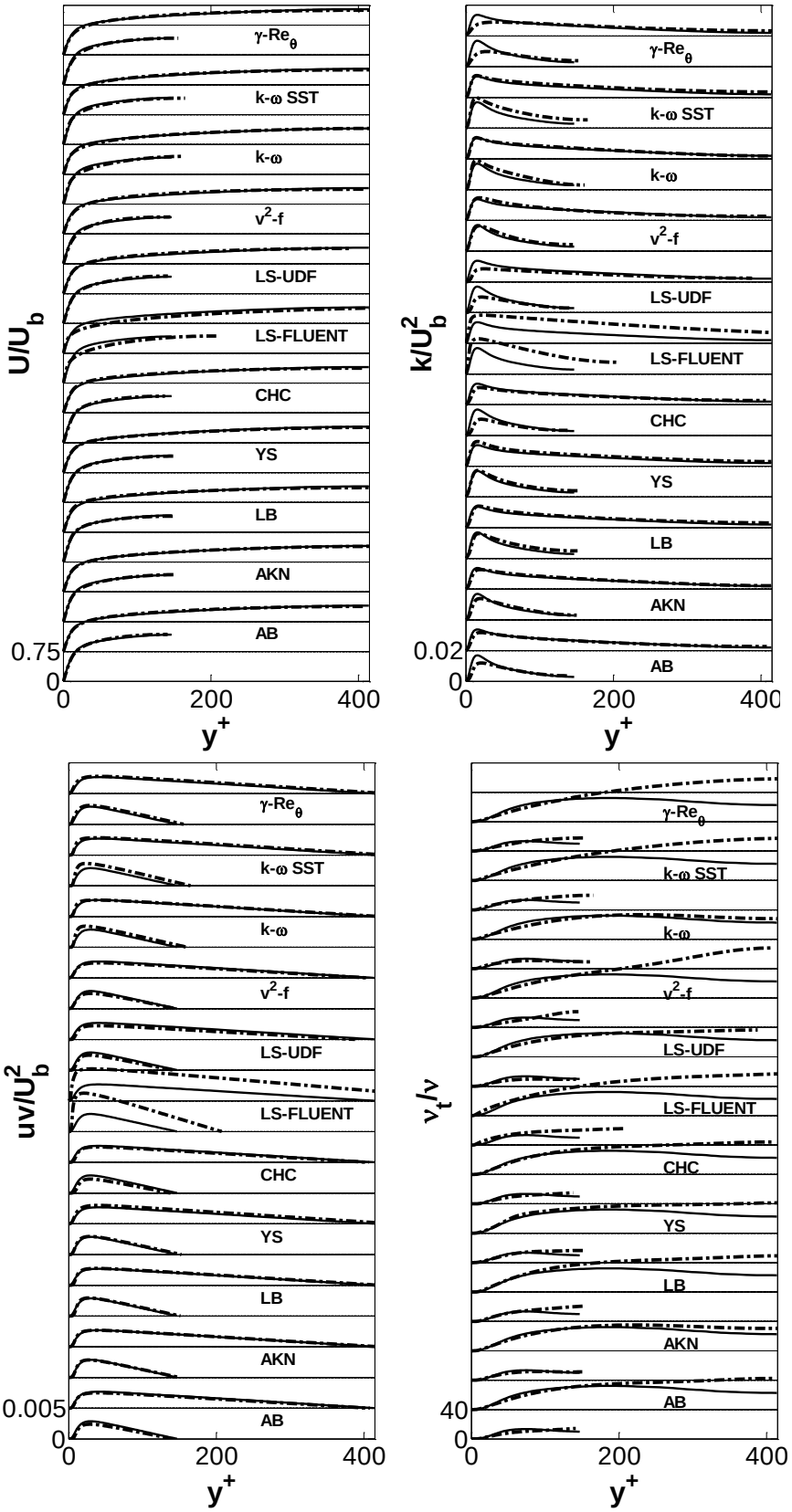

Figure 7.2. Steady flows with $Re_0 = 9{,}308$ (short curves) and $Re_1 = 29{,}650$ (longer curves): comparisons of predicted flow properties from various turbulence models (dashed line) with DNS data (solid line).

It should be noted that in the framework of eddy viscosity models the only connection between the turbulence model and the mean flow field is through the turbulent shear stress $\overline{uv}$, which is mostly dependent on the eddy viscosity. It can be seen that $\overline{uv}$ is well predicted by all models (excluding LS-FLUENT) for both the high and the low Reynolds number flows. This is true despite the turbulent viscosity being not well predicted in the core region by some models. In fact, the most important part of the flow is the wall region, where the turbulent viscosity is predicted fairly well by most of the models. In the core region, the role of turbulent viscosity is not of major importance to the performance of the models.

Results obtained for the higher Reynolds number flow are generally more reliable (i.e. agree better with the DNS results) than those for the lower Reynolds number flow. We note that turbulence models are often tuned for relatively high Reynolds number flows, and applying such models to relatively low Reynolds number flows can result in poor performance.

Figure 7.3 presents the wall shear stress predicted by the various turbulence models, together with the DNS results. Among the turbulence models considered, AKN, LB and $k-\omega$ are seen to yield the most accurate predictions of wall shear stress for both the lower and higher Reynolds number flows.

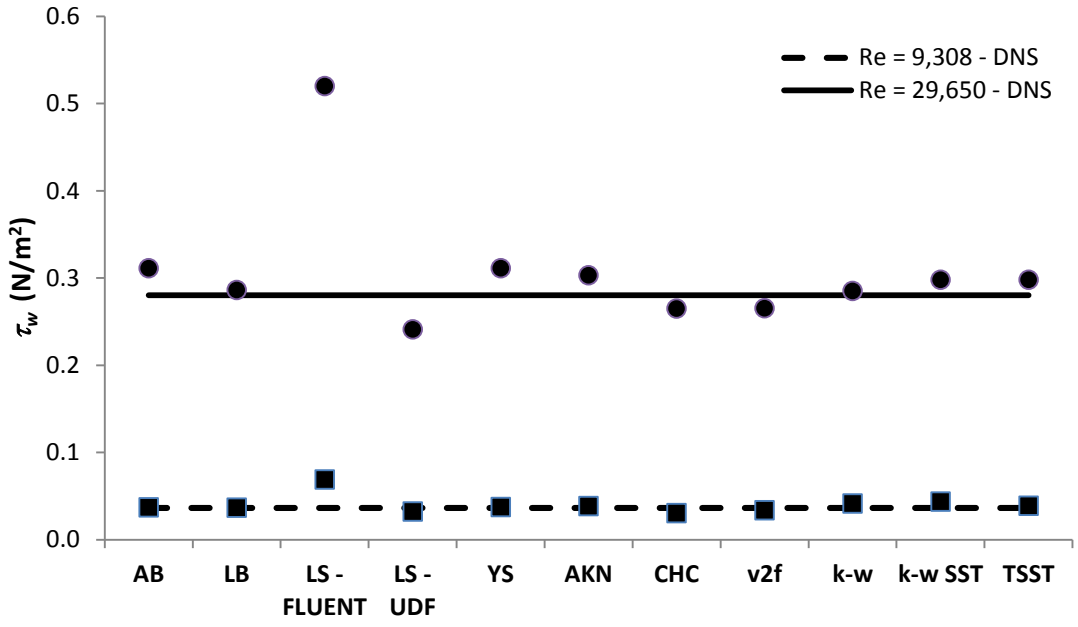

Figure 7.3. Predictions of steady flow wall shear stress for two Reynolds numbers by the various turbulence models (symbols) and by DNS (lines).

In contrast to the LS-FLUENT, LS-UDF performs well overall, leading to our conclusion that the poor performance of the FLUENT built-in LS model is due to its implementation within FLUENT,

not due to any inherent fault with the model itself. The results obtained from LS-FLUENT are not further presented or discussed in the remainder of this chapter.

7.4 Comparisons for unsteady flow

7.4.1 Key features of unsteady flow from DNS

The main features of the unsteady flows as predicted by DNS are first summarised in this section in order to facilitate the assessment of the performance of the turbulence models in the next section. The discussion largely follows that of He and Jackson (2000), He et al. (2011) and (He and Seddighi, 2013), where more detailed discussion can be found.

Figure 7.4 shows the DNS-predicted time histories of wall shear stress, turbulent viscosity, turbulent shear stress and turbulent kinetic energy for the three unsteady flow cases. Considering first the wall shear stress evolution for Case A (Figure 7.4 (a)), we can identify a three-stage development in the wall shear stress and turbulence. Stage 1 is initially dominated by large inertial effects, causing the wall shear stress to overshoot the corresponding quasi-steady values. However, due to the delayed turbulence response, the growth rate of wall shear stress decreases during the final moments of stage 1. Stage 2 corresponds to the time period when the generation of new turbulence causes the unsteady wall shear stresses to increase rapidly towards the corresponding quasi-steady values. During stage 3, the bulk flow is no longer accelerating and the wall shear stress gets gradually closer to the quasi-steady flow shear stress.

The flow acceleration is higher in Case B (Figure 7.4 (b)), and Re_1 is reached while flow response is still in stage 1 (a). As a result of the sudden removal of the acceleration, a strong but negative inertial effect is imposed on the flow, which results in a sharp decrease in the wall shear stress (stage 1 (b)). Afterwards, the trend is reversed when turbulence production starts to increase the wall shear stress, which eventually reaches the quasi-steady values. Increasing the acceleration even further (Case C, Figure 7.4 (c)) causes overshooting of the unsteady wall shear stress over the quasi-steady wall shear stress to occur in an instant (stage 1 (a), not shown on the figure), because of the very sudden change in flow rate. This is then followed by a sharp reduction (stage 1 (b)). During stage 2, the wall shear stress rapidly increases again as a result of turbulence production. The wall shear stress approaches the corresponding quasi steady values in stage 3.

The DNS-predicted time-histories of turbulent viscosity at selected y_0^+ locations (where $y_0^+ = yu_{\tau 0}/\nu$, $u_{\tau 0}$ representing friction velocity at Re_0) are also shown in Figure 7.4. It can be seen from the Figure 7.4 that turbulent viscosity close to the wall ($y_0^+ = 5$) remains more or less

unchanged during stage 1, but begins to increase rapidly at approximately 5, 4 and 2 seconds for cases A, B and C respectively, corresponding to the onset of stage 2. It can also be seen that the delays of turbulent viscosity are roughly constant across the channel for all three flow cases. However, the response of the turbulent viscosity to the imposed excursion in the wall region is of greater importance for modelling purposes as discussed in §7.4.2.

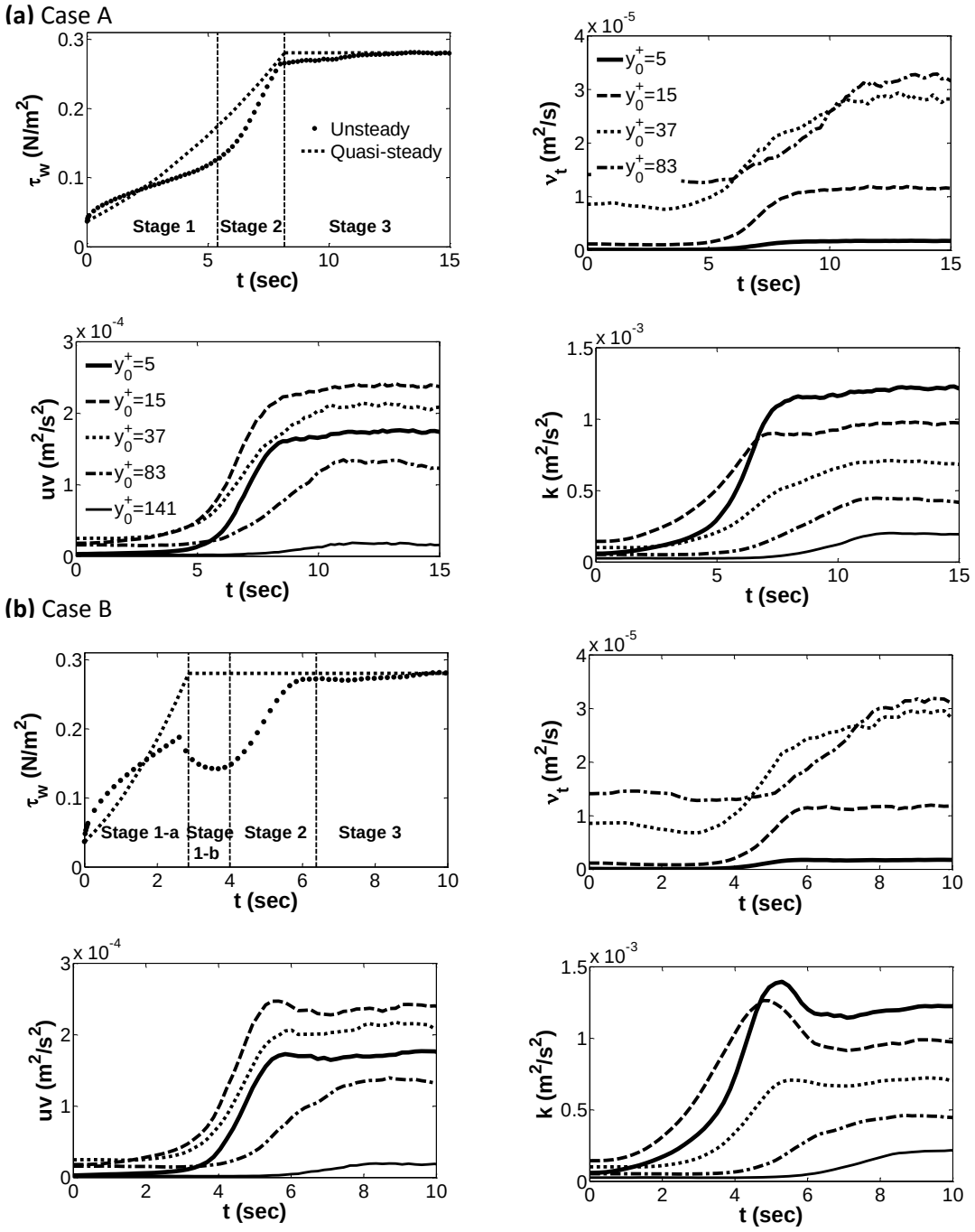

Figure 7.4 continued on next page.

(c) Case C

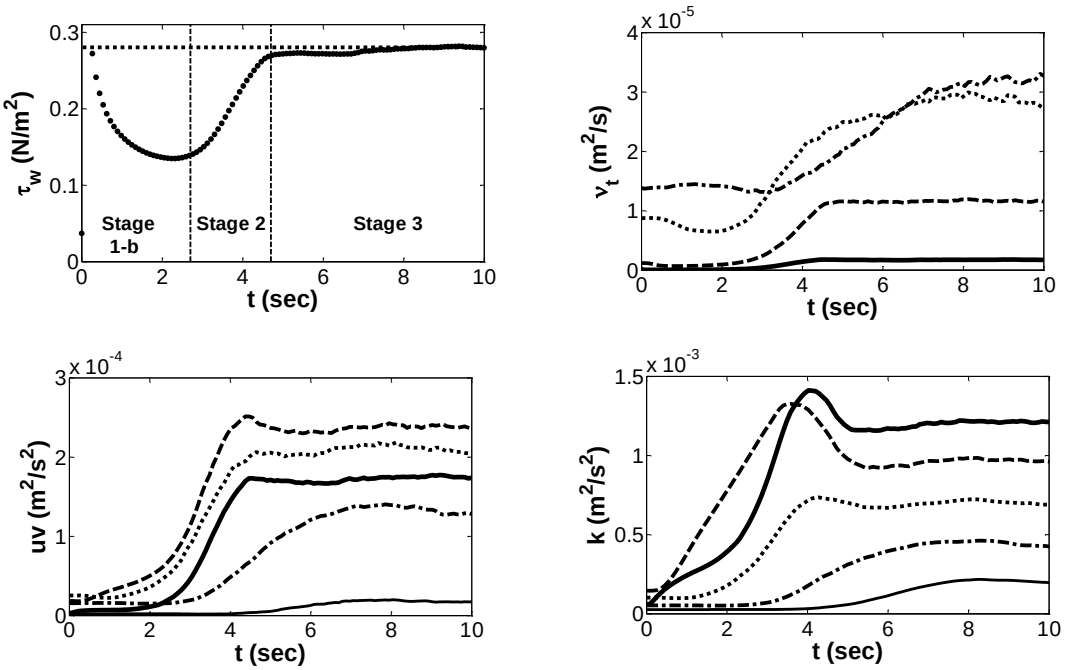

Figure 7.4. Time-history of wall shear stress and turbulence quantities for the three unsteady flow cases predicted by DNS.

The response of the turbulent shear stress is consistent with that of the turbulent viscosity. Turbulent shear stress very close to the wall (at $y_0^+ = 5$) stays mainly constant during stage 1. Its response to the acceleration is initially observed in the wall region, while the delay period becomes progressively longer with distance from the wall.

The overall picture of the development of turbulent kinetic energy with time is similar to that of turbulent shear stress. Delays associated with the response of turbulence increase with distance from the wall. However, the delay in turbulent kinetic energy in the wall region is much shorter than that for the shear stress. Also, turbulent kinetic energy increases slowly during stage 1, while turbulent shear stress and viscosity stay reasonably constant. During this period, the streamwise turbulent normal stress ($\overline{uu}$) increases due to the stretching of the existing eddies, while the turbulent shear stress ($\overline{uv}$), the wall-normal stress ($\overline{vv}$) and the spanwise stress ($\overline{ww}$) are unaffected ((He and Jackson, 2000)). This strong anisotropic behaviour in the near-wall turbulence is the key feature of the unsteady flow and is likely to pose a challenge for linear eddy viscosity models.

7.4.2 **Performance of the turbulence models**

Figure 7.5 shows the RANS models predictions of wall shear stress of the various turbulence models for all three unsteady flow cases; the benchmark DNS results are also shown. It is seen that AB, CHC, LS, $v^2 - f$ and $\gamma - Re_\theta$ (referred to as Group I hereafter) capture the basic features of the flow exhibited by the DNS results rather well, whereas the other models (referred

to as Group II) are not able to do so. All Group I models reproduce the three stage development: a delay stage followed by a rapid response in stage 2 and then a slow adjustment phase (stage 3). Focusing on more detail, $\gamma - Re_\theta$ appears to predict time scales that are very close to those of DNS for all three flow cases. The LS and the CHC models predict time scales close to those of DNS, but are slightly shorter as the acceleration is increased. Note that CHC shows instability in the simulation of Case C. Although able to predict the general features of the unsteady turbulence response, the AB and $v^2 - f$ results always show time scales that are much shorter than those of DNS. The Group II models fail to predict the main features of the unsteady flows, mostly because of their inability to predict the delayed response of turbulence which controls the response of the flow. All of the models (both groups) are able to capture the initial overshoot of the shear stress in early stage 1 since this behaviour is due to the effect of the inertial forces, which is not strongly dependent on turbulence (and hence not dependent on the choice of turbulence model). We note once more that the simulations of the LS model are based on the UDF version; predictions based on FLUENT's built-in LS model (not presented) are very different from the results described above, with very small delays that are much like the predictions of Group II models.

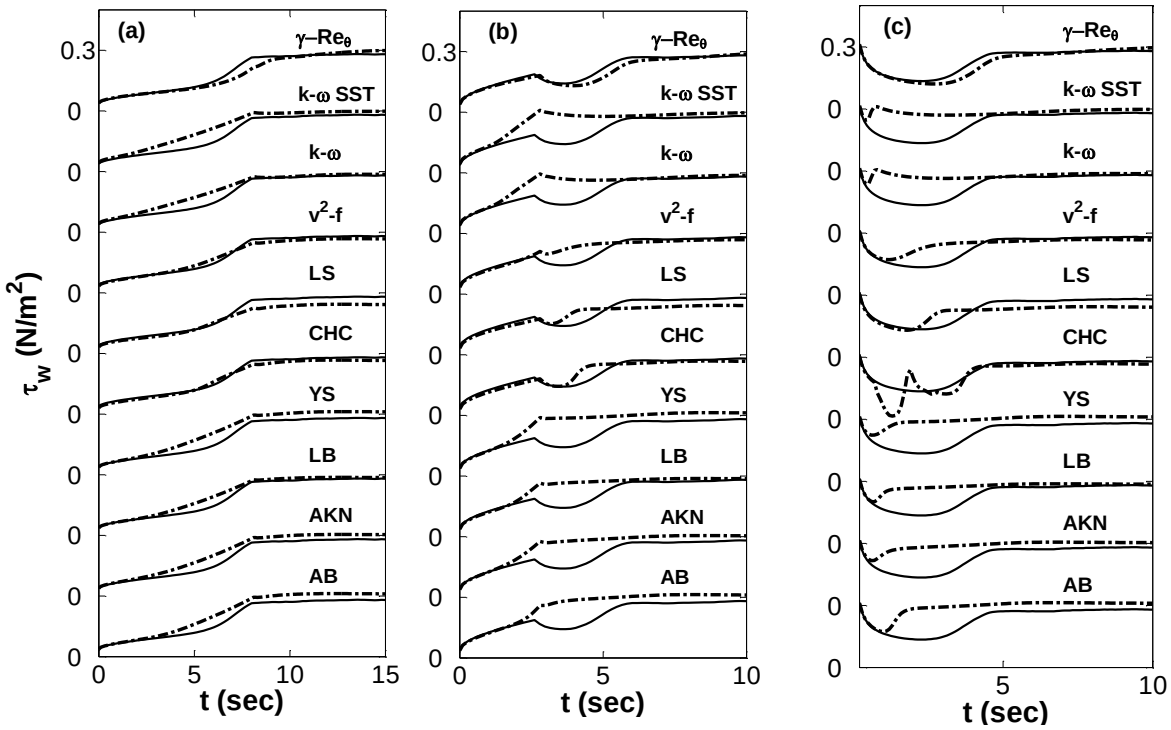

Figure 7.5. Wall shear stress time-histories for unsteady flows; a) Case A, b) Case B and c) Case C. DNS (solid lines) and RANS with various models (dashed lines).

The model predictions of turbulent viscosity at y_0^+=5 due to the various models are shown in Figure 7.6. The turbulent viscosity time histories reflect the trends in wall shear stress predicted

by each model. It is apparent that the characteristic delay in turbulent viscosity in the wall region is well reproduced by LS, CHC and $\gamma - Re_\theta$, and to some extent by AB and $v^2 - f$. Once more, $\gamma - Re_\theta$ slightly over predicts the delays in all flow cases. CHC predicts the delay for flow Cases A and B rather accurately, whilst predicting unrealistic oscillation for flow Case C (not visible in the current scale of the figure). Even though $v^2 - f$ does not predict the delay period correctly for any of the cases, it is the only model to return accurate values of turbulent viscosity during the pre- and post-ramp periods for all three flows. The delays predicted by AKN, LB and YS are much shorter than those of DNS, whereas $k - \omega$ and $k - \omega$ SST return even shorter delays. These observations are consistent with the predictions of wall shear stress from the respective models, as shown in Figure 7.5.

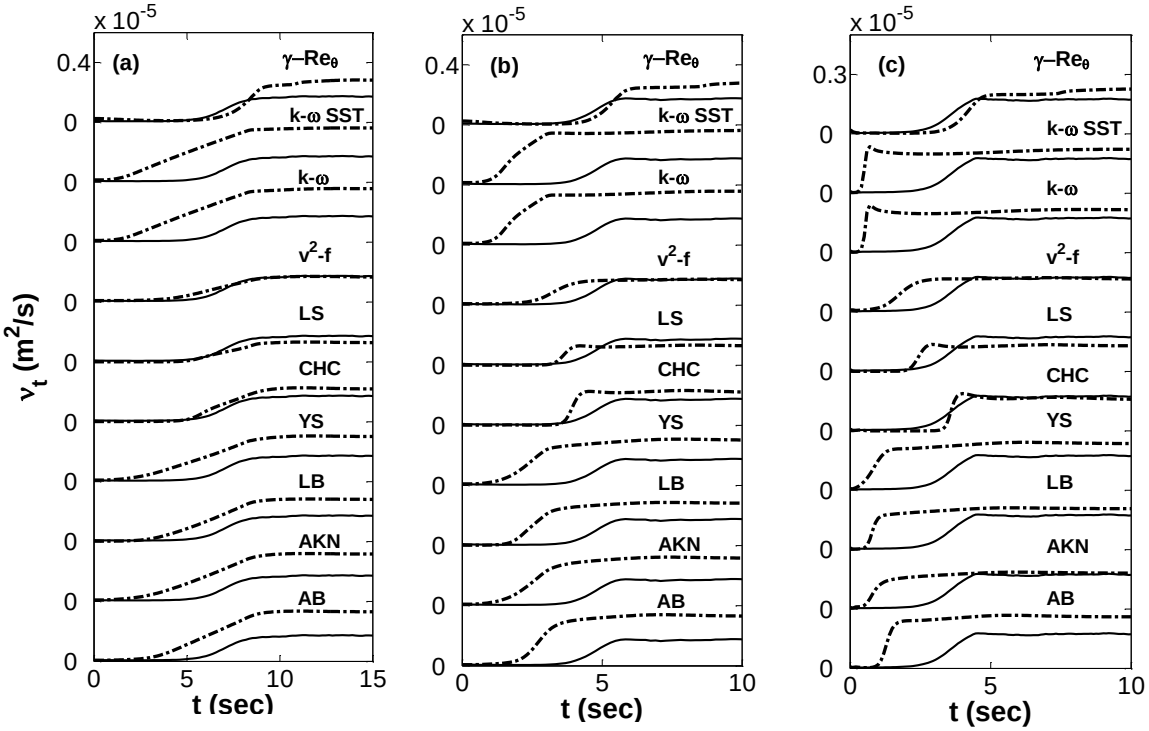

Figure 7.6. Turbulent viscosity time-histories at $y_0^+ = 5$ for unsteady flows; a) Case A, b) Case B and c) Case C. DNS (solid lines) and RANS with various models (dashed lines).

Figure 7.7, 7.8 and 7.9 show the comparisons for turbulent shear stress. For brevity results obtained from selected turbulence models only are presented. Focusing on the wall region first ($y_0^+ = 15$), it is apparent that once more LS, CHC and $\gamma - Re_\theta$ (some not shown) predict the initial and the subsequent response rather well, whereas models AB, AKN, YS, LB and $v^2 - f$ (some not shown) predict much shorter delays; hardly any delays are observed from the predictions of the $k - \omega$ and $k - \omega$ SST models (not shown). Considering the turbulent shear stress development in the core region, the DNS data show progressively longer delays as one moves away from the wall. All models are capable of capturing this feature, with some models

performing slightly better than others. The delay in the core region results from the fact that the turbulence response occurs initially in the wall region, propagating towards the centre through diffusion. The above comparison shows that all models are capable of reproducing this feature because the diffusion term is explicitly included in the transport equations of the turbulent kinetic energy and its dissipation rate. Once more CHC and $\gamma - Re_\theta$ are outperforming the rest in reproducing the trends associated with the development of turbulent shear stress across the channel; CHC's prediction for Case A is nearly indistinguishable from the DNS data although it is less so for Case B. In Case C, CHC's instability in predicting turbulence quantities in the wall region is once more evident in the trends of the turbulent shear stress. The LS model predicts the delay period fairly well, especially for cases A and B, but it returns magnitudes that are lower than those of DNS in the final plateau (not shown). The trends obtained by the AB and $v^2 - f$ are close to those of DNS only in the core region, failing to predict the delays close to the wall.

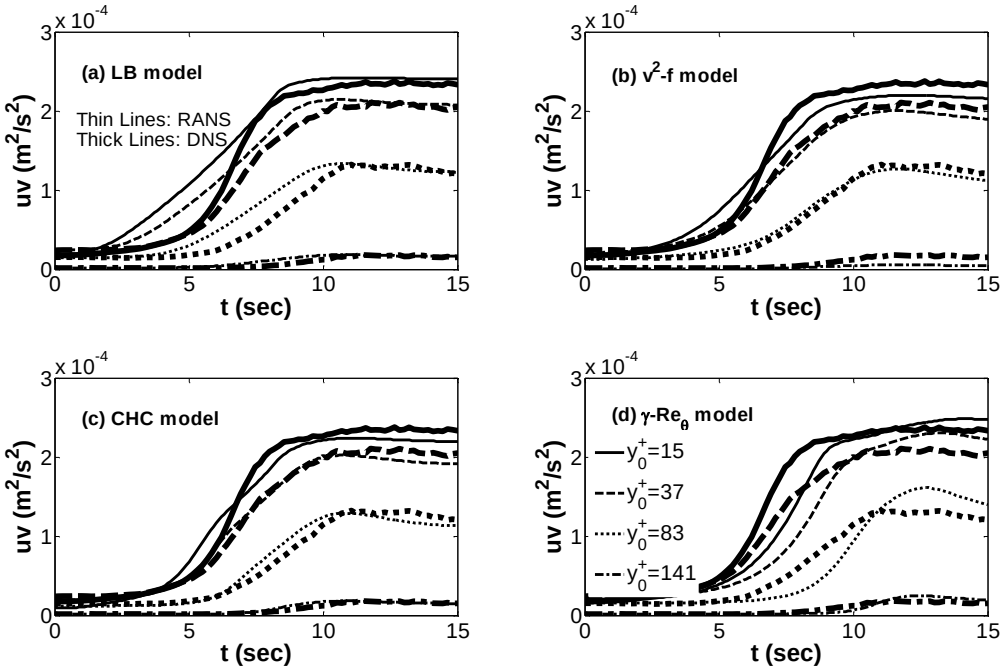

Figure 7.7. Time-histories of turbulent shear stress at selected y_0^+ for unsteady flow case A: RANS model (thin lines) and DNS (thick lines).

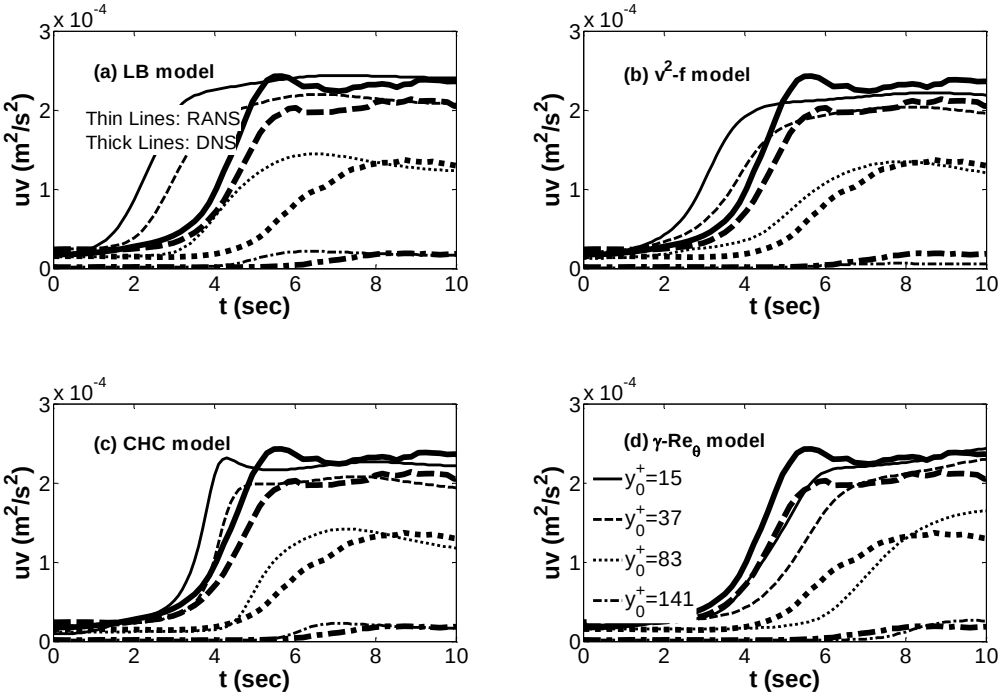

Figure 7.8. Time-histories of turbulent shear stress at selected y_0^+ for unsteady flow case B: RANS model (thin lines) and DNS (thick lines).

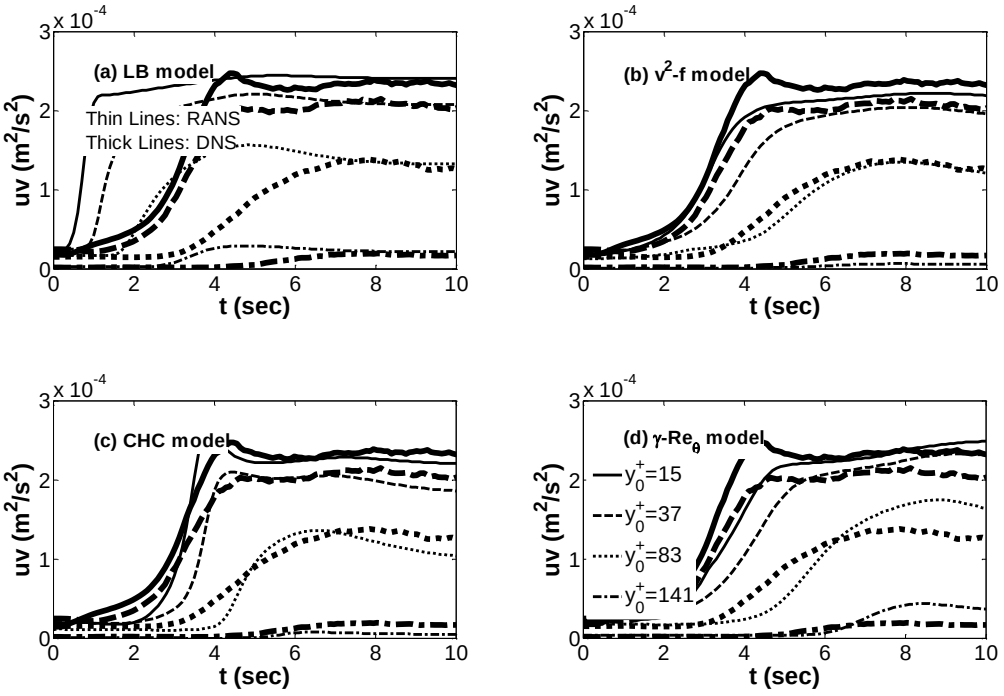

Figure 7.9. Time-histories of turbulent shear stress at selected y_0^+ for unsteady flow case C: RANS model (thin lines) and DNS (thick lines).

Figure 7.10, 7.11 and 7.12 show the predictions of turbulent kinetic energy for several wall-normal locations across the channel. Unlike turbulent shear stress, the turbulent kinetic energy shows a rather small delay in the wall region for the reasons explained in §7.4.1. It is interesting

that all models except CHC, LS and $\gamma - Re_\theta$ can predict this near wall response fairly well. The $v^2 - f$ prediction of turbulent kinetic energy in the wall region is almost indistinguishable from the DNS data during the early stages of the three flows. $\gamma - Re_\theta$ on the other hand predicts a much longer delay, which is similar to that of the turbulent shear stress. It is noted that the important requirement for any eddy viscosity model is to faithfully represent the turbulent viscosity itself or the turbulent shear stress. In this particular case, since turbulent kinetic energy and shear stress show different characteristics, it is actually desirable that the early response of the kinetic energy is not reproduced so that the turbulent shear stress ($\overline{uv}$) can be well represented. This is what CHC, LS and $\gamma - Re_\theta$ have done in order to capture the delay of the wall shear stress correctly. Clearly it is desirable for a model to decouple the prediction of turbulent shear stress and the prediction of turbulent kinetic energy so that both can be predicted faithfully. In principle, this is readily achievable with second momentum closure models. Regarding the performance of the models in the core region, all models reproduce the kinetic energy delay fairly well.

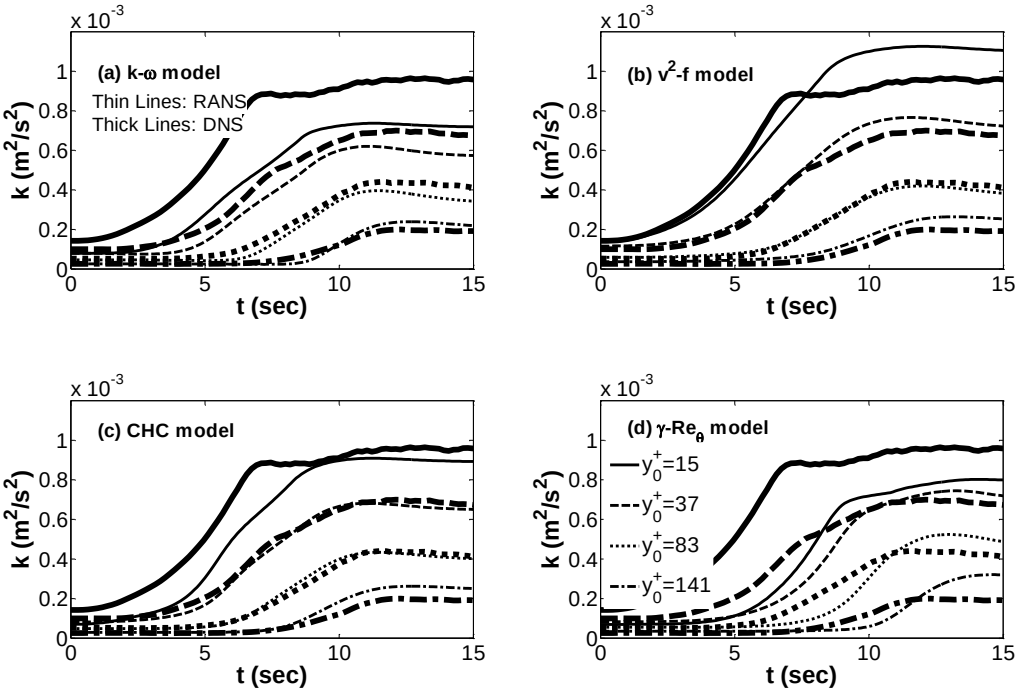

Figure 7.10. Time-histories of turbulent kinetic energy at selected y_0^+ for unsteady flow case A: RANS model (thin lines) and DNS (thick lines).

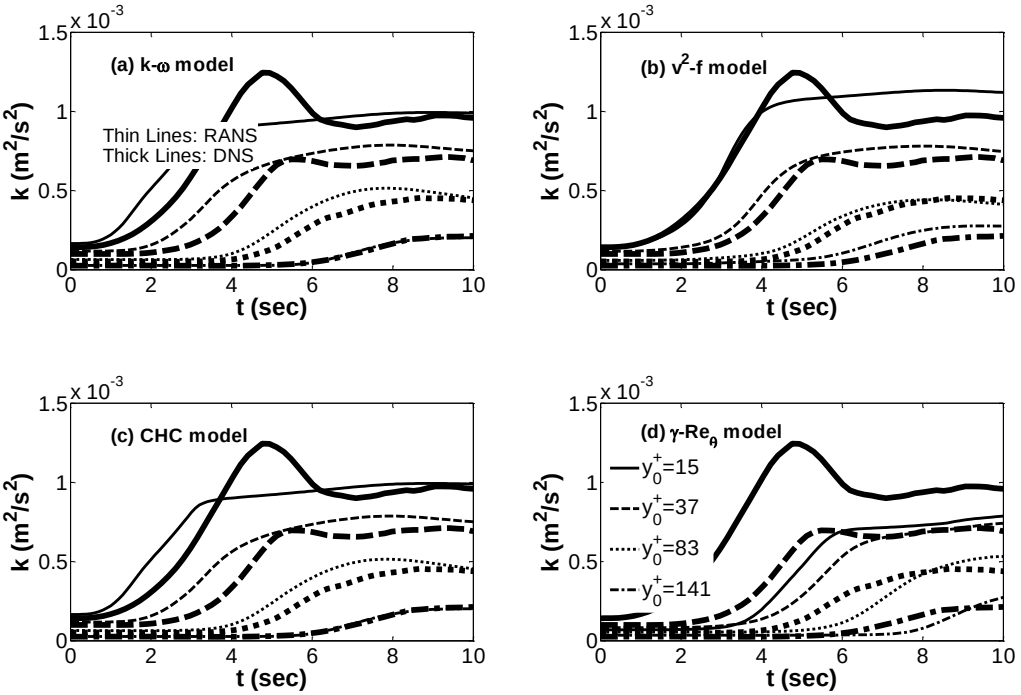

Figure 7.11. Time-histories of turbulent kinetic energy at selected y_0^+ for unsteady flow case B: RANS model (thin lines) and DNS (thick lines).

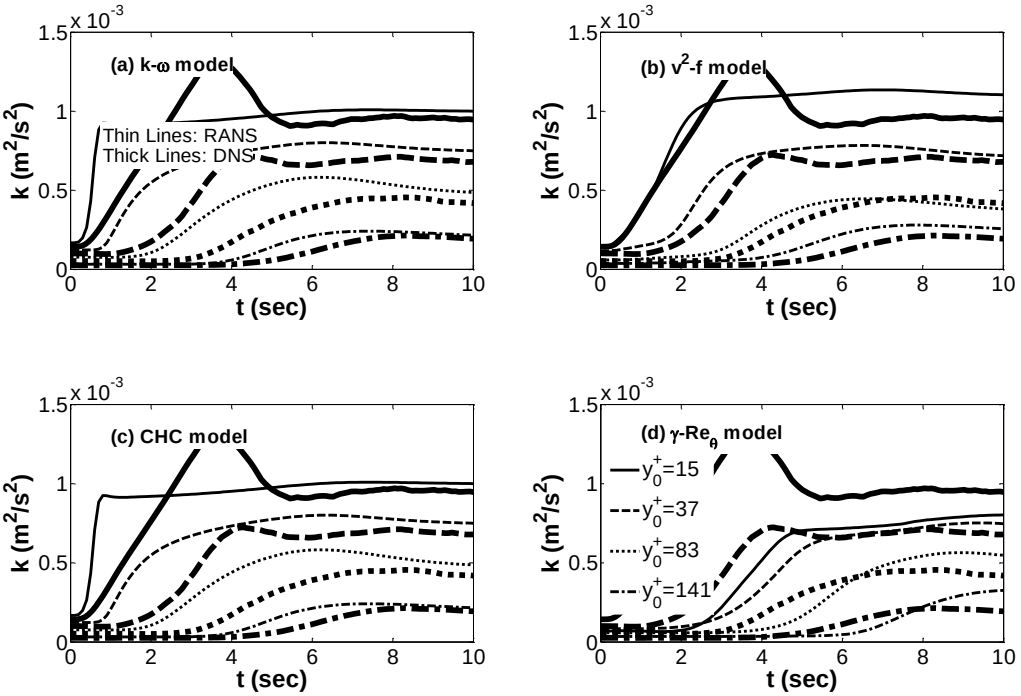

Figure 7.12. Time-histories of turbulent kinetic energy at selected y_0^+ for unsteady flow case C: RANS model (thin lines) and DNS (thick lines).

One of the main features of the turbulent viscosity formulation in the $k-\varepsilon$ models considered in this study is the damping function (f_μ), the major role of which is to reduce turbulent viscosity

in the wall region. Figure 7.13 shows the cross-channel profile of damping function f_μ at selected times, as predicted by four $k-\varepsilon$ models (AB, YS, LB and CHC) for flow Case B. It is seen that the near-wall values of f_μ predicted by CHC is the only one that is sensitive to the imposed excursion. f_μ in CHC begins to respond to the imposed flow rate immediately after the first stage of wall shear stress evolution (inertial-dominated period). The increased f_μ at the early stages of the excursion keeps turbulent kinetic energy and therefore turbulent shear stress low, reproducing the delay effect needed.

A damping function does not exist in the v^2-f or in the $\gamma-Re_\theta$ model. This correction function is replaced by the wall-normal stress component, as discussed in §7.2.3 for the v^2-f model. However, in the $\gamma-Re_\theta$ model the production of turbulent kinetic energy is controlled via intermittency factor derived from its transport equation. Figure 7.14 shows the temporal evolution of the intermittency at selected y_0^+ for the three flow cases. It can be seen that the intermittency is reduced significantly at the early stages followed by a period of delay before increasing again. The turbulent viscosity trend shows similar behaviour. Such a reduction in the intermittency leads to further reduction in turbulent kinetic energy and shear stress in the wall region.

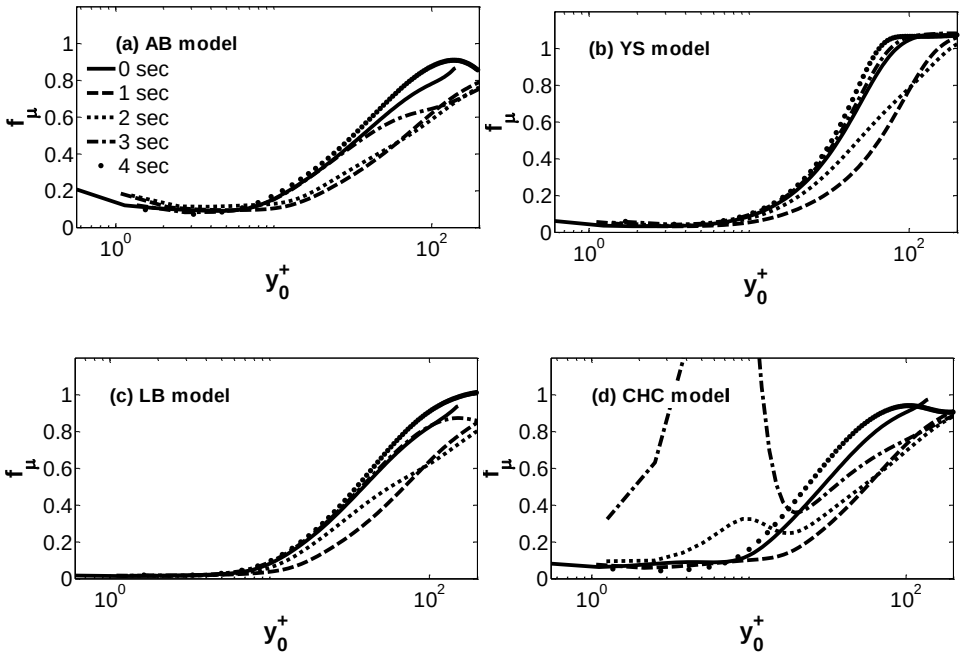

Figure 7.13. Damping function profiles at selected times, as predicted by AB, YS, LB and CHC turbulence models for flow case B.

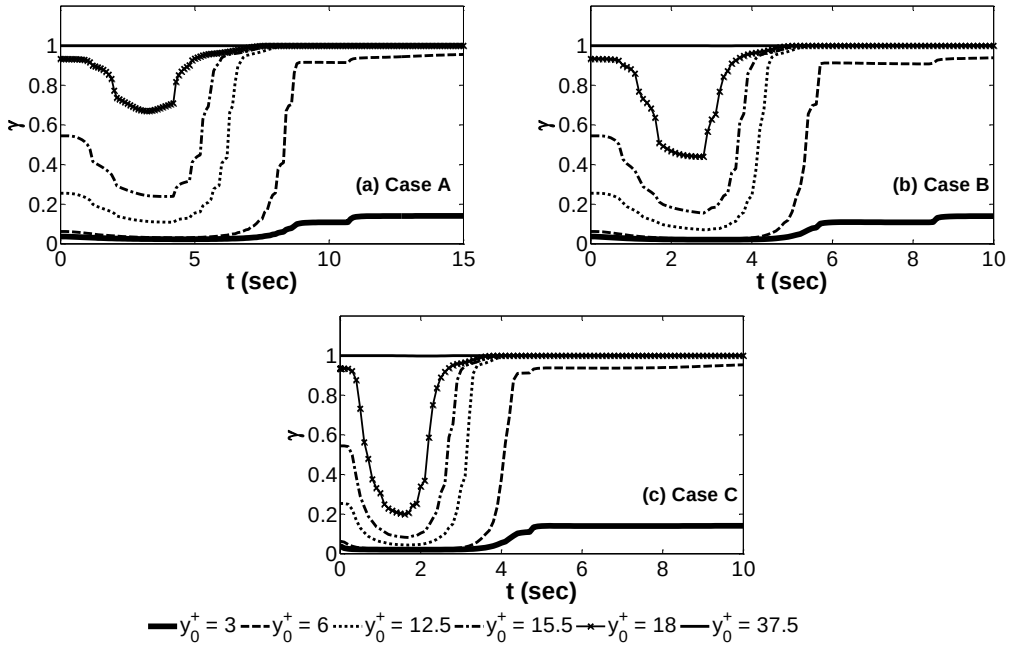

Figure 7.14. Time-histories of intermittency at selected y_0^+, as predicted by $\gamma - Re_\theta$ for unsteady flow cases A, B and C.

7.5 Summary

This chapter reports a systematic study of the behaviour of various low-Reynolds number linear eddy-viscosity turbulence models under steady and unsteady flow conditions over smooth channels. Three different acceleration rates were studied to identify the applicability and robustness of different turbulence models in predicting various features of unsteady flows from the response of mean and Reynolds stresses to the behaviour of wall shear stress.

Chapter 8. Conclusions and Future Work

This chapter gathers the conclusions on the study of turbulence under unsteady conditions. These are the concluding remarks on the development of the flow loop facility as well as the mean and turbulence behaviour of unsteady flows over smooth and rough surfaces. The concluding remarks on the numerical modelling of the unsteady flows in the RANS framework is discussed as well. Finally, future work and further investigations are presented in the last section of this chapter.

8.1 Flow loop facility

A water flow loop facility is designed, constructed and commissioned to study the behaviour of mean flow and turbulence under unsteady conditions. This facility was built to provide the experimental evidence for new understanding of transient channel flow as well as to generate benchmark data for the verification of new models for both smooth and rough flows.

The flow loop consists of a header and a collecting tank with available head of 4.5 metres, capable of generating bulk Reynolds numbers (based on half-height and bulk velocity) up 25,000. The unsteady flows examined herein belong to the category of non-periodic flows with flow variation obtained from either sudden or controlled valve opening. Flow manipulation is performed by means of a customised pneumatically operated control valve capable of generating sudden flow transients.

The test section was designed and later verified to provide a fully developed, two dimensional flow at the measurement station $\sim 140H$ downstream of the inlet. The physical length, width

and height of the channel are 8, 0.35 and 0.05 metres, respectively. The channel facility was designed so that the bottom plates of the test section could be removed to facilitate the study of different surface topologies.

Particle Image Velocimetry (PIV) and Laser Doppler Velocimetry (LDV) were used to measure the mean and turbulence flow features under steady and unsteady flow conditions. Bulk flow and static pressure variations were measured by a magnetic flow meter and a pressure transducer, respectively. Thermocouples are also used to measure the temperature of the water. The statistics obtained from the present steady investigations are in good agreement with previous Direct Numerical Simulation (DNS) studies of channel flows.

The rough surface investigated in the present investigations consists of a carefully CNC machined square based pyramids with the height of 0.9 mm ($h/k = 28$) and wavelength of 7.5 mm. The flow properties over the roughness elements were measured to vary between the hydrodynamically smooth to fully rough regimes over a range of bulk Reynolds numbers of 2,300 to 25,000.

The mean velocity as well as the Reynolds stresses obtained from the various steady flows over rough surfaces provide a strong support for the Townsend's wall and Reynolds number similarity hypotheses throughout the transitionally and fully rough regimes.

8.2 Unsteady flows over smooth and rough surfaces

LDV and PIV were used to measure mean and turbulence flow characteristics over the smooth surfaces, while only PIV was employed for the rough surface investigations.

Present investigations support the concept regarding the transient channel flow transition initially introduced by He and Seddighi (2013). It was shown that the turbulence in an unsteady channel flow due to sudden flow rate excursion undergoes a process that resembles the bypass transition due to free-stream turbulence in boundary layers. Near-wall measurements show a three-stage development namely the pre-transition, transition and fully turbulent phases, resembling the buffeted laminar, intermittent turbulent spot generation and fully turbulent states of Jacobs and Durbin (2001). During the pre-transition phase, existing streaky structures are stretched in the streamwise and narrowed in the spanwise direction resembling the Klebanoff modes present in the laminar buffeted regime of the transitional boundary layers. The period of the pre-transition phase (or the critical Reynolds number) depends on the surface conditions as well as the levels of the initial free-stream turbulence intensity (Tu_0). It was shown

that a high level of Tu_0 as well as the presence of roughness on the surface can diminish the period of pre-transition.

It was shown that during the transient process a new boundary layer is formed on the wall surface evolving with respect to time. Perturbing velocity ($\overline{U}^{\wedge}$) was used to illustrate this temporal evolving boundary layer. $\overline{U}^{\wedge}$ obtained from various unsteady flows, regardless of the surface condition, was shown to collapse on a single curve during the pre-transition process governed by the Stokes solution. Similarly, the perturbing streamwise and wall-normal rms velocities due to various cases was shown to collapse during this regime.

The first signs of instability occur as isolated packets of high amplitude turbulent bursts that eventually propagate throughout the spanwise surface, leading to a complete breakdown of the existing structures. These features were clearly identifiable from the spanwise PIV measurements over both smooth and rough surfaces. Period of transition was shown to have a power-law and a linear relationship with the critical Reynolds number for smooth and rough surfaces, respectively. This period was shown to be significantly reduced for flows over rough surfaces in comparison to their corresponding smooth-wall flows.

Furthermore, It was shown in the present investigations that the mechanisms of turbulence production in the near-wall region, its redistribution to wall-normal (and likely spanwise) component as well as its diffusion towards the centre, initially introduced by He and Jackson (2000) are valid for unsteady flows over rough surfaces. Despite the fact that the duration of the associated delays are dependent on the regime of the rough flows and are likely to be much shorter in comparison to similar smooth-wall flows.

8.3 RANS study of unsteady turbulent flows

The performance of ten eddy viscosity turbulence models in predicting unsteady, ramp-up-type turbulent channel flows has been examined by comparing predictions with DNS results for the same flows. Three ramp-up flows with different acceleration rates have been considered. The key features of the unsteady flow as seen in the DNS data are the distinct delays in the response of the turbulent shear stress and turbulent viscosity to the imposed change in the flow rate. These delays are in turn responsible for the response of the wall shear stress. It is shown that the wall shear stress goes through a three-stage development. The first stage is influenced by the frozen turbulence and inertia forces. In the early part of the first stage, inertial forces dominate, causing the wall shear stress to overshoot the corresponding quasi-steady values. Then the effect of frozen (or delayed) turbulence takes over, causing the wall shear stress to

undershoot the quasi-steady values. The second stage corresponds to a rapid response of turbulence, causing a rapid increase in wall shear stress. In the final stage the wall shear stress approaches the quasi-steady value.

The diffusion of turbulence from the wall to the core region is another feature of unsteady flows, leading to relatively long delays in the response of turbulent kinetic energy and turbulent shear stress in the core region. However, the duration of the delay period of turbulence response in the wall region is different for kinetic energy and for turbulent shear stress because of the stretching of turbulence structures.

The following are the main conclusions regarding the performance of the various turbulence models examined in this study:

- The most important feature that needs to be modelled in order to capture the overall behaviour of the flow is the delayed response of turbulent shear stress (and turbulent viscosity). Among the models examined, only the LS, CHC and $\gamma - Re_\theta$ models can capture this accurately, making them the only suitable models for such unsteady flows. LS and CHC achieve this through an appropriately designed damping function (f_μ), while $\gamma - Re_\theta$ employs an intermittency parameter that responds suitably to the variation in flow rate. However, it should be pointed out that the performance of the CHC model in high acceleration flow case was not satisfactory because of its instability. The AB and $v^2 - f$ model can also reproduce the basic trends but with much shorter time scales than expected.
- All models reproduce the overshoot in wall shear stress over the corresponding quasi-steady shear stress that occurs in the early stage of the flow rate excursion, with only minor differences between the predictions of each model. In fact, the overshoot is an inertia-dominated effect that is not related to turbulence. For this reason we expect the predictions of the various turbulence models to be similar at this early stage.
- The delay in the response of turbulence in the core region is governed by diffusion, represented explicitly in the transport equations of the $k - \varepsilon/\omega$ models. As a result, such delays are reasonably well predicted by all models.

For accelerating flows, it is desirable that the early response of turbulent kinetic energy is not reflected in the model predictions unless turbulent kinetic energy and shear stress formulations are decoupled. It is also noted that due to the similarities between channel and pipe flows, performance of turbulence models are expected to be similar for both geometries.

8.4 Suggestions for future work

Below are some suggestions for future investigations of the unsteady channel flows:

- The concept of transient channel flow transition was originally introduced for sudden excursions of flow rate in He and Seddighi (2013). Generating high acceleration rates was a challenge to the employed gravity-driven flow loop facility and therefore any effort to improve the acceleration rate of the system in future studies would be extremely advantageous.
- Sudden opening flow scenarios in the present investigations suffered from the poor repeatability of the control valve in the first few seconds. Therefore, improvement of the control system would significantly improve the quality of the measurements.
- One of the main parameters in the study of unsteady channel flows is the skin friction or wall shear stress. Despite the efforts made during the design and commissioning process of the apparatus for the implementation of the hot-film sensors, they only worked for a short period. In future studies, effort should be made to achieve accurate data on the behaviour of the wall shear stress during the transition which is of great importance in characterising the flow features.
- The present investigations on the unsteady rough flows can only be considered to be a scratch on the surface as there are many parameters that require a separate and thorough investigation such as the geometrical properties of the roughness as well as the initial and final regimes of the unsteady flow.

List of publications

1. Vardy, A., Brown, J., He, S., Ariyaratne, C., & Gorji, S. 2015. Applicability of frozen-viscosity models of unsteady wall shear stress. *Journal of Hydraulic Engineering*, 141(1): 04014064.
2. Gorji, S., He, S., Seddighi, M., O'Donoghue, T., Pokrajac, D., & Vardy, A. 2014. Experimental study of a turbulent flow under transient conditions. *Bulletin of the American Physical Society*, 59.
3. Gorji, S., Seddighi, M., Ariyaratne, C., Vardy, A. E., O'Donoghue, T., Pokrajac, D., & He, S. 2014. A comparative study of turbulence models in a transient channel flow. *Computers & Fluids*, 89(0): 111-123.

References

ABE, K., KONDOH, T. & NAGANO, Y. 1995. A new turbulence model for predicting fluid flow and heat transfer in separating and reattaching flows-I. Flow field calculations. *International Journal of Heat and Mass Transfer,* 37**,** 139-151.

ABID, R. 1993. Evaluation of two-equation turbulence models for predicting transitional flows. *International Journal of Engineering Science,* 31**,** 831-840.

ABU-GHANNAM, B. J. & SHAW, R. 1980. Natural transition of boundary layers - the effects of turbulence, pressure gradient, and flow history. *Journal of Mechanical Engineering Science,* 22**,** 213-228.

AL-SHARIF, S. F., COTTON, M. A. & CRAFT, T. J. 2010. Reynolds stress transport models in unsteady and non-equilibrium turbulent flows. *International Journal of Heat and Fluid Flow,* 31**,** 401-408.

ALLEN, J. J., SHOCKLING, M. A. & SMITS, A. J. 2005. Evaluation of a universal transitional resistance diagram for pipes with honed surfaces. *Physics of Fluids,* 17**,** 1-4.

ANDERSSON, P., BERGGREN, M. & HENNINGSON, D. S. 1999. Optimal disturbances and bypass transition in boundary layers. *Physics of Fluids,* 11**,** 134-150.

ARIYARATNE, C., HE, S. & VARDY, A. E. 2010. Wall friction and turbulence dynamics in decelerating pipe flows. *Journal of Hydraulic Research,* 48**,** 810-821.

ARNAL, D. & JUILLEN, J. 1978. Contribution expérimentale à l'étude de la reptivité d'une couche limite laminaire à la turbulence de l'écoulement général. *Rapport Technique,* 1**,** 22.

BANDYOPADHYAY, P. R. 1987. Rough-wall turbulent boundary layers in the transition regime. *Journal of Fluid Mechanics,* 180**,** 231-266.

BHAGANAGAR, K. 2008. Direct numerical simulation of unsteady flow in channel with rough walls. *Physics of Fluids,* 20.

BILLARD, F. & LAURENCE, D. 2012. A robust k-ε-v2/k elliptic blending turbulence model applied to near-wall, separated and buoyant flows. *International Journal of Heat and Fluid Flow,* 33**,** 45-58.

BINDER, G., TARDU, S. & VEZIN, P. 1995. Cyclic modulation of Reynolds stresses and length scales in pulsed turbulent channel flow. *Proceedings of the Royal Society of London. Series A: Mathematical and Physical Sciences,* 451**,** 121-139.

BIRCH, D. M. & MORRISON, J. F. 2011. Similarity of the streamwise velocity component in very-rough-wall channel flow. *Journal of Fluid Mechanics,* 668**,** 174-201.

BLUMER, C. & VAN DRIEST, E. 1963. Boundary layer transition-freestream turbulence and pressure gradient effects. *AIAA Journal,* 1**,** 1303-1306.

BRITZ, D. & ANTONIA, R. A. 1996. A comparison of methods of computing power spectra of LDA signals. *Measurement Science and Technology,* 7**,** 1042-1053.

BUCHHAVE, P., GEORGE JR, W. K. & LUMLEY, J. L. 1979. Measurement of the turbulence with the laser-Doppler anemometer. *Annual Review of Fluid Mechanics,* 11**,** 443-503.

BUSHNELL, D. M. & MCGINLEY, C. B. 1989. Turbulence control in wall flows. *Annual Review of Fluid Mechanics,* 21**,** 1-20.

CHANG, K. C., HSIEH, W. D. & CHEN, C. S. 1995. A Modified low-Reynolds-number turbulence model applicable to recirculating flow in pipe expansion. *Journal of Fluids Engineering, Transactions of the ASME,* 117**,** 417-423.

CHEN, D., CHEN, C., TANG, F. E., STANSBY, P. & LI, M. 2007. Boundary layer structure of oscillatory open-channel shallow flows over smooth and rough beds. *Experiments in Fluids,* 42**,** 719-736.

CHUNG, Y. M. 2005. Unsteady turbulent flow with sudden pressure gradient changes. *International Journal for Numerical Methods in Fluids,* 47**,** 925-930.

COLEBROOK, C. F. 1939. Turbulent Flow in Pipes, with particular reference to the Transition Region between the Smooth and Rough Pipe Laws. *Journal of the ICE,* 11**,** 133-156.

COTTON, M. A., CRAFT, T. J., GUY, A. W. & LAUNDER, B. E. 2001. On modelling periodic motion with turbulence closures. *Flow, Turbulence and Combustion,* 67**,** 143-158.

DEAN, R. B. 1978. Reynolds number dependence of skin friction and other bulk flow variables in two-dimensional rectangular duct flow. *Journal of Fluids Engineering, Transactions of the ASME,* 100**,** 215-223.

DEAN, R. B. & BRADSHAW, P. 1976. Measurements of interacting turbulent shear layers in a duct. *Journal of Fluid Mechanics,* 78**,** 641-676.

DEGRAAFF, D. B. & EATON, J. K. 2001. A high-resolution laser Doppler anemometer: Design, qualification, and uncertainty. *Experiments in Fluids,* 30**,** 522-530.

DEN TOONDER, J. M. J. & NIEUWSTADT, F. T. M. 1997. Reynolds number effects in a turbulent pipe flow for low to moderate Re. *Physics of Fluids,* 9**,** 3398-3409.

DHAWAN, S. & NARASIMHA, R. 1958. Some properties of boundary layer flow during the transition from laminar to turbulent motion. *Journal of Fluid Mechanics,* 3**,** 418-436.

DI LIBERTO, M. & CIOFALO, M. 2011. Unsteady turbulence in plane channel flow. *Computers and Fluids,* 49**,** 258-275.

DJENIDI, L., ELAVARASAN, R. & ANTONIA, R. A. 1999. The turbulent boundary layer over transverse square cavities. *Journal of Fluid Mechanics,* 395**,** 271-294.

DURBIN, P. & WU, X. 2007. Transition beneath vortical disturbances. *Annual Review of Fluid Mechanics.*

DURBIN, P. A. 1991. Near-wall turbulence closure modeling without "damping functions". *Theoretical and Computational Fluid Dynamics,* 3**,** 1-13.

DURBIN, P. A. 1995. Separated flow computations with the k-ε-v2 model. *AIAA Journal,* 33**,** 659-664.

DURST, F., FISCHER, M., JOVANOVIĆ, J. & KIKURA, H. 1998. Methods to set up and investigate low Reynolds number, fully developed turbulent plane channel flows. *Journal of Fluids Engineering, Transactions of the ASME,* 120**,** 496-503.

DURST, F., JOVANOVIC, J. & SENDER, J. 1995. LDA measurements in the near-wall region of a turbulent pipe flow. *Journal of Fluid Mechanics,* 295**,** 305-335.

DURST, F., KIKURA, H., LEKAKIS, I., JOVANOVIĆ, J. & YE, Q. 1996. Wall shear stress determination from near-wall mean velocity data in turbulent pipe and channel flows. *Experiments in Fluids,* 20**,** 417-428.

FLACK, K. A., SCHULTZ, M. P. & SHAPIRO, T. A. 2005. Experimental support for Townsend's Reynolds number similarity hypothesis on rough walls. *Physics of Fluids,* 17**,** 035102-1-035102-9.

FLORES, O., JIMÉNEZ, J. & DEL ÁLAMO, J. C. 2007. Vorticity organization in the outer layer of turbulent channels with disturbed walls. *Journal of Fluid Mechanics,* 591**,** 145-154.

FORNARELLI, F. & VITTORI, G. 2009. Oscillatory boundary layer close to a rough wall. *European Journal of Mechanics, B/Fluids,* 28**,** 283-295.

FRANSSON, J. H. M., MATSUBARA, M. & ALFREDSSON, P. H. 2005. Transition induced by free-stream turbulence. *Journal of Fluid Mechanics,* 527**,** 1-25.

GILBERT, N. & KLEISER, L. Turbulence model testing with the aid of direct numerical simulation results. Proc. of 8th Symposium on Turbulent Shear Flows, Sept. 9-11 1991 Munich. Paper 26-1

GORJI, S., SEDDIGHI, M., ARIYARATNE, C., VARDY, A. E., O'DONOGHUE, T., POKRAJAC, D. & HE, S. 2014. A comparative study of turbulence models in a transient channel flow. *Computers & Fluids,* 89**,** 111-123.

GREENBLATT, D. & MOSS, E. A. 1999. Pipe-flow relaminarization by temporal acceleration. *Physics of Fluids,* 11**,** 3478-3481.

GREENBLATT, D. & MOSS, E. A. 2004. Rapid temporal acceleration of a turbulent pipe flow. *Journal of Fluid Mechanics,* 514**,** 65-75.

GUSTAVSSON, L. H. 1991. Energy growth of three-dimensional disturbances in plane Poiseuille flow. *Journal of Fluid Mechanics,* 224**,** 241-260.

HANJALIC, K. & LAUNDER, B. E. 1972. Fully developed asymmetric flow in a plane channel. *Journal of Fluid Mechanics,* 51**,** 301-&.

HE, S. & ARIYARATNE, C. 2011. Wall shear stress in the early stage of unsteady turbulent pipe flow. *Journal of Hydraulic Engineering,* 137**,** 606-610.

HE, S., ARIYARATNE, C. & VARDY, A. E. 2008. A computational study of wall friction and turbulence dynamics in accelerating pipe flows. *Computers and Fluids,* 37**,** 674-689.

HE, S., ARIYARATNE, C. & VARDY, A. E. 2011. Wall shear stress in accelerating turbulent pipe flow. *Journal of Fluid Mechanics,* 685**,** 440-460.

HE, S. & JACKSON, J. D. 2000. A study of turbulence under conditions of transient flow in a pipe. *Journal of Fluid Mechanics,* 408**,** 1-38.

HE, S. & JACKSON, J. D. 2009. An experimental study of pulsating turbulent flow in a pipe. *European Journal of Mechanics, B/Fluids,* 28**,** 309-320.

HE, S. & SEDDIGHI, M. 2013. Turbulence in transient channel flow. *Journal of Fluid Mechanics,* 715**,** 60-102.

HE, S. & SEDDIGHI, M. 2015. Transition of transient channel flow after a change in Reynolds number. *Journal of Fluid Mechanics,* 764**,** 395-427.

HONG, J., KATZ, J., MENEVEAU, C. & SCHULTZ, M. P. 2012. Coherent structures and associated subgrid-scale energy transfer in a rough-wall turbulent channel flow. *Journal of Fluid Mechanics***,** 1-37.

HONG, J., KATZ, J. & SCHULTZ, M. P. 2011. Near-wall turbulence statistics and flow structures over three-dimensional roughness in a turbulent channel flow. *Journal of Fluid Mechanics,* 667**,** 1-37.

HOYAS, S. & JIMÉNEZ, J. 2008. Reynolds number effects on the Reynolds-stress budgets in turbulent channels. *Physics of Fluids,* 20.

IACCARINO, G. 2001. Predictions of a turbulent separated flow using commercial CFD codes. *Transactions-American Society of Mechanical Engineers Journal of Fluids Engineering,* 123**,** 819-828.

JACOBS, R. & DURBIN, P. 2001. Simulations of bypass transition. *Journal of Fluid Mechanics,* 428**,** 185-212.

JIMÉNEZ, J. 2004. Turbulent flows over rough walls. *Annual Review of Fluid Mechanics,* 36**,** 173-196.

JUNG, S. Y. & CHUNG, Y. M. 2012. Large-eddy simulation of accelerated turbulent flow in a circular pipe. *International Journal of Heat and Fluid Flow,* 33**,** 1-8.

KATAOKA, K., KAWABATA, T. & MIKI, K. 1975. The start-up response of pipe flow to a step change in flow rate. *Journal of Chemical Engineering of Japan,* 8**,** 266-271.

KEANE, R. D. & ADRIAN, R. J. 1990. Optimization of particle image velocimeters. Part I. Double pulsed systems. *Measurement Science and Technology,* 1**,** 1202-1215.

KEANE, R. D. & ADRIAN, R. J. 1991. Optimization of particle image velocimeters. II. Multiple pulsed systems. *Measurement Science and Technology,* 2**,** 963-974.

KEANE, R. D. & ADRIAN, R. J. 1992. Theory of cross-correlation analysis of PIV images. *Applied Scientific Research,* 49**,** 191-215.

KHALEGHI, A., PASANDIDEH-FARD, M., MALEK-JAFARIAN, M. & CHUNG, Y. M. 2010. Assessment of common turbulence models under conditions of temporal acceleration in a pipe. *Journal of Applied Fluid Mechanics,* 3**,** 25-33.

KIM, J., MOIN, P. & MOSER, R. 1987. Turbulence statistics in fully developed channel flow at low Reynolds number. *Journal of Fluid Mechanics,* 177**,** 133-166.

KROGSTAD, P. Å., ANDERSSON, H. I., BAKKEN, O. M. & ASHRAFIAN, A. 2005. An experimental and numerical study of channel flow with rough walls. *Journal of Fluid Mechanics,* 530**,** 327-352.

KROGSTAD, P. A., ANTONIA, R. A. & BROWNE, L. W. B. 1992. Comparison between rough- and smooth-wall turbulent boundary layers. *Journal of Fluid Mechanics,* 245**,** 599-617.

LAM, C. K. G. & BREMHORST, K. 1981. Modified form of the k- epsilon model for predicting wall turbulence. *Journal of Fluids Engineering, Transactions of the ASME,* 103**,** 456-460.

LANDAHL, M. T. 1980. A note on an algebraic instability of inviscid parallel shear flows. *Journal of Fluid Mechanics,* 98**,** 243-251.

LANGELANDSVIK, L. I., KUNKEL, G. J. & SMITS, A. J. 2008. Flow in a commercial steel pipe. *Journal of Fluid Mechanics,* 595**,** 323-339.

LANGTRY, R. B. & MENTER, F. R. 2009. Correlation-based transition modeling for unstructured parallelized computational fluid dynamics codes. *AIAA Journal,* 47**,** 2894-2906.

LAUNDER, B. E. 1986. Low-Reynolds number turbulence near walls. *Report TFD/86/4.* UMIST.

LAUNDER, B. E. & SHARMA, B. I. 1974. Application of the energy-dissipation model of turbulence to the calculation of flow near a spinning disc. *Letters in Heat and Mass Transfer,* 1**,** 131-137.

LEE, S. H. & SUNG, H. J. 2007. Direct numerical simulation of the turbulent boundary layer over a rod-roughened wall. *Journal of Fluid Mechanics,* 584**,** 125-146.

LEFEBVRE, P. J. 1987. *Characterization of accelerating pipe flow.* University of Rhode Island.

LEONARDI, S., ORLANDI, P., DJENIDI, L. & ANTONIA, R. A. 2004. Structure of turbulent channel flow with square bars on one wall. *International Journal of Heat and Fluid Flow,* 25**,** 384-392.

LIEN, F. S. & KALITZIN, G. 2001. Computations of transonic flow with the v2-f turbulence model. *International Journal of Heat and Fluid Flow,* 22**,** 53-61.

LIGRANI, P. M. & MOFFAT, R. J. 1986. Structure of transitionally rough and fully rough turbulent boundary layers. *Journal of Fluid Mechanics,* 162**,** 69-98.

LUCHINI, P. 1996. Reynolds-number-independent instability of the boundary layer over a flat surface. *Journal of Fluid Mechanics,* 327**,** 101-115.

LUCHINI, P. 2000. Reynolds-number-independent instability of the boundary layer over a flat surface: Optimal perturbations. *Journal of Fluid Mechanics,* 404**,** 289-309.

MARUSIC, I., MATHIS, R. & HUTCHINS, N. 2010. High Reynolds number effects in wall turbulence. *International Journal of Heat and Fluid Flow,* 31**,** 418-428.

MARUYAMA, T., KURIBAYASHI, T. & MIZUSHINA, T. 1976. Structure of the turbulence in transient pipe flows. *Journal of Chemical Engineering of Japan,* 9**,** 431-439.

MATHUR, A. & HE, S. 2013. Performance and implementation of the Launder-Sharma low-Reynolds number turbulence model. *Computers and Fluids,* 79**,** 134-139.

MATSUBARA, M. & ALFREDSSON, P. H. 2001. Disturbance growth in boundary layers subjected to free-stream turbulence. *Journal of Fluid Mechanics,* 430**,** 149-168.

MAYLE, R. E. 1991. The role of laminar-turbulent transition in gas turbine engines. *Journal of Turbomachinery,* 113**,** 509-537.

MCKEON, B. J., ZAGAROLA, M. V. & SMITS, A. J. 2005. A new friction factor relationship for fully developed pipe flow. *Journal of Fluid Mechanics,* 538**,** 429-443.

MEHTA, R. D. & BRADSHAW, P. 1979. Design rules for small low-speed wind tunnels. Royal Aeronautical Soc 4 Hamilton Pl, London, England W1V OBQ.

MENTER, F. R. 1994. Two-equation eddy-viscosity turbulence models for engineering applications. *AIAA Journal,* 32**,** 1598-1605.

MOFFATT, H. 1967. The interaction of turbulence with strong wind shear. *Atmospheric Turbulence and Radio Wave Propagation***,** 139-156.

MOIN, P., SHIH, T. H., DRIVER, D. & MANSOUR, N. N. 1990. Direct numerical simulation of a three-dimensional turbulent boundary layer. *Physics of Fluids A,* 2**,** 1846-1853.

MONTY, J. P. 2005. *Developments in smooth wall turbulent duct flows.* PhD Thesis, The University of Melbourne.

MOODY, L. F. 1944. Friction factors for pipe flow. *Trans. Asme,* 66**,** 671-684.

MORKOVIN, M. 1969. Viscous Drag Reduction. *On the Many Faces of Transition***,** 1-31.

MYONG, H. K. & KASAGI, N. 1990. New approach to the improvement of κ-ε turbulence model for wall-bounded shear flows. *JSME International Journal,* 33**,** 63-72.

NAGARAJAN, S., LELE, S. & FERZIGER, J. 2007. Leading-edge effects in bypass transition. *Journal of Fluid Mechanics,* 572**,** 471-504.

NAGIB, H. M. & CHAUHAN, K. A. 2008. Variations of von Kármán coefficient in canonical flows. *Physics of Fluids,* 20.

NARASIMHA, R. 1985. The laminar-turbulent transition zone in the boundary layer. *Progress in Aerospace Sciences,* 22**,** 29-80.

NIKURADSE, J. 1933. Str {ö} mungsgestze in rauhen Rohren.

OLDENGARM, J., VAN KRIEKEN, A. H. & VAN DER KLOOSTER, H. W. 1975. Velocity profile measurements in a liquid film flow using the laser Doppler technique. *Journal of Physics E: Scientific Instruments,* 8**,** 203-205.

ÖSTERLUND, J. M., JOHANSSON, A. V., NAGIB, H. M. & HITES, M. H. 2000. A note on the overlap region in turbulent boundary layers. *Physics of Fluids,* 12**,** 1-4.

OVCHINNIKOV, V., CHOUDHARI, M. M. & PIOMELLI, U. 2008. Numerical simulations of boundary-layer bypass transition due to high-amplitude free-stream turbulence. *Journal of Fluid Mechanics,* 613**,** 135-169.

PATEL, V. C., RODI, W. & SCHEUERER, G. 1985. Turbulence models for near-wall and low Reynolds number flows. *AIAA Journal,* 23**,** 1308-1319.

PERRY, A. E. & ABELL, C. J. 1975. Scaling laws for pipe-flow turbulence. *Journal of Fluid Mechanics,* 67**,** 257-271.

PERRY, A. E., SCHOFIELD, W. H. & JOUBERT, P. N. 1969. Rough wall turbulent boundary layers. *Journal of Fluid Mechanics,* 37**,** 383-413.

PHILLIPS, O. M. 1969. Shear-Flow Turbulence. *Annual Review of Fluid Mechanics,* 1**,** 245-264.

RAFFEL, M., WILLERT, C. E. & KOMPENHANS, J. 2007. *Particle image velocimetry: a practical guide*, Springer Verlag.

RAUPACH, M., ANTONIA, R. & RAJAGOPALAN, S. 1991. Rough-wall turbulent boundary layers. *Applied Mechanics Reviews,* 44**,** 1-25.

REDDY, S. C., SCHMID, P. J., BAGGETT, J. S. & HENNINGSON, D. S. 1998. On stability of streamwise streaks and transition thresholds in plane channel flows. *Journal of Fluid Mechanics,* 365**,** 269-303.

REVELL, A. J., CRAFT, T. J. & LAURENCE, D. R. 2011. Turbulence modelling of unsteady turbulent flows using the stress strain lag model. *Flow, Turbulence and Combustion,* 86**,** 129-151.

ROACH, P. & BRIERLEY, D. 1992. The influence of a turbulent free stream on zero pressure gradient transitional boundary layer development part I: test cases T3A and T3B. In

Numerical Simulation of Unsteady Flows and Transition to Turbulence (ed. O. Pironneau, W. Rodi, A. M. Rhyming, L. Savill & T. V. Truong)**,** pp. 319–347.

SARKAR, A. & SO, R. M. C. 1997. A critical evaluation of near-wall two-equation models against direct numerical simulation data. *International Journal of Heat and Fluid Flow,* 18**,** 197-208.

SCHLICHTING, H. 1936. Experimentelle untersuchungen zum rauhigkeitsproblem. *Archive of Applied Mechanics,* 7**,** 1-34.

SCHLICHTING, H., GERSTEN, K. & GERSTEN, K. 2000. *Boundary-layer theory*, Springer.

SCHULTZ, M. P. & FLACK, K. A. 2009. Turbulent boundary layers on a systematically varied rough wall. *Physics of Fluids,* 21.

SCHULTZ, M. P. & FLACK, K. A. 2013. Reynolds-number scaling of turbulent channel flow. *Physics of Fluids,* 25.

SCOTTI, A. & PIOMELLI, U. 2001. Numerical simulation of pulsating turbulent channel flow. *Physics of Fluids,* 13**,** 1367-1384.

SCOTTI, A. & PIOMELLI, U. 2002. Turbulence models in pulsating flows. *AIAA Journal,* 40**,** 537-544.

SEDDIGHI, M., HE, S., ORLANDI, P. & VARDY, A. E. 2011. A comparative study of turbulence in ramp-up and ramp-down unsteady flows. *Flow, Turbulence and Combustion,* 86**,** 439-454.

SEDDIGHI, M., HE, S., VARDY, A. E., O'DONOGHUE, T. & POKRAJAC, D. 2013. DNS of a transitionally rough channel flow with a 3-D roughness. *TSFP8.*

SEDDIGHI, M., HE, S., VARDY, A. E. & ORLANDI, P. 2014. Direct numerical simulation of an accelerating channel flow. *Flow, Turbulence and Combustion,* 92**,** 473-502.

SHAW, R. 1960. The influence of hole dimensions on static pressure measurements. *Journal of Fluid Mechanics,* 7**,** 550-564.

SHIH, W. C. L., WANG, C., COLES, D. & ROSHKO, A. 1993. Experiments on flow past rough circular cylinders at large Reynolds numbers. *Journal of Wind Engineering and Industrial Aerodynamics,* 49**,** 351-368.

SHIMA, N. 1989. Calculation of a variety of boundary layers with a second-moment closure applicable up to a wall *Proceedings of 7th Symposium on Turbulent Shear Flows.* Stanford University.

SINGH, K. M., SANDHAM, N. D. & WILLIAMS, J. J. R. 2007. Numerical simulation of flow over a rough bed. *Journal of Hydraulic Engineering,* 133**,** 386-398.

SLEATH, J. F. A. 1987. Turbulent oscillatory flow over rough beds. *Journal of Fluid Mechanics,* 182**,** 369-409.

SMITS, A. J. & WOOD, D. H. 1985. The response of turbulent boundary layers to sudden perturbations. *Annual Review of Fluid Mechanics***,** 321-358.

TANI, I. 1987. Turbulent boundary layer development over rough surfaces. *Perspectives in turbulence studies.* Springer.

TARDU, S. F. & DA COSTA, P. 2005. Experiments and modeling of an unsteady turbulent channel flow. *AIAA Journal,* 43**,** 140-148.

TAYLOR, G. I. 1938. The spectrum of turbulence. *Proceedings of the Royal Society of London Series a-Mathematical and Physical Sciences,* 164**,** 0476-0490.

TOIT, C. G. D. & SLEATH, J. F. A. 1981. Velocity measurements close to rippled beds in oscillatory flow. *Journal of Fluid Mechanics,* 112**,** 71-96.

TOWNSEND, A. A. 1976. *The structure of turbulent shear flow*, Cambridge University Press.

TU, S. W. & RAMAPRIAN, B. R. 1983. Fully developed periodic turbulent pipe flow. Part 1. Main experimental results and comparison with predictions. *Journal of Fluid Mechanics,* 137**,** 31-58.

UCHIDA, S. 1956. The pulsating viscous flow superposed on the steady laminar motion of incompressible fluid in a circular pipe. *Zeitschrift für angewandte Mathematik und Physik ZAMP,* 7**,** 403-422.

VAUGHAN, N. J. & ZAKI, T. A. 2011. Stability of zero-pressure-gradient boundary layer distorted by unsteady Klebanoff streaks. *Journal of Fluid Mechanics,* 681**,** 116-153.

WEBB, R. L., ECKERT, E. R. G. & GOLDSTEIN, R. J. 1971. Heat transfer and friction in tubes with repeated-rib roughness. *International Journal of Heat and Mass Transfer,* 14**,** 601-617.

WEI, T. & WILLMARTH, W. W. 1989. Reynolds-number effects on the structure of a turbulent channel flow. *Journal of Fluid Mechanics,* 204**,** 57-95.

WILCOX, D. C. 1994. Simulation of transition with a two-equation turbulence model. *AIAA journal,* 32**,** 247-255.

WU, X. & MOIN, P. 2009. Direct numerical simulation of turbulence in a nominally zero-pressure-gradient flat-plate boundary layer. *Journal of Fluid Mechanics,* 630**,** 5-41.

YANG, Z. & SHIH, T. H. 1993. New time scale based κ-ε model for near-wall turbulence. *AIAA Journal,* 31**,** 1191-1198.

ZAGAROLA, M. V. & SMITS, A. J. 1998. Mean-flow scaling of turbulent pipe flow. *Journal of Fluid Mechanics,* 373**,** 33-79.

ZAKI, T. A. 2013. From Streaks to Spots and on to Turbulence: Exploring the Dynamics of Boundary Layer Transition. *Flow, Turbulence and Combustion***,** 1-23.

ZANOUN, E. S., DURST, F. & NAGIB, H. 2003. Evaluating the law of the wall in two-dimensional fully developed turbulent channel flows. *Physics of Fluids,* 15**,** 3079-3089.

Appendix

A. Unsteady history profiles for various cases over smooth surfaces

This section provides the dimensional data obtained from the LDV of smooth unsteady flows. The water temperature is provided for reference above the figures.

S23-250, measured at 22 (°C):

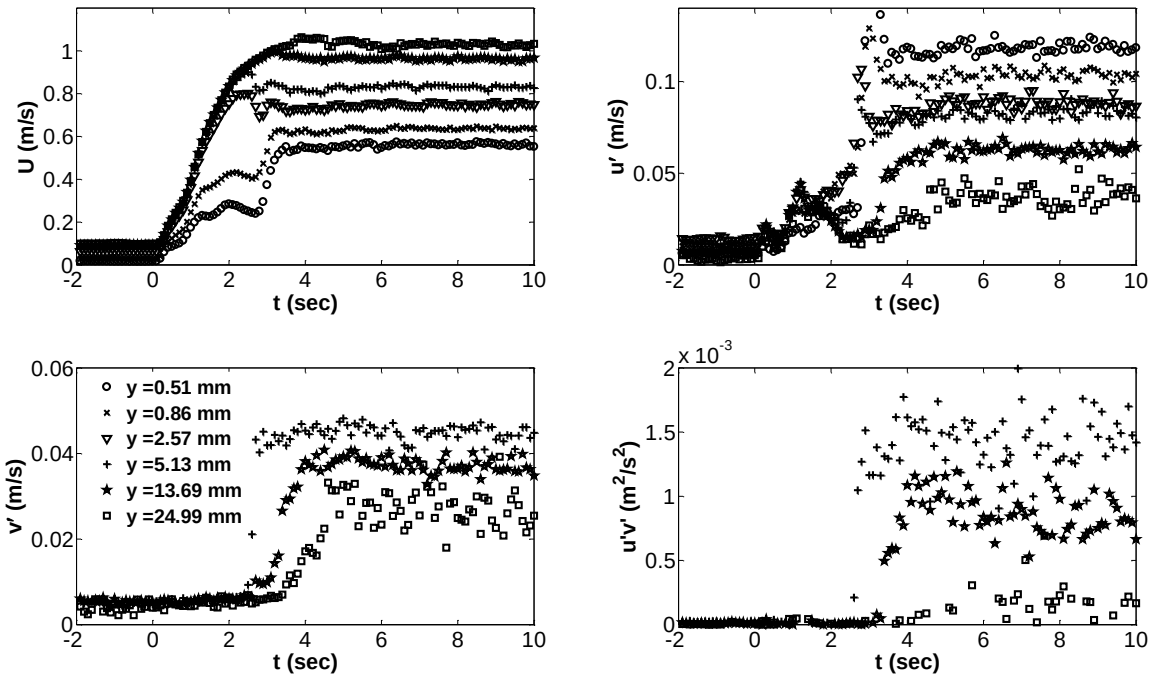

Figure A. 1 continued on next page.

S23-200, measured at 26 (°C):

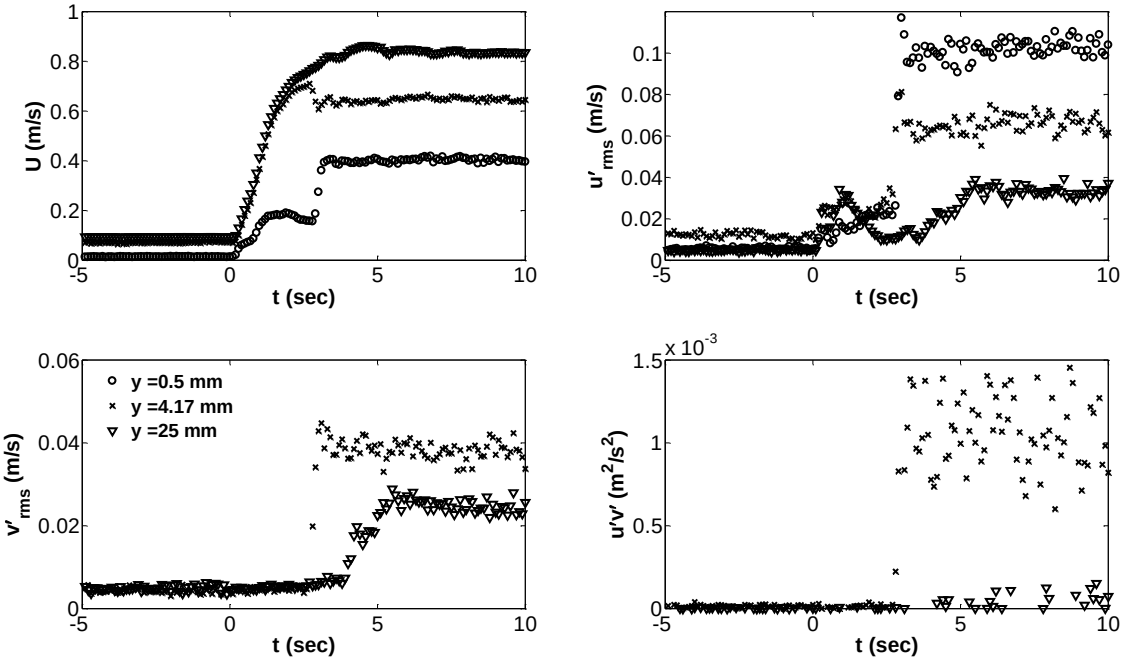

S23-180, measured at 26 (°C):

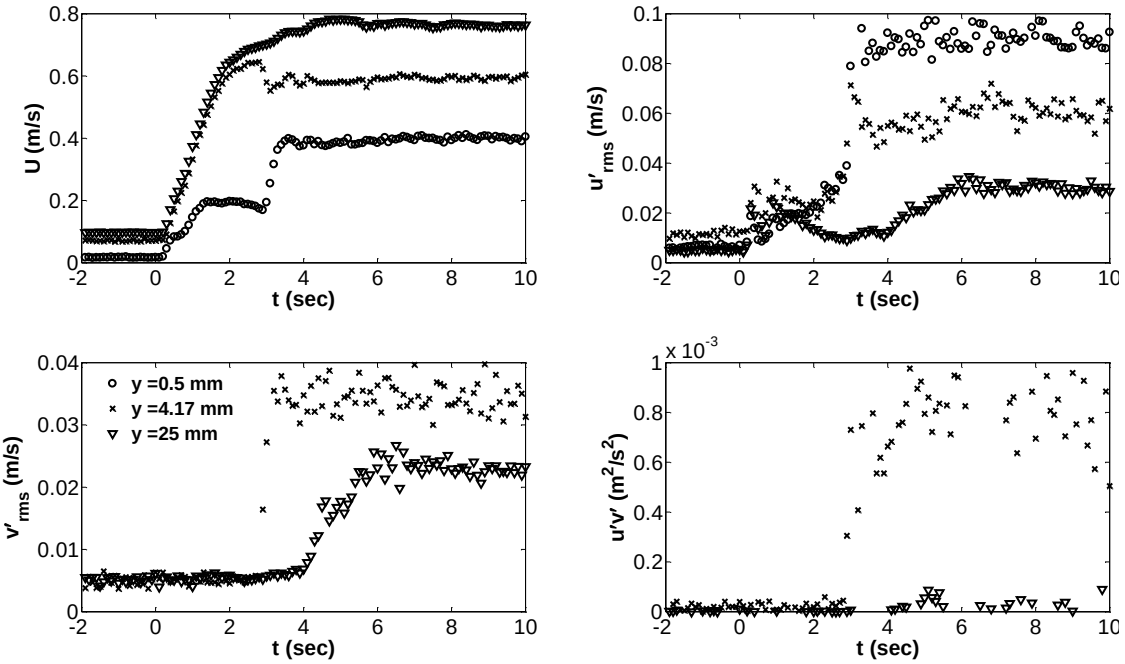

Figure A. 1 continued on next page.

S23-135, measured at 26 (°C):

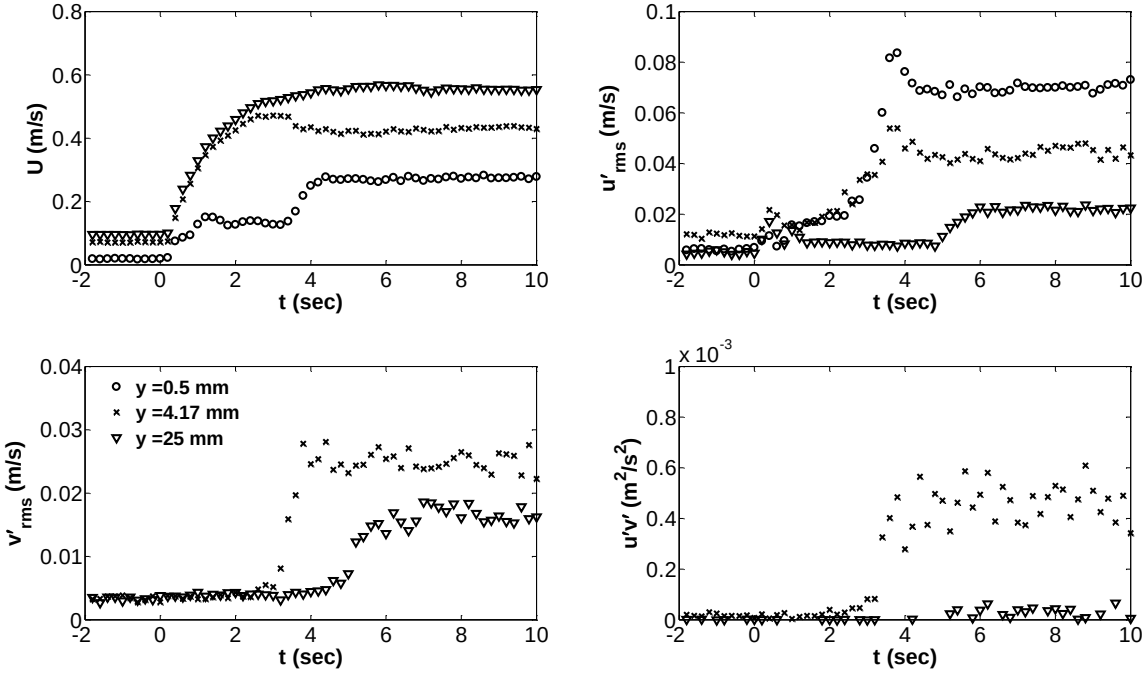

S23-93, measured at 26 (°C):

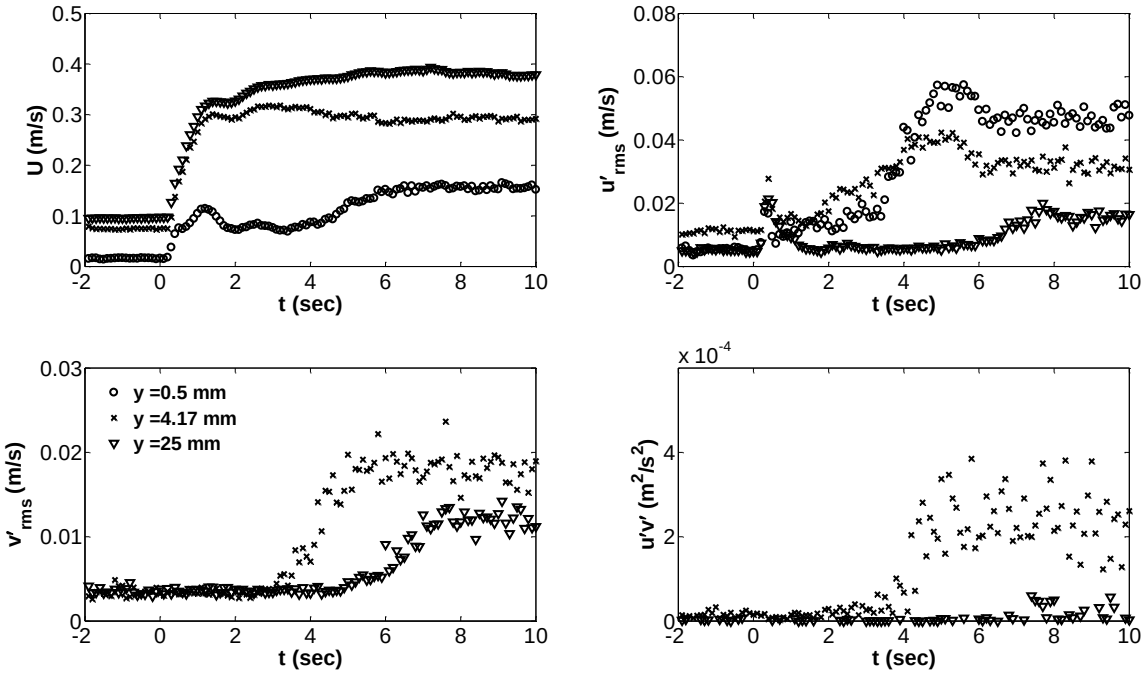

Figure A. 1 continued on next page.

S29-250, measured at 26 (°C):

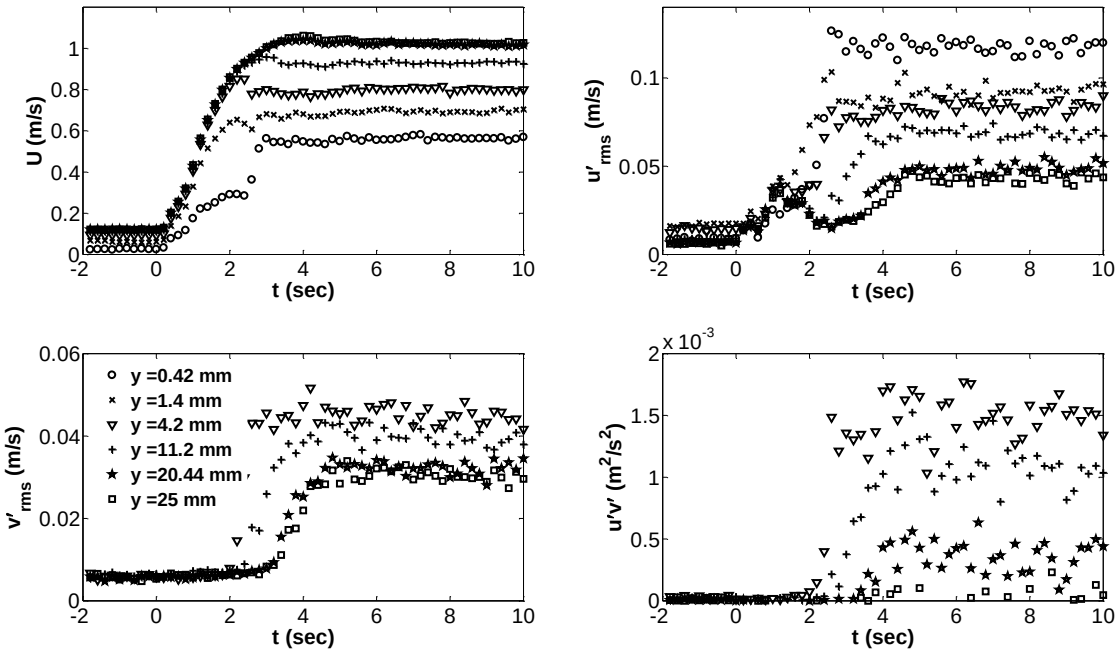

S29-76, measured at 22 (°C):

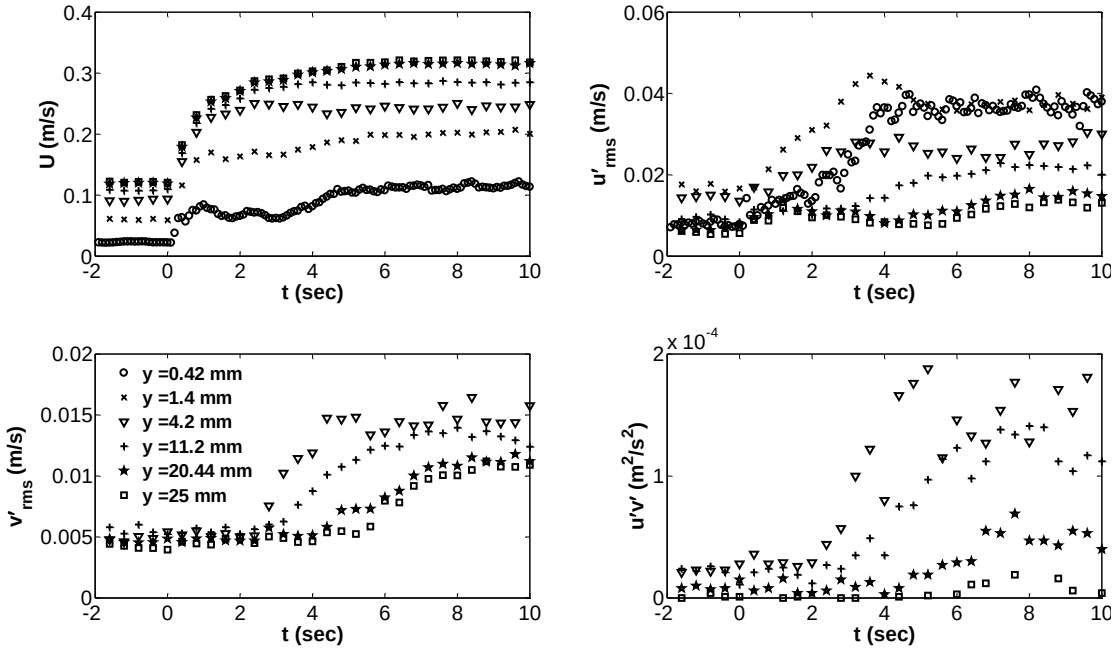

Figure A. 1 continued on next page.

S29-53, measured at 26 (°C):

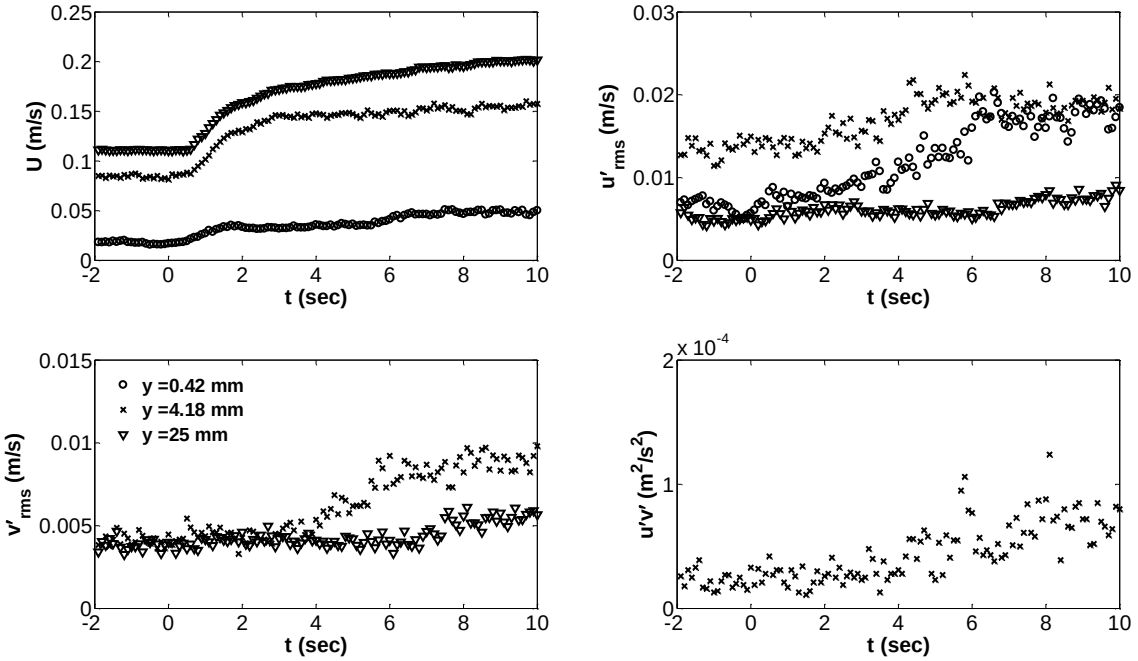

S35-250, measured at 23 (°C):

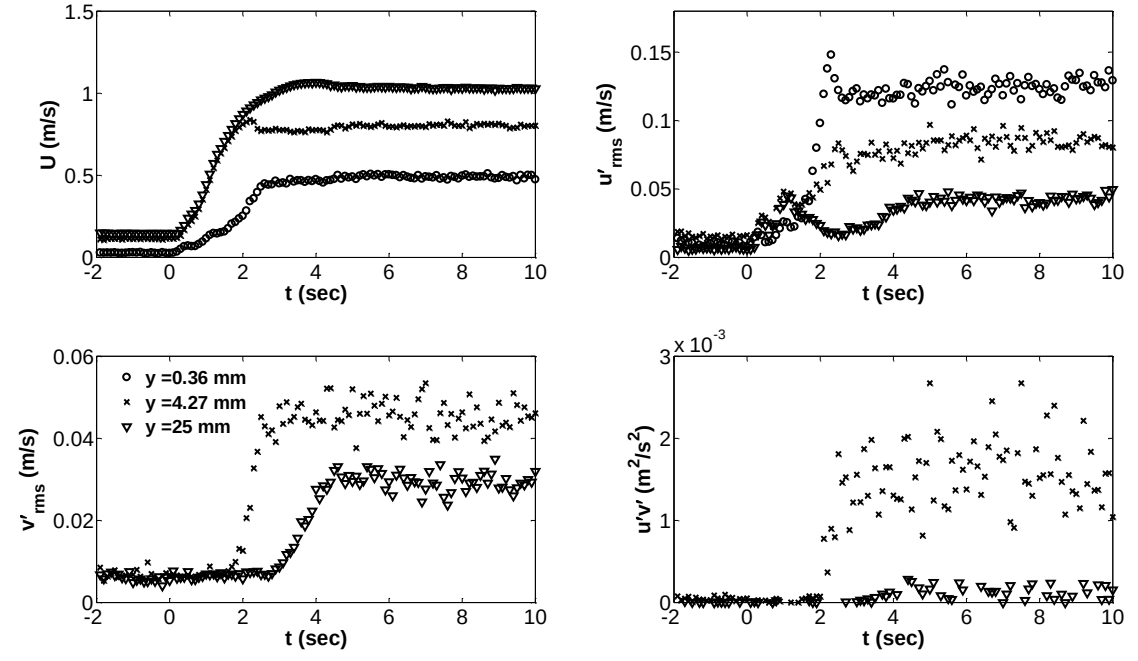

Figure A. 1 continued on next page.

S60-250, measured at 26 (°C):

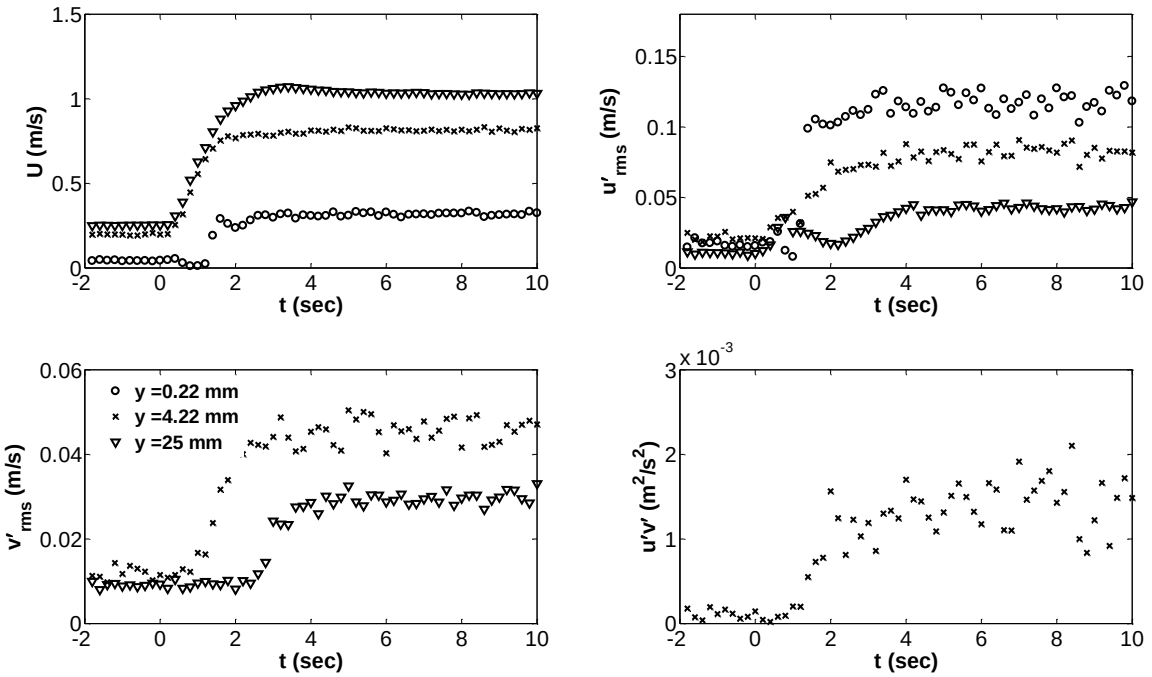

S90-250, measured at 26 (°C):

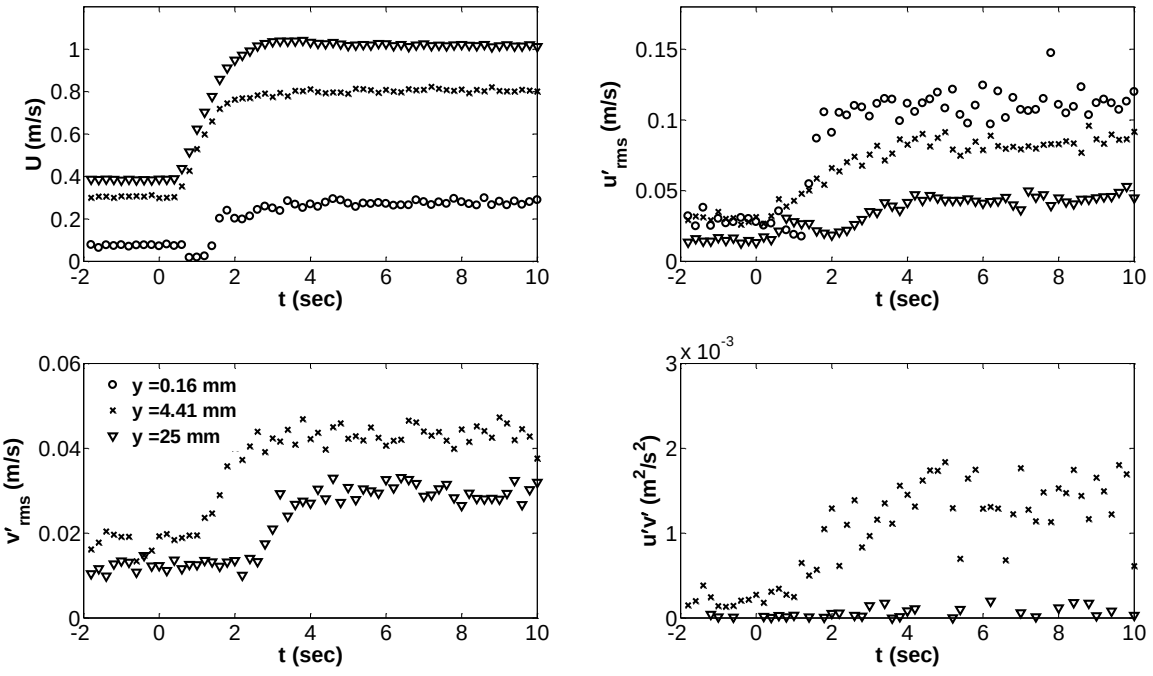

Figure A. 1 Mean and turbulent quantities for various unsteady flows over smooth surfaces.

B. Unsteady history profiles for various cases over rough surfaces

This section provides the dimensional data obtained from the PIV of rough unsteady flows. The water temperature is provided for reference above the figures.

R23-250, measured at 21 (°C):

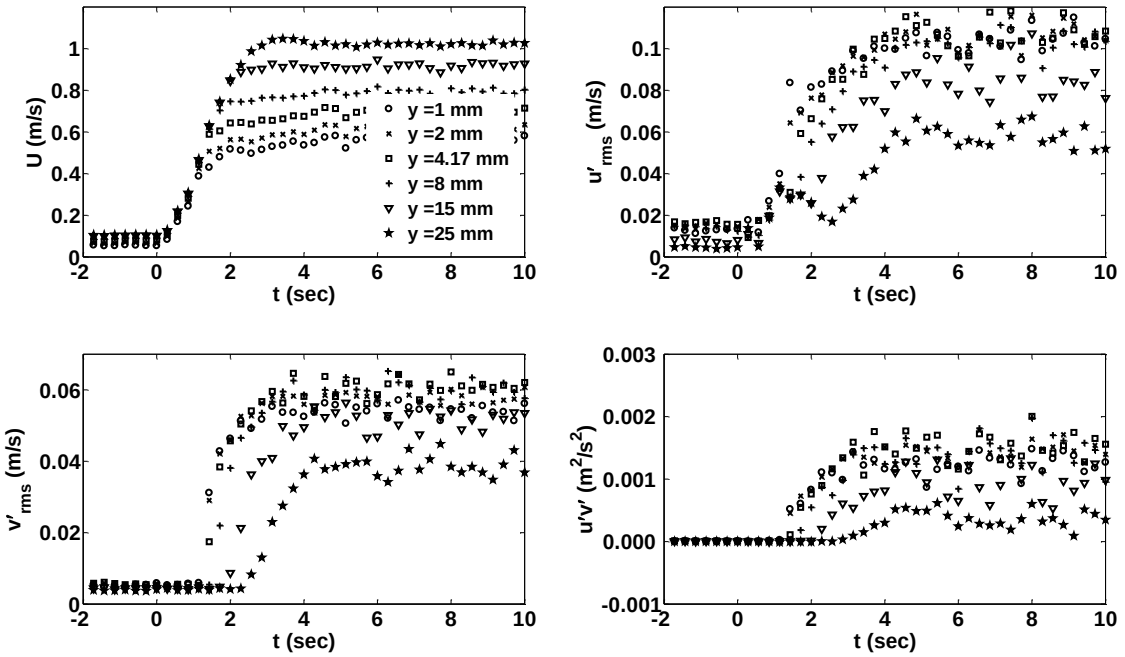

R23-200, measured at 22 (°C):

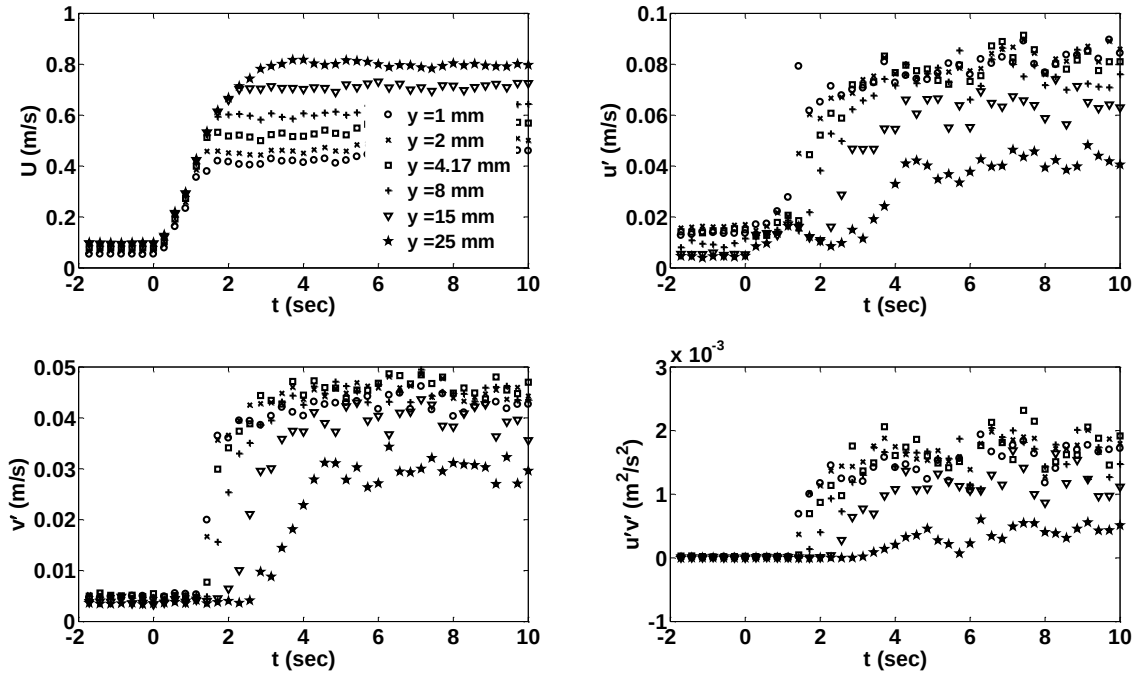

Figure B. 1 continued on next page.

R23-180, measured at 23 (°C):

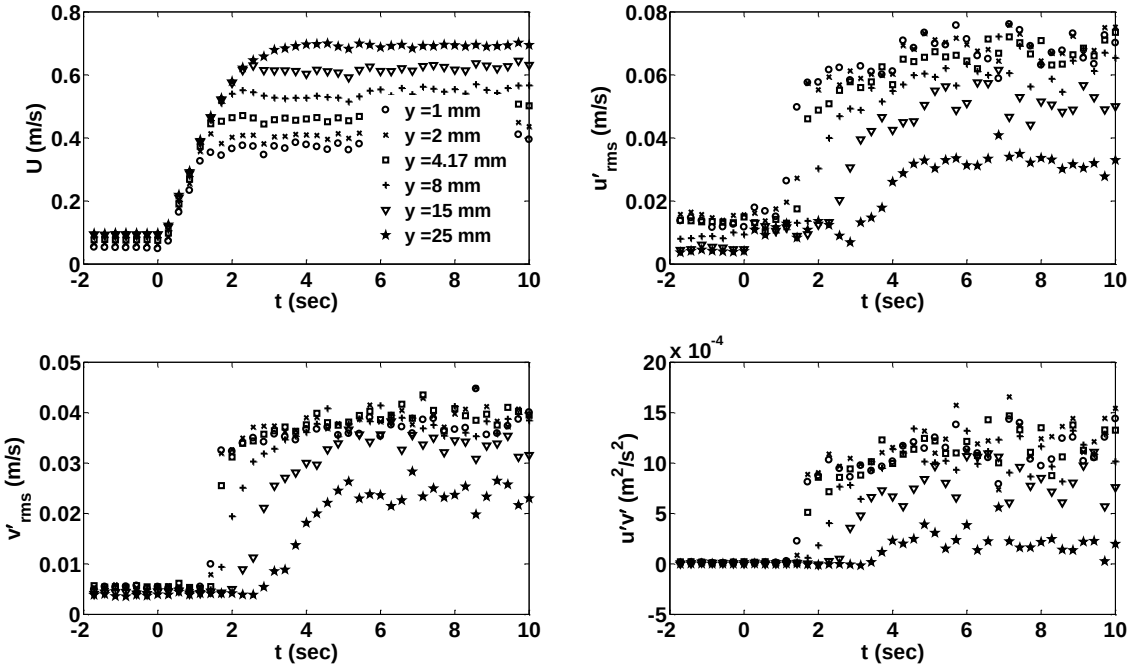

R23-135, measured at 24 (°C):

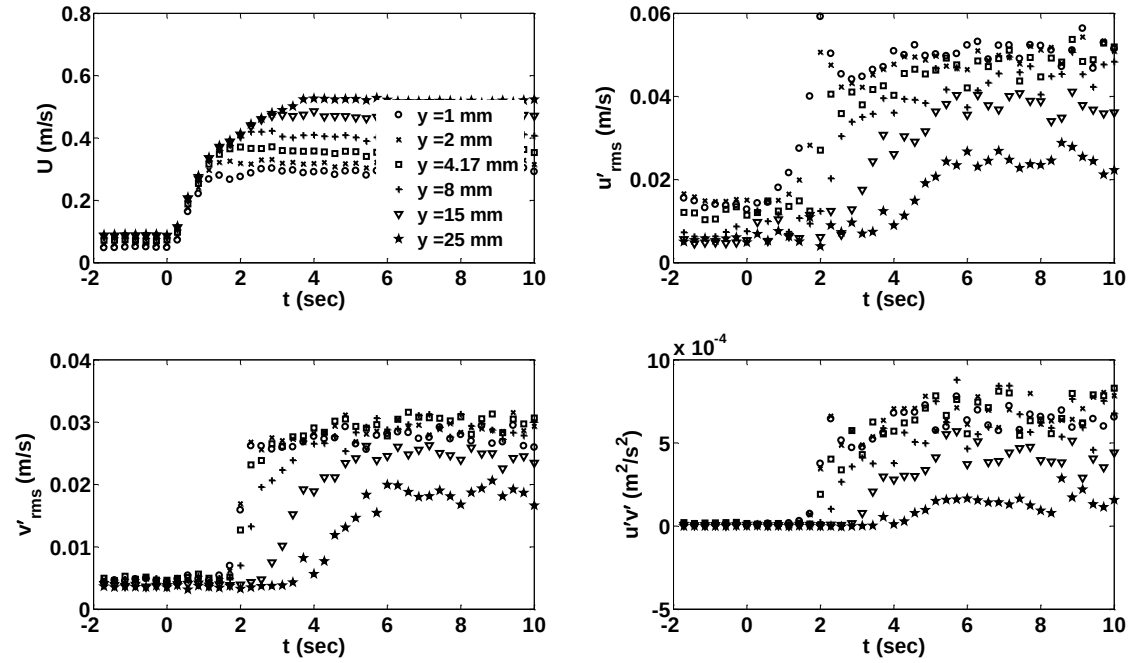

Figure B. 1 continued on next page.

R23-93, measured at 23 (°C):

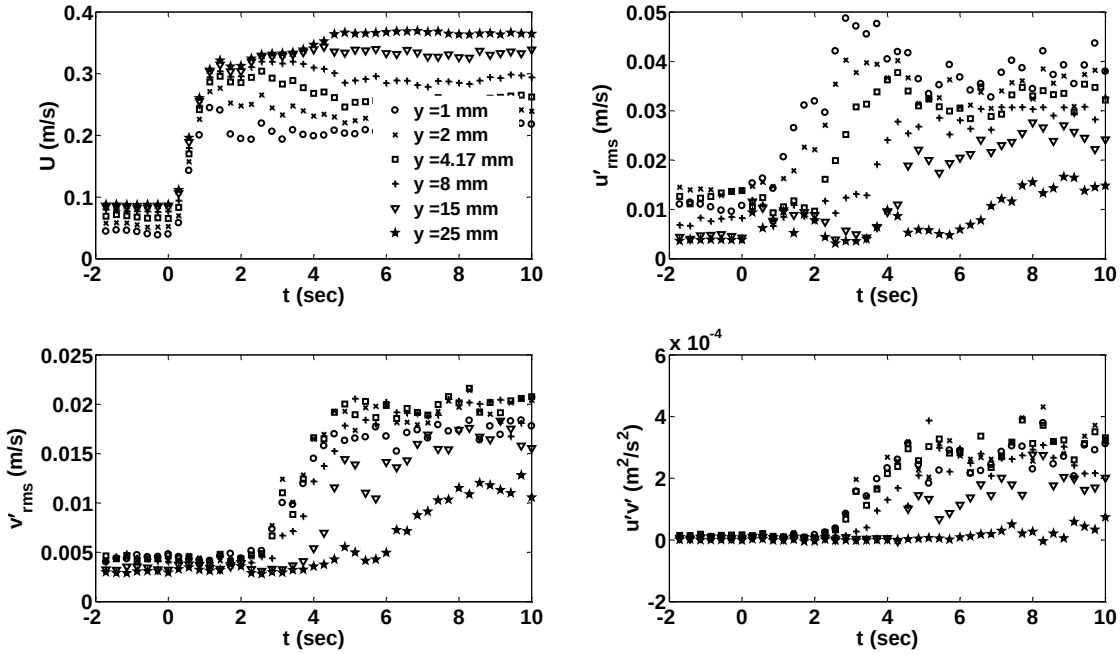

R29-250, measured at 23 (°C):

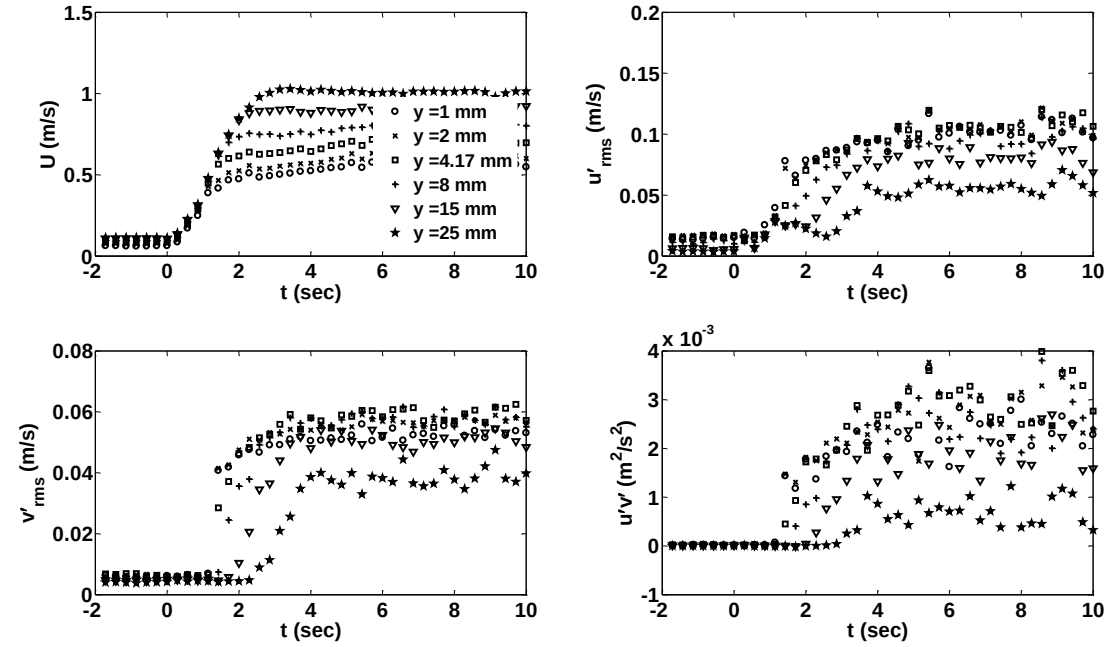

Figure B. 1 continued on next page.

R29-76, measured at 24 (°C):

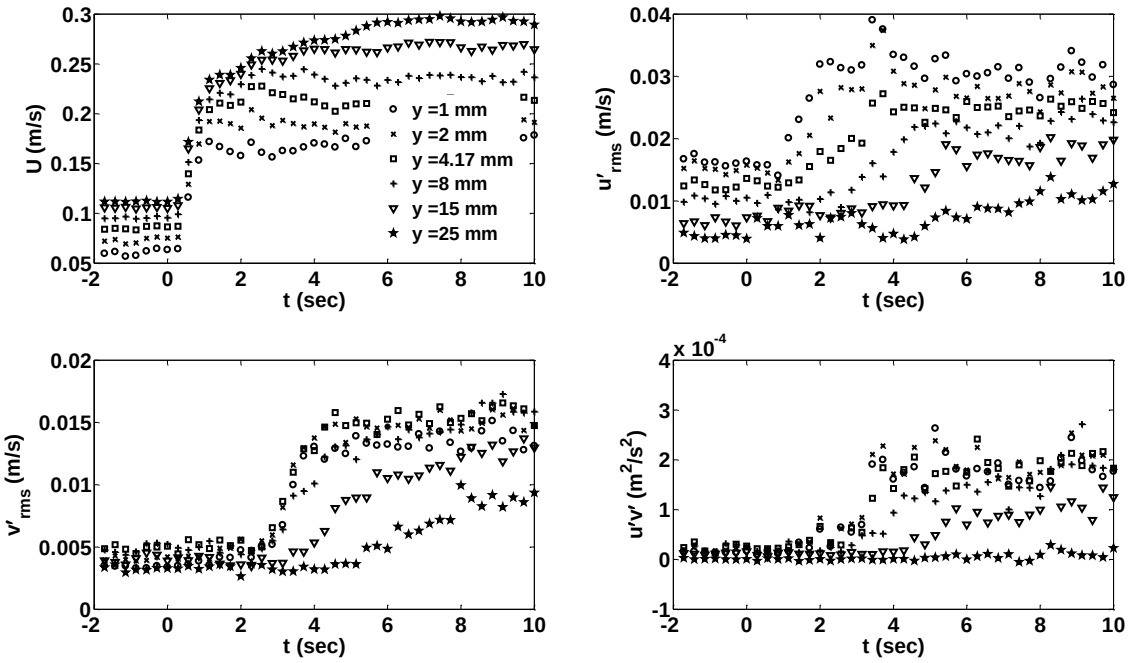

Figure B. 1 Mean and turbulent quantities for various unsteady flows over rough surfaces.